COLLOIDAL SEMICONDUCTOR NANOCRYSTALS: SYNTHESIS, PROPERTIES, AND APPLICATIONS

EDITED BY: Vladimir Lesnyak, Maksym Yarema and Shiding Miao
PUBLISHED IN: Frontiers in Chemistry

frontiers Research Topics

frontiers

ISSN 1664-8714
ISBN 978-2-88963-269-5
DOI 10.3389/978-2-88963-269-5

About Frontiers

Frontiers is more than just an open-access publisher of scholarly articles: it is a pioneering approach to the world of academia, radically improving the way scholarly research is managed. The grand vision of Frontiers is a world where all people have an equal opportunity to seek, share and generate knowledge. Frontiers provides immediate and permanent online open access to all its publications, but this alone is not enough to realize our grand goals.

Frontiers Journal Series

The Frontiers Journal Series is a multi-tier and interdisciplinary set of open-access, online journals, promising a paradigm shift from the current review, selection and dissemination processes in academic publishing. All Frontiers journals are driven by researchers for researchers; therefore, they constitute a service to the scholarly community. At the same time, the Frontiers Journal Series operates on a revolutionary invention, the tiered publishing system, initially addressing specific communities of scholars, and gradually climbing up to broader public understanding, thus serving the interests of the lay society, too.

Dedication to Quality

Each Frontiers article is a landmark of the highest quality, thanks to genuinely collaborative interactions between authors and review editors, who include some of the world's best academicians. Research must be certified by peers before entering a stream of knowledge that may eventually reach the public - and shape society; therefore, Frontiers only applies the most rigorous and unbiased reviews.
Frontiers revolutionizes research publishing by freely delivering the most outstanding research, evaluated with no bias from both the academic and social point of view. By applying the most advanced information technologies, Frontiers is catapulting scholarly publishing into a new generation.

What are Frontiers Research Topics?

Frontiers Research Topics are very popular trademarks of the Frontiers Journals Series: they are collections of at least ten articles, all centered on a particular subject. With their unique mix of varied contributions from Original Research to Review Articles, Frontiers Research Topics unify the most influential researchers, the latest key findings and historical advances in a hot research area! Find out more on how to host your own Frontiers Research Topic or contribute to one as an author by contacting the Frontiers Editorial Office: researchtopics@frontiersin.org

COLLOIDAL SEMICONDUCTOR NANOCRYSTALS: SYNTHESIS, PROPERTIES, AND APPLICATIONS

Topic Editors:
Vladimir Lesnyak, TU Dresden, Germany
Maksym Yarema, ETH Zürich, Switzerland
Shiding Miao, Jilin University, China

Citation: Lesnyak, V., Yarema, M., Miao, S., eds. (2020). Colloidal Semiconductor Nanocrystals: Synthesis, Properties, and Applications. Lausanne: Frontiers Media SA. doi: 10.3389/978-2-88963-269-5

Table of Contents

04 ***Editorial: Colloidal Semiconductor Nanocrystals: Synthesis, Properties, and Applications***
Vladimir Lesnyak, Maksym Yarema and Shiding Miao

06 ***Chemical Synthesis and Applications of Colloidal Metal Phosphide Nanocrystals***
Hui Li, Chao Jia, Xianwei Meng and Hongbo Li

21 ***Influence of the Core/Shell Structure of Indium Phosphide Based Quantum Dots on Their Photostability and Cytotoxicity***
Karl David Wegner, Fanny Dussert, Delphine Truffier-Boutry, Anass Benayad, David Beal, Lucia Mattera, Wai Li Ling, Marie Carrière and Peter Reiss

33 ***Robust Hydrophobic and Hydrophilic Polymer Fibers Sensitized by Inorganic and Hybrid Lead Halide Perovskite Nanocrystal Emitters***
Paris G. Papagiorgis, Andreas Manoli, Androniki Alexiou, Petroula Karacosta, Xenofon Karagiorgis, Georgia Papaparaskeva, Caterina Bernasconi, Maryna I. Bodnarchuk, Maksym V. Kovalenko, Theodora Krasia-Christoforou and Grigorios Itskos

45 ***Water-Borne Perovskite Quantum Dot-Loaded, Polystyrene Latex Ink***
Keke Huang, Lucheng Peng, Baijun Liu, Dongze Li, Qiang Ma, Mingyao Zhang, Renguo Xie, Dayang Wang and Wensheng Yang

53 ***Challenges and Prospects of Photocatalytic Applications Utilizing Semiconductor Nanocrystals***
Pavel Moroz, Anthony Boddy and Mikhail Zamkov

60 ***Impact of Crystal Structure and Particles Shape on the Photoluminescence Intensity of CdSe/CdS Core/Shell Nanocrystals***
Lukas Ludescher, Dmity N. Dirin, Maksym V. Kovalenko, Michael Sztucki, Peter Boesecke and Rainer T. Lechner

71 ***Quantum Dots Synthesis Through Direct Laser Patterning: A Review***
Francesco Antolini and Leonardo Orazi

87 ***Photoluminescence Lifetime Based Investigations of Linker Mediated Electronic Connectivity Between Substrate and Nanoparticle***
Jan F. Miethe, Franziska Lübkemann, Nadja C. Bigall and Dirk Dorfs

98 ***Road Map for Nanocrystal Based Infrared Photodetectors***
Clément Livache, Bertille Martinez, Nicolas Goubet, Julien Ramade and Emmanuel Lhuillier

frontiers in Chemistry

EDITORIAL
published: 22 October 2019
doi: 10.3389/fchem.2019.00684

Editorial: Colloidal Semiconductor Nanocrystals: Synthesis, Properties, and Applications

Vladimir Lesnyak[1]*, *Maksym Yarema*[2]* and *Shiding Miao*[3]

[1] Physical Chemistry, TU Dresden, Dresden, Germany, [2] Chemistry and Materials Design Group, Department of Information Technology and Electrical Engineering, ETH Zurich, Zurich, Switzerland, [3] Key Laboratory of Automobile Materials of Ministry of Education, Department of Materials Science and Engineering, Jilin University, Changchun, China

Keywords: semiconductor nanocrystals, quantum dots, colloids, perovskite, phosphide, photocatalysis, infrared photodetectors, laser patterning

Editorial on the Research Topic

Colloidal Semiconductor Nanocrystals: Synthesis, Properties, and Applications

OPEN ACCESS

Edited by:
Fan Zhang,
Fudan University, China

Reviewed by:
Benjamin T. Diroll,
Argonne National Laboratory (DOE), United States
Xiaoji Xie,
Nanjing Tech University, China

***Correspondence:**
Vladimir Lesnyak
vladimir.lesnyak@chemie.tu-dresden.de
Maksym Yarema
yaremam@ethz.ch

Specialty section:
This article was submitted to Nanoscience, a section of the journal Frontiers in Chemistry

Received: *09 July 2019*
Accepted: *01 October 2019*
Published: *22 October 2019*

Citation:
Lesnyak V, Yarema M and Miao S (2019) Editorial: Colloidal Semiconductor Nanocrystals: Synthesis, Properties, and Applications. Front. Chem. 7:684. doi: 10.3389/fchem.2019.00684

Colloidal semiconductor nanocrystals (also known as quantum dots) have evolved during the last few decades from purely fundamental concepts to industry-scale commercial products (e.g., Samsung QLED TV displays, in which quantum dots are utilized as color converters). A vivid interest to and rapid development of colloidal nanomaterials is caused by their unique size-dependent optoelectronic properties (based on quantum confinement effects) and by the solution-based synthesis and device fabrication protocols (which are remarkably simple, fast but highly customizable processes).

To date, a large variety of semiconductors are prepared in the form of colloidal nanocrystals, including most-common families of semiconductor materials (i.e., II–VI, IV–VI, III–V, I–III–VI, I–II–IV–VI, and I–IV–VII compounds with corresponding examples being CdSe, PbS, InP, $CuInS_2$, Cu_2ZnSnS_4, and $CsPbBr_3$). Manipulating the reaction conditions (temperature, time, chemistry choice, etc.) provides an accurate control over size and size distribution, morphology, and crystal structure of colloidal nanocrystals. Two or more semiconductors can be combined in one nano-object, resulting in various segmented morphology (e.g., core-shell, dot-in-rod, Janus-type particles, etc.). The surface chemistry of semiconductor colloids can also be tailored via post-synthetic functionalization and ligand exchange surface reactions. Colloidal semiconductor nanocrystals thus become truly interdisciplinary field of science with complex chemistry and physics underlying these apparently simple materials.

In this Research Topic we present a collection of original research and review articles touching upon different aspects of semiconductor nanocrystals, including their synthesis in liquid media (Li et al.) and in solid state via laser patterning (Antolini and Orazi), integration into polymer matrices (Huang et al.; Papagiorgis et al.), applications in photocatalysis, and infrared photodetectors (Livache et al.; Moroz et al.). The Research Topic provides interesting insights into the impact of crystal structure of quantum dots on their fluorescence properties (Ludescher et al.) and into the linking of semiconductor nanocrystals to widely used transparent conductive substrates (Miethe et al.). Materials highlighted in this Topic span from classical CdSe-based structures (Ludescher et al.; Miethe et al.) to nowadays booming lead halide-based perovskite nanocrystals (Huang et al.; Papagiorgis et al.), metal phosphides family (Li et al.; Wegner et al.), and infrared active quantum dots (Livache et al.).

Original research papers of Itskos and Xie groups address well-known problem of insufficient stability of lead halide perovskite nanocrystals, a roadblock toward many

industry-scale applications (Huang et al.; Papagiorgis et al.). Papagiorgis et al. employ an electrospinning to produce nanocrystals-in-polymer fibers. The robust composites are prepared either by direct electrospinning mixtures of the nanocrystals in toluene with hydrophobic poly(methyl methacrylate) dissolved in chloroform or by immersion of electrospun hydrophilic polyvinylpyrrolidone membranes into the nanocrystal solutions. Remarkably, the authors achieve a yearlong stability of the prepared composites. Huang et al. propose a facile embedding strategy of nanocrystals into polysterene microparticles (beads) via deliberate control of their swelling in a mixture of solvents. Such nanocrystals-in-polymer composite particles can be tranferred into water, forming stable dispersions with outstanding structural and chemical stability upon prolonged storage time, intense light irradiation, and heat. These approaches help toward successful applications of the perovskite-in-polymer composites as efficient color converters in displays and textile-based flexible light emitting devices (Huang et al.; Papagiorgis et al.).

The work of Lechner group investigates a structural origin of excellent photoluminescence properties of CdSe-CdS core-shell nanocrystals (Ludescher et al.). Using X-ray scattering techniques, the authors retrieve the mean shape and surface of nanocrystals and reveal an elliptical shape with pronounced surface facets for larger nanocrystals related to a mixture of crystal phases within the CdSe core. Correlating the structural and optical data, Ludescher et al. establish the structure-property link between the shape and shell thickness of CdSe-CdS nanocrystals and their photoluminescence efficiency. Dorfs and Bigall groups utilize dot-in-rod CdSe-CdS nanocrystals as an optically addressable probe for the electronic surface states of the transparent indium tin oxide (ITO) conductive glass (Miethe et al.). This study provides the proof of electronic interconnections in ITO-coated glass/linker/nanorod electrodes via easy reproducible functionalization and polishing experiments. Optical characterization reveals changes in the charge carrier dynamics within the system depending on linker molecules.

The contribution of Reiss group concerns a shell engineering of InP-based core-shell nanocrystals, a key Cd-free color converter material nowadays (Wegner et al.). The authors investigate a photostability of InP-based nanocrystals for three different shell compositions: single gradient $ZnSe_xS_{1-x}$ shell, additional ZnS shell on top of $ZnSe_xS_{1-x}$, and alumina-coated InP-$ZnSe_xS_{1-x}$-ZnS nanocrystals. The latter heterostructures exhibit the highest stability upon continuous irradiation with simulated sunlight in a climate chamber.

This Research Topic features several review articles with distinct scopes (Antolini and Orazi; Li et al.; Livache et al.; Moroz et al.). Li et al. discuss metal phosphide nanocrystal colloids. In particular, the authors detail synthetic strategies for InP nanocrystals, highlighting benefits of employing zinc precursors as reaction additives and the importance of different phosphorus precursors to improve the quality of the materials. The authors discuss synthetic approaches for other metal phosphide nanocrystals, such as II–V metal phosphides (Cd_3P_2, Zn_3P_2) and transition metal phosphides (Cu_3P, FeP), and summarize their potential applications in photovoltaics, light-emitting diodes, and lithium-ion batteries. Moroz et al. review photocatalytic systems based on colloidal semiconductor nanocrystals coupled to metal catalysts. In such systems, nanocrystal sensitizers demonstrate a compelling performance in homogeneous photoreduction reactions (e.g., the degradation of organic dyes and hydrogen generation), however, the progress beyond half-cycle reactions remains limited. The authors state main challenges and outline perspective directions in the field of photocatalytic applications of nanocrystal colloids (i.e., the possibility of harvesting triplet excitons and utilizing nanocrystal assemblies to accumulate multiple charges at the reaction site). Livache et al. provide a comprehensive view on state-of-the-art nanocrystal-based infrared photodetectors. After a decade of intensive research, infrared colloidal nanocrystals reach high maturity level to be considered as an alternative to the epitaxially-grown infrared semiconductors. The authors highlight the benefits of colloidal nanocrystals, including full tunability of their infrared absorption, reduced production costs, realization of background-limited impurity photoconductor photodiodes, and demonstration of nanocrystal-based focal plane arrays. The authors propose a road map to address remaining challenges in order to promote the infrared nanocrystal-based technology to the industrial level. Antolini and Orazi introduce direct laser patterning approaches to the II-VI semiconductor nanocrystals (e.g., a laser-assisted conversion of precursors) as a simple yet powerful way to produce quantum dots in the solid state. The authors discuss laser parameters (wavelength, pulse duration) and chemistry of precursors to fabricate quantum dot thin film structures with excellent optical properties.

We hope this Research Topic attracts interested readers, providing novel literature insights, synergistic research ideas and enthusiasm in research and studies. Enjoy its reading!

AUTHOR CONTRIBUTIONS

All authors listed have made a substantial, direct and intellectual contribution to the work, and approved it for publication.

ACKNOWLEDGMENTS

MY acknowledges financial support from the Swiss National Science foundation via an Ambizione Fellowship (No. 161249).

Conflict of Interest: The authors declare that the research was conducted in the absence of any commercial or financial relationships that could be construed as a potential conflict of interest.

frontiers in Chemistry

REVIEW
published: 08 January 2019
doi: 10.3389/fchem.2018.00652

Chemical Synthesis and Applications of Colloidal Metal Phosphide Nanocrystals

Hui Li[1], *Chao Jia*[1], *Xianwei Meng*[2] *and Hongbo Li*[1]*

[1] *Beijing Key Laboratory of Construction-Tailorable Advanced Functional Materials and Green Applications, School of Materials Science & Engineering, Beijing Institute of Technology, Beijing, China,* [2] *Laboratory of Controllable Preparation and Application of Nanomaterials, CAS Key Laboratory of Cryogenics, Technical Institute of Physics and Chemistry, Chinese Academy of Sciences, Beijing, China*

Colloidal nanocrystals (NCs) have emerged as promising materials in optoelectronic devices and biological imaging application due to their tailorable properties through size, shape, and composition. Among these NCs, metal phosphide is an important class, in parallel with metal chalcogenide. In this review, we summarize the recent progress regarding the chemical synthesis and applications of colloidal metal phosphide NCs. As the most important metal phosphide NCs, indium phosphide (InP) NCs have been intensively investigated because of their low toxicity, wide and tunable emission range from visible to the near-infrared region. Firstly, we give a brief overview of synthetic strategies to InP NCs, highlighting the benefit of employing zinc precursors as reaction additive and the importance of different phosphorus precursors to improve the quality of the InP NCs, in terms of size distribution, quantum yield, colloidal stability, and non-blinking behavior. Next, we discuss additional synthetic techniques to overcome the issues of lattice mismatch in the synthesis of core/shell metal phosphide NCs, by constructing an intermediate layer between core/shell or designing a shell with gradient composition in a radial direction. We also envision future research directions of InP NCs. The chemical synthesis of other metal phosphide NCs, such as II–V metal phosphide NCs (Cd_3P_2, Zn_3P_2) and transition metal phosphides NCs (Cu_3P, FeP) is subsequently introduced. We finally discuss the potential applications of colloidal metal phosphide NCs in photovoltaics, light-emitting diodes, and lithium ion battery. An overview of several key applications based on colloidal metal phosphide NCs is provided at the end.

Keywords: colloidal nanocrystals, indium phosphide, phosphorus precursors, II-V metal phosphide nanocrystals, transition metal phosphides nanocrystals

OPEN ACCESS

Edited by:
Vladimir Lesnyak, Technische Universität Dresden, Germany

Reviewed by:
Sergey V. Gaponenko, BI Stepanov Institute of Physics (NASB), Belarus
Zhenmeng Peng, University of Akron, United States

***Correspondence:**
Hongbo Li
hbli@mail.ipc.ac.cn

Specialty section:
This article was submitted to Nanoscience, a section of the journal Frontiers in Chemistry

Received: *28 September 2018*
Accepted: *13 December 2018*
Published: *08 January 2019*

Citation:
Li H, Jia C, Meng X and Li H (2019) Chemical Synthesis and Applications of Colloidal Metal Phosphide Nanocrystals. Front. Chem. 6:652. doi: 10.3389/fchem.2018.00652

INTRODUCTION

Colloidal nanocrystals (NCs) that exhibit unique optical and electrical properties have attracted considerable attention due to diverse applications such as photovoltaics, optoelectronics, (Coe et al., 2002; Dai et al., 2014; Pietryga et al., 2016; Panfil et al., 2018), and biomedical imaging (Michalet et al., 2005; Hong et al., 2017). Among these NCs, metal phosphide NCs are chemical compounds containing phosphorus and one or more metals, with formula of M_xP_y. Phosphorus is known to be able to form at least one stable compounds (e.g., InP, Cu_3P) with d-group metals and most of the rare earth metals. Besides, many metal phosphides have multiple stoichiometry,

providing various crystal structures for binary metal phosphides. Most of the metal phosphide NCs share metal–metalloid bonds (M–P) with a strong covalent component (Greenwood et al., 1966). These bonds are often combined with highly covalent metalloid–metalloid bonds (P–P) (Carenco et al., 2013), where the formation of covalent bond requires harsher reaction conditions for the colloidal chemical synthesis, such as highly active precursors or high reaction temperature. Unlike the metal chalcogenide, metal phosphide can be semiconductors, insulators, and conductors, which are highly dependent on the chemical composition, crystal structure, and electronic state. These specific features provide metal phosphides with unique properties, and also facilitate many potential applications.

Nowadays, conventional cadmium and lead based NCs have been judged because of environmental concerns on heavy metals. Therefore, InP NCs present an attractive alternative owing to low toxicity and emission tunability ranging from visible to near-infrared region (Ramasamy et al., 2017). Zinc phosphide (Zn_3P_2) is an intriguing material for photovoltaic (Luber et al., 2013). It has a band gap of 1.5 eV, a large absorption coefficient, a long minority-carrier diffusion length. Transition metal phosphides also have great potential in energy conversion and storage applications.

To synthesize colloidal NCs, cationic, and anionic precursors are indispensable with ligands, non-coordinating solvent as well as high temperature exposure to advance reaction. As for anion precursors in metal phosphide NCs, phosphorus precursors that have been used in the colloidal synthesis can be classified into different types, including the single source precursor ($In(PBu^t_2)_3$) (Green and O'Brien, 1998), $P(SiMe_3)_3$, metal phosphorus (Na_3P) (Jun et al., 2006), magic sized clusters (MSCs) (Friedfeld et al., 2017), elemental phosphorus precursor (Ung et al., 2008; Bang et al., 2017), and PH_3 gas (Zan and Ren, 2012). **Figure 1** shows different types of phosphorus precursors that have been applied in the chemical synthesis of metal phosphide NCs. Regardless of investigations of various phosphorus precursors, $P(SiMe_3)_3$ tend to obtain high quality of InP NCs. However, air and water-free conditions are necessary for the sensitive, hazardous nature of $P(SiMe_3)_3$. In addition, scalability is also a crucial factor because of the demand of large quantity of NCs in commercial applications. In this case, aminophosphine precursors are found to give access to NCs with comparable characteristics as $P(SiMe_3)_3$. In the following sections, the reaction mechanism of InP formation with aminophosphine precursors will be summarized. Several colloidal syntheses utilize TOP and $P(SiMe_3)_3$ to obtain zinc phosphide and transition metal phosphides NCs, which borrow experiences from other metal phosphide NCs (Luber et al., 2013; Ramasamy et al., 2017).

The undercoordinated surface atoms in NC surfaces, acting as trap states, will affect the lifetime, efficiency of electron hole pairs, radiative recombination. Coating an additional shell provides extra means to manipulate the properties. Typically, type I core/shell NCs feature a strongly enhanced photoluminescence quantum yield (PLQY), such as InP/ZnS, and InP/ZnSe. Moreover, insert buffer layers (InP/GaP/ZnS) or adjust the lattice constant of core and shell (InZnP/ZnSeS) can minimize strain and alleviate interfacial defects, which is resulted from lattice mismatch in core/shell NCs.

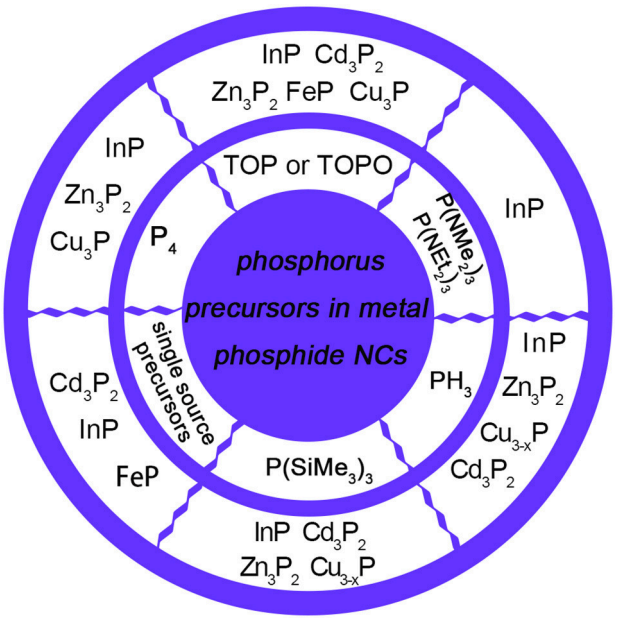

FIGURE 1 | Various types of phosphorus precursors used in the synthesis of metal phosphide NCs. InP NCs could be synthesized by TOP (Lauth et al., 2013), $P(NMe_2)_3$ (Song et al., 2013), $P(NEt_2)_3$ (Tessier et al., 2015), PH_3 (Li et al., 2008), $P(SiMe_3)_3$ (Micic et al., 1994), P_4 (Ung et al., 2008), and single source precursors, including $In(PBu^t_2)_3$ (Green and O'Brien, 1998) and magic-size clusters (MSCs) (Gary et al., 2015). Zn_3P_2 NCs could be synthesized by TOP (Mobarok et al., 2014), PH_3 (Miao et al., 2013), $P(SiMe_3)_3$ (Ho et al., 2015), and P_4 (Carenco et al., 2010). Cd_3P_2 NCs could be synthesized by TOP (Khanna et al., 2010), PH_3 (Miao et al., 2012), $P(SiMe_3)_3$ (Miao et al., 2010), and MSCs (Li et al., 2014) acting as single source precursors. FeP could be synthesized by TOP (Henkes and Schaak, 2007) and $(CO)_4Fe(PH_3)$ (Hunger et al., 2013) acting as single source precursors. Copper phosphides could be synthesized by TOP (Henkes and Schaak, 2007), PH_3 (Manna et al., 2013), $P(SiMe_3)_3$ (Liu et al., 2016), and P_4 (Bichat et al., 2004a).

In this review, a representative introduction on the physical properties of metal phosphide NCs is given firstly. Selecting suitable precursor plays an important role in the chemical synthesis of NCs. Different from the synthesis of metal chalcogenide, much more phosphorus precursors have been tested with the purpose of improving the quality, and reducing the production cost of metal phosphide NCs. We give a detail discussion regarding the underlying chemical mechanism on the phosphorus chemistry in the synthesis of metal phosphide NCs. As one key example of metal phosphide, strategies to obtain high quality InP NCs and their core/shell system with ZnS and ZnSe as passivating shells are summarized. A passivizing shell is of critical importance for InP NCs, because their surfaces are prone to be easily oxidized. We also conclude by pointing out challenges to be addressed in future research, such as broad emission, shape control, and doping of InP NCs. Next, II-V metal phosphide NCs (e.g., Cd_3P_2, Zn_3P_2) and transition metal phosphides (e.g., copper phosphide, iron phosphide) are presented. Finally, an overview of state-of-the-art applications

with metal phosphide NCs is provided, such as light-emitting devices (LEDs), photovoltaic cells, and biomedical applications.

PHOSPHORUS PRECURSORS IN COLLOIDAL SYNTHESIS OF INP NANOCRYSTALS

As the most important metal phosphide, InP has attracted intensive attention. (Green and O'Brien, 1998; Jun et al., 2006; Ung et al., 2008; Zan and Ren, 2012; Bang et al., 2017; Friedfeld et al., 2017). The direct band gap of 1.35 eV, high fraction of covalent bonding and the large Bohr exciton radius of 9.6 nm make the InP NCs an excellent candidate as visible and near-IR emitting materials. The first liquid colloidal synthesis of InP NCs with narrow size distribution was realized by Nozik in 1994 by using $P(SiMe_3)_3$ (Micic et al., 1994). The P–Si bond in the compound of $P(SiMe_3)_3$ exhibits relatively low dissociation energy (around 363 kJ mol^{-1}), which leads to its high reactivity in the case of reacting with an indium precursor. Besides, the phosphorus atom bonded to the highly electropositive Si atom imparts the necessary driving force to react with indium precursors. Therefore, the resulting InP NCs show well-crystallized zinc blende structure and modest exciton peak attributed to InP, which is the first time to show an exciton peak for an III-V NC. This strategy was also applied to the synthesis of other binary and ternary III-V QDs, e.g., GaP. $GaInP_2$ (Micic et al., 1995). Since this pioneering report, $P(SiMe_3)_3$ has become the most widely used phosphorus precursor in the colloidal synthesis of metal phosphide NCs. Then, utilizing $P(SiMe_3)_3$ precursor, Micic et al. treated the NCs with a solution of HF or NH_4F, resulting in highly efficient band-edge emission (Micic et al., 1996, 1997).

In view of their highly reactivity, $P(SiMe_3)_3$ will be consumed in a few seconds. In this context, the growth of NCs tends to proceed via the Ostwald ripening mechanism, which widens the size distribution (Clark et al., 2011). Furthermore, due to pyrophoric nature, high cost, and hazardous reagents of $P(SiMe_3)_3$ and secondary products involved in production, several alternatives for $P(SiMe_3)_3$ are already studied (Reiss et al., 2016). Up to now, following the first synthesis of InP NCs, a variety of phosphorus precursors have been investigated with the main purpose of improving the size distribution. A diversity of phosphorus precursors in the synthesis of InP NCs is summarized in **Table 1.**

Similar to $P(SiMe_3)_3$ precursor, single-source precursor is a highly reactive precursor, which can shorten the reaction time and avoid the formation of side products, such as of In_2O_3. Mark et al. reported the synthesis of high quality InP NCs by using the single source precursor of $(In(PBu^t_2)_3)$ (Green and O'Brien, 1998). It is noted that the preparation and storage of such a highly reactive precursor requires great cautions. To address these issues, Li et al. synthesized high quality InP NCs by using the *in situ* generated PH_3 gas as the phosphorus precursor (Li et al., 2008; Zan and Ren, 2012). PH_3 is a more stable and safer phosphorus precursor, compared to pyrophoric $P(SiMe_3)_3$ precursor. Furthermore, the method based on PH_3 gas gives access to larger sized InP NCs. In 2008, Reiss et al. reported the synthesis of InP NCs using an elemental P precursor (red P allotropes) as the phosphorus precursor. To stimulate the reaction, $NaBH_4$ was introduced as the reducing agent. The reaction could proceed with a very high reaction yield approaching 100% (Ung et al., 2008). Park et al. reported the synthesis of highly luminescent InP/ZnS NCs using an elemental P precursor of P_4 (white P) (Bang et al., 2017). They demonstrated that the direct reaction of P_4 precursor with In precursor without reducing agent. The sublimation of red P powder can simply produce P_4, therefore P_4 precursor represents an additional low-cost P precursor and provides an important way to the large-scale synthesis on InP NCs.

In order to avoid the rapid depletion of $P(SiMe_3)_3$, phosphorus precursors with decreased precursor reactivity have been synthesized. Different strategies have been implemented, such as replacing the Si with Ge or Sn (Harris and Bawendi, 2012), substituting methyl group with butyl or aryl group (Joung et al., 2012; Gary et al., 2014). Replacing Si in the Si–P bond with Ge or Sn reduces the reactivity of the precursor by decreasing the polarity of the bond. Likewise, altering the methyl groups to sterically hindering moieties can reduce the reactivity as well. It is believed that using less reactive precursor is helpful to segregate the nucleation and growth and is essential to reach InP NCs with narrow size distribution. Despite great efforts, these alternatives exhibited either largely unchanged or very slowed conversions compared with $P(SiMe_3)_3$.

Aminophosphine presents an alternative phosphorus precursor with advantages of low cost, high stability, decent reactivity, and easy handling (Xie et al., 2007; Laufersky et al., 2018; Mundy et al., 2018). Song and coworkers reported for the first time of high-quality InP NCs using $P(NMe_2)_3$ as a phosphorus precursor (Song et al., 2013). The synthesis was performed by rapid injection of $P(NMe_2)_3$ into the $InCl_3$ and $ZnCl_2$ solution with oleylamine at 220°C. They found that the size and size distributions of InP NCs are depended on the amount of $P(NMe_2)_3$, $ZnCl_2$ as well as the growth temperature and time. The presence of $ZnCl_2$ in the synthesis plays a role in activating the aminophosphine to undergo a disproportionation reaction and form P^{3-}, which is helpful to achieve narrow size distribution (Laufersky et al., 2018).

Later, Tessier presented an investigation into the chemical reactions of InP formation with $InCl_3$ and aminophosphine precursors (Tessier et al., 2016). Using NMR spectroscopy and single crystal X-ray diffraction and mass spectrometry, they demonstrated that the InP formation underwent 4P(+III) → P(–III) + 3P(+V) disproportionation reaction. Since aminophosphines are P(III) compounds, reduction steps are needed to form InP with an In (III) precursor. As shown in **Scheme 1A**, an exchange between primary amines and amino groups of phosphorus precursor occurs, indicating that apart from acting as solvent or ligand, primary amines also play an important role in the whole precursor chemistry. Then, 1 equiv of InP is formed by oxidating 3 equiv of the substituted aminophosphine to a phosphonium salt (**Scheme 1B**). Namely, substituted aminophosphine has a double role in the reaction, both phosphorus precursor and reducing agent. Based on double

TABLE 1 | Summary of phosphorus precursors in colloidal synthesis of InP NCs.

	P precursors	In precursors	Methods	Results	References
1998	$In(PBu^t_2)_3$		Decomposition of $In(PBu^t_2)_3$	Quantum confinement effects	Green and O'Brien, 1998
2006	Na_3P	$InCl_3$	Heat-up	Spherical NCs with 5 nm	Jun et al., 2006
2008	P_4	$InCl_3$	Hot-injection	Cubic structure with 3–4 nm	Ung et al., 2008
2008	PCl_3	$In(Ac)_3$	Heat-up	Size tunability; HF-etching improved the quantum yield (QY)	Liu et al., 2008
2008, 2012	PH_3	$In(Ac)_3$	Gas-liquid phase synthesis	InP/ZnS NCs: QY of 30–60%	Li et al., 2008; Zan and Ren, 2012
2012	$P(SiMe_2\text{-tert-Bu})_3$	$In(Ac)_3$	Hot-injection	Large size of InP NCs: InP/ZnS NCs: QY of 18–28%	Joung et al., 2012
2012	$P(GeMe_3)_3$	$In(MA)_3$	Hot-injection	Improved size distribution	Harris and Bawendi, 2012
2013	$P(NMe_2)_3$	$InCl_3$	Hot-injection	Size tunability; InP/ZnS NCs: emission FWHM:60–64 nm; QY: 51–53%	Song et al., 2013
2013	TOP	$InCl_3$, InF_3, $InBr_3$	Hot-injection	Size tunability	Lauth et al., 2013
2014	$P(SiPh_3)_3$,$P(SiMe_3)_3$	$In(MA)_3$	Hot-injection	Separated the nucleation and growth	Gary et al., 2014
2015	Single-source precursors: InP MA MSCs from $P(SiMe_3)_3$ and $In(MA)_3$		Hot-injection	Conversion of InP MSCs to NCs proceeded via a supersaturated solution	Gary et al., 2015
2015	$P(NEt_2)_3$	$InCl_3$,InI_3,$InBr_3$	Hot-injection	InP/ZnS NCs: emission FWHM of 46–63 nm; QY: 50–60%	Tessier et al., 2015
2017	$P(SiMe_3)_3$	$In(Ac)_3$	Heat-up	Zn–P intermediate complex lowered the reactivity of $P(SiMe_3)_3$	Koh et al., 2017
2017	P_4	$InCl_3$, InI_3	Hot-injection	Large-scale production; InP/ZnS NCs: emission FWHM: 50–80 nm; QY: 60%	Bang et al., 2017

role of phosphorus, this mechanism assumes a nucleophilic attack by the phosphorus center of one aminophosphine on an amino group of another aminophosphine. Firstly, $InCl_3$ reacts with $P(NHR)_3$ to form adducts with different resonance structures (**Scheme 1B-I**), thus, the positive charge can delocalize over the phosphorus center and the nitrogen atoms, making it possible for residual $P(NHR)_3$ to nucleophilic attack nitrogen atoms, as showed in **Scheme 1B-II**. Subsequent phosphorus nucleophilic substitution results in InP unit formation. This mechanism explains why full conversion of the In precursor is only attained for a 4:1 P/In ratio.

Since then, InP NCs with aminophosphine precursors have been further investigated: utilizing the precursors, the resulting green NCs achieved comparable PL performance to previous work with $P(SiMe_3)_3$ (PLQY: 82 vs. 85%) (Jang et al., 2018). Tetrahedrally shaped InP NCs with improved stability ascribed to oleylamine and chloride ligands (Kim et al., 2016). Zinc salts were also found to activate the aminophosphine precursors by accelerating the formation of the In–P(I) pseudomonomer. Moreover, admixing Cd into a ZnSe shell could also be valid in synthesizing strain-free NCs, suppressing self-absorption, and reducing the amount of NCs for application (Dupont et al., 2017; Rafipoor et al., 2018). Cossairt et al. also demonstrated that aminophosphines were versatile precursors for metal phosphide NCs beyond InP (Mundy et al., 2018).

In short, InP NCs synthesized with aminophosphine precursor, have competitive properties to those from $P(SiMe_3)_3$ routes, indicating that aminophosphine is a promising option for the synthesis of InP NCs. Recently, mechanism of reaction and surface states has been confirmed by X-ray absorption spectroscopy, Raman scattering measurements, and NMR Spectroscopy, etc. (Janke et al., 2018; Laufersky et al., 2018; Tessier et al., 2018). These progresses indicate that synthesis of high quality and efficient InP NCs with the low cost, high stability, decent reactivity, and easy handling precursor will enable to obtain InP NCs on a large scale for a variety of applications, and lead to the extension of colloidal synthesis toward other pnictide NCs.

INDIUM PHOSPHIDE NANOCRYSTALS

InP quantum emitting materials have been considered as an alternative substitution to the conventional quantum dots (QDs), with advantages of less toxicity. Technically speaking, the heavy metal of Cd or Pb in quantum dots-based electronics devices will cause minor environment issue because of the very low concentrations. These heavy metal issues can be further reduced to an even low level by appropriate encapsulation technique and recycling policy after disposal. However, the introduction of heavy-metal materials in electrical and electronic equipment has been restricted the regulation released by Restriction of Hazardous Substances Directive in the EU. Therefore, many researchers have shifted the interests from Cd or Pb based NCs to Cd-free alternatives, i.e., InP QDs.

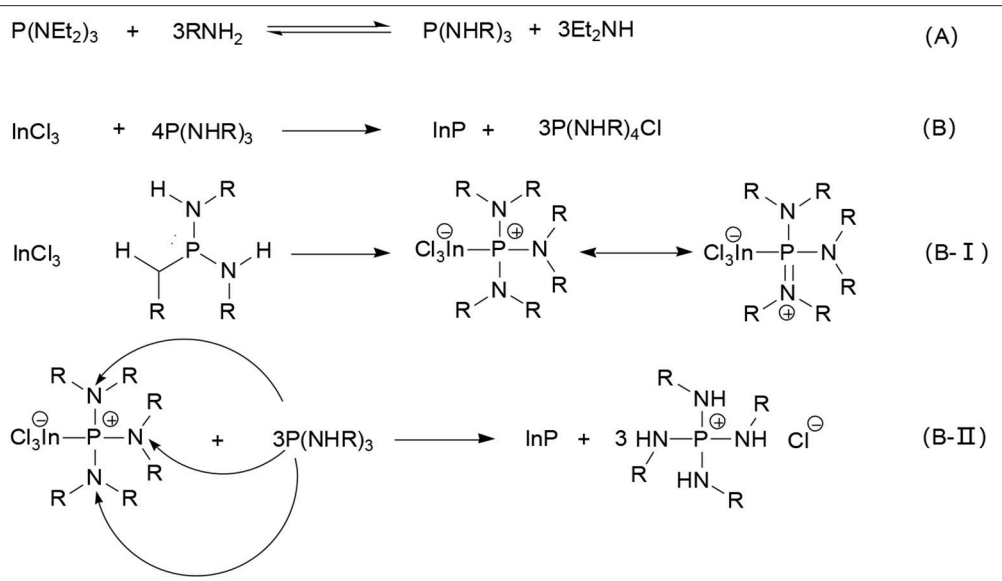

SCHEME 1 | Mechanism of reaction of $P(NEt_2)_3$ with InP NCs **(A)**. $P(NEt_2)_3$ first reacts with the primary amine to obtain $P(NHR)_3$, then **(B)**1 equiv of InP is formed by oxidating 3 equiv of the substituted aminophosphine to a phosphonium salt. Namely, **(B-1)** after the synthesis of In-P complex, **(B-II)** P nucleophilic substitution reaction, finally InP unit is obtained. Reproduced with permission from Tessier et al. (2016). © 2016 American Chemical Society.

Indeed, toxicological evaluation reveals that InP QDs display minor toxicity and decent bio-compatibility, thereby suggesting that they can be utilized for potential bio-imaging applications. For instance, Lin et al. found that no observable toxicity *in vivo* after intravenous injection of InP/ZnS QDs in mice for 84 days (Lin et al., 2015). Brunetti et al. studied the toxicity of CdSe/ZnS and InP/ZnS QDs *in vitro* as well as for *in vivo* applications (Brunetti et al., 2013). CdSe/ZnS QDs were shown to induce cell membrane damage, interference with Ca^{2+} homeostasis, which ascribed to the presence of Cd^{2+}, while InP/ZnS QDs exhibited low toxicity. Chibli et al. showed that the cytotoxicity induced by the generation of reactive oxygen species was shown to be significantly lower in the case of InP/ZnS QDs as compared to CdTe/ZnS QDs (Chibli et al., 2011). Taken together, toxicity studies demonstrate that these InP based QDs constitute a less toxic alternative to Cd based QDs. All these toxicity evaluations support that the InP QDs pose less environment concerns and guarantee the commercialization of InP QDs based electronics devices.

At the early stages, InP NCs were characterized as low PLQY, poor photo-stability, in particular its wide PL linewidth, in contrast to Cd-based NCs. In the following decades, the synthesis of InP NCs has achieved progress toward the improvements on the PLQY, PL stability, and narrowing the PL linewidth. **Figure 2** shows optical absorption, PL spectra, and TEM images of different NCs. The highest QY in literature for InP QDs was reported above 80%, which is close to unity PLQY of CdSe QDs and cesium lead halide perovskites ($CsPbX_3$) NCs (Zhang et al., 2013; Nedelcu et al., 2015). Coating InP NCs with a shell can afford improved photostability, which allows for many applications. However, the wide PL linewidth limits their applications where narrow emission is required, i.e., multiple-color displays. The narrowest PL linewidth, estimated as full-width at half maximum (fwhm), for InP-based core/shell or alloy NCs is 35 nm at 488 nm (**Figure 2A**) (Ramasamy et al., 2017), which is still inferior to CdSe QDs and $CsPbX_3$ QDs.

In fact, intrinsic emission line width of InP NCs is comparable to CdSe NCs (**Figure 3A-IV**) (Cui et al., 2013), suggesting that the emission of InP NCs is heterogeneously broadened due to size distribution. The very broad size distribution of InP NCs indicates that separating nucleation and growth is difficult to achieve (Tamang et al., 2016), due to the more covalent nature of the III-V precursors and the fast depletion of precursors at high temperature (Allen et al., 2010).

Several methods have been used to improve size tunability and size distribution, including employing zinc chloride as reaction additive, and replacing $P(SiMe_3)_3$ with lower cost, toxicity, and higher stability phosphorus precursors. Effects of Zn species in InP NC synthesis include the reduction of surface defects, facilitation of subsequent shell growth, and improvement of size distribution (Yang et al., 2012). The use of aminophosphine precursors ($P(NMe_2)_3$ and ($P(NEt_2)_3$) enable the preparation of InP NCs with state-of-the-art quality in the literature.

Increasing core growth time also results in broadened size distribution of InP NCs. Hens et al. expanded this approach by replacing $P(NMe_2)_3$ with $P(NEt_2)_3$, attaining a close to full yield conversion of indium precursor, and demonstrating size tuning was possible by changing the indium halide salt (Tessier et al., 2015). Changing of the precursor concentration is a size-tuning strategy, i.e., higher concentrations lead to smaller NCs, whereas decreasing the concentration appears to deteriorate the size distribution. Inspired by changing the free ligand concentration or the ligand chain length with CdSe NCs (Abe et al., 2013). Tessier and coworkers changed the indium salt halide. When all other reaction conditions were kept constant,

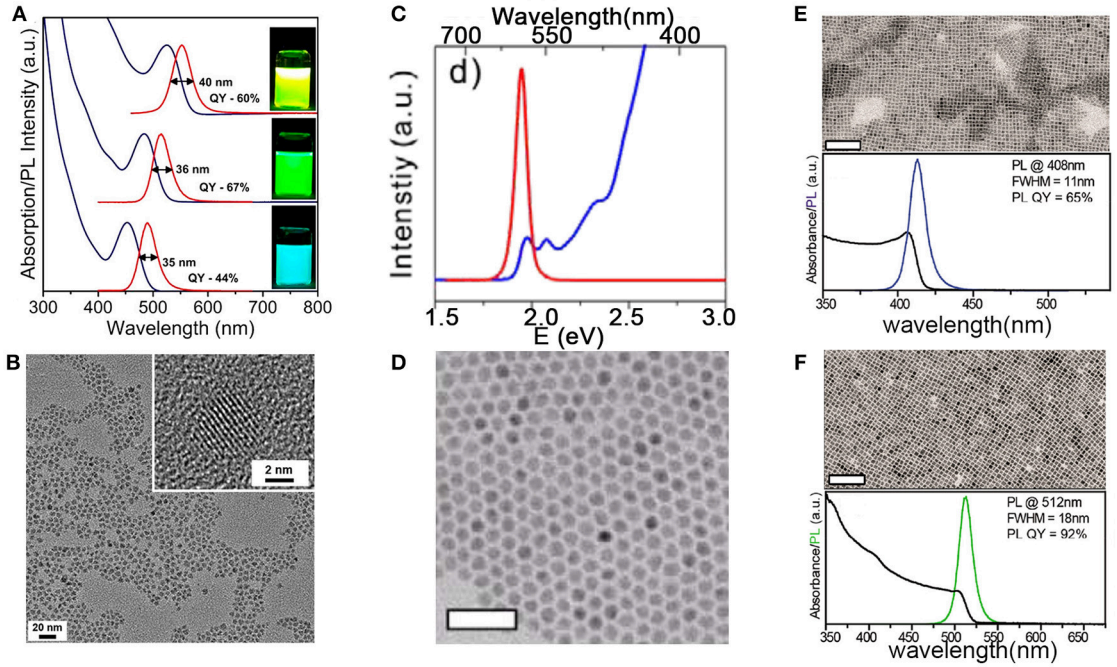

FIGURE 2 | (A) In(Zn)P/ZnSe/ZnS NCs emitting at 488, 516, and 552 nm have fwhm of 35, 36, and 40 nm. **(B)** 535 nm emitting In(Zn)P/ZnSe/ZnS NCs with the size of 4.2 nm. Reproduced with permission from Ramasamy et al. (2017). © 2017 American Chemical Society. **(C,D)** Absorption, PL spectra, and TEM images of CdSe/CdS NCs with CdSe core diameters of 5.4 nm and CdS shell thickness of 2.3 nm. Reproduced with permission from Chen et al. (2013) © 2013 Springer Nature. Scale bars are 50 nm. TEM images, absorption, and PL spectra of **(E)** $CsPbCl_3$, **(F)** $CsPbBr_3$ NCs. Reproduced with permission from Imran et al. (2018). © 2018 American Chemical Society. Scale bars are 100 nm. https://pubs.acs.org/doi/10.1021/jacs.7b13477. Notice:further permissions related to the material excerpted should be directed to the ACS.

the first exciton position can be tuned from 570 to 550 or 520 nm by replacing $InCl_3$ by $InBr_3$ or InI_3, respectively, allowing for an efficient size tuning by changing of the indium halide precursor.

Up to now, the narrowest emission of ensemble InP NCs were reported to be ca. 40 nm (Ramasamy et al., 2018), which is still wider than the line widths of PL acquired at the single particle level, suggesting that colloidal synthesis gave rise to the intrinsic inhomogeneity in InP NCs, that was previously attributed to broadened size distribution. Interestingly, recent report reveals that the broad emission may be caused by surface states and lattice disorder, that was confirmed by utilizing X-ray absorption spectroscopy and Raman scattering measurements (Janke et al., 2018). These findings suggest that developing new colloidal synthesis with the purpose of decreasing surface and lattice defects will be the future challenges to achieve comparable performance to CdSe NCs. Furthermore, dopant ions within lattice of NCs were found to be as important as control of the surface states to obtain bright dopant emission (Pu et al., 2017). Ag^+ dopants can be introduced into lattice of CdSe NCs precisely (Sahu et al., 2012), while few works exist on the doped InP NCs. Recent reports demonstrate that Ag and Cu are of interest as doping agents for dual-emissive InP NCs, therefore, the NCs have potential applications in biological and LEDs applications (Zhang et al., 2015; Yang et al., 2017; Vinokurov et al., 2018). In conclusion, synthetic development specifically for these applications is an interesting avenue to explore.

So far, quite limited progress has been achieved in shape control of InP NCs, only tetrahedral (Kim et al., 2016) and spherical NCs are reported. Colloidal nanoplatelets differ from NCs due to the strong quantum confinement acting in one dimension, which have been most extensively studied. CdSe nanoplatelets can be synthesized with a thickness controlled with monolayer precision, gaining access to a wide spectral range (Christodoulou et al., 2018). Hence, as for InP, development of such 2D heterostructures can be a promising and exciting future direction.

INDIUM PHOSPHIDE-BASED CORE/SHELL NANOCRYSTALS

The concept of core/shell in NCs has been widely implemented for the conventional CdSe based core/shell structures. Coating an additional shell around the initial seeds provides extra means to manipulate their properties. The obvious benefit is allowing one to easily obtain NCs with enhanced fluorescence efficiency and improved stability against photo-oxidation. This is of particularly importance for the InP NCs, because even freshly synthesized colloidal InP NCs exhibit PLQY of <1% due to surface defects related to P atoms. Talapin et al. found that treating InP NCs with HF can reconstruct the surface and enhance the PLQY up to 40% (Adam et al., 2005). Besides, InP NCs without protecting shell are prone to surface oxidation and photodegradation. Therefore,

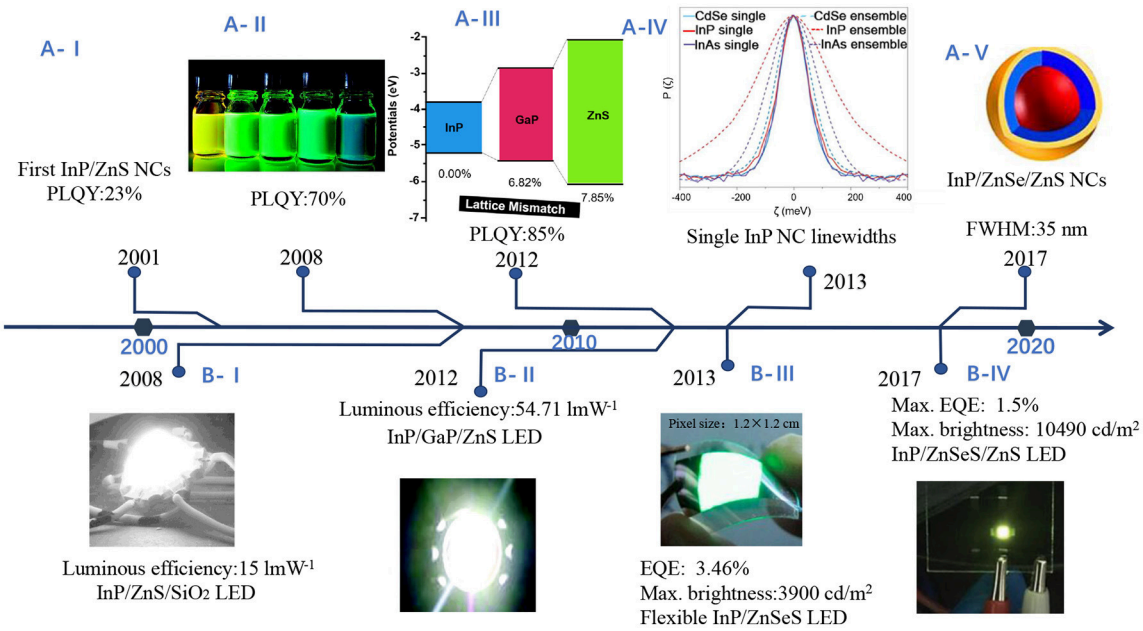

FIGURE 3 | Research timeline illustrating **(A)** improvements on luminescence performance **(B)** progress toward to various applications of InP NCs in light-emitting diodes. **(A-I)** InP/ZnS NCs with PLQY of 23% (Haubold et al., 2001) **(A-II)**. Highly luminescent InP/ZnS NCs. Reproduced with permission from Li and Reiss (2008). © 2008 American Chemical Society. **(A-III)** InP/GaP/ZnS NCs with a maximum PLQY of 85%. Reproduced with permission from Kim et al. (2012) © 2012 American Chemical Society. **(A-IV)** Single InP NC linewidths. Reproduced with permission from Cui et al. (2013) © 2013 Springer Nature. **(A-V)** In(Zn)P/ZnSe/ZnS NCs with emission fwhm as narrow as 35 nm. Reproduced with permission from Ramasamy et al. (2017). © 2017 American Chemical Society. **(B-I)** InP/ZnS NCs as converter material in white LEDs. Reproduced with permission from Ziegler et al. (2008) with permission of John Wiley and Sons. **(B-II)** White LEDs with InP/GaP/ZnS NCs. Reproduced with permission from Kim et al. (2012). © 2012 American Chemical Society. **(B-III)** LEDs with InP/ZnSeS. Reproduced with permission from Lim et al. (2013). © 2013 American Chemical Society. **(B-IV)** LEDs with InP/ZnSeS/ZnS. Reproduced with permission from Wang et al. (2017) with permission of John Wiley and Sons.

coating InP with a passivating shell is the prerequisite for further their applications.

Most importantly, band gap offsets and lattice strain between core and shell significantly modify the intraband and interband states, and affect the carrier dynamics of exciton (Dupont et al., 2017; Rafipoor et al., 2018). Therefore, it is possible to prepare the core/shell QDs with unusual and practical photophysical properties. Brainis found that a thick ZnSe shell coating is helpful to reach nearly non-blinking NCs (Chandrasekaran et al., 2017). Hollingsworth et al. reported that coating InP NCs with 11 monolayers of CdS can significantly increase the bi-exciton lifetime up to 7 ns, indicating dramatic suppression of nonradiative Auger recombination (Dennis et al., 2012). So far, ZnSe and ZnS are often used as shell materials for the obvious reason of their large band gap and low toxicity. Herein, we will summarize recent progress toward the synthesis of InP based core/shell direction.

The first issue encountered in the synthesis of core/shell structured InP/ZnSe and InP/ZnS NCs is the relatively large lattices mismatch. In case of former is 3.3%, and in the latter is approaching to 7.7%. The epitaxial growth of shell on top of InP NCs has been proved to be challenging, due to the large lattice constant (a = 5.93 Å). Besides, defects may exist due to the strain at the core/shell interfaces induced by lattice mismatch. Therefore, finding appropriate strategies to avoid defect formation represents one of the main challenges in the synthesis of InP based core/shell NCs.

Overcoating the NCs with a shell of ZnS leads to high PLQY, as shown in **Figure 3A**. Haubold et al. first passivated the InP core with ZnS, enhanced the PLQY to 23% (**Figure 3A-I**) (Haubold et al., 2001). They used diethylzinc and bis(trimethylsilyl) sulfide to grow ZnS on InP NCs at 260°C for a limited time, aiming to avoid Ostwald ripening. TEM images and XPS data indicated the formation of ZnS passivated InP NCs. Then one-pot synthesis without precursor injection gave access to InP/ZnS NCs with a maximum PLQY of 70% (**Figure 3A-II**), narrow emission line width (40–60 nm fwhm) and excellent photostability (Li and Reiss, 2008). The high PLQY is likely attributed to the "smooth" core/shell interface with few defect states. So far, the highest PLQY (85%) (**Figure 3A-III**) has been reported for the InP/GaP/ZnS NCs with superior photostability as compared to InP/ZnS NCs (Kim et al., 2012), where In^{3+} ions are effectively replaced by Ga^{3+} ions near the surface. The intermediate layer GaP mitigates the effect of lattice mismatch between InP and ZnS. Lattice strain with a ZnS shell may limit a shell thickness <1 nm, making NCs vulnerable against degradable conditions. To alleviate lattice strain, Lee et al. used ZnSe as a lattice adaptor to achieve thicker shells (1.9 nm), the NCs exhibited high PLQY, and enhanced stability under UV irradiation, ligand exchange or rigorous purification (Lim et al., 2011).

Pietra et al. found that In_xZn_yP alloy NCs with a tunable lattice constant can be prepared by changing the amount of zinc precursor, which can match a chosen shell material, possibly creating strain-free core/shell NCs (Pietra et al., 2016). As a result, PLQY of InZnP/ZnSeS NCs can reach as high as 60%. Optical spectra, PLQY and TEM images of In_xZn_yP NCs are shown in **Figures 4A–C**. They also found that a preferential Ga-for-Zn cation exchange leaded to a InZnP/InGaP core/shell system with increased PLQY when Zn/In $\geq$0.5. Another GaP and ZnSeS outer shell of InZnP/InGaP NCs exhibit enhanced PLQY (over 70%) and stability (Pietra et al., 2017). Structure and optical spectra of InZnP/InGaP/GaP/ZnSeS NCs are shown in **Figures 4D–F**.

COLLOIDAL SYNTHESIS OF II–V METAL PHOSPHIDE NANOCRYSTALS

Cadmium phosphide has been the subject of intensive interest owing to its unique physical properties. Cd_2P_3 is a narrow bandgap semiconductor (0.55 eV in bulk) with high dielectric constant (5.8), large Bohr exciton radius (36 nm). All these features suggest that Cd_2P_3 in quantum-dot form presents a new material with emission wavelengths span the visible through the near-infrared.

Miao et al. for the first time, reported the colloidal synthesis of cadmium phosphide NCs using $P(SiMe_3)_3$ as a phosphorus precursor in the presence of oleylamine and trioctylphosphine as ligands (Miao et al., 2010). By varying the temperature and growth time, they obtained high quality Cd_3P_2 NCs with tunable emission ranging from 650 to 1,200 nm, and with high PLQY up to ca. 40%. Further research from the same group found that replacing $P(SiMe_3)_3$ by PH_3 will reach cadmium phosphide NCs with different stoichiometric (Cd_6P_7 instead of Cd_3P_2,) and improved size distribution (Miao et al., 2012). **Figure 5A** shows the absorption spectra with multiple transition of Cd6P7 NCs for the first time. TEM images in **Figure 5B** show that Cd_6P_7 NCs are monodisperse with nearly spherical shape, and the average size of NCs is 6.5 $\pm$ 0.3 nm. Since PH_3 is less reactive compared to $P(SiMe_3)_3$, size of NCs is well controlled by the low reaction rate. This simple and inexpensive strategy paves the way to large-scale production of metal phosphide NCs.

Xie et al. reported an advanced synthesis of Cd_3P_2 NCs using $P(SiMe_3)_3$ as a phosphorus precursor and using oleic acid as the only ligand (Xie et al., 2010). They found that under these conditions, the size of the obtained NCs can be tuned in in the range of 1.6–12 nm by simply adjusting the concentration of the oleic acid. **Figure 5C** shows PL spectra of Cd_3P_2 NCs with various sizes, which covers the whole visible and near-IR (450 to over 1,500 nm) region. The optical properties make the NCs useful in optical amplification and lighting. TEM images of Cd_3P_2 NCs with 12 nm are given in **Figure 5D**, where a square array of the NCs is observed.

Cadmium phosphide NCs in the absence of protecting shell can be easily oxidized, which hinders their application in open air. Delpech reported a method for the coating of cadmium phosphide NCs (Ojo et al., 2012). The coating procedure was performed by using zinc acetate and ethylene sulfide as the zinc and sulfur precursors, respectively. They obtained high-quality Cd_3P_2/ZnS NCs with PLQY over 50% with modest air stability.

Zinc phosphide (Zn_3P_2) has great potential as a solar absorber in thin film photovoltaics, because of its high absorption coefficient in the order of 10^{-4}-10^{-5} cm^{-1}, large carries diffusion length of 5–10 μm, mostly importantly suitable band gap of 1.5 eV (Green and O'Brien, 2001). The band gap of Zn_3P_2 is very close that of CdTe and slightly narrower than CdSe, indicating its high solar absorption capability. Fabrication of Zn_3P_2 in the quantum size has been intensively pursued for a long time, because Zn_3P_2 NCs can potentially be an emitting material like CdTe and CdSe NCs (Luber et al., 2013). Besides, Zn_3P_2 exhibits superior features in contrast to CdTe, CdSe, and InP, because both the Zn and the P are nontoxic and earth abundant elements.

Up to now, there have been several reports on the synthesis of Zn_3P_2 NCs. The reported synthetic approaches of colloidal Zn_3P_2 NCs borrow experiences from the synthesis of other metal phosphide NCs, utilizing the same phosphorus precursor, such as P_4, TOP, PH_3, and $P(SiMe_3)_3$ and the same ligands such as TOP. The zinc precursor includes dimethylzinc, diethylzinc, and zinc stearate. It is worth noting that the formation of Zn_3P_2 compounds in liquid solution is difficult compared with other metal phosphides. For instance, significant quantity of $ZnCl_2$ is often used, during the synthesis of InP NCs. However, Extensive analysis suggests that under the conditions of the InP synthesis, zincs are not incorporated into the core of the final InP NCs. This feature explains the reason that early reports on the synthesis of NCs usually give poor crystalline and low PL product. This is also consistent with many observations that the synthesis of Zn_3P_2 NCs requires much higher temperatures.

Green reported the first colloidal synthesis of Zn_3P_2 NCs displaying quantum confined emission (Green and O'Brien, 2001). The synthesis was performed by using dimethylzinc as zinc precursor and the primary phosphine H_2P^tBu as phosphorus source. The obtained particles were revealed as a mixture of both crystalline and amorphous materials. Miao et al. reported the synthesis of Zn_3P_2 NCs by using either gas PH_3 or $P(SiMe_3)_3$ as phosphorus precursor and diethylzinc or zinc stearate as the zinc source (Miao et al., 2013) Buriak and coworkers synthesized monodisperse and pure crystalline Zn_3P_2 NCs at low temperature (Mobarok et al., 2014). From the selected area electron diffraction (SAED) pattern in **Figure 5E** and XRD spectrum, these NCs were found to possess the crystalline tetragonal α-Zn_3P_2 structure. TEM image in **Figure 5F** shows the average size of NCs is 14.7 $\pm$ 2.1 nm, with a distribution of 14%. In general, to date the reported synthesis of Zn_3P_2 NCs is more limited than cadmium and indium based NCs, mostly likely due to the large differences in reactivity between traditional zinc and cadmium precursors with conventional pnictide sources. Literature on colloidal Zn_3P_2 NCs mainly focuses on designing the synthesis and understanding the structure and properties of the NCs instead of their practical device application.

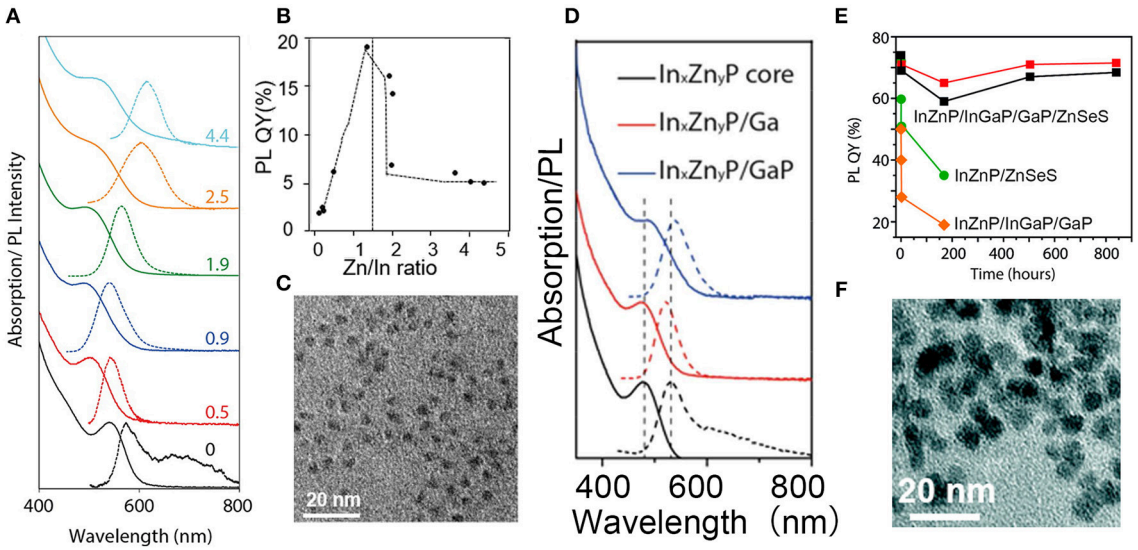

FIGURE 4 | (A) Absorption and PL spectra of In_xZn_yP NCs. **(B)** PLQY of In_xZn_yP NCs obtained by Inductively Coupled Plasma (ICP) Optical Emission Spectroscopy (OES) elemental analysis. **(C)** TEM image of In_xZn_yP/ $ZnSe_zS_{1-z}$ core/shell NCs. Reproduced with permission from Pietra et al. (2016). © 2016 American Chemical Society. **(D)** Absorption and emission spectra of InZnP NCs (Zn/In = 1.5). **(E)** PLQYs for four suspensions of NCs. Four samples were measured: two batches of purified InZnP/InGaP/GaP/ZnSeS NCs (red and black squares), InZnP/ZnSeS NCs (green dots), and InZnP/InGaP/GaP NCs (orange diamonds). **(F)** TEM images of InZnP/InGaP/GaP/ZnSeS NCs. Reproduced with permission from Pietra et al. (2017). © 2017 American Chemical Society. https://pubs.acs.org/doi/abs/10.1021/acs.chemmater.7b00848. Notice:further permissions related to the material excerpted should be directed to the ACS.

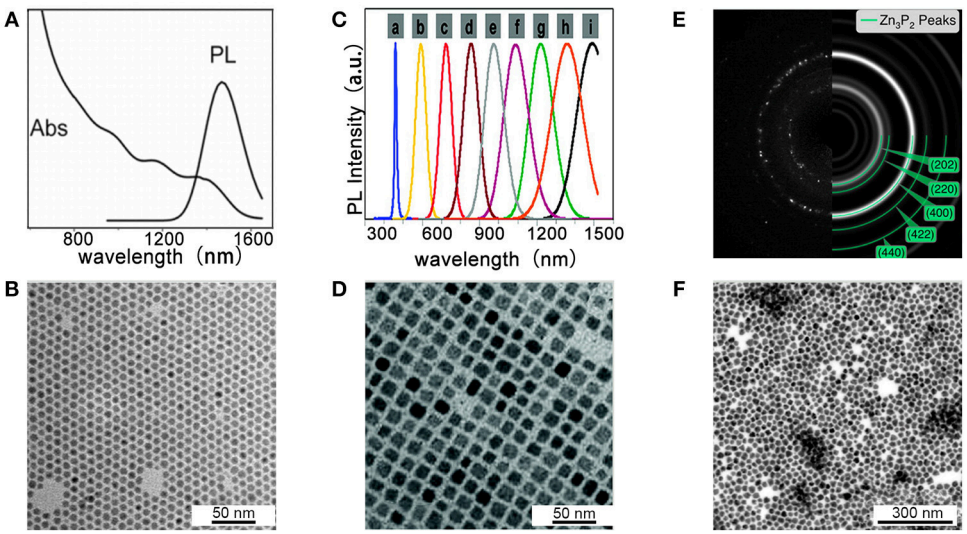

FIGURE 5 | (A,B) Cd_6P_7 NCs synthesized at 250°C with 40 min growth-time. Reproduced with permission from Miao et al. (2012). © 2012 American Chemical Society. **(A)** Absorption and PL spectra of Cd_6P_7 NCs. **(B)** TEM images show high quality of Cd_6P_7 NCs. **(C,D)** Cd_3P_2 NCs prepared at 250°C with $P(SiMe_3)_3$. Reproduced with permission from Xie et al. (2010). © 2010 American Chemical Society. **(C)** PL spectra of Cd_3P_2 NCs with various sizes. **(D)** TEM images of Cd_3P_2 NCs with 12 nm **(E,F)**. Zn_3P_2 NCs synthesized with $P(SiMe_3)_3$ for 1 h. Reproduced with permission from Mobarok et al. (2014). © 2014 American Chemical Society. **(E)** SAED pattern and simulation of α-Zn_3P_2 ring pattern. **(F)** TEM of Zn_3P_2 NCs.

COLLOIDAL SYNTHESIS OF TRANSITION METAL PHOSPHIDE NANOCRYSTALS

Recently, transition metal phosphide NCs have attracted intense interest for their potential in catalysis, magnetic recording media, and as anode materials in lithium ion batteries (Bichat et al., 2004b; Brock and Senevirathne, 2008). Among these, iron phosphides exist in a wide range of stoichiometry, their properties depend on their physical and electronic structures, such as Fe_3P and Fe_2P are ferromagnetic, FeP is super magnetic,

FeP_2 and FeP_4 are antimagnetic semiconductors (Blanchard et al., 2008). Cu_3P NCs are air-stable and environmentally friendly materials. When they are used in batteries, their theoretical weight capacitances are slightly higher than that of graphite, and volumetric capacities are more than three times greater than that of graphite (Bichat et al., 2004a).

Nowadays, TOP is often used as a phosphorus precursor in the synthesis of transition metal phosphide NCs. Schaak et al. reported the colloidal synthesis of Cu_3P NCs for the first time, by injecting the Cu NCs and TOP into the TOPO at high temperature (Henkes and Schaak, 2007). It is found that metals can cause cleavage of the P-C bond, resulting in diffusion of phosphorus into the metal. Falqui et al. optimized the synthesis by replacing Cu NCs with cuprous chloride (CuCl) to react with TOP, and obtained Cu_3P NCs with improved size distributions (De Trizio et al., 2012). The ratio of TOP and CuCl determined Cu_3P NCs either by a direct formation of Cu_3P nucleation or by forming Cu NCs first and then converting into Cu_3P NCs. The former way leads to reproducible and size controllable pure Cu_3P, while the latter way results in the formation of Cu-Cu_3P Janus-like NCs, which is unsuitable for applications in batteries with larger copper domains. Manna et al. reported the synthesis of by using PH_3 as the P precursor (Manna et al., 2013). The synthesis can be performed under relatively lower reaction temperature. The obtained Cu_3P nanoplatelets was found to be single crystalline and possess the semiconducting, plasmonic, and rectification properties. More recently, Liu et al. used the more active $P(SiMe_3)_3$ as the P precursor and prepared the $Cu_{3-x}P$ NCs at very low reaction temperature (Liu et al., 2016). They further demonstrated that the localized surface plasmon resonance and nonlinear optical absorption of the $Cu_{3-x}P$ NCs can be modulated by thermal treatment.

Perera et al. firstly reported the synthesis of iron phosphides NCs by reaction of $Fe(acac)_3$ with $P(SiMe_3)_3$ in TOPO at 260°C, resulting product in pure FeP phase, round shape, narrow size distribution, and high colloidal stability (Perera et al., 2003; Brock and Senevirathne, 2008). Park and coworkers synthesized uniform-sized FeP and Fe_2P nanorods from thermal decomposition of iron-phosphine complexes (Park et al., 2005). Schaak et al. reported the synthesis of FeP NCs by using pre-synthesized Fe NCs to react with TOP in hexadecylamine (Henkes and Schaak, 2007). Recently, Liu et al. used inexpensive and air-stable triphenyl phosphite (**Figure 6A**) as the phosphorus sources and prepared rod-shaped Fe_2P NCs (Liu et al., 2018). **Figure 6** displays representative TEM images of the 5 ± 1 nm $\times$ 22 ± 5 nm rod-shaped Fe_2P nanoparticles (**Figures 6B,C**), 4.5 ± 1 nm $\times$ 17 ± 1 nm disk-shaped Cu_3P nanoparticles (**Figures 6E,F**).

APPLICATION

Colloidal NCs are covered by a layer of ligands, which can stabilize the colloidal NCs in suitable solvents. This unique feature enables the fabrication of thin film electronic devices by well-established coating and printing techniques. In view of great progress toward the synthesis by means of inexpensive and scalable, wet-chemical synthetic procedures, colloidal QDs are emerging as a versatile class material in electronic devices, in contrast to expensive physically manufacturing processes. Besides, colloidal NCs open up new opportunities to integrate inorganic semiconductors devices with advanced features such as high-performance, large-area, and flexibility.

Among them, colloidal metal phosphide NCs offer a powerful platform for solution-processable electronic and optoelectronic devices, including photodetectors (Keuleyan et al., 2011), photovoltaic cells and light-emission devices (Steckel et al., 2003; Li et al., 2008; Qian et al., 2011), as shown in **Figure 7**. The actual active element in electronic and optoelectronic devices is macroscopic array of NCs (Talapin et al., 2010), which act as the key components with functions of light absorption or emission and charge transportation (Gaponenko et al., 2016; Kagan et al., 2016). **Figure 3B** shows progress toward to various applications of InP NCs in LEDs.

Commercialization of conventional quantum dots-based lighting emitting diodes are facing the strict regulation on the using of hazardous substances, such as Cd and Pb. Recent progress toward the synthesis of high-quality InP QDs provides a solution to address this issue. InP QDs have been widely applied in white lighting emitting devices as down conversion phosphor (Ziegler et al., 2008; Yang et al., 2012) and in the framework of electroluminescence devices (Lim et al., 2013; Shen et al., 2017; Wang et al., 2017; Ramasamy et al., 2018). Lim et al. reported design of InP QDs based electroluminescence light emitting diodes (Lim et al., 2013). The device structure based on InP QDs is shown in **Figure 7A**. By optimizing the charge balance, they observed direct formation of exciton within QDs and efficient radiative exciton recombination. The external quantum efficiency is reported as 3.46% and brightness is 3,900 cd m^{-2}. In a recent report, the brightness was improved to 10,000 cd m^{-2} by using ZnMgO as the electron transporting layer to improve the electron injection (Wang et al., 2017). The effect of Auger recombination, Förster resonant energy transfer among the closely packed QDs in a thin film of QLEDs, have a negative effect on device efficiency of QLED. Thus, thick shells or interfacial alloy layer acting as an effective spacer can suppress the above effects. A record of external quantum efficiency of 6.6% in heavy-metal-free red QLEDs have been achieved with a thick ZnS shell of InP/ZnSe/ZnS QDs (15 nm) (Cao et al., 2018). That means there is still more room for improvement and optimization. Moreover, replacing red, green, blue (RGB) color filters with narrow-band green, red InP/ZnSeS/ZnS QD films in color-by-blue QD-emissive liquid-crystal displays (LCDs) results in 1.49 times greater in the relative luminance levels, 2.42 times higher in EQE values than conventional color filter (CF)-LCD, making it possible to replace conventional RGB CF-assisted LCDs (Kang et al., 2018).

Cd_3P_2 NCs and Zn_3P_2 NCs have been considered as promising materials for photovoltaic applications. Cao et al. proposed PbS/Cd_3P_2 quantum heterojunction for NC photovoltaic cells, where p- and n-layers were quantum-tunable and solution-processed infrared light absorbers (Cao et al., 2015). The increased thickness of an n-layer type Cd_3P_2 from

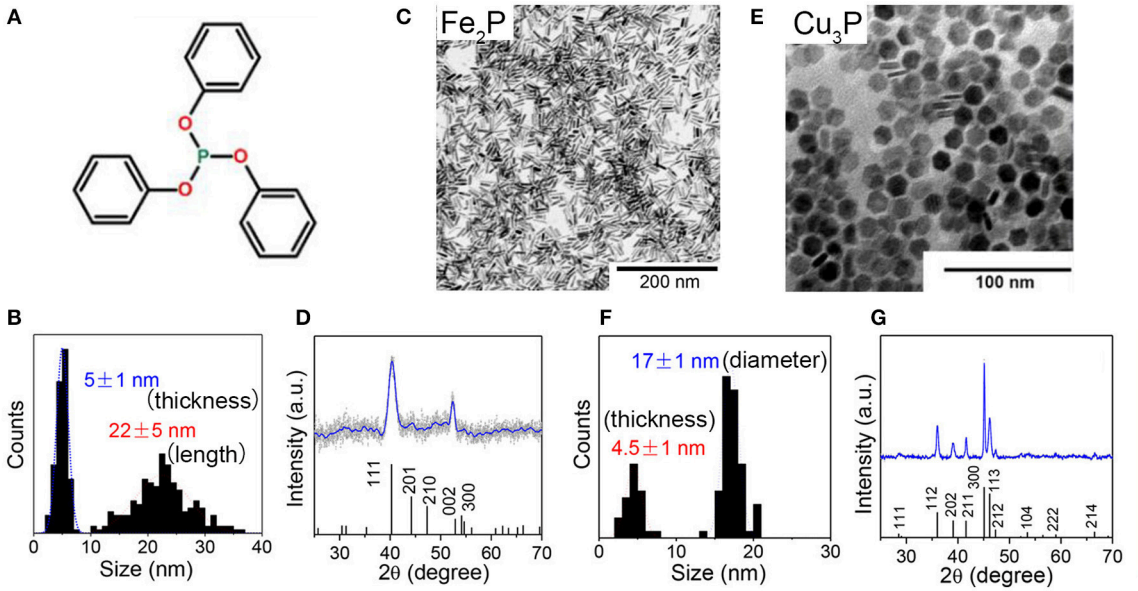

FIGURE 6 | (A) Chemical structure of triphenyl phosphite. **(B,C)** TEM images and nanorod length and thickness distribution histograms of Fe_2P. nanoparticles **(D)** XRD pattern of Fe_2P nanoparticles. The reference JCPDS pattern of Fe_2P (01-076-089) is also included in the XRD graph. **(E,F)** TEM images and disk diameter and thickness distribution histograms of Cu_3P nanoparticles **(G)** XRD pattern of Cu_3P nanoparticles. The reference JCPDS pattern of Cu_3P (01-071-2261) is also included in the XRD graph. Reproduced with permission from Liu et al. (2018). © 2018 American Chemical Society.

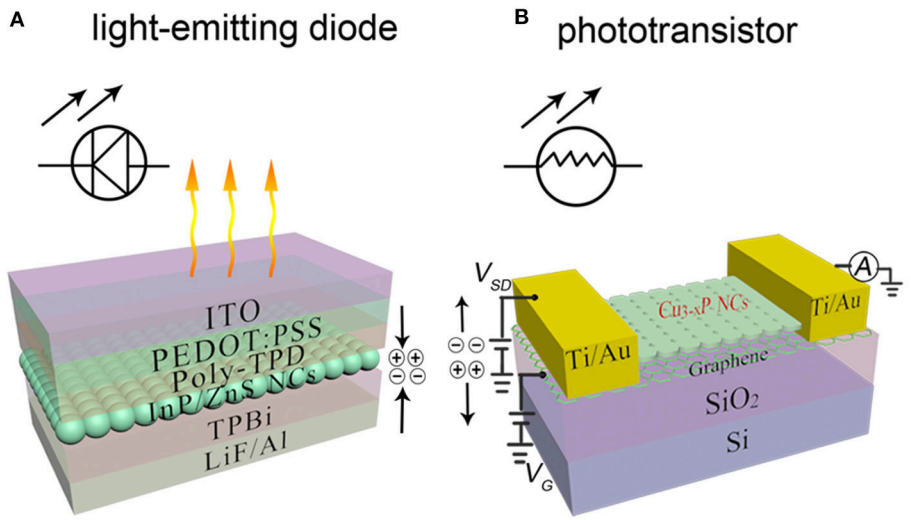

FIGURE 7 | Colloidal nanocrystal device architectures with metal phosphide NCs. **(A)** A white-LED using InP/ZnS NCs. Reproduced with permission from Yang et al. (2012) with permission of John Wiley and Sons. **(B)** Phototransistors based on the hybrid graphene-$Cu_{3-x}P$ NC structure. Reproduced with permission from Sun et al. (2017) with permission of John Wiley and Sons.

one layer to two layers resulted in devices exhibiting a power conversion of 1.5%, with an open-circuit voltage of 0.39 V, a short-circuit current of 8.4 mA cm^{-2} and a fill factor of 45%. Luber and coworkers tested photovoltaic performance of heterojunction devices consisting of ITO/ZnO/Zn_3P_2/MoO_3/Ag (Luber et al., 2013). The device possessed excellent rectification behavior (rectification ratio of 600) and photosensitivity (on/off ratio of $\sim 10^2$ under 100 mW cm^{-2} AM 1.5G illumination). Charge carrier mobilities and lifetimes for InP and InZnP QDs are comparable to those of PbS QDs after an $(NH_4)_2S$ ligand-exchange procedure, making it possible to utilize In(Zn)P QD films in solar cells. Power conversion efficiencies of 0.65 and 1.2% were achieved of the solar cells based on InP and InZnP QDs, respectively (Crisp et al., 2018).

Recently, Sun demonstrated high-performance, broadband photodetectors with the hybrid graphene-$Cu_{3-x}P$ NC structure (Sun et al., 2017). The efficient three-terminal photodetectors (phototransistors) (**Figure 7B**) exhibit photoresponse from 400 to 1,550 nm with an ultrahigh responsivity (1.59×10^5 A W^{-1}) and high photoconductive gain (6.66×10^5) at 405 nm, and a good responsivity of 9.34 A W^{-1} at 1,550 nm. The light-activated functionality of device is provided by a layer of strongly light-absorbing colloidal NCs and an ultrafast carrier transportation graphene layer.

In summary, the prospect of employing metal phosphide NCs in optoelectronic devices offers a number of unique benefits related to their photo-physical properties. Therefore, the colloidal synthesis of various types of metal phosphide NCs has been steadily increasing in recent years and further stimulates their applications. Among them, InP, Cd_3P_3, and Zn_3P_2 NCs are of significant importance in many light absorption and emission-based applications, such as photovoltaics and light emitting diodes. Particularly, InP and Zn_3P_3 are of great interest due to their suitable band gap and low intrinsic toxicity. Despite excellent properties, they are still facing critical issues before they can replace conventional NCs. Compared to chalcogenide-based NCs, metal phosphide NCs exhibit synthetically induced broad size distributions, and low PLQYs and poor thermo- and photo-stability stability. Significant attention has been given to improving these aspects, from viewpoint of chemistry. However, additional attention must be paid to the optimization of their photo-physical properties via structure engineering at the interface and controlling the exciton dynamics. Currently, the performance of optoelectronic devices based on metal phosphide NCs is largely limited due to the undeveloped synthetic methods. Future development of the synthetic approach for metal phosphide NCs is expected to lead to the high-performance optoelectronic devices, i.e., displays.

AUTHOR CONTRIBUTIONS

All authors listed have made a substantial, direct and intellectual contribution to the work, and approved it for publication.

ACKNOWLEDGMENTS

We gratefully appreciate the financial support from the National Natural Science Foundation of China (21701015 and 21811530054).

REFERENCES

Abe, S., Capek, R. K., De Geyter, B., and Hens, Z. (2013). Reaction chemistry/nanocrystal property relations in the hot injection synthesis, the role of the solute solubility. *ACS Nano* 7, 943–949. doi: 10.1021/nn3059168

Adam, S., Talapin, D. V., Borchert, H., Lobo, A., McGinley, C., de Castro, A. R. B., et al. (2005). The effect of nanocrystal surface structure on the luminescence properties: photoemission study of HF-etched InP nanocrystals. *J. Chem. Phys.* 123:084706. doi: 10.1063/1.2004901

Allen, P. M., Walker, B. J., and Bawendi, M. G. (2010). Mechanistic insights into the formation of InP quantum dots. *Angew. Chem. Int. Edn.* 49, 760–762. doi: 10.1002/anie.200905632

Bang, E., Choi, Y., Cho, J., Suh, Y. H., Ban, H. W., Son, J. S., et al. (2017). Large-scale synthesis of highly luminescent InP@ZnS quantum dots using elemental phosphorus precursor. *Chem. Mater.* 29, 4236–4243. doi: 10.1021/acs.chemmater.7b00254

Bichat, M. P., Politova, T., Pascal, J. L., Favier, F., and Monconduit, L. (2004a). Electrochemical reactivity of Cu3P with lithium. *J. Electrochem. Soc.* 151, A2074–A2081. doi: 10.1149/1.1815156

Bichat, M. P., Politova, T., Pfeiffer, H., Tancret, F., Monconduit, L., Pascal, J. L., et al. (2004b). Cu3P as anode material for lithium ion battery: powder morphology and electrochemical performances. *J. Power Sources* 136, 80–87. doi: 10.1016/j.jpowsour.2004.05.024

Blanchard, P. E. R., Grosvenor, A. P., Cavell, R. G., and Mar, A. (2008). X-ray photoelectron and absorption spectroscopy of metal-rich phosphides M2P and M3P (M = Cr-Ni). *Chem. Mater.* 20, 7081–7088. doi: 10.1021/cm802123a

Brock, S. L., and Senevirathne, K. (2008). Recent developments in synthetic approaches to transition metal phosphide nanoparticles for magnetic and catalytic applications. *J. Solid State Chem.* 181, 1552–1559. doi: 10.1016/j.jssc.2008.03.012

Brunetti, V., Chibli, H., Fiammengo, R., Galeone, A., Malvindi, M. A., Vecchio, G., et al. (2013). InP/ZnS as a safer alternative to CdSe/ZnS core/shell quantum dots: in vitro and in vivo toxicity assessment. *Nanoscale* 5, 307–317. doi: 10.1039/C2NR33024E

Cao, F., Wang, S., Wang, F. J., Wu, Q. Q., Zhao, D. W., and Yang, X. Y. (2018). A layer-by-layer growth strategy for large-size InP/ZnSe/ZnS core–shell quantum dots enabling high-efficiency light-emitting diodes. *Chem. Mater.* 30, 8002–8007. doi: 10.1021/acs.chemmater.8b03671

Cao, H. F., Liu, Z. K., Zhu, X. X., Peng, J., Hu, L., Xu, S. M., et al. (2015). PbS/Cd3P2 quantum heterojunction colloidal quantum dot solar cells. *Nanotechnology* 26:035401. doi: 10.1088/0957-4484/26/3/035401

Carenco, S., Demange, M., Shi, J., Boissiere, C., Sanchez, C., Le Floch, P., et al. (2010). White phosphorus and metal nanoparticles: a versatile route to metal phosphide nanoparticles. *Chem. Commun.* 46, 5578–5580. doi: 10.1039/c0cc00684j

Carenco, S., Portehault, D., Boissiere, C., Mezailles, N., and Sanchez, C. (2013). Nanoscaled metal borides and phosphides: recent developments and perspectives. *Chem. Rev.* 113, 7981–8065. doi: 10.1021/cr400020d

Chandrasekaran, V., Tessier, M. D., Dupont, D., Geiregat, P., Hens, Z., and Brainis, E. (2017). Nearly blinking-free, high-purity single-photon emission by colloidal InP/ZnSe quantum dots. *Nano Lett.* 17, 6104–6109. doi: 10.1021/acs.nanolett.7b02634

Chen, O., Zhao, J., Chauhan, V. P., Cui, J., Wong, C., Harris, D. K., et al. (2013). Compact high-quality CdSe-CdS core-shell nanocrystals with narrow emission linewidths and suppressed blinking. *Nat. Mater.* 12, 445–451. doi: 10.1038/nmat3539

Chibli, H., Carlini, L., Park, S., Dimitrijevic, N. M., and Nadeau, J. L. (2011). Cytotoxicity of InP/ZnS quantum dots related to reactive oxygen species generation. *Nanoscale* 3, 2552–2559. doi: 10.1039/c1nr10131e

Christodoulou, S., Climente, J. I., Planelles, J., Brescia, R., Prato, M., Martin-Garcia, B., et al. (2018). Chloride-Induced thickness control in CdSe nanoplatelets. *Nano Lett.* 18, 6248–6254. doi: 10.1021/acs.nanolett.8b02361

Clark, M. D., Kumar, S. K., Owen, J. S., and Chan, E. M. (2011). Focusing nanocrystal size distributions via production control. *Nano Lett.* 11, 1976–1980. doi: 10.1021/nl200286j

Coe, S., Woo, W. K., Bawendi, M., and Bulovic, V. (2002). Electroluminescence from single monolayers of nanocrystals in molecular organic devices. *Nature* 420, 800–803. doi: 10.1038/nature01217

Crisp, R. W., Kirkwood, N., Grimaldi, G., Kinge, S., Siebbeles, L. D. A., and Houtepen, A. J. (2018). Highly photoconductive InP quantum dots films and solar cells. *ACS Appl. Energy Mater.* 1, 6569–76. doi: 10.1021/acsaem.8b01453

Cui, J., Beyler, A. P., Marshall, L. F., Chen, O., Harris, D. K., Wanger, D. D., et al. (2013). Direct probe of spectral inhomogeneity reveals synthetic tunability of single-nanocrystal spectral linewidths. *Nat. Chem.* 5, 602–606. doi: 10.1038/nchem.1654

Dai, X. L., Zhang, Z. X., Jin, Y. Z., Niu, Y., Cao, H. J., Liang, X. Y., et al. (2014). Solution-processed, high-performance light-emitting diodes based on quantum dots. *Nature* 515, 96–99. doi: 10.1038/nature13829

De Trizio, L., Figuerola, A., Manna, L., Genovese, A., George, C., Brescia, R., et al. (2012). Size-tunable, hexagonal plate-like Cu3P and Janus-like Cu-Cu3P Nanocrystals. *ACS Nano* 6, 32–41. doi: 10.1021/nn203702r

Dennis, A. M., Mangum, B. D., Piryatinski, A., Park, Y. S., Hannah, D. C., Casson, J. L., et al. (2012). Suppressed blinking and Auger recombination in near-infrared type-II InP/CdS nanocrystal quantum dots. *Nano Lett.* 12, 5545–5551. doi: 10.1021/nl302453x

Dupont, D., Tessier, M. D., Smet, P. F., and Hens, Z. (2017). Indium phosphide-based quantum dots with shell-enhanced absorption for luminescent down-conversion. *Adv. Mater.* 29:1700686. doi: 10.1002/adma.201700686

Friedfeld, M. R., Stein, J. L., and Cossairt, B. M. (2017). Main-group-semiconductor cluster molecules assynthetic intermediates to nanostructures. *Inorg. Chem.* 56, 8689–8697. doi: 10.1021/acs.inorgchem.7b00291

Gaponenko, S., Demir, H. V., Seassal, C., and Woggon, U. (2016). Colloidal nanophotonics: the emerging technology platform. *Optics Express* 24, A430–A433. doi: 10.1364/OE.24.00A430

Gary, D. C., Glassy, B. A., and Cossairt, B. M. (2014). Investigation of indium phosphide quantum dot nucleation and growth utilizing triarylsilylphosphine precursors. *Chem. Mater.* 26, 1734–1744. doi: 10.1021/cm500102q

Gary, D. C., Terban, M. W., Billinge, S. J. L., and Cossairt, B. M. (2015). Two-step nucleation and growth of InP quantum dots via magic-sized cluster intermediates. *Chem. Mater.* 27, 1432–1441. doi: 10.1021/acs.chemmater.5b00286

Green, M., and O'Brien, P. (1998). A novel metalorganic route for the direct and rapid synthesis of monodispersed quantum dots of indium phosphide. *Chem. Commun.* 22, 2459–2460. doi: 10.1039/a806419i

Green, M., and O'Brien, P. (2001). A novel metalorganic route to nanocrystallites of zinc phosphide. *Chem. Mater.* 13, 4500–4505. doi: 10.1021/cm011009i

Greenwood, N. N., Parish, R. V., and Thornton, P. (1966). Metal borides. *Q. Rev.* 20, 441–464. doi: 10.1039/qr9662000441

Harris, D. K., and Bawendi, M. G. (2012). Improved precursor chemistry for the synthesis of III-V quantum dots. *J. Am. Chem. Soc.* 134, 20211–20213. doi: 10.1021/ja309863n

Haubold, S., Haase, M., Kornowski, A., and Weller, H. (2001). Strongly luminescent InP/ZnS core-shell nanoparticles. *Chemphyschem* 2, 331–334. doi: 10.1002/1439-7641(20010518)2:5<331::AID-CPHC331>3.0.CO;2-0

Henkes, A. E., and Schaak, R. E. (2007). Trioctylphosphine: a general phosphorus source for the low-temperature conversion of metals into metal phosphides. *Chem. Mater.* 19, 4234–4242. doi: 10.1021/cm071021w

Ho, M. Q., Esteves, R. J. A., Kedarnath, G., and Arachchige, I. U. (2015). Size-dependent optical properties of luminescent Zn3P2 quantum dots. *J. Phys. Chem. C* 119, 10576–10584. doi: 10.1021/acs.jpcc.5b01747

Hong, G. S., Antaris, A. L., and Dai, H. J. (2017). Near-infrared fluorophores for biomedical imaging. *Nat. Biomed. Eng.* 1:0010. doi: 10.1038/s41551-016-0010

Hunger, C., Ojo, W. S., Bauer, S., Xu, S., Zabel, M., Chaudret, B., et al. (2013). Stoichiometry-controlled FeP nanoparticles synthesized from a single source precursor. *Chem. Commun.* 49, 11788–11790. doi: 10.1039/c3cc46863a

Imran, M., Caligiuri, V., Wang, M. J., Goldoni, L., Prato, M., Krahne, R., et al. (2018). Benzoyl halides as alternative precursors for the colloidal synthesis of lead-based halide perovskite nanocrystals. *J. Am. Chem. Soc.* 140, 2656–2664. doi: 10.1021/jacs.7b13477

Jang, E. P., Jo, J. H., Lim, S. W., Lim, H. B., Kim, H. J., Han, C. Y., et al. (2018). Unconventional formation of dual-colored InP quantum dot-embedded silica composites for an operation-stable white light-emitting diode. *J. Mater. Chem. C* 6, 11749–11756. doi: 10.1039/C8TC04095H

Janke, E. M., Williams, N. E., She, C. X., Zherebetskyy, D., Hudson, M. H., Wang, L. L., et al. (2018). Origin of broad emission spectra in InP quantum dots: contributions from structural and electronic disorder. *J. Am. Chem. Soc.* 140, 15791–15803. doi: 10.1021/jacs.8b08753

Joung, S., Yoon, S., Han, C. S., Kim, Y., and Jeong, S. (2012). Facile synthesis of uniform large-sized InP nanocrystal quantum dots using tris(tert-butyldimethylsilyl)phosphine. *Nanoscale Res. Lett.* 7:93. doi: 10.1186/1556-276X-7-93

Jun, K. W., Khanna, P. K., Hong, K. B., Baeg, J. O., and Suh, Y. D. (2006). Synthesis of InP nanocrystals from indium chloride and sodium phosphide by solution route. *Mater. Chem. Phys.* 96, 494–497. doi: 10.1016/j.matchemphys.2005.07.041

Kagan, C. R., Lifshitz, E., Sargent, E. H., and Talapin, D. V. (2016). Building devices from colloidal quantum dots. *Science* 353:aac5523. doi: 10.1126/science.aac5523

Kang, H., Kim, S., Oh, J. H., Yoon, H. C., Jo, J. H., Yang, H., et al. (2018). Color-by-blue QD-emissive LCD enabled by replacing RGB color filters with narrow-band GR InP/ZnSeS/ZnS QD films. *Adv. Optic. Mater.* 6:1701239. doi: 10.1002/adom.201701239

Keuleyan, S., Lhuillier, E., Brajuskovic, V., and Guyot-Sionnest, P. (2011). Mid-infrared HgTe colloidal quantum dot photodetectors. *Nat. Photo.* 5, 489–493. doi: 10.1038/nphoton.2011.142

Khanna, P. K., Singh, N., and More, P. (2010). Synthesis and band-gap photoluminescence from cadmium phosphide nano-particles. *Curr. Appl. Phys.* 10, 84–88. doi: 10.1016/j.cap.2009.05.002

Kim, K., Yoo, D., Choi, H., Tamang, S., Ko, J. H., Kim, S., et al. (2016). Halide-amine co-passivated indium phosphide colloidal quantum dots in tetrahedral shape. *Angew. Chem. Int. Ed. Engl.* 55, 3714–3718. doi: 10.1002/anie.201600289

Kim, S., Kim, T., Kang, M., Kwak, S. K., Yoo, T. W., Park, L. S., et al. (2012). Highly luminescent InP/GaP/ZnS nanocrystals and their application to white light-emitting diodes. *J. Am. Chem. Soc.* 134, 3804–3809. doi: 10.1021/ja210211z

Koh, S., Eom, T., Kim, W. D., Lee, K., Lee, D., Lee, Y. K., et al. (2017). Zinc-phosphorus complex working as an atomic valve for colloidal growth of monodisperse indium phosphide quantum dots. *Chem. Mater.* 29, 6346–6355. doi: 10.1021/acs.chemmater.7b01648

Laufersky, G., Bradley, S., Frecaut, E., Lein, M., and Nann, T. (2018). Unraveling aminophosphine redox mechanisms for glovebox-free InP quantum dot syntheses. *Nanoscale* 10, 8752–8762. doi: 10.1039/C8NR01286E

Lauth, J., Strupeit, T., Komowski, A., and Weller, H. (2013). A transmetalation route for colloidal GaAs nanocrystals and additional III-V semiconductor materials. *Chem. Mater.* 25, 1377–1383. doi: 10.1021/cm3019617

Li, D. Z., Peng, L. C., Zhang, Z. L., Shi, Z., Xie, R. G., Han, M. Y., et al. (2014). Large scale synthesis of air stable precursors for the preparation of high quality metal arsenide and phosphide nanocrystals as efficient emitters covering the visible to near infrared region. *Chem. Mater.* 26, 3599–3602. doi: 10.1021/cm500581m

Li, L., Protiere, M., and Reiss, P. (2008). Economic synthesis of high quality InP nanocrystals using calcium phosphide as the phosphorus precursor. *Chem. Mater.* 20, 2621–2623. doi: 10.1021/cm7035579

Li, L., and Reiss, P. (2008). One-pot synthesis of highly luminescent InP/ZnS nanocrystals without precursor injection. *J. Am. Chem. Soc.* 130, 11588–11589. doi: 10.1021/ja803687e

Lim, J., Bae, W. K., Lee, D., Nam, M. K., Jung, J., Lee, C., et al. (2011). InP@ZnSeS, core@composition gradient shell quantum dots with enhanced stability. *Chem. Mater.* 23, 4459–4463. doi: 10.1021/cm201550w

Lim, J., Park, M., Bae, W. K., Lee, D., Lee, S., Lee, C., et al. (2013). Highly efficient cadmium-free quantum dot light-emitting diodes enabled by the direct formation of excitons within InP@ZnSeS quantum dots. *ACS Nano* 7, 9019–9026. doi: 10.1021/nn403594j

Lin, G. M., Ouyang, Q. L., Hu, R., Ding, Z. C., Tian, J. L., Yin, F., et al. (2015). *In vivo* toxicity assessment of non-cadmium quantum dots in BALB/c mice. *Nanomed. Nanotechnol. Biol. Med.* 11, 341–350. doi: 10.1016/j.nano.2014.10.002

Liu, J. F., Meyns, M., Zhang, T., Arbiol, J., Cabot, A., and Shavel, A. (2018). Triphenyl phosphite as the phosphorus source for the scalable and cost-effective production of transition metal phosphides. *Chem. Mater.* 30, 1799–1807. doi: 10.1021/acs.chemmater.8b00290

Liu, Z. K., Mu, H. R., Xiao, S., Wang, R. B., Wang, Z. T., Wang, W. W., et al. (2016). Pulsed lasers employing solution-processed plasmonic Cu3-xPcolloidal nanocrystals. *Adv. Mater.* 28, 3535–3542. doi: 10.1002/adma.201504927

Liu, Z. P., Kumbhar, A., Xu, D., Zhang, J., Sun, Z. Y., and Fang, J. Y. (2008). Coreduction colloidal synthesis of III-V nanocrystals: the case of InP. *Angew. Chem. Int. Edn.* 47, 3540–3542. doi: 10.1002/anie.200800281

Luber, E. J., Mobarok, M. H., and Buriak, J. M. (2013). Solution-processed zinc phosphide (α-Zn3P2) colloidal semiconducting nanocrystals for thin film photovoltaic applications. *ACS Nano* 7, 8136–8146. doi: 10.1021/nn4034234

Manna, G., Bose, R., and Pradhan, N. (2013). Semiconducting and plasmonic copper phosphide platelets. *Angew. Chem. Int. Edn.* 52, 6762–6766. doi: 10.1002/anie.201210277

Miao, S., Yang, T., Hickey, S. G., Lesnyak, V., Rellinghaus, B., Xu, J. Z., et al. (2013). Emissive ZnO@Zn3P2 nanocrystals: synthesis, optical, and optoelectrochemical properties. *Small* 9, 3415–3422. doi: 10.1002/smll.201203023

Miao, S. D., Hickey, S. G., Rellinghaus, B., Waurisch, C., and Eychmuller, A. (2010). Synthesis and characterization of cadmium phosphide quantum dots emitting in the visible red to near-infrared. *J. Am. Chem. Soc.* 132, 5613–5615. doi: 10.1021/ja9105732

Miao, S. D., Hickey, S. G., Waurisch, C., Lesnyak, V., Otto, T., Rellinghaus, B., et al. (2012). Synthesis of monodisperse cadmium phosphide nanoparticles using *ex-situ* produced phosphine. *ACS Nano* 6, 7059–7065. doi: 10.1021/nn3021037

Michalet, X., Pinaud, F. F., Bentolila, L. A., Tsay, J. M., Doose, S., Li, J. J., et al. (2005). Quantum dots for live cells, *in vivo* imaging, and diagnostics. *Science* 307, 538–544. doi: 10.1126/science.1104274

Micic, O. I., Cheong, H. M., Fu, H., Zunger, A., Sprague, J. R., Mascarenhas, A., et al. (1997). Size-dependent spectroscopy of InP quantum dots. *J. Phys. Chem. B* 101, 4904–4912. doi: 10.1021/jp9704731

Micic, O. I., Curtis, C. J., Jones, K. M., Sprague, J. R., and Nozik, A. J. (1994). Synthesis and characterization of InP quantum dots. *J. Phys. Chem.* 98, 4966–4969. doi: 10.1021/j100070a004

Micic, O. I., Sprague, J., Lu, Z. H., and Nozik, A. J. (1996). Highly efficient band-edge emission from InP quantum dots. *Appl. Phys. Lett.* 68, 3150–3152.

Micic, O. I., Sprague, J. R., Curtis, C. J., Jones, K. M., Machol, J. L., Nozik, A. J., et al. (1995). Synthesis and characterization of InP, GaP, and GalnP2 quantum dots. *J. Phys. Chem.* 99, 7754–7759.

Mobarok, M. H., Luber, E. J., Bernard, G. M., Peng, L., Wasylishen, R. E., and Buriak, J. M. (2014). Phase-pure crystalline zinc phosphide nanoparticles: synthetic approaches and characterization. *Chem. Mater.* 26, 1925–1935. doi: 10.1021/cm500557f

Mundy, M. E., Ung, D., Lai, N. L., Jahrman, E. P., Seidler, G. T., and Cossairt, B. M. (2018). Aminophosphines as versatile precursors for the synthesis of metal phosphide nanocrystals. *Chem. Mater.* 30, 5373–5379. doi: 10.1021/acs.chemmater.8b02206

Nedelcu, G., Protesescu, L., Yakunin, S., Bodnarchuk, M. I., Grotevent, M. J., and Kovalenko, M. V. (2015). Fast anion-exchange in highly luminescentnanocrystals of cesium lead halide perovskites (CsPbX3, X = Cl, Br, I). *Nano Lett.* 15, 5635–5640. doi: 10.1021/acs.nanolett.5b02404

Ojo, W. S., Xu, S., Delpech, F., Nayral, C., and Chaudret, B. (2012). Room-temperature synthesis of air-stable and size-tunable luminescent ZnS-coated Cd3P2 nanocrystals with high quantum yields. *Angew. Chem. Int. Edn.* 51, 738–741. doi: 10.1002/anie.201104864

Panfil, Y. E., Oded, M., and Banin, U. (2018). Colloidal quantum nanostructures: emerging materials for display applications. *Angew. Chem. Int. Edn.* 57, 4274–4295. doi: 10.1002/anie.201708510

Park, J., Koo, B., Yoon, K. Y., Hwang, Y., Kang, M., Park, J. G., et al. (2005). Generalized synthesis of metal phosphide nanorods via thermal decomposition of continuously delivered metal-phosphine complexes using a syringe pump. *J. Am. Chem. Soc.* 127, 8433–8440. doi: 10.1021/ja0427496

Perera, S. C., Fodor, P. S., Tsoi, G. M., Wenger, L. E., and Brock, S. L. (2003). Application of de-silylation strategies to the preparation of transition metal pnictide nanocrystals: the case of FeP. *Chem. Mater.* 15, 4034–4038. doi: 10.1021/cm034443o

Pietra, F., De Trizio, L., Hoekstra, A. W., Renaud, N., Prato, M., Grozema, F. C., et al. (2016). Tuning the lattice parameter of InxZnyP for highly luminescent lattice-matched core/shell quantum dots. *ACS Nano* 10, 4754–4762. doi: 10.1021/acsnano.6b01266

Pietra, F., Kirkwood, N., De Trizio, L., Hoekstra, A. W., Kleibergen, L., Renaud, N., et al. (2017). Ga for Zn cation exchange allows for highly luminescent and photostable InZnP-based quantum dots. *Chem. Mater.* 29, 5192–5199. doi: 10.1021/acs.chemmater.7b00848

Pietryga, J. M., Park, Y. S., Lim, J. H., Fidler, A. F., Bae, W. K., Brovelli, S., et al. (2016). Spectroscopic and device aspects of nanocrystal quantum dots. *Chem. Rev.* 116, 10513–10622. doi: 10.1021/acs.chemrev.6b00169

Pu, C., Qin, H., Gao, Y., Zhou, J., Wang, P., and Peng, X. (2017). Synthetic control of exciton behavior in colloidal quantum dots. *J. Am. Chem. Soc.* 139, 3302–3311. doi: 10.1021/jacs.6b11431

Qian, L., Zheng, Y., Xue, J. G., and Holloway, P. H. (2011). Stable and efficient quantum-dot light-emitting diodes based on solution-processed multilayer structures. *Nat. Photo.* 5, 543–548. doi: 10.1038/nphoton.2011.171

Rafipoor, M., Dupont, D., Tornatzky, H., Tessier, M. D., Maultzsch, J., Hens, Z., et al. (2018). Strain engineering in InP/(Zn,Cd)Se core/shell quantum dots. *Chem. Mater.* 30, 4393–4400. doi: 10.1021/acs.chemmater.8b01789

Ramasamy, P., Kim, N., Kang, Y. S., Ramirez, O., and Lee, J. S. (2017). Tunable, bright, and narrow-band luminescence from colloidal indium phosphide quantum dots. *Chem. Mater.* 29, 6893–6899. doi: 10.1021/acs.chemmater.7b02204

Ramasamy, P., Ko, K. J., Kang, J. W., and Lee, J. S. (2018). Two-step "seed-mediated" synthetic approach to colloidal indium phosphide quantum dots with high-purity photo- and electroluminescence. *Chem. Mater.* 30, 3643–3647. doi: 10.1021/acs.chemmater.8b02049

Reiss, P., Carriere, M., Lincheneau, C., Vaure, L., and Tamang, S. (2016). Synthesis of semiconductor nanocrystals, focusing on nontoxic and earth-abundant materials. *Chem. Rev.* 116, 10731–10819. doi: 10.1021/acs.chemrev.6b00116

Sahu, A., Kang, M. S., Kompch, A., Notthoff, C., Wills, A. W., Deng, D., et al. (2012). Electronic impurity doping in CdSe nanocrystals. *Nano Lett.* 12, 2587–2594. doi: 10.1021/nl300880g

Shen, W., Tang, H. Y., Yang, X. L., Cao, Z. L., Cheng, T., Wang, X. Y., et al. (2017). Synthesis of highly fluorescent InP/ZnS small-core/thick-shell tetrahedral-shaped quantum dots for blue light-emitting diodes. *J. Mater. Chem. C* 5, 8243–8249. doi: 10.1039/C7TC02927F

Song, W. S., Lee, H. S., Lee, J. C., Jang, D. S., Choi, Y., Choi, M., et al. (2013). Amine-derived synthetic approach to color-tunable InP/ZnS quantum dots with high fluorescent qualities. *J. Nanopart. Res.* 15:1750. doi: 10.1007/s11051-013-1750-y

Steckel, J. S., Coe-Sullivan, S., Bulovic, V., and Bawendi, M. G. (2003). 1.3 μm to 1.55 μm tunable electroluminescence from PbSe quantum dots embedded within an organic device. *Adv. Mater.* 15, 1862–1866. doi: 10.1002/adma.200305449

Sun, T., Wang, Y. J., Yu, W. Z., Wang, Y. S., Dai, Z. G., Liu, Z. K., et al. (2017). Flexible broadband graphene photodetectors enhanced by plasmonic Cu3-xP colloidal nanocrystals. *Small* 13:1701881. doi: 10.1002/smll.201701881

Talapin, D. V., Lee, J. S., Kovalenko, M. V., and Shevchenko, E. V. (2010). Prospects of colloidal nanocrystals for electronic and optoelectronic applications. *Chem. Rev.* 110, 389–458. doi: 10.1021/cr900137k

Tamang, S., Lincheneau, C., Hermans, Y., Jeong, S., and Reiss, P. (2016). Chemistry of InP nanocrystal syntheses. *Chem. Mater.* 28, 2491–2506. doi: 10.1021/acs.chemmater.5b05044

Tessier, M. D., Baquero, E. A., Dupont, D., Grigel, V., Bladt, E., Bals, S., et al. (2018). Interfacial oxidation and photoluminescence of InP-based core/shell quantum dots. *Chem. Mater.* 30, 6877–6883. doi: 10.1021/acs.chemmater.8b03117

Tessier, M. D., De Nolf, K., Dupont, D., Sinnaeve, D., De Roo, J., and Hens, Z. (2016). Aminophosphines: a double role in the synthesis of colloidal indium phosphide quantum dots. *J. Am. Chem. Soc.* 138, 5923–5929. doi: 10.1021/jacs.6b01254

Tessier, M. D., Dupont, D., De Nolf, K., De Roo, J., and Hens, Z. (2015). Economic and size-tunable synthesis of InP/ZnE (E = S, Se)colloidal quantum dots. *Chem. Mater.* 27, 4893–4898. doi: 10.1021/acs.chemmater.5b02138

Ung, T. D. T., Tran, T. T. H., Nguyen, Q. L., and Reiss, P. (2008). Low temperature synthesis of InP nanocrystals. *Mater. Chem. Phys.* 112, 1120–1123. doi: 10.1016/j.matchemphys.2008.07.051

Vinokurov, A., Chernysheva, G., Mordvinova, N., and Dorofeev, S. (2018). Optical properties and structure of Ag-doped InP quantum dots prepared by a phosphine synthetic route. *Dalton Trans.* 47, 12414–12419. doi: 10.1039/C8DT02434K

Wang, H. C., Zhang, H., Chen, H. Y., Yeh, H. C., Tseng, M. R., Chung, R. J., et al. (2017). Cadmium-free InP/ZnSeS/ZnS heterostructure-based quantum dot light-emitting diodes with a ZnMgO electron transport layer and a brightness of over 10 000 cd m(-2). *Small* 13:1603962. doi: 10.1002/smll.201603962

Xie, R., Battaglia, D., and Peng, X. G. (2007). Colloidal InP nanocrystals as efficient emitters covering blue to near-infrared. *J. Am. Chem. Soc.* 129, 15432–15433. doi: 10.1021/ja076363h

Xie, R. G., Zhang, J. X., Zhao, F., Yang, W. S., and Peng, X. G. (2010). Synthesis of monodisperse, highly emissive, and size-tunable Cd3P2 nanocrystals. *Chem. Mater.* 22, 3820–3822. doi: 10.1021/cm1008653

Yang, W., He, G. X., Mei, S. L., Zhu, J. T., Zhang, W. L., Chen, Q. H., et al. (2017). Controllable synthesis of dual emissive Ag:InP/ZnS quantum dots with high fluorescence quantum yield. *Appl. Surf. Sci.* 423, 686–694. doi: 10.1016/j.apsusc.2017.06.048

Yang, X., Zhao, D. W., Leck, K. S., Tan, S. T., Tang, Y. X., Zhao, J. L., et al. (2012). Full visible range covering InP/ZnS nanocrystals with high photometric performance and their application to white quantum dot light-emitting diodes. *Adv. Mater.* 24, 4180–4185. doi: 10.1002/adma.201104990

Zan, F., and Ren, J. C. (2012). Gas-liquid phase synthesis of highly luminescent InP/ZnS core/shell quantum dots using zinc phosphide as a new phosphorus source. *J. Mater. Chem.* 22, 1794–1799. doi: 10.1039/C1JM13982G

Zhang, A. D., Dong, C. Q., Liu, H., and Ren, J. C. (2013). Blinking behavior of CdSe/CdS quantum dots controlled by alkylthiols as surface trap modifiers. *J. Phys. Chem. C* 117, 24592–24600. doi: 10.1021/jp408544x

Zhang, Z. L., Liu, D., Li, D. Z., Huang, K. K., Zhang, Y., Shi, Z., et al. (2015). Dual emissive Cu:InP/ZnS/InP/ZnS nanocrystals: single-source "greener"emitters with flexibly tunable emission from visible to near-infrared and their application in white light-emitting diodes. *Chem. Mater.* 27, 1405–1411. doi: 10.1021/cm5047269

Ziegler, J., Xu, S., Kucur, E., Meister, F., Batentschuk, M., Gindele, F., et al. (2008). Silica-coated InP/ZnS nanocrystals as converter material in white LEDs. *Adv. Mater.* 20, 4068–4073. doi: 10.1002/adma.200800724

Conflict of Interest Statement: The authors declare that the research was conducted in the absence of any commercial or financial relationships that could be construed as a potential conflict of interest.

frontiers in Chemistry

ORIGINAL RESEARCH
published: 27 June 2019
doi: 10.3389/fchem.2019.00466

Influence of the Core/Shell Structure of Indium Phosphide Based Quantum Dots on Their Photostability and Cytotoxicity

Karl David Wegner[1†], Fanny Dussert[2], Delphine Truffier-Boutry[3], Anass Benayad[3], David Beal[2], Lucia Mattera[1], Wai Li Ling[4], Marie Carrière[2*] and Peter Reiss[1*]*

[1] Univ. Grenoble Alpes, CEA, CNRS, IRIG, SyMMES, STEP, Grenoble, France, [2] Univ. Grenoble Alpes, CEA, CNRS, IRIG, SyMMES, CIBEST, Grenoble, France, [3] Univ. Grenoble Alpes, CEA-LITEN L2N, Grenoble, France, [4] Univ. Grenoble Alpes, CEA, CNRS, IRIG, IBS, Grenoble, France

With the goal to improve their photostability, InP-based QDs are passivated with three types of inorganic shells, namely (i) a gradient $ZnSe_xS_{1-x}$ shell, (ii) an additional ZnS shell on top of the gradient shell with two different thicknesses (core/shell/shell, CSS), (iii) an alumina coating on top of ZnS. All three systems have photoluminescence quantum yields (PLQY) > 50% and similar PL decay times (64–67 ns). To assess their photostability they are incorporated into a transparent poly (methyl methacrylate) (PMMA) matrix and exposed to continuous irradiation with simulated sunlight in a climate chamber. The alumina coated core/shell system exhibits the highest stability in terms of PLQY retention as well as the lowest shift of the PL maximum and lowest increase of the PL linewidth, followed by the CSS QDs and finally the gradient shell system. By means of XPS studies we identify the degradation of the ZnS outer layer and concomitant oxidation of the emissive InZnP core as the main origins of degradation in the gradient structure. These modifications do not occur in the case of the alumina-capped sample, which exhibits excellent chemical stability. The gradient shell and CSS systems could be transferred to the aqueous phase using surface ligand exchange with penicillamine. Cytotoxicity studies on human primary keratinocytes revealed that exposure for 24 h to 6.25–100 nM of QDs did not affect cell viability. However, a trend toward reduced cell proliferation is observed for higher concentrations of gradient shell and CSS QDs with a thin ZnS shell, while CSS QDs with a thicker ZnS shell do not exhibit any impact.

Keywords: quantum dots, photostability, cytotoxcity, indium phosphide, core/shell structure, alumina coating

OPEN ACCESS

Edited by:
Vladimir Lesnyak, Dresden University of Technology, Germany

Reviewed by:
Hongbo Li, Beijing Institute of Technology, China
Aliaksei Dubavik, ITMO University, Russia

****Correspondence:***
Karl David Wegner
wegner.karldavid@gmail.com
Marie Carrière
marie.carriere@cea.fr
Peter Reiss
peter.reiss@cea.fr

†Present Address:
Karl David Wegner, Biophotonics (BAM-1.2), BAM Federal Institute for Materials Research and Testing, Berlin, Germany

Specialty section:
This article was submitted to Nanoscience, a section of the journal Frontiers in Chemistry

Received: *22 February 2019*
Accepted: *12 June 2019*
Published: *27 June 2019*

Citation:
Wegner KD, Dussert F, Truffier-Boutry D, Benayad A, Beal D, Mattera L, Ling WL, Carrière M and Reiss P (2019) Influence of the Core/Shell Structure of Indium Phosphide Based Quantum Dots on Their Photostability and Cytotoxicity. Front. Chem. 7:466. doi: 10.3389/fchem.2019.00466

INTRODUCTION

In the quest for toxic-heavy-metal-free quantum dots (QDs), indium phosphide has been shown to be a valid alternative to cadmium-based materials (Reiss et al., 2016; Allocca et al., 2019). The chemical synthesis of InP QDs and their core/shell structures has been strongly developed in the past decade with the goal to bring the optical properties to a level comparable with CdSe based QDs (Cossairt, 2016; Tamang et al., 2016). Concerning the core synthesis, it has been established that the addition of zinc, in form of carboxylate (e.g., stearate, undecylenate, oleate) improves

both the size distribution and hence the emission linewidth and the emission efficiency (Li and Reiss, 2008; Xu et al., 2008; Ung et al., 2010b; Stein et al., 2016). Nonetheless, for achieving high photoluminescence quantum yields (PLQY) and enhanced photostability the precise engineering of core/shell heterostructures is a prerequisite, and ideally, the InP or InZnP core should be covered by a thick shell of a large band gap, chemically stable semiconductor such as ZnS (Reiss et al., 2009). The synthesis of InP/ZnS nanocrystals in a single-step one-pot method by adding a sulfur source (dodecanethiol, DDT) during the core synthesis leads to an alloy structure capped with a thin ZnS shell (Huang et al., 2010). Due to the large lattice mismatch of 7.7% between zinc blende InP and ZnS it is challenging to obtain a thick shell. ZnSe has a lower mismatch (3.3%) and several works reported the growth of either pure ZnSe or graded $ZnSe_xS_{1-x}$ shells on InP or InZnP (Lim et al., 2011; Tessier et al., 2015; Pietra et al., 2016; Chandrasekaran et al., 2017). However, ZnSe provides a weaker carrier confinement than ZnS due to the smaller band gap and is more sensitive to oxidation than ZnS (Toufanian et al., 2018). Therefore, it has been suggested to add a thicker outer ZnS shell on a graded intermediate $ZnSe_xS_{1-x}$ shell (Lim et al., 2013; Ramasamy et al., 2017; Wang et al., 2017). The latter acts as a lattice adapter between the core and the outer shell leading to a core/shell/shell (CSS) system, as already demonstrated in the case of II-VI semiconductors (Reiss et al., 2003; Talapin et al., 2004). Li et al. proposed another way to enhance the photostability of CdSe- or $CuInS_2$- based QDs by generating an alumina coating on their surface (Li et al., 2015; Yan et al., 2016). In this case, the nanocrystal surface is treated with an appropriate aluminum precursor (e.g., aluminum isopropoxide), which transforms to alumina via oxidation. The different above-mentioned strategies for the surface passivation of InP and InZnP QDs are summarized in **Figure 1**.

The goal of the present work is to investigate the impact of the different core/shell systems discussed—core/gradient shell and CSS structures with different thickness of the outer ZnS shell and a newly developed alumina coating—on the photostability and cytotoxicity behavior of InZnP QDs. Aging experiments were carried out in a controlled and reproducible manner by integrating the QDs into a solid polymer matrix (PMMA) and irradiating them with simulated solar light in a climatic chamber. Finally, the cytotoxicity of the obtained QDs was assessed using human primary keratinocytes.

MATERIALS AND METHODS

Chemicals

Indium acetate (99.99%), zinc acetate (99,9%), myristic acid (>99%), tris (trimethylsilyl)phosphine (95%, $(TMS)_3P$), 1-octadecene (90%, ODE), trioctylphosphine (97%, TOP), sulfur (99.99%), selenium (99.99%), dimethylformamide (DMF), poly (methyl methacrylate) (PMMA, M_W ~350,000 GPC), aluminum isopropoxide (Al $(IPA)_3$ 98%), toluene, methanol, chloroform, acetone, hexane, D-penicillamine, tetramethylammonium hydroxide (TMAOH), phosphate-buffered saline solution (1xPBS), and tris (2-carboxyethyl) phosphine hydrochloride solution 0.5 M (TCEP) were purchased from Sigma-Aldrich. Zinc stearate (90%, $ZnSt_2$) was acquired from Riedel de Haën. Oleic acid (70%) came from Fisher Chemicals. All chemicals were used as received without any further purification, unless stated otherwise.

Zinc Ethylxanthate

Zinc ethylxanthate was prepared according to the procedure reported in Protiere and Reiss (2006).

Preparation of Indium-Myristate

Indium acetate (6.9 mmol), myristic acid (21.4 mmol), and ODE (15 mL) were mixed in a 50 mL three neck flask. The solution was stirred and degassed under vacuum for 3 h at 120°C. After cooling down to room temperature the precipitated indium-myristate was washed with ca. 150 mL of dry hexane before drying under vacuum.

Preparation of Zinc-Oleate

Zinc acetate (5 mmol), oleic acid (10 mmol), and 9.35 mL ODE were mixed in a 50 mL three neck flask. The solution was stirred and degassed under vacuum at 120°C for 1 h. After cooling down to room temperature the flask was backfilled with Ar and the mixture was stored in the glove box.

Preparation of TOP-Se and TOP-S

For a 0.4 M TOP-Se stock solution, 2 mmol of selenium powder were dissolved in 5 mL of trioctylphosphine (TOP) for 24 h. The preparation of a 0.4 M TOP-S stock solution was prepared similarly using elemental sulfur.

Synthesis of InZnP Core Nanocrystals

Indium-myristate (0.1 mmol), $ZnSt_2$ (0.2 mmol), and 8.5 mL ODE were mixed in a 50 mL three-neck flask and degassed for 1 h. The flask was backfilled with Ar and the reaction mixture was rapidly heated to 300°C in a molten salt bath. At 100°C 0.1 mmol $(TMS)_3P$, dissolved in 1 mL ODE, was swiftly injected. After 20 min the reaction was quenched by removing the salt bath and letting cool down to room temperature.

Synthesis of InZnP/$ZnSe_xS_{1-x}$ Core/Gradient Shell Nanocrystals

The InZnP core was prepared as mentioned before but instead of cooling down to room temperature the mixture was kept at 220°C. 2.5 mL of the 0.4 M zinc-oleate (1 mmol) stock solution was added dropwise followed by the swift injection of 0.444 mL of TOP-Se (0.2 mmol) stock solution mixed with 0.5 mL ODE and 1.57 mL of TOP-S (0.7 mmol) stock solution. The reaction mixture was heated to 300°C using a heating mantle with a heating ramp of 10°C per minute. The overall shell growth time was ca. 30 min and the reaction was quenched by cooling down to room temperature. The NCs were purified three times by a precipitation (1:1 v/v mixture of methanol/chloroform and acetone) and redispersion (chloroform) cycle and finally stored in hexane.

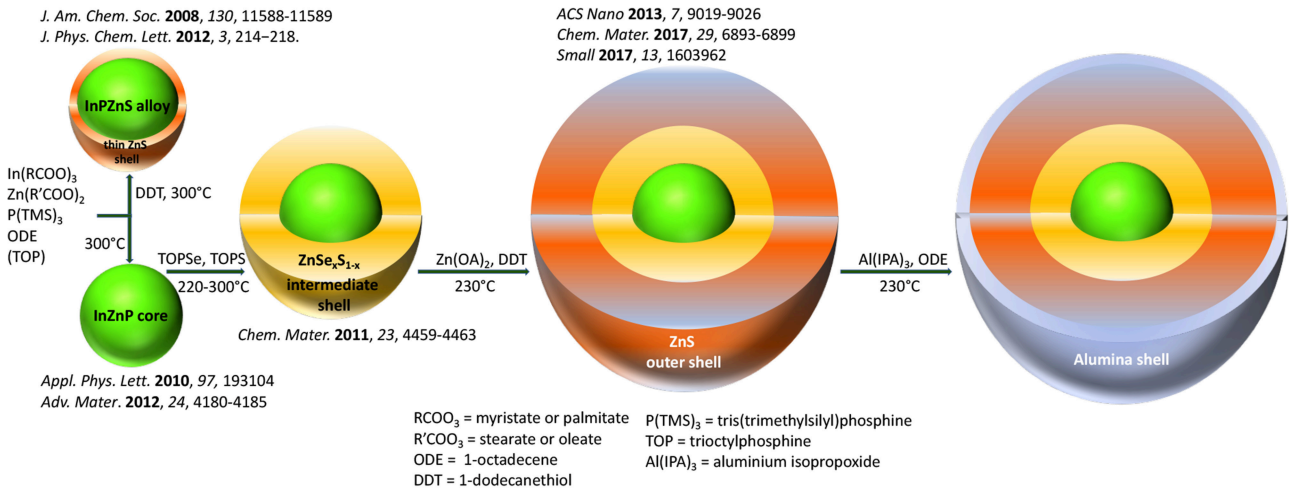

FIGURE 1 | Strategies for the surface passivation of InP-based QDs, leading ultimately to the In(Zn)P/ZnSe$_x$S$_{1-x}$/ZnS core/shell/shell system, illustrated with representative references. The additional surface coating with an alumina shell as described in this work is also displayed in this scheme.

Synthesis of InZnP/ ZnSe$_x$S$_{1-x}$/ZnS Core/Shell/Shell Nanocrystals of Variable ZnS Shell Thickness

The synthesis of the InZnP/ZnSe$_x$S$_{1-x}$ NCs was performed as described above but instead of cooling down to room temperature the mixture was kept at a temperature of 230°C using a heating mantle. In order to prepare the second (thin) ZnS shell, a mixture of 0.1 mmol zinc ethylxanthate dissolved in 100 µL DMF and 1 mL toluene was added to 0.8 mmol $ZnSt_2$ dissolved in 3 mL ODE and injected into the reaction mixture using a syringe pump with a pump rate of 8 mL/h. After 30 min of shell growth the reaction was quenched by cooling down to room temperature and the NCs purified as described above for the gradient shell. To grow a thick ZnS shell the amount of zinc ethylxanthate and zinc stearate solution was doubled and the shell growth time was extended to 60 min before quenching the reaction by cooling down to room temperature.

Synthesis of InZnP/ZnSe$_x$S$_{1-x}$/ZnS-Alumina

InZnP/ZnSe$_x$S$_{1-x}$ NCs synthesis was performed as described above and the mixture was kept at 230°C after gradient shell growth for 30 min. With a syringe pump, a shell mixture used for the preparation of a thin second ZnS shell was injected over the course of 30 min (0.1 mmol zinc ethylxanthate dissolved in 100 µL DMF and 1 mL toluene was mixed with 0.8 mmol $ZnSt_2$ dissolved in 3 mL ODE). When the injection of shell mixture started, 1 mL of a solution prepared by dissolving 1.12 mmol Al $(IPA)_3$ in 3 mL ODE at 40°C was slowly injected. At 10 and 20 min of the shell growth another 1-mL volume of the Al-mixture was injected. The mixture was kept for a total of 60 min at 230°C before cooling down to room temperature and purifying as mentioned before.

Embedding InP-Based QDs in PMMA

To prepare a 30wt % PMMA solution, 3 g of PMMA were dissolved in 7 mL chloroform, stirred for 1 h and ultrasonicated several times in between for 2 min. The QD solutions had a concentration of approximately of 20 mg/mL and in order to prepare a PMMA disc with 0.4 wt% ($\sim 10^{-6}$ mol·L^{-1}), ca. 12 mg (620 µL) InP-based NCs were added to the PMMA solution. The mixture was stirred for another hour and ultrasonicated in between until the QDs were homogenously distributed. 1.5 mL of the QD-PMMA solution was filled in a Teflon mold (diameter 20 mm) and kept for 3 days in the dark to enable the slow evaporation of chloroform. The dried PMMA discs were checked to ensure the absence of any bubbles, which can appear in case the chloroform evaporates too fast. They were then unmolded and cut using a gauge in order to have the same geometry and volume for all samples (disc diameter: 15 mm, thickness: 1 mm).

Phase Transfer Using Penicillamine

The InZnP QDs with different shells (except for alumina coating) were rendered water-soluble via ligand exchange using D-penicillamine. Therefore, a 0.2 M solution of D-penicillamine was prepared in 1 mL of degassed MilliQ water. After addition of 200 µL TCEP the pH was adjusted to 9 with TMAOH (25 wt% in methanol) solution. After thorough degassing, 0.5 mL of the ligand solution was added to 1 mL degassed colloidal solution of QDs dissolved in chloroform with a concentration of ca. 3–5 µM. The biphasic mixture was stirred vigorously for 45 min at room temperature. The mixture was quickly centrifuged to obtain a clear phase separation. The upper layer containing the QDs in the aqueous phase was separated from the organic phase and purified from excess ligands using a NAP^{TM}10 size exclusion column (Sephadex^{TM} G-25 DNA Grade from GE Healthcare). The column was equilibrated with a 1X PBS buffer, which was further used as eluent and storage buffer. The transferred QD samples were stored at 4°C.

Characterization

Photophysical Characterization

Absorbance measurements were performed using a Hewlett Packard 8452A spectrometer and the emission spectra were

recorded using a Fluorolog FL3-22 spectrometer from Horiba-Jobin Yvon equipped with a 150 W xenon lamp for steady-state measurements and a NanoLED laser diode from Horiba with a wavelength of 350 nm and 1 MHz repetition for time-resolved measurements. Decay curves were fitted using Decay Analysis software from Horiba Scientist and intensity averaged decay times calculated according to Equation 1.

$$\tau < int >= \frac{\sum_i A_i^* \tau_i^2}{\sum_i A_i^* \tau_i} \quad (1)$$

In Equation 1 A_i is the amplitude of the respective decay time t_i. Photoluminescence quantum yield measurements were performed at room temperature using an integration sphere, Hamamatsu Quantaurus Absolute PL quantum yield spectrometer.

Structural Characterization

Powder X-ray diffraction was performed using a Panalytical X'Pert diffractometer equipped with copper anode ($\lambda K_{\alpha 1}$ = 1.5406 A, $\lambda K_{\alpha 2}$ = 1.5444 A) and an X'Celerator 1D detector. The elemental composition was analyzed using a Zeiss Ultra 55+ scanning electron microscope equipped with an EDX probe. The XRD and EDX samples were prepared by drop-casting a concentrated NCs dispersion either on a disoriented silicon substrate or on a cleaned silicon substrate. Transmission electron microscopy (TEM) was performed at cryogenic temperature on a FEI Polara microscope operating at 300 kV and images were recorded on a Gatan K2 camera. For sample preparation, around 4 μL of a diluted QD dispersion was applied onto a 400-mesh copper TEM grid covered with a homemade carbon film and the solvent was allowed to evaporate.

XPS Studies

Chemical characterization by XPS was carried out using a Versaprobe II ULVAC-PHI spectrometer. A monochromatic beam (X-ray source Al-K_α 1486.6 eV) of 100 μm diameter and 97 W power was focused on the surface of the samples. Survey spectra were measured over a spectral range of 0–1200 eV to identify the elements present in the material using a pass energy of 117 eV which corresponds to a resolution of 1.6 eV. High-resolution spectral analyses were performed using a pass energy of 23 eV which corresponds to a resolution of 0.5 eV. All XPS measurements were carried out in an ultra-high vacuum chamber (7.10^{-8} mbar).

All XPS spectra binding energies were corrected using the C 1s line of alkyl groups of PMMA at 285.0 eV. Curve fitting and background subtraction were accomplished using Casa XPS software. The spectra curve fitting was performed using Voigt function, convolution product of Gaussian (80%) and Lorentzian (20%) distributions.

Aging Tests in a Climatic Chamber

The QD-PMMA disks were placed in a Q-SUN Xe-1 Xenon arc test chamber (Q-LAB) providing full sunlight spectrum and continuously irradiated up to 32 h. Weathering conditions were adapted from the ISO norm 4892-2:2006, developed for studying the aging of plastics. The irradiance and temperature were fixed at 1.44 W/m² (measured at 420 nm) and 40°C, respectively, with no humidity control. PL measurements were performed after an irradiance time of 6, 12, 24, and 32 h.

Toxicity Testing

Human skin samples were obtained following breast surgery from healthy female donors with their informed consent (Centre Hospitalier Universitaire de Grenoble, Grenoble, France). Keratinocytes were isolated as previously described (Mouret et al., 2006). They were grown at 37°C, 5% CO_2, in keratinocyte serum-free medium (KSF-M) supplemented with 1.5 ng/ml EGF, 25 μg/ml bovine pituitary extract, 75 μg/ml primocin. For all experiments, cells were used at passages 1 or 2. They were seeded in 96-well plates at 5,000 cells per well. When they reached 60% of confluence, they were exposed for 24 h to 6.25–100 nM of QDs. Exposure medium was then sampled and used to assess the release of lactate dehydrogenase (LDH) from cells (LDH assay kit, Sigma-Aldrich), which is a marker of cell membrane integrity, i.e., cell viability. The ability of these cells to proliferate was evaluated by quantifying the incorporation of 5-Bromo-2'-deoxy-uridine (BrdU) in their DNA (BrdU assay kit, Roche). Both assays were performed following manufacturer's instructions. Triton X100 (0.1%) was used as positive control.

RESULTS AND DISCUSSION

Characterization of the Different Core/Shell Systems

Figure 2 shows the UV-vis absorption and photoluminescence (PL) spectra as well as EDX data of InZnP/$ZnSe_xS_{1-x}$ core/gradient shell QDs before and after growth of an additional ZnS shell. In contrast to literature methods, the monomolecular precursor zinc ethylxanthate has been applied for ZnS growth. As expected, the absorption spectra show an enhanced absorbance below 350 nm with increasing ZnS shell thickness. The EDX data (**Figure 2C**) also confirms unambiguously the successful growth of the thin and thick ZnS shells on the core/gradient shell system (**Figures 4C,D**). The same core diameter (2.67 ± 0.32 nm from TEM measurements) was used for all samples. In accordance with the elemental increase determined from EDX and TEM data, the thicknesses of the shells are around 2 monolayers (gradient shell), 3 monolayers (thin ZnS shell) and 4–5 monolayers (thick ZnS shell). Due to the fact that the gradient shell already provides a very good surface passivation, the additional ZnS growth only slightly improves the PL intensity (PLQY: 50.9% gradient shell, 56.5% CSS thin, 63.6% CSS thick). A small blue shift of the PL maximum with increasing shell thickness (cf. **Table S1**, up to 9 nm for the thick ZnS shell) likely originates from the strain exerted on the core due to the smaller lattice parameter of ZnS. This hypothesis is confirmed by powder X-ray analyses, showing a shift of the diffraction peaks characteristic of InZnP to wider angles upon ZnS shell growth (cf. **Figure 2D**). Time-resolved PL studies (**Figure S1**, **Table S2**) reveal similar averaged decay times on the order of 65–67 ns before and after ZnS shell growth, however, the shortest lifetime is constantly decreasing with

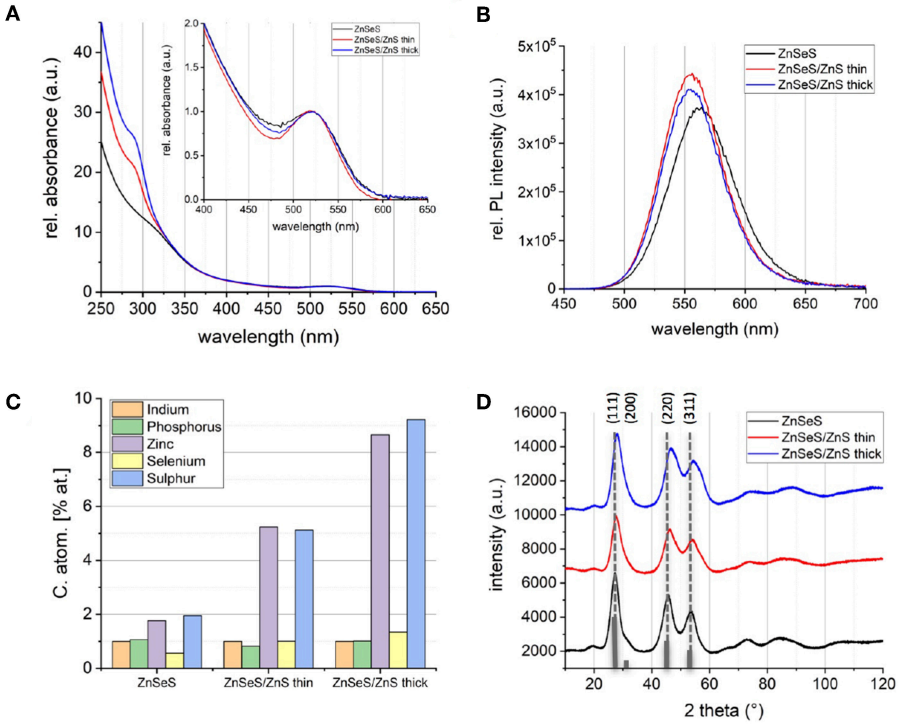

FIGURE 2 | Normalized absorbance spectra **(A)** and absorbance corrected PL spectra **(B)** of InZnP QDs with ZnSeS (black), ZnSeS/ZnS thin (red), and ZnSeS/ZnS thick shell (blue). **(C)** Indium normalized composition determined with EDX. **(D)** Powder X-ray diffractograms (Cu-Kα); the reference pattern of bulk zinc blende InP (JCPDS file #32-0452) is added as gray bars.

increasing ZnS shell thickness, suggesting a smaller contribution of surface trap states (Wegner et al., 2019).

As an additional surface passivation step, coating with an alumina layer was explored. While this treatment has been shown to yield a significant stability enhancement of CdSe and $CuInS_2$-based NCs (Li et al., 2015; Yan et al., 2016), it has not yet been applied to indium phosphide based QDs. To induce the formation of the alumina coating, we added a well-defined amount of aluminum isopropoxide during the growth of the (thin) ZnS shell on the gradient shell (cf. Experimental Section). While the absorption and PL spectra remain essentially unchanged with respect to the CSS system (**Figure S2**) and a high PL QY is maintained (48%), aluminum treatment induces a higher value of the averaged PL decay time (82.8 ns, cf. **Table S3**). EDX analysis shows that a significant amount of aluminum has been incorporated into the QDs with an In:Al ratio of 1:9. Such a high ratio is indeed required for forming, as hypothesized, a monolayer of alumina on an In(Zn)P core already passivated with a gradient and a thin ZnS shell.

Photostability in PMMA

For assessing the photostability under controlled conditions, the QDs were first integrated into a PMMA matrix. The main advantages of PMMA are its optical transparency (**Figure S3**), stability under irradiation, amorphous character, ease of composites processing, and the mechanical stability of the obtained monolithic materials. **Figure 3** depicts the different steps of composite preparation and aging experiments. By optimizing the PMMA concentration in chloroform (30 wt%) and slow drying, homogeneous composites without air-bubbles could be obtained, suitable for optical measurements. A QD loading of 0.4 wt% resulted in the best compromise of film homogeneity and PL QY (cf. **Table S4**).

Incorporation into the PMMA matrix leads to a significant bathochromic shift of the PL emission maximum with increasing QD concentration in the composite (cf. **Figure 3**, **Figure S4**), accompanied by a small reduction of the PL line width. For the gradient shell and CSS system this shift accounts for 26 and 24 nm (97 meV/93 meV), respectively, while it is less pronounced in the case of the aluminum treated sample (14 nm, 56 meV). At the same time, a significant decrease of the PLQY is observed with the retained QY following the order CSS (16.9%, decrease: 73%) > aluminum treated (10.1%, decrease: 79%) > gradient shell (7.6%, decrease: 85%). Similar effects have been observed in other studies on QD incorporation into a PMMA matrix via physical mixing of both components (Zvaigzne et al., 2015). We attribute both phenomena (PL shift and QY decrease) to the fact that in the thick QD-polymer composite radiative or non-radiative energy or charge transfer processes take place favored by the close proximity of the QDs and their size distribution.

As already studied in close-packed InP-based QD films without polymer matrix (Ung et al., 2010a), in principle three processes can occur: (i) resonance photon reabsorption; (ii) Förster resonance energy transfer; (iii) direct excited charge

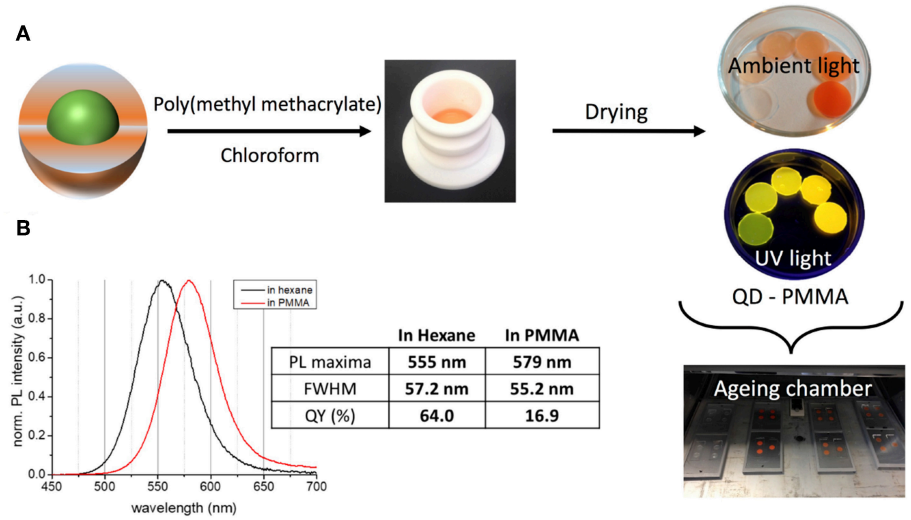

FIGURE 3 | (A) Processing of the QDs for aging experiments using a PMMA matrix and different concentrations of QDs. **(B)** Comparison of the PL properties of InZnP/ZnSeS/ZnS (thick shell) QDs in colloidal solution (hexane) and after embedding in the PMMA matrix.

carrier transfer from one QD to another. Due to the expected increased spatial separation of the QDs in the polymer as compared to close-packed films, process (i) could be favored here. However, it has been shown in many literature examples that the physical mixing of QDs with the polymer matrix can induce phase segregation and aggregation of the QDs (Ghimire et al., 2018). Therefore, processes (ii) and (iii) can also take place in the present case. The identification of the predominant mechanisms requires additional studies which go beyond the scope of the present work.

During 32 h of continuous irradiation with simulated solar light in an aging chamber at 40°C, the gradient shell system exhibits a hypsochromic shift of the PL maximum of 55 meV, while the position of the other two samples is essentially stable (**Figure 4A**). Nonetheless, all samples show an increase of the emission linewidth, which is most pronounced for the gradient shell, followed by the thick shell and the aluminum treated sample (**Figure 4B**). The evolution of the PLQY confirms this last sample to be the most photostable one: as visible from the comparison of the relative QY loss under irradiation (**Figure 4D**), the gradient shell and CSS systems present identical behavior, while the aluminum treated sample maintains a higher fraction of the initial PL intensity. Intriguingly, all studied samples exhibit a very similar degradation kinetics displaying a fast PL loss during the first 6 h of irradiation before reaching a regime exhibiting a much slower slope and eventually a plateau for extended durations. To confirm the absence of influences arising from potential aging effects of the PMMA matrix the latter has been submitted to identical irradiation experiments on its own (i.e., without QDs) (**Figure S5**).

Noteworthy, the general trends of PL intensity evolution of the three systems are similar when keeping the composites at room temperature in the dark (cf. **Figure S6**), while no evolution of the optical properties is observed for samples kept in the colloidal state either in organic solvent or in PBS buffer after aqueous phase transfer (vide infra). In the PMMA matrix, the QY gradually decreases over time for the CSS and gradient shell systems, while it remains stable for the aluminum treated sample. In contrast to the case of solar irradiation, no fast QY loss during the first hours is observed, which clearly confirms that this fast degradation is light induced. As visible from the evolution of the normalized PL spectra with irradiation duration (**Figure S7**), in all three samples the contribution of trap-state emission in the 650–750 nm range markedly increases over time. One possible explanation for the activation of trap states and the observed PL decrease in the first 6 h of irradiation is light-induced rearrangement of the nanocrystal surface (Saba et al., 2013). This process, leading ultimately to photocharging and charge trapping, is influenced in the present case by interaction of the QD surface with the polymer matrix.

XPS Analysis

To probe the change of surface chemistry of QDs as well as PMMA stability over aging, we performed XPS analyses for which the probed depth is about 5 nm. Two samples were studied before and after 6 h of irradiation: InZnP/ZnSeS gradient shell QDs, most affected by the aging, and aluminum treated CSS QDs, least affected, both embedded in the PMMA matrix. **Figure 5** shows the C1s core level of the pristine and irradiated samples. The main feature of the spectra is that the signatures of PMMA are preserved after 6 h of irradiation, for instance the C-C (285.0 eV), C-O (286.7 eV), and COO (288.7 eV) signals, indicating that PMMA remains stable during the selected aging time.

The valence change of zinc was studied through the analyses of the Zn 2p core peak and Zn $L_3M_{45}M_{45}$ Auger lines (**Figure 6**). The Zn 2p signal shows a main peak at 1022.7 eV assigned to the +II valence state of zinc. The binding energy of Zn $2p_{3/2}$ does not change during aging in the case of the aluminum treated sample, while a slight shift (+0.3 eV) to higher binding

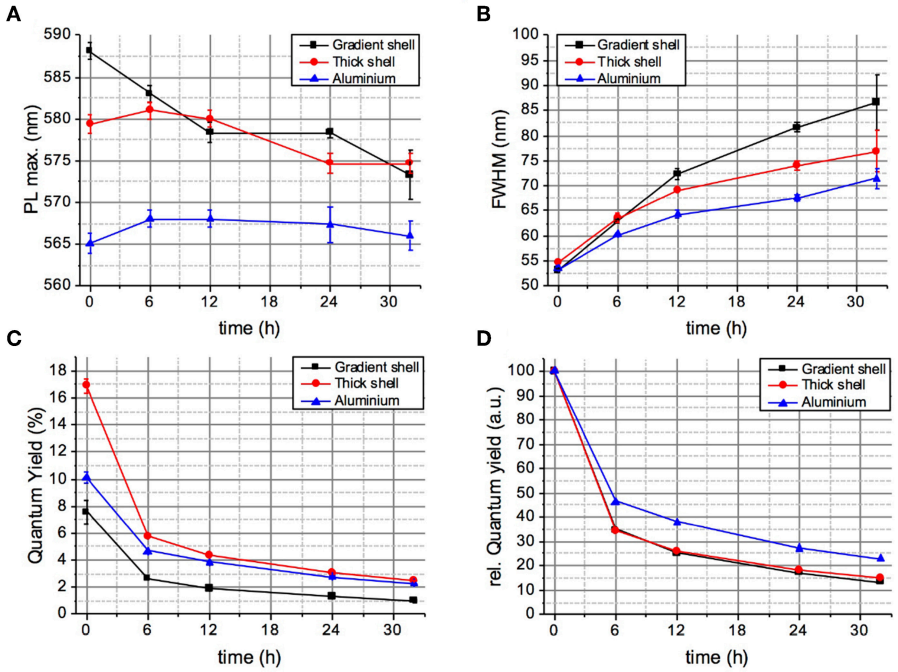

FIGURE 4 | Evolution of the PL maximum wavelength **(A)**, linewidth **(B)**, absolute PLQY **(C)**, and relative PLQY **(D)** of the QD-PMMA composites during 32 h of continuous aging (irradiation with a solar simulator at 40°C).

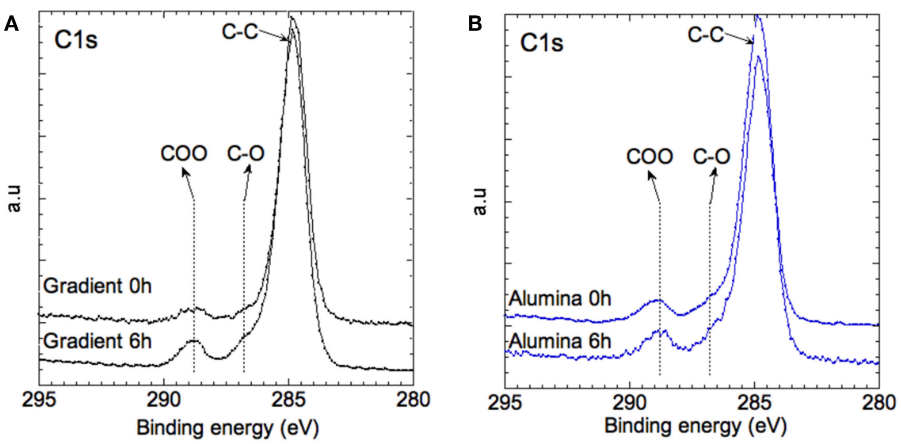

FIGURE 5 | XPS spectra of the C1s core level of **(A)** the gradient shell sample and **(B)** the aluminum treated sample at 0 and 6 h of aging.

energies is observed for the gradient QDs after 6 h of irradiation. To further investigate the chemical environment of the zinc atoms, analysis of the Zn $L_3M_{45}M_{45}$ Auger peaks provides detailed information, which can be extracted from the shapes, intensities, and locations of the Auger lines involving deep Zn $2p_{3/2}$ (L_3) and shallow Zn $3d_{5/2-3/2}$ (M_{45}) core levels. The Auger line arises from the three nearly degenerated levels 1D, 3P, and 1G, and two extreme levels 1S and 3F constituting the higher and lower energy shoulders of the Auger line (inset of **Figure 6**). As a first approximation, the main peak of each chemical group can be represented by the 1D, 3P, and 1G triad (nX) symbolized by a dashed line (Lee et al., 2014). With these information, the Wagner parameter can be defined (Wagner, 1972):

$$\alpha = E_b(\mathrm{Zn2p_{3/2}}) + \mathrm{E_K(Zn\ LMM)}$$

where E_k is the kinetic energy of the core–valence–valence Auger transition electron, and E_b the binding energy of the $Zn2p_{3/2}$ core electron referred to the Fermi energy.

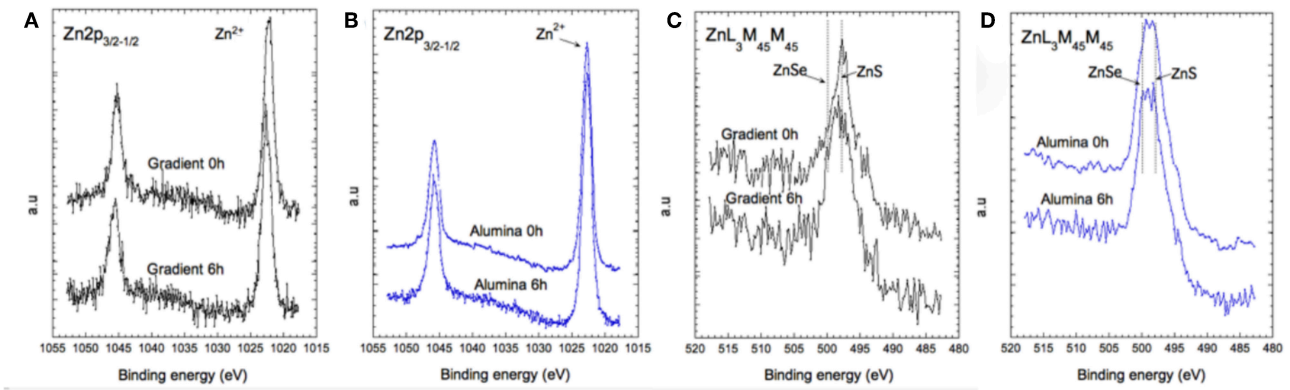

FIGURE 6 | XPS spectra of the Zn 2p core level **(A,B)** and of the Auger transition Zn $L_3M_{45}M_{45}$ **(C,D)** for the gradient shell sample and the aluminum treated sample at 0 and at 6 h of aging.

Materials with similar Wagner parameters have closely similar extra-atomic relaxation arising from multiplet coupling in the final states, i.e., the extra-atomic polarization energy and the local electronic structure of the material. Hence, we can distinguish at least three families of zinc-ligand species for both types of samples (gradient shell and aluminum treated), since we can extract at least three Wagner parameters: α_1 at 2009.6 eV, α_2 at 2011.1 eV and α_3 at 2013.1 eV. They can be assigned to zinc in ZnSe, ZnS, and Zn-Zn chemical environment, respectively. At this stage, the contribution of the ZnSe and ZnS phases is difficult to quantify from the spectral signature. However, it appears that in the case of the aluminum treated QDs the zinc related environment remains stable over time. In the case of the gradient shell QDs, the ZnS related bonds are dominant in the pristine material and decrease after 6 h of aging, while the ZnLMM spectral shape becomes similar to that recorded in the case of aluminum treated QDs.

Figures 7A,B reports the Se 3d core level of both systems. In the case of the gradient shell, the spectra show one doublet at 54.1–55.0 eV (associated to spin-orbit coupling), signature of Se^{2-} ions in ZnSe. In the case of the aluminum treated QDs, we observe two doublets at 54.1–55.0 and 54.9–55.8 eV associated with ZnSe and $ZnSe_xS_{(1-x)}$, respectively. These differences are unexpected, as the core and gradient shell were synthesized in the same manner for both systems. On the other hand, as the additional growth steps in the case of the alumina-capped sample imply prolonged heating to 230°C, a more pronounced interdiffusion of the ZnSe and ZnS phases may take place giving rise to the mixed $ZnSe_xS_{(1-x)}$ phase. The S 2p doublet (**Figure 7D**) at 162–164 eV is the signature of S^{2-} ions in ZnS environment. The ZnS:ZnSe ratio remains stable during aging (cf. **Table S5**). For the gradient shell, the presence of oxidized sulfur ($-SO_4$) is observed (**Figure 7C**) whose concentration increases slightly after aging.

At a first approximation, the In $3d_{5/2}$ peak recorded at the surface centered at 445.4 eV can be assigned to In^{3+} ions in In_2O_3 and/or In $(OH)_3$. The presence of In (S, Se, P) cannot be excluded since the P 2p core level peak (not shown) exhibits two contributions, a major one around 134 eV attributed to phosphate groups (InPOx) and a low intensity peak around 130 eV assigned to In-P bonds (**Figure 8**). Oxidation of the core/shell interface in InP-based QDs occurring during the synthesis under similar experimental conditions has been reported by Delpech and coworkers (Virieux et al., 2012). It has been attributed to the *in situ* generation of minute amounts of water due to side reactions of the fatty acid ligands (e.g., myristate, stearate).

In the case of the aluminum treated sample, the ratio between both indium species remains quasi-stable whereas in the case of the gradient system significate changes are observed (**Figures 8A,B**).

The Al 2p core level is the signature of Al^{3+} like in Al_2O_3. It stays the same after 6 h of aging, confirming that the aluminum coating is very stable and does not degrade under irradiation (**Figure 8C**). Taken together, the presented XPS results fully underpin the stability differences of the two systems expected from the photophysical studies. In the case of the gradient shell, the initial ZnS outer layer already shows distinct signs of oxidation right from the start ($-SO_4$ species), which are not detectable in the aluminum treated sample. Furthermore, during the aging process the degradation of the gradient shell sample continues, as visible by the XPS spectral changes, in particular the decrease of the signals characteristic for ZnS related bonds and increase of the oxidized indium component. The latter implies a reduction of the emissive core size, which is supposed to be at the origin of the observed hypsochromic shift of the PL maximum (cf. **Figure 4A**).

Cytotoxicity Studies

Aqueous phase transfer of the QDs was achieved by surface ligand exchange with zwitterionic penicillamine (**Figure 9**) (Tamang et al., 2011; Mattera et al., 2016). In this procedure, the QDs in chloroform are brought into intimate contact with an aqueous solution of penicillamine. The pH of the aqueous phase is adjusted in the basic range (around 9), to favor the deprotonation of the thiol moiety leading to efficient binding to the ZnS surface of the QDs. In the case of the alumina-coated system, however, this approach was not successful. Other types

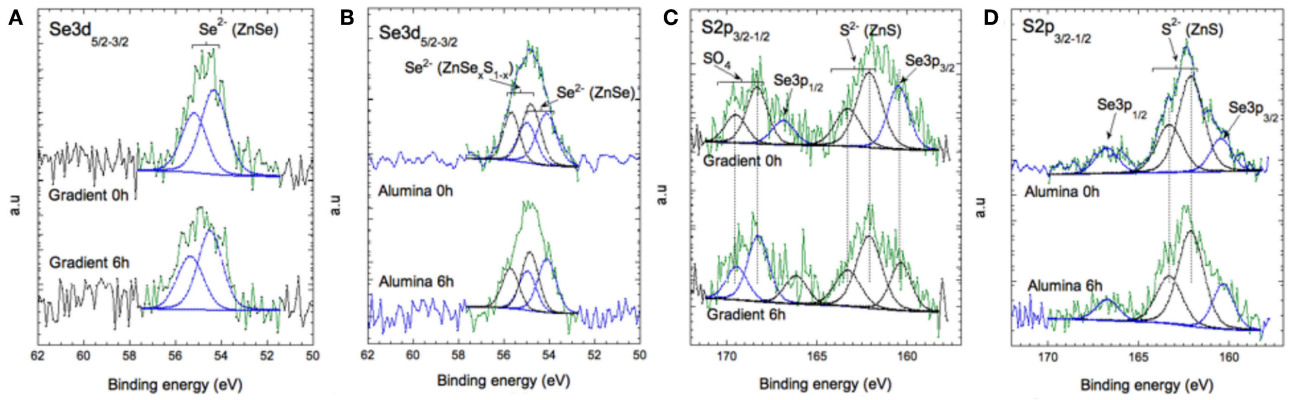

FIGURE 7 | XPS spectra of Se 3d **(A,B)** and of S 2p and Se 3p **(C,D)** for the gradient shell sample and the aluminum treated sample at 0 and 6 h of aging.

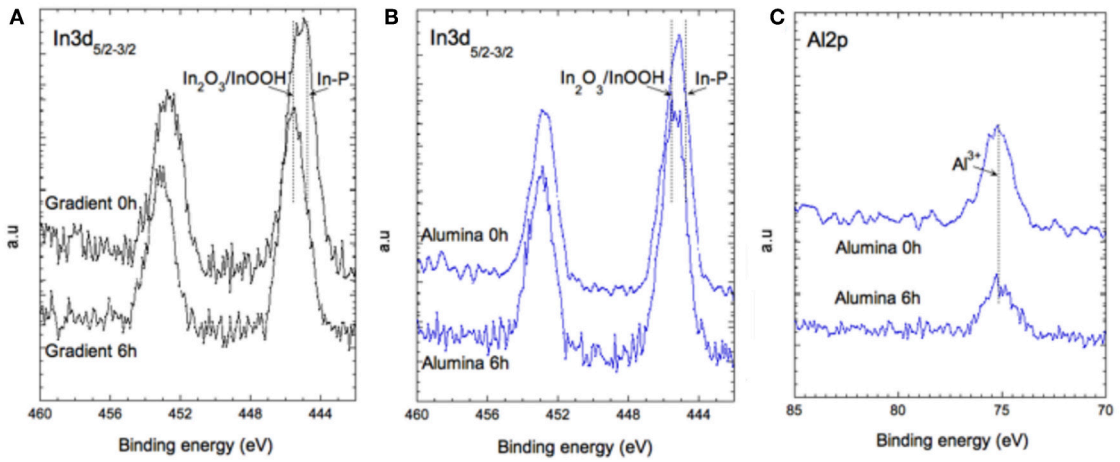

FIGURE 8 | XPS spectra of In 3d for **(A)** the gradient shell sample and **(B)** the aluminum treated sample at 0 and 6 h of aging. **(C)** XPS spectra of Al 2p for the aluminum treated sample.

of surface chemistries have to be developed there, which are the subject of ongoing research. Therefore, in the remaining part of this article we will focus on the core/shell systems without aluminum treatment.

While the absorbance properties are not affected by the phase transfer, the PL peaks exhibit a bathochromic shift of around 10–15 nm accompanied by a slight line broadening (**Table S6**). The PL intensity strongly depends on the shell thickness of the QDs as seen in the photograph in **Figure 9A** and in the spectra in **Figure 9B**. As generally observed in phase transfer methods applying direct surface ligand exchange, the PLQY significantly decreases. This decrease is particularly pronounced for the gradient shell sample (QY: 6.0%) whereas the systems with additional ZnS shells exhibit enhanced PL conservation (QY: 15.5% CSS thin; 17.1% CSS thick). The gradient shell sample shows a significant decrease in the average decay time after phase transfer and a concomitant increase of the amplitude of the shortest lifetime (**Figure S8**, **Table S7**). All three systems exhibit an increase of the latter, albeit the trend of the contribution of the short lifetime component is maintained in the order gradient shell > CSS thin > CSS thick, as in the samples before phase transfer. All in all, these results indicate that surface trap states induced by the ligand exchange reaction are at the origin of the PLQY decrease. As expected this detrimental effect can be reduced by increasing the shell thickness. Dynamic light scattering (DLS) measurements (**Figure S9**) confirm the absence of larger-sized aggregates. The hydrodynamic diameters of the samples extracted from DLS are consistent with the values obtained from TEM analysis (**Figure S10**). However, the precise determination of the QD sizes is challenging due to the low contrast of the ZnS shell in TEM and the small diameters in the 4–6 nm range.

Since the QDs are synthesized in liquid phase with no risk of aerosolisation, the most probable exposure route for humans is through skin contact (Reiss et al., 2016). Impact of these QDs was assessed *in vitro* on skin cells, i.e., primary keratinocytes isolated from human donors. As shown in **Figure 10A**, exposure to 6.5–100 nM of QDs for 24 h do not

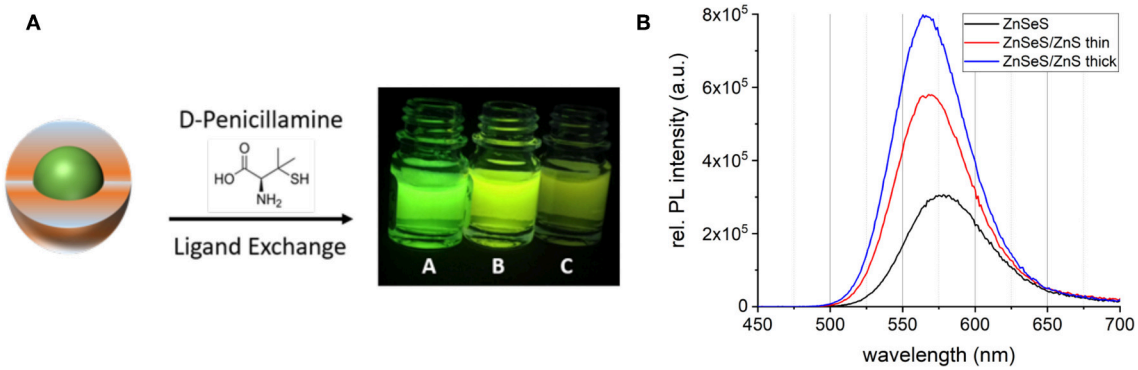

FIGURE 9 | (A) Schematic representation of the aqueous phase transfer using penicillamine. The photograph shows the phase transferred samples: InZnP/ZnSeS/ZnS thick (A), InZnP/ZnSeS/ZnS thin (B), and InZnP/ZnSeS (C) in PBS buffer. **(B)** Absorbance corrected PL spectra of the phase-transferred samples.

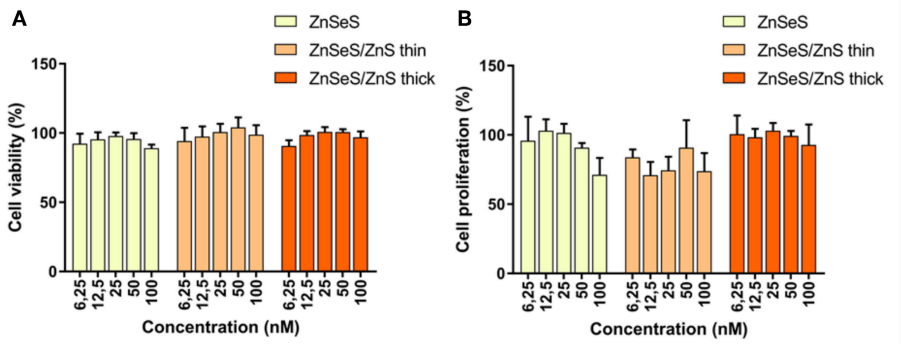

FIGURE 10 | Cell viability **(A)** and cell proliferation **(B)** of human keratinocytes exposed to increasing concentrations of QDs with different shells.

cause any leakage of lactate dehydrogenase from cells, i.e., do not affect cell membrane integrity, which is classically used as a proxy for cell viability. BrdU, an analog of the nucleoside thymidine which is incorporated into DNA during replication, was used as an indicator of QD impact on cell proliferation. A trend toward reduced cell proliferation is observed in cells exposed to QDs (**Figure 10B**). This trend is observed in cells exposed to QDs with a gradient shell and CSS with a thin shell, but not to CSS with a thick shell. This shows that the thick shell not only facilitates the phase transfer and preserves best the photophysical properties but is also beneficial from a cytotoxicity point of view. These features combined with the compact size of the penicillamine-capped CSS QDs make them particularly interesting for further applications in biosensing.

CONCLUSIONS

With the goal to improve the photostability of InP-based QDs, we have synthesized three different types of core/shell structures. The first one uses a $ZnSe_xS_{1-x}$ gradient shell as reported by Lim et al. (2011). In the second, CSS system, additional growth of a ZnS shell of controlled thickness on top of the gradient shell has been undertaken, using the monomolecular precursor zinc ethylxanthate (Protiere and Reiss, 2006). Finally, in the third system alumina coating was performed on top of the ZnS shell. When incorporated into a PMMA matrix and submitted to continuous irradiation in a climate chamber, the three systems exhibit distinctly different behavior. While all of them show a marked drop of QY within the first 6 h of irradiation, the aluminum treated sample retains most of the initial PL intensity. The gradient shell and CSS systems show a minor but continuous loss of QY also in the dark, which is attributed to the interaction of the PMMA matrix with the Zn-based shell. It has been shown that PMMA-type polymers can act as efficient sorbents for Zn (II) ion removal (Jakóbik-Kolon et al., 2017). To the contrary, the aluminum treated sample is fully stable in the dark.

XPS studies revealed that upon irradiation the degradation of the ZnS outer layer and oxidation of the In(Zn)P core are at the origin of the observed decrease of PL intensity and hypsochromic shift of the PL maximum. XPS also confirmed the formation of an Al_2O_3-type layer in the case of the aluminum treated sample, which effectively protects against degradation. The chemical stability of the alumina capped sample being thus demonstrated, the observed decrease of PLQY upon continuous irradiation is ascribed to light-induced surface reconstruction. The modification of the configuration of surface

atoms and capping ligands can introduce defect states favoring photocharging of the QDs and charge carrier trapping. Similar processes are also at work in the case of the gradient and CSS systems, in addition to photo-oxidation. These detrimental effects could likely be overcome by increasing the inorganic shell thickness, providing a more efficient separation of the emissive core and the environment.

With the gradient shell and CSS systems phase transfer was achieved using surface ligand exchange with penicillamine and a clear correlation between the retained PLQY and shell thickness was observed. Cytotoxicity studies indicate that the different types of QDs do not influence the cell viability of human keratinocytes. On the other hand, a trend of reduced cell proliferation is observed for cells exposed to higher concentrations of gradient shell and CSS QDs with a thin ZnS outer shell. This trend is not visible for the CSS QDs with a thicker ZnS shell, confirming both the necessity and advantageous features of thicker shells protecting InP-based QDs. Ongoing studies concern the aqueous phase transfer of alumina-coated QDs, either via encapsulation with ambipolar macromolecules (e.g., phospholipids) or through the identification of appropriate bifunctional molecules for ligand exchange. Furthermore, with the goal to reduce PL losses during the QD incorporation in the matrix, different types of suitable polymers (e.g., polystyrene, polydimethylsiloxane, or block copolymers) deserve attention as well as approaches preventing from undesired phase-segregation of the QDs and the polymer by introducing specific interactions between both components (Ghimire et al., 2018).

Concluding, the presented results contribute to the better understanding of the degradation mechanisms of core/shell QDs and to the development of InP-based QD heterostructures combining enhanced chemical and photostability, bringing them closer to the requirements of real-life applications.

DATA AVAILABILITY

All datasets generated for this study are included in the manuscript and/or the **Supplementary Files**.

AUTHOR CONTRIBUTIONS

MC and PR conceived and designed the study. KW performed the synthetic work and data analysis with assistance of PR and MC. AB performed the XPS studies and analysis. DT-B carried out the aging experiments and assisted in the XPS analysis. FD and DB performed cytotoxicity studies. LM helped with QD phase transfer. WL performed transmission electron microscopy. PR wrote the manuscript with assistance of KW and MC. All authors contributed to its finalization.

FUNDING

This work is a contribution to the Labex Serenade (ANR-11-LABX-0064) funded by the French Government's Investissements d'Avenir ANR program, through the A*MIDEX project (ANR-11-IDEX-0001-02). The authors thank the French National Research agency ANR for financial support (grants NEUTRINOS, ANR-16-CE09-0015-03 and FLUO, ANR-18-CE09-0039-01). We thank the CEA DRF Impulsion program (Cryo-ME_NP) for partial financial support of this work. This work used the platforms of the Grenoble Instruct-ERIC Centre (ISBG; UMS 3518 CNRS-CEA-UGA-EMBL) with support from FRISBI (ANR-10-INSB-05-02) and GRAL (ANR-10-LABX-49-01) within the Grenoble Partnership for Structural Biology (PSB). The IBS electron microscope facility is supported by the Auvergne-Rhône-Alpes Region, the fonds FEDER, the Fondation Recherche Médicale (FRM), C GIS-IBISA.

ACKNOWLEDGMENTS

We thank the electron microscopy platform, especially Dr. G. Schoehn and Dr. M. Bacia.

SUPPLEMENTARY MATERIAL

The Supplementary Material for this article can be found online at: https://www.frontiersin.org/articles/10.3389/fchem.2019.00466/full#supplementary-material

REFERENCES

Allocca, M., Mattera, L., Bauduin, A., Miedziak, B., Moros, M., De Trizio, L., et al. (2019). An integrated multilevel analysis profiling biosafety and toxicity induced by indium- and cadmium-based quantum dots *in vivo*. *Environ. Sci. Technol.* 53, 3938–3947. doi: 10.1021/acs.est.9b00373

Chandrasekaran, V., Tessier, M. D., Dupont, D., Geiregat, P., Hens, Z., and Brainis, E. (2017). Nearly blinking-free, high-purity single-photon emission by colloidal InP/ZnSe quantum dots. *Nano Lett.* 17, 6104–6109. doi: 10.1021/acs.nanolett.7b02634

Cossairt, B. M. (2016). Shining light on indium phosphide quantum dots: understanding the interplay among precursor conversion, nucleation, and growth. *Chem. Mater.* 28, 7181–7189. doi: 10.1021/acs.chemmater.6b03408

Ghimire, S., Sivadas, A., Yuyama, K.-I., Takano, Y., Francis, R., and Biju, V. (2018). Quantum dot–polymer conjugates for stable luminescent displays. *Nanoscale* 10, 13368–13374. doi: 10.1039/C8NR01501E

Huang, K., Demadrille, R., Silly, M. G., Sirotti, F., Reiss, P., and Renault, O. (2010). Internal structure of InP/ZnS nanocrystals unraveled by high-resolution soft X-ray photoelectron spectroscopy. *ACS Nano* 4, 4799–4805. doi: 10.1021/nn100581t

Jakóbik-Kolon, A., Milewski, A., Zdybał, D., Mitko, K., Laskowska, E., Mielanczyk, A., et al. (2017). Zinc sorption on modified waste poly (methyl methacrylate). *Materials* 10:755. doi: 10.3390/ma10070755

Lee, E., Benayad, A., Shin, T., Lee, H., Ko,s D.-S., Kim, T. S., et al. (2014). Nanocrystalline ZnON; High mobility and low band gap semiconductor material for high performance switch transistor and image sensor application. *Sci. Rep.* 4:4948. doi: 10.1038/srep06897

Li, L., and Reiss, P. (2008). One-pot synthesis of highly luminescent InP/ZnS nanocrystals without precursor injection. *J. Am. Chem. Soc.* 130, 11588–11589. doi: 10.1021/ja803687e

Li, Z., Yao, W., Kong, L., Zhao, Y., and Li, L. (2015). General method for the synthesis of ultrastable core/shell quantum dots by aluminum doping. *J. Am. Chem. Soc.* 137, 12430–12433. doi: 10.1021/jacs.5b05462

Lim, J., Bae, W. K., Lee, D., Nam, M. K., Jung, J., Lee, C., et al. (2011). InP@ZnSeS, Core@Composition gradient shell quantum dots with enhanced stability. *Chem. Mater.* 23, 4459–4463. doi: 10.1021/cm201550w

Lim, J., Park, M., Bae, W. K., Lee, D., Lee, S., Lee, C., et al. (2013). Highly efficient cadmium-free quantum dot light-emitting diodes enabled by the direct formation of excitons within InP@ZnSeS quantum dots. *ACS Nano* 7, 9019–9026. doi: 10.1021/nn403594j

Mattera, L., Bhuckory, S., Wegner, K. D., Qiu, X., Agnese, F., Lincheneau, C., et al. (2016). Compact quantum dot-antibody conjugates for FRET immunoassays with subnanomolar detection limits. *Nanoscale* 8, 11275–11283. doi: 10.1039/C6NR03261C

Mouret, S., Baudouin, C., Charveron, M., Favier, A., Cadet, J., and Douki, T. (2006). Cyclobutane pyrimidine dimers are predominant DNA lesions in whole human skin exposed to UVA radiation. *Proc. Natl. Acad. Sci. USA.* 103, 13765–13770. doi: 10.1073/pnas.0604213103

Pietra, F., De Trizio, L., Hoekstra, A. W., Renaud, N., Prato, M., Grozema, F. C., et al. (2016). Tuning the lattice parameter of InxZnyP for highly luminescent lattice-matched core/shell quantum dots. *ACS Nano* 10:4754. doi: 10.1021/acsnano.6b01266

Protiere, M., and Reiss, P. (2006). Facile synthesis of monodisperse ZnS capped CdS nanocrystals exhibiting efficient blue emission. *Nanoscale Res. Lett.* 1, 62–67. doi: 10.1007/s11671-006-9001-0

Ramasamy, P., Kim, N., Kang, Y.-S., Ramirez, O., and Lee, J.-S. (2017). Tunable, bright, and narrow-band luminescence from colloidal indium phosphide quantum dots. *Chem. Mater.* 29, 6893–6899. doi: 10.1021/acs.chemmater.7b02204

Reiss, P., Carayon, S., Bleuse, J., and Pron, A. (2003). Low polydispersity core/shell nanocrystals of CdSe/ZnSe and CdSe/ZnSe/ZnS type: preparation and optical studies. *Synth. Met.* 139, 649–652. doi: 10.1016/S0379-6779 (03)00335-7

Reiss, P., Carrière, M., Lincheneau, C., Vaure, L., and Tamang, S. (2016). Synthesis of semiconductor nanocrystals, focusing on nontoxic and earth-abundant materials. *Chem. Rev.* 116, 10731–10819. doi: 10.1021/acs.chemrev.6b00116

Reiss, P., Protiere, M., and Li, L. (2009). Core/shell semiconductor nanocrystals. *Small* 5, 154–168. doi: 10.1002/smll.200800841

Saba, M., Aresti, M., Quochi, F., Marceddu, M., Loi, M. A., Huang, J., et al. (2013). Light-induced charged and trap states in colloidal nanocrystals detected by variable pulse rate photoluminescence spectroscopy. *ACS Nano* 7, 229–238. doi: 10.1021/nn305031k

Stein, J. L., Mader, E. A., and Cossairt, B. M. (2016). Luminescent InP quantum dots with tunable emission by post-synthetic modification with lewis acids. *J. Phys. Chem. Lett.* 7, 1315–1320. doi: 10.1021/acs.jpclett.6b00177

Talapin, D. V., Mekis, I., Gotzinger, S., Kornowski, A., Benson, O., and Weller, H. (2004). CdSe/CdS/ZnS and CdSe/ZnSe/ZnS core-shell-shell nanocrystals. *J. Phys. Chem. B* 108, 18826–18831. doi: 10.1021/jp046481g

Tamang, S., Beaune, G., Texier, I., and Reiss, P. (2011). Aqueous phase transfer of InP/ZnS nanocrystals conserving fluorescence and high colloidal stability. *ACS Nano* 5, 9392–9402. doi: 10.1021/nn203598c

Tamang, S., Lincheneau, C., Hermans, Y., Jeong, S., and Reiss, P. (2016). Chemistry of InP nanocrystal syntheses. *Chem. Mater.* 28, 2491–2506. doi: 10.1021/acs.chemmater.5b05044

Tessier, M. D., Dupont, D., De Nolf, K., De Roo, J., and Hens, Z. (2015). Economic and size-tunable synthesis of InP/ZnE (E = S, Se) colloidal quantum dots. *Chem. Mater.* 27, 4893–4898. doi: 10.1021/acs.chemmater.5b02138

Toufanian, R., Piryatinski, A., Mahler, A. H., Iyer, R., Hollingsworth, J. A., and Dennis, A. M. (2018). Bandgap engineering of indium phosphide-based core/shell heterostructures through shell composition and thickness. *Front. Chem.* 6:567. doi: 10.3389/fchem.2018.00567

Ung, T. D. T., Pham, T. T., Nguyen, Q. L., Li, L., and Reiss, P. (2010a). Comparative photoluminescence study of close-packed and colloidal InP/ZnS quantum dots. *Appl. Phys. Lett.* 96:073102. doi: 10.1063/1.3291049

Ung, T. D. T., Reiss, P., and Nguyen, Q. L. (2010b). Luminescence properties of In(Zn)P alloy core/ZnS shell quantum dots. *Appl. Phys. Lett.* 97:193104. doi: 10.1063/1.3515417

Virieux, H., Le Troedec, M., Cros-Gagneux, A., Ojo, W.-S., Delpech, F., Nayral, C., et al. (2012). InP/ZnS nanocrystals: coupling NMR and XPS for fine surface and interface description. *J. Am. Chem. Soc.* 134, 19701–19708. doi: 10.1021/ja307124m

Wagner, C. D. (1972). Auger lines in x-ray photoelectron spectrometry. *Anal. Chem.* 44, 967–973. doi: 10.1021/ac60314a015

Wang, H. C., Zhang, H., Chen, H. Y., Yeh, H. C., Tseng, M. R., Chung, R. J., et al. (2017). Cadmium-free InP/ZnSeS/ZnS heterostructure-based quantum dot light-emitting diodes with a ZnMgO electron transport layer and a brightness of over 10 000 cd m−2. *Small* 13:1603962. doi: 10.1002/smll.201603962

Wegner, K. D., Pouget, S., Ling, W. L., Carrière, M., and Reiss, P. (2019). Gallium – a versatile element for tuning the photoluminescence properties of InP quantum dots. *Chem. Commun.* 55, 1663–1666. doi: 10.1039/C8CC09740B

Xu, S., Ziegler, J., and Nann, T. (2008). Rapid synthesis of highly luminescent InP and InP/ZnS nanocrystals. *J. Mater. Chem.* 18, 2653–2656. doi: 10.1039/b803263g

Yan, L., Li, Z., Sun, M., Shen, G., and Li, L. (2016). Stable and flexible CuInS2/ZnS:Al-TiO2 film for solar-light-driven photodegradation of soil fumigant. *ACS Appl. Mater. Interfaces* 8, 20048–20056. doi: 10.1021/acsami.6b05587

Zvaigzne, M., Martynov, I., Samokhvalov, P., Mochalov, K., and Chistyakov, A. (2015). Influence of surface ligands on the luminescent properties of cadmium selenide quantum dots in a polymethylmethacrylate matrix. *Phys. Procedia* 73, 150–155. doi: 10.1016/j.phpro.2015.09.140

Conflict of Interest Statement: The authors declare that the research was conducted in the absence of any commercial or financial relationships that could be construed as a potential conflict of interest.

frontiers in Chemistry

ORIGINAL RESEARCH
published: 26 February 2019
doi: 10.3389/fchem.2019.00087

Robust Hydrophobic and Hydrophilic Polymer Fibers Sensitized by Inorganic and Hybrid Lead Halide Perovskite Nanocrystal Emitters

*Paris G. Papagiorgis[1], Andreas Manoli[1], Andronikí Alexiou[1], Petroula Karacosta[1], Xenofon Karagiorgis[2], Georgia Papaparaskeva[2], Caterina Bernasconi[3,4], Maryna I. Bodnarchuk[3,4], Maksym V. Kovalenko[3,4], Theodora Krasia-Christoforou[2] and Grigorios Itskos[1]**

[1] Experimental Condensed Matter Physics Laboratory, Department of Physics, University of Cyprus, Nicosia, Cyprus, [2] Department of Mechanical and Manufacturing Engineering, University of Cyprus, Nicosia, Cyprus, [3] Empa - Swiss Federal Laboratories for Materials Science and Technology, Dübendorf, Switzerland, [4] Laboratory for Inorganic Chemistry, Department of Chemistry and Applied Biosciences, ETH Zürich, Zurich, Switzerland

OPEN ACCESS

Edited by:
Vladimir Lesnyak, Technische Universität Dresden, Germany

Reviewed by:
Soong Ju Oh, Korea University, Japan
Raquel Galian, University of Valencia, Spain

***Correspondence:**
Grigorios Itskos
itskos@ucy.ac.cy

Specialty section:
This article was submitted to Nanoscience, a section of the journal Frontiers in Chemistry

Received: *02 November 2018*
Accepted: *31 January 2019*
Published: *26 February 2019*

Citation:
Papagiorgis PG, Manoli A, Alexiou A, Karacosta P, Karagiorgis X, Papaparaskeva G, Bernasconi C, Bodnarchuk MI, Kovalenko MV, Krasia-Christoforou T and Itskos G (2019) Robust Hydrophobic and Hydrophilic Polymer Fibers Sensitized by Inorganic and Hybrid Lead Halide Perovskite Nanocrystal Emitters. Front. Chem. 7:87. doi: 10.3389/fchem.2019.00087

Advances in the technology and processing of flexible optical materials have paved the way toward the integration of semiconductor emitters and polymers into functional light emitting fabrics. Lead halide perovskite nanocrystals appear as highly suitable optical sensitizers for such polymer fiber emitters due to their ease of fabrication, versatile solution-processing and highly efficient, tunable, and narrow emission across the visible spectrum. A beneficial byproduct of the nanocrystal incorporation into the polymer matrix is that it provides a facile and low-cost method to chemically and structurally stabilize the perovskite nanocrystals under ambient conditions. Herein, we demonstrate two types of robust fiber composites based on electrospun hydrophobic poly(methyl methacrylate) (PMMA) or hydrophilic polyvinylpyrrolidone (PVP) fibrous membranes sensitized by green-emitting all-inorganic $CsPbBr_3$ or hybrid organic-inorganic $FAPbBr_3$ nanocrystals. We perform a systematic investigation on the influence of the nanocrystal-polymer relative content on the structural and optical properties of the fiber nanocomposites and we find that within a wide content range, the nanocrystals retain their narrow and high quantum yield emission upon incorporation into the polymer fibers. Quenching of the radiative recombination at the higher/lower bound of the nanocrystal:polymer mass ratio probed is discussed in terms of nanocrystal clustering/ligand desorption due to dilution effects, respectively. The nanocomposite's optical stability over an extended exposure in air and upon immersion in water is also discussed. The studies confirm the demonstration of robust and bright polymer-fiber emitters with promising applications in backlighting for LCD displays and textile-based light emitting devices.

Keywords: perovskites, lead halides, nanocrystals, electrospinning, polymer fibers

INTRODUCTION

Lead halide perovskite nanocrystals (LHP NCs) of the $APbX_3$-type with A being cesium (Cs) or formamidinium (FA) and X being a halide ion (Cl, Br, I) have emerged as outstanding light emitting materials (Protesescu et al., 2015, 2016, 2017; Kovalenko et al., 2017; Akkerman et al., 2018), exhibiting tunable, bright emission across the visible spectrum with excellent optical amplification properties, confirming their high potential for photonic applications (Yakunin et al., 2015; Sutherland and Sargent, 2016). Realization of practical LHP NC emitters is critically dependent upon improving their structural, thermodynamical, and optical stability under ambient conditions, which remains the foremost challenge for such nanomaterials (Huang et al., 2017; Kovalenko et al., 2017; Akkerman et al., 2018; Zhao et al., 2018). Encapsulation of perovskite NCs into macro- or nanoscale polymeric structures has been recently demonstrated (Huang et al., 2016; Raja et al., 2016; Wang et al., 2016, 2017; Hou et al., 2017; Lu et al., 2017; Ma et al., 2017; Murphy et al., 2017; Demkiv et al., 2018; Liao et al., 2018; Lin et al., 2018; Sygletou et al., 2018; Tsai et al., 2018; Wong et al., 2018; Xin et al., 2018; Yang M. et al., 2018; Yang S. et al., 2018; Zhang et al., 2018; Zhu et al., 2018) as simple and low-cost methodologies to preserve the LHP NC chemical integrity by suppressing water and oxygen transmission, improving the thermal stability, and reducing structural modifications, to which LHP NCs are highly susceptible, such as ligand desorption and nanocrystal sintering. Furthermore, integration of the NCs into polymers provides a method to improve their solid-state processability into films, microspheres, fibers, or more complex composites while offering new functionalities such as polarizing PL (Raja et al., 2016; Lu et al., 2017), light detection (Wang et al., 2016), biological labeling and sensing (Wang et al., 2017; Zhu et al., 2018) or device applications such as light emitting diodes (Huang et al., 2016; Liao et al., 2018; Lin et al., 2018; Tsai et al., 2018; Xin et al., 2018; Yang M. et al., 2018; Zhang et al., 2018; Zhu et al., 2018).

All the studies above employ Cs-based all-inorganic NC sensitizers with the notable exception of refs (Lu et al., 2017; Liao et al., 2018; Yang S. et al., 2018), in which methylammonium lead halide NCs were utilized. On the other hand, the polymer encapsulation of the closely related hybrid analog, but more chemically robust and equally bright formamidinium lead halide NCs (Protesescu et al., 2016, 2017) has not received much attention. In addition, a particularly important parameter for such polymer-nanocrystal emitters is the influence of the relative polymer-nanocrystal concentration on the optical properties of the composite which has not been thoroughly investigated. Motivated by these considerations, we present herein a thorough investigation of electrospun polymer fiber nanocomposites sensitized with green-emitting all-inorganic $CsPbBr_3$ and hybrid organic-inorganic $FAPbBr_3$ NCs. Electrospinning allows for a simple, cost-effective and industrially scalable fabrication of long and continuous polymer fibers (Persano et al., 2013; Yu et al., 2017; Savva and Krasia-Christoforou, 2018), enabling the incorporation of a variety of inorganic nanoparticles and thus generating functional nanocomposites (Chronakis, 2015). Fiber composite emitters appear particularly attractive for optoelectronics bearing unique properties such as tolerance to extremely small bending radii and large tensile strains while preserving the structural integrity and bright emission of the perovskite NCs (Wang et al., 2016, 2017; Murphy et al., 2017; Liao et al., 2018; Lin et al., 2018; Tsai et al., 2018; Yang M. et al., 2018). In particular, enhanced water/optical (Wang et al., 2016, 2017; Murphy et al., 2017; Liao et al., 2018; Lin et al., 2018; Tsai et al., 2018; Yang M. et al., 2018) and thermal (Liao et al., 2018) stabilities have been demonstrated upon nanocrystal encapsulation into polymer fibers. Elaborate core/shell NC-fiber geometries with new functionalities have been produced (Murphy et al., 2017; Yang M. et al., 2018;) while applications such as white light emitting diodes (Liao et al., 2018; Lin et al., 2018; Tsai et al., 2018; Yang M. et al., 2018;), fluorescence detection (Wang et al., 2016), and biological/metal ion sensing (Wang et al., 2017) have also been reported. We demonstrate herein the realization of two robust NC-polymer fiber emitter types via the following: (i) encapsulation of the perovskite NCs into hydrophobic poly(methyl methacrylate) (PMMA) fibers using an electrospinning process, and (ii) NC coating hydrophilic cross-linked polyvinylpyrrolidone (PVP) fibrous membranes via a simple immersion process. A thorough investigation of the structure-property relations with emphasis on the optical properties upon varying the NC concentration over three orders of magnitude is reported and compared with the respective characteristics of reference pristine and polymer-NC blend films. Air- and water-stability luminescence experiments confirm the attractive encapsulating properties of PMMA fibers, confirming the demonstration of robust, bright and versatile polymer-fiber emitters.

MATERIALS AND METHODS

Synthesis of $CsPbBr_3$ Nanocrystals

In a 25 ml three-necked flask, $PbBr_2$ (69 mg, 0.188 mmol, ABCR) was suspended in octadecene (5 ml, Sigma-Aldrich), dried at 100°C for 30 min and mixed with oleic acid (0.5 ml, Sigma-Aldrich, vacuum-dried at 100°C) and oleylamine (0.5 ml, STREM, vacuum-dried at 100°C). When $PbBr_2$ was dissolved, the reaction mixture was heated up to 180°C and preheated cesium oleate in octadecene (0.4 ml, 0.125 M) was injected. The reaction mixture was cooled immediately with an ice bath to room temperature.

Purification and Size-Selection of $CsPbBr_3$ Nanocrystals

The crude solution was centrifuged at 12,100 rpm for 5 min, following which the supernatant was discarded, and the precipitate was dissolved in 300 μl hexane. The hexane solution was centrifuged again and the precipitate was discarded. The supernatant was diluted two times and used for the subsequent DDAB-treatment.

DDAB-Treatment of $CsPbBr_3$ Nanocrystals

0.6 milliliter toluene was added to $CsPbBr_3$ NC colloidal solution prepared as described above. Then 30 μl of oleic acid and 160

μl of DDAB (didodecyldimethylammonium bromide, 0.05 M in toluene) were added to the colloidal solution of $CsPbBr_3$ NCs. The mixture was stirred for 1 h, followed by the precipitation with 1.8 ml of ethyl acetate and centrifuged at 12.1 krpm for 3 min. The precipitate was redispersed in 0.5 ml toluene and this solution was additionally filtered through a 0.45-μm PTFE-filter.

Synthesis of $FAPbBr_3$ Nanocrystals

Preparation of Oleylammonium Bromide (OAmBr)

Oleylamine (12.5 ml, Acros Organics, 80–90%) and ethanol (100 ml, Aldrich) were mixed in a 250 ml flask. The reaction mixture was cooled in an ice-water bath and 8.56 ml HBr (48% aqueous solution, Aldrich) was added. The reaction mixture was left to react overnight under nitrogen flow. Then the solution was dried in a rotary evaporator and the obtained product was washed multiple times with diethyl ether and then a white powder was dried under vacuum at room temperature for several hours. OAmBr was stored in the glovebox.

Synthesis of $FAPbBr_3$ Nanocrystals

In a 25 ml three-necked flask, lead (II) acetate trihydrate (76 mg, 0.2 mmol, Sigma-Aldrich) and formamidinium acetate (78 mg, 0.75 mmol, Sigma) were suspended in octadecene (8 ml) and oleic acid (2 ml, Sigma-Aldrich), heated to 50°C and then dried under vacuum for 30 min. Then the reaction mixture was heated to 130°C and, at this point, the mixture of 266 mg (0.8 mmol) of OAmBr in anhydrous toluene (2 ml) was injected into the reaction flask (to dissolve OAmBr in toluene, a mixture of them should be preheated at 40–50°C). After another 1 min, the reaction mixture was cooled by an ice-water bath.

Isolation and Purification of Nanocrystals

Sixteen milliliter of methyl acetate (ABCR) were added to the crude solution followed by the centrifugation at 12.1 krpm for 5 min (Centrifuge: Eppendorf 5804) and the supernatant was discarded. The precipitate was dissolved in toluene (5 ml) and the solution was centrifuged again (3 krpm, 2 min). The supernatant, containing monodisperse nanocrystals, was retained for the DDAB-treatment, while the precipitated NCs were discarded.

DDAB-Treatment of $FAPbBr_3$ Nanocrystals

Five milliliter toluene was added to FAPbBr3 colloidal solution prepared as described above. Then 0.1 ml of oleic acid and 0.6 ml of DDAB (didodecyldimethylammonium bromide, 0.05 M in toluene) was added to 10 ml colloidal solution of FAPbBr3 nanocrystals. The mixture was stirred for 1 h, followed by the precipitation with 16 ml of ethyl acetate and centrifuged at 12.1 krpm for 3 min. Precipitate was re-dispersed in 5 ml toluene and this solution was additionally filtered through a 0.45-μm PTFE-filter.

PMMA/LHP Fibers

Poly(methyl methacrylate) (PMMA, Mn = 350,000 g/mol) was obtained from Sigma-Aldrich and used without further purification. Chloroform ($CHCl_3$, reagent grade, Scharlau) was the solvent employed in the preparation of the PMMA/LHP electrospun fiber emitters. Initially, a homogeneous solution of PMMA was prepared in $CHCl_3$ (solution concentration 20% w/v). Subsequently, 2 mL of the above solution was mixed together with 134 μL of the $CsPbBr_3$ and $FAPbBr_3$ perovskite nanocrystal solutions prepared in toluene, as described in sections Synthesis of $CsPbBr_3$ Nanocrystals and Synthesis of $FAPbBr_3$ nanocrystals (0.33% wt in respect to the polymer mass). The same procedure was repeated to obtain a series of PMMA/LHP ($FAPbBr_3$) solutions having different nanocrystal content, i.e., 0.05% wt (∼20 μL), 0.1% wt (∼40 μL), 0.22% wt (∼80 μL), 0.66% wt (∼242 μL), 1% wt (∼367 μL), and 5% wt (∼2 ml). The obtained solutions were then loaded into a 10 mL glass syringe in the electrospinning set-up to be electrospun. All electrospinning experiments were performed at room temperature. Equipment included a controlled-flow, four-channel volumetric microdialysis pump (KD Scientific, Model: 789252), syringes (16G) with specially connected spinneret needle electrodes, a high-voltage power generator (10–50 kV, ES50P-20W Gamma High Voltage Research) and a custom-designed grounded target collector (282 mm length × 279 mm height), inside an interlocked Faraday enclosure safety cabinet. The electrospinning conditions employed in all cases were the following: Flow rate: 1.4 ml/h; applied voltage: 17 kV; needle-to-collector distance: 12 cm.

PVP/LHP Fibers

Polyvinylpyrrolidone (PVP, Mn = 1,300,000 g/mol) was obtained from Sigma-Aldrich and used without further purification. A PVP polymer solution prepared in methanol (CH_3OH, analytical grade, Scharlau) with a concentration of 25% w/v was used to electrospin the PVP fibers using the same setup as described in 2.4. The optimum electrospinning conditions to obtain uniform bead-free fibers were the following: Applied voltage: 22–33 kV; flow rate: 4.6 mL/h; needle diameter: 16G; needle-to-collector-distance: 25 cm. Subsequently, the as-prepared PVP fibers were placed in an oven and they were thermally crosslinked by following a three-step controlled heating procedure (de Mello et al., 1997; Chronakis, 2015): 1st step 100°C (3 h), 2nd step:140°C (3 h), and 3rd step: 170°C (3 h). After their fabrication, the hydrophilic PVP cross-linked fibers were functionalized with octyltriethoxysilane (96%) to increase their wettability to the hydrophobic LHP NC solution. NC loading of the functionalized fibrous membranes was achieved via their simple immersion into NC toluene solutions or via spin coating of the NC solutions onto the membrane, with the latter method yielding more uniform dispersion of the NCs within the fibers. The NC concentration within the fibers was measured by weighting before each step, namely (a) before functionalization, (b) after functionalization, and (c) after the NC deposition. Each step was executed allowing sufficient time within to ensure solvent evaporation.

Structural Characterization

Transmission electron microscopy (TEM/STEM) images of nanocrystals were captured using a JEOL JEM-2200FS microscope operated at 200 kV. Powder X-ray diffraction (XRD) was recorded using a powder diffractometer (STOE STADI P) with Cu Kα1 radiation operated in transmission mode combined with a germanium monochromator and a silicon strip

detector (Dectris Mythen). The morphological characteristics of the electrospun fibers were obtained via scanning electron microscopy (SEM) (Vega TS5136LS-Tescan). The samples were gold-sputtered (∼30 nm) (sputtering system K575X Turbo Sputter Coater–Emitech) prior to SEM inspection. Fluorescence microscopy was used to probe the spatial distribution of NCs within the electrospun fibers. The samples were placed on glass slides, covered with coverslips and measured under an Olympus fluorescence microscope (U-RLF-T model). The fluorescence intensity of each sample was determined using the CY3 filter (Excitation: 450 nm, Emission: 513–556 nm). Images were taken at 20× and 100× magnifications and analyzed using the ImageJ software.

Optical Characterization

NC film/solution absorption was carried out by a Perkin Elmer Lamda 1050 spectrophotometer equipped with a three-detector module covering the 300–3,000 nm spectral range. Steady state photoluminescence (PLE, PL) experiments were performed on a 0.35 m FluoroLog FL3 Horiba Jobin Yvon spectrofluorimeter equipped with a TBX-04 visible PMT with detection range from 250 to 850 nm. Excitation of the samples for the PLE experiments was achieved via monochromator-filtered output of a 450 W ozone-free Xe lamp. PL quantum yield (QY) experiments were executed according to reference (de Mello et al., 1997) using a 4-inch Labsphere integrating sphere, from which the light was collected via a fiber bundle and detected by a 0.75 m Acton750i Princeton spectrometer equipped with a 1024 × 256-pixel PIXIS charge-coupled device (CCD) camera with spectral response in the range of 250–950 nm. The samples were excited using an Oxxius, 375 nm, 5 mW laser diode.

Time-resolved photoluminescence (TRPL) was acquired using a monochromator-based time-correlated single-photon counting (TCSPC) method on the same setup as that used for the steady-state PL experiments. PL was excited by a laser diode at 375 nm with a pulse width of ∼150 ps, operating at a repetition rate of 100–250 KHz. The beam diameter of the exciting beam was ∼0.5 mm. To allow spatial averaging over the probed samples, multiple spots were probed. The PL decays were obtained while monitoring the PL emission peak with a spectral bandwidth of 10 nm. The average transient PL lifetime τ_{avg} for TRPL decays was calculated from the relation:

$$\tau_{av} = \frac{\sum_i A_i \tau_i^2}{\sum_i A_i \tau_i}$$

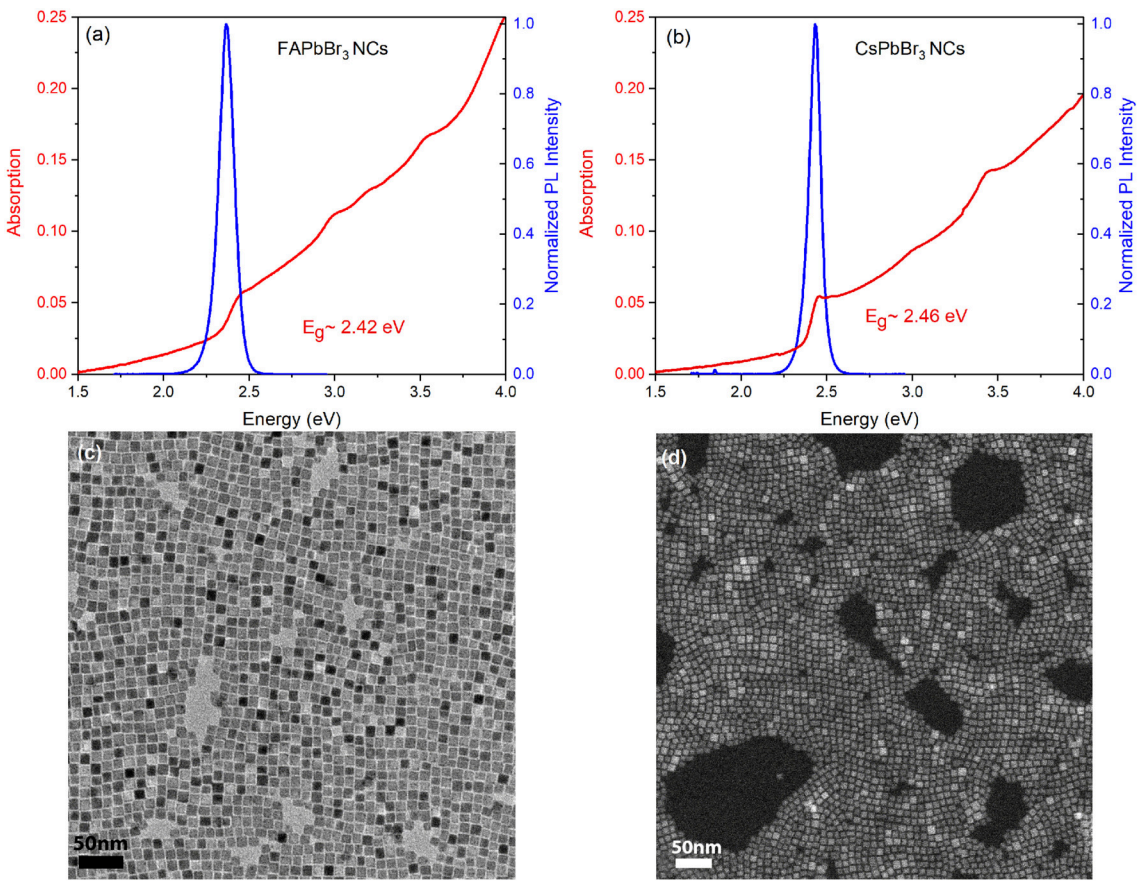

FIGURE 1 | Absorption and PL spectra of the film of pristine **(a)** $FAPbBr_3$ **(b)** $CsPbBr_3$ NC. High resolution TEM images illustrating the cubic-shaped **(c)** $FAPbBr_3$, and **(d)** $CsPbBr_3$ NCs employed in our studies.

where τ_i are the decay times and A_i the respective decay amplitudes extracted from multi-exponential fits of the PL transients. All optical data were acquired in free space and ambient conditions and were corrected to take into account the spectral response of the grating and detector used.

RESULTS AND DISCUSSION

PMMA-LHP NC Fibers

Figures 1a,b displays typical absorption and photoluminescence (PL) spectra from pristine $FAPbBr_3$ and $CsPbBr_3$ NC films employed in this work. Both types of nanocrystals are treated by didodecyldimethylammonium bromide ligands that have been shown to efficiently heal surface traps improving overall the robustness and the emission properties of the material (Bodnarchuk et al., 2019). The produced NCs are cubic-shaped with average sizes in the ∼10–12 nm range, as seen in the high resolution TEM images of **Figure 1**. Powder X-ray diffraction data, presented in **Figure S1,** indicate that the DDAB-capped NCs exhibit an orthorhombic crystal structure. The high quality of the NC material is witnessed by the narrow linewidth, i.e., FWHM <100 meV, and the bright emission reaching quantum yields as high as 86% in the solid state.

The macroscopic cotton-like and the microscopic fibrous morphology of an electrospun PMMA/$FAPbBr_3$ NC membrane with an NC:polymer mass ratio of 1:100 are displayed in **Figures 2a,b**, respectively. From software analysis of the SEM images, the average diameters of fibers are estimated and found equal to ∼3.3 ± 0.3 μm and ∼5.5 ± 1.3 μm for fibers containing 0.1% wt $FAPbBr_3$ and $CsPbBr_3$ NCs, respectively. As more NCs are loaded into fibers, the average fiber diameter increases, i.e., an increase in the NC content by one order of magnitude results in an increase of the fiber diameter by ∼45%, as observed in **Figure S2**. **Figures 2c,d** contain fluorescence microscopy images of the $FAPbBr_3$ NC-sensitized sample at different magnifications illustrating the uniform encapsulation of NCs within the PMMA

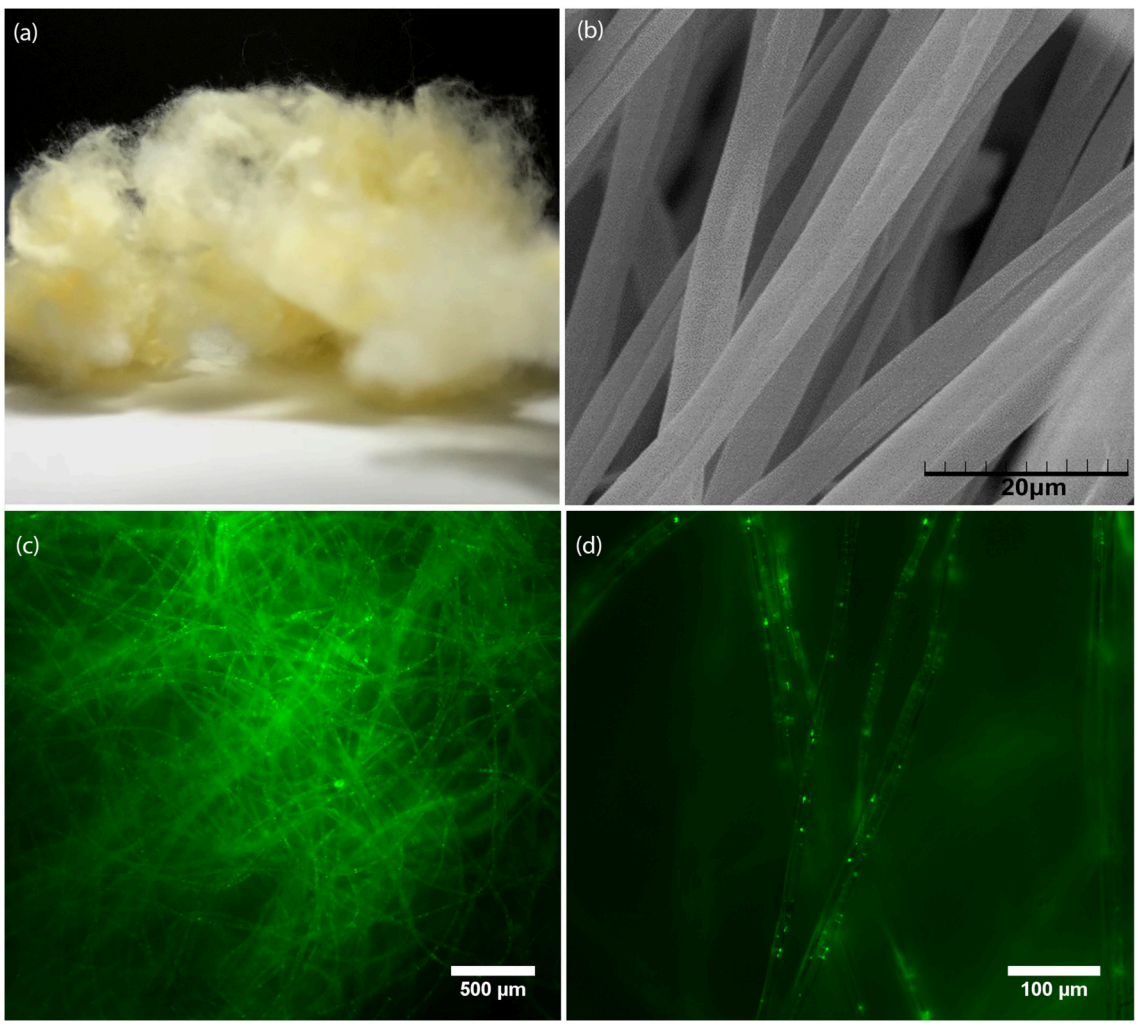

FIGURE 2 | (a) Photograph, **(b)** SEM image, **(c,d)** Fluorescence microscopy images at different magnifications for electrospun $FAPbB_{r3}$ NC:PMMA fibers with polymer:NC mass ratio of 100:1 (1%wt).

fibers. A general observation based on the spatial distribution of the emission observed, vividly illustrated in representative fluorescence images in **Figure S3**, is that the FA-based NCs appear to spatially disperse more orderly compared to the Cs-based NCs that tend to cluster within the PMMA fibers.

Typical optical characteristics of the PMMA-NC membranes are displayed in **Figures 3A,B** for fibers containing $FAPbBr_3$ and $CsPbBr_3$ NCs, respectively. The membranes are opaque to visible light, so optical absorption experiments could not be employed to measure the energy gap of the fiber-embedded perovskite NCs. Instead, the optical gap of the perovskite NCs within the fibers is estimated by the onset of the band-edge luminescence identified by excitation photoluminescence (PLE) experiments, as seen in **Figure 3**.

In **Figures 3C–F**, comparative steady-state and transient PL spectra of the two NC systems are displayed in the colloidal, solid and fibrous states. PL transients in NC solutions are well-approximated with double exponentials while NC decays in the solid state, i.e., films and fibers exhibit more complex decays requiring curve fits by triple exponentials. Typically, the decays are dominated by a short decay of ∼2–4 ns that is assigned to the radiative recombination while weaker and longer component(s) in the ∼8–40 ns range are attributed to non-radiative quenching channels via defects. The assignment is based on the observation that the relative weight of the longer PL transient appears inversely proportional to the emission quantum yield of the samples, i.e., the most efficient emitters exhibit faster PL transients with a weaker amplitude of the long-lived recombination channel. An overall characterization of the dynamics is quantified by the average PL lifetimes, computed as described in Materials and Methods section. A consistent red shift of the band-edge PL NCs, compared to the PL peak in dilute NC solutions and films, is observed upon encapsulation of both types of nanocrystals into the polymer fibers. The bathochromic (toward red) PL shift is accompanied by a slightly broader emission linewidth and average PL lifetimes decreased/increased compared to the colloid/solid samples, respectively. The progressively stronger dielectric environment as the NCs are dispersed from toluene solutions to PMMA fibers and finally to close-packed NC films can explain the trend in the observed PL dynamics; however, dielectric considerations are not consistent with the respective variation of the PL peaks in the steady-state regime.

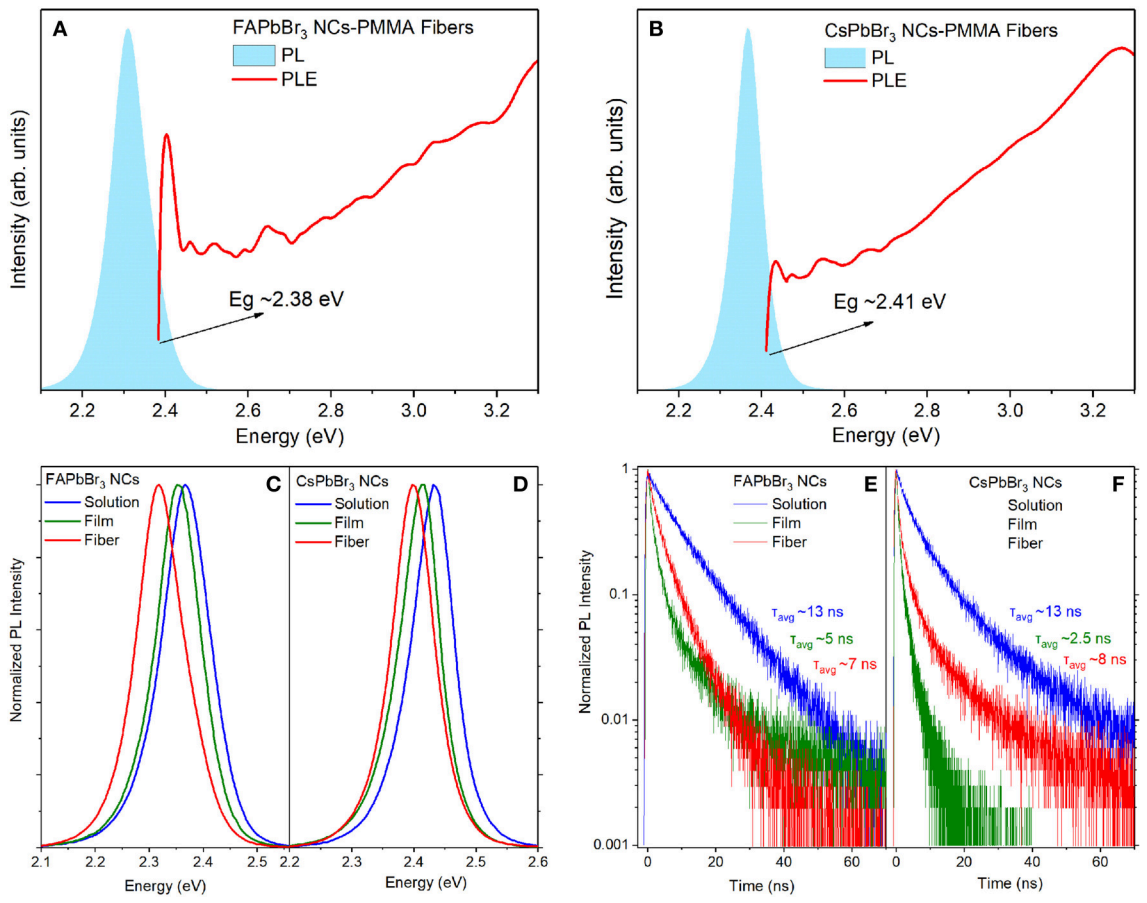

FIGURE 3 | PL and PLE spectra from 0.33% wt/wt NC:PMMA fibers containing **(A)** $FAPbBr_3$ NCs, **(B)** $CsPbBr_3$ NCs. Comparative study of normalized PL spectra in the colloidal, solid and fibrous state for **(C)** $FAPbBr_3$ NCs, **(D)** $CsPbBr_3$ NCs. Transient PL decays in the three states from **(E)** $FAPbBr_3$ NCs, **(F)** $CsPbBr_3$ NCs.

To provide further insight into the spectral and dynamical modifications of the NC emission upon incorporation into the PMMA fibers, we performed a systematic NC concentration-dependent study of their luminescence properties while varying the NC loading by two orders of magnitude and employing appropriate statistics by probing multiple fiber and reference pristine NC samples produced out of the same parent NC solution. $FAPbBr_3$ NC-based membranes were selected for the study due to the better spatial dispersion of the NCs they exhibit, as discussed previously. The study summary that includes the variation of the band-edge, PL peak, PL lifetime, and PL QY with NC content is shown in **Figure 4**, with the relevant optical data listed in **Table S1**. The respective raw PLE/PL and TR-PL data from which the energy gap/PL peak and average PL lifetimes are extracted, are displayed in **Figures S4A,C**, **S5A**, respectively.

The plots reveal clear trends, namely a moderate but monotonic blue-shift of the energy gap and the PL peak by ∼50 meV, a respective increase by a factor of ∼2 in the PL QY and a dramatic quenching of the average PL lifetime by an order of magnitude as NC content in the PMMA membranes increases from 0.05 to 5% wt. It can also be observed that the fibers containing a higher NC density exhibit luminescence characteristics that resemble more the respective characteristics of the reference NC films. Insight into the interpretation of the concentration-dependent properties of the fibers is provided by control experiments on PMMA:LHP NC blend films, where the respective emission characteristics are monitored as a function of the polymer:NC mass ratio. The observed trend in PL lifetime and emission QY, displayed in **Figure S6**, matches well with the respective dependencies observed in **Figures 4B,C** for the NC-sensitized fibers.

Based on all the experimental evidence, we can interpret the photophysical changes of the NC properties upon electrospinning into the PMMA fibers via a combination of concentration-dependent NC stabilization and dielectric effects. The latter result in emission blue-shift and an increase of the PL quantum yield upon NC insertion into the low dielectric polymer environment, while the former yields a bathochromic shift and dampening of the NC emission at the limit of low NC content. In particular, dielectric screening is nominally expected to increase the exciton binding energy and the oscillator strength relative to pristine films (Takagahara, 1993), blue-shifting the band edge and increasing the radiative recombination rate, thus overall enhancing the emission quantum yield. Such effects are evident in the fibers for NC:polymer weight ratios higher than 1% wt and in the polymer:NC blend films for a concentration higher than 30% wt, as observed in **Figure 4** and **Figure S6**, respectively. On the other hand, as the NC content in PMMA fibers or solid matrixes decreases to lower levels, the monotonic quenching of the QY and the concomitant dramatic increase of the average PL lifetime observed indicate a significant reduction in the $FAPbBr_3$ NC radiative recombination rate. Indeed, the exponential fits of the decays indicate that the fast recombination decay channel attributed to radiative recombination reduces substantially in favor of the two other longer decay channels for low NC content, effectively lengthening the average PL lifetime. The quenching of radiative recombination is attributed to a reduced stabilization of the NCs when inserted at low concentrations in the PMMA matrix. At low concentrations, the ligands from the NC surface tend to desorb faster, due to the dilution effect shifting equilibrium toward desorption. This is a common problem for colloidal NCs which appears somewhat pronounced for perovskite NCs due to the more dynamic and looser binding equilibrium (De Roo et al., 2016). It is interesting that the optical manifestation of the NC degradation appears at a significantly lower NC content in the PMMA-NC fibers compared to the respective blend films, which indicates an improved structural and chemical integrity of the perovskite NCs upon polymer fiber encapsulation.

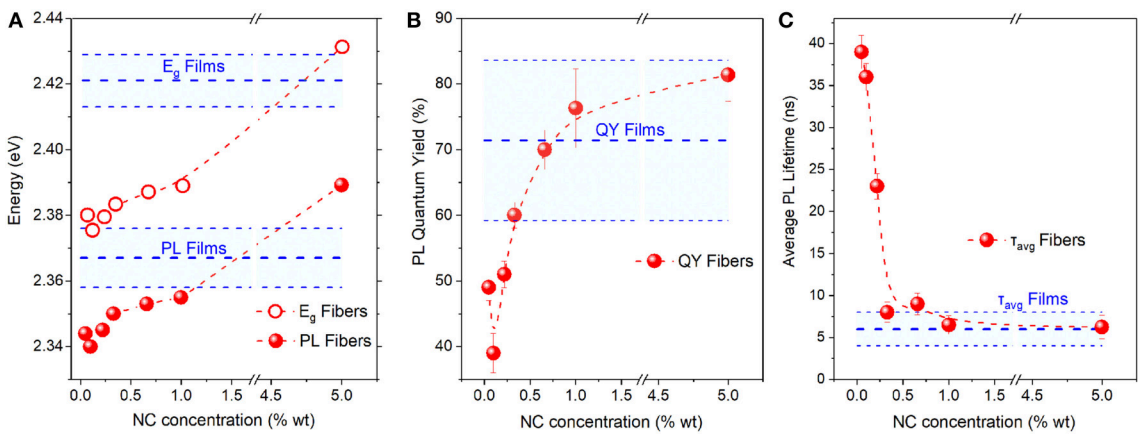

FIGURE 4 | (A) Energy gap (E_g) and PL Peak, **(B)** PL quantum yield, and **(C)** PL lifetime vs. NC concentration for the PMMA/$FAPbBr_3$ NC composite. Respective characteristics for reference pristine NC films are also displayed; the main blue dotted line defines the mean values and the error bands/cyan highlighted area denotes the standard deviation of the PL characteristics yielded by statistics on different fibers/films. All displayed data points have been produced out of the same parent $FAPbBr_3$ NC solution.

PVP-LHP NC Fibers

The NC loading of the electrospun PMMA fibers was limited by the use of different solvents employed to dissolve the PMMA and perovskite NC components, namely chloroform and toluene, respectively. For solvent mixtures containing up to 5% wt of the toluene NC to chloroform PMMA solution, the formation of a desired emulsion was achieved. Mixtures with a higher ratio of the toluene solution produced emulsions with viscosity properties not suitable for the electrospinning process. To demonstrate NC-sensitized membranes with higher NC loadings for potential textile-based light emitting applications, a different approach was adopted, in which NCs in toluene were simply immersed or coated into hydrophilic cross-linked membranes of the PVP polymer, produced via electrospinning. Before immersion, the PVP fibers were functionalized via an amphiphilic polymer silane coating, allowing efficient wetting of the hydrophilic PVP fibers with the hydrophobic nanocrystal surface. It is noted that the NC loading in the fibers appears stable over a period of a year and no nanocrystal loss is observed as confirmed by repeated measurements of the membrane weight after immersion and drying.

As seen in **Figure 5a**, the NC-containing PVP membranes exhibit a paper-like texture and bright yellow-green color as a result of the strong absorption/scattering properties of the incorporated lead bromide perovskite NCs. An SEM analysis yields an average PVP fiber diameter of $\sim$0.70 $\pm$ 0.12 μm. Unlike the case of PMMA fibers, both hybrid $FAPbBr_3$ NCs and all-inorganic $CsPbBr_3$ NCs sensitize uniformly the PVP fibers as seen in **Figures 5c,d**, with attainable NC loadings for both as high as a 2:1 NC:PVP mass ratio (200% wt); overall, the two PVP-NC fiber types exhibit very similar morphological and optical properties. For high NC content, clustering of the perovskite nanocrystals in between cross-linked fibers and around individual fibers is vividly illustrated in the SEM and fluorescence microscopy images of **Figures 5b,e**, respectively.

Representative optical properties of the PVP-NC membranes for the two NC systems presented in **Figure 6**, **Figures S4B,D**, **S5B**, reveal effects similar to those observed in the PMMA-based composites, such as a bathochromically shifted emission and energy gap and triple-exponential PL dynamics with prolonged PL lifetime compared to NC films. Concentration-dependent luminescence properties were probed for the $CsPbBr_3$ NC-sensitized PVP fibers over the NC content range of 2–200% and plotted in the summary graphs of **Figure 7**, with the relevant optical data listed in **Table S2**.

The optical characteristics of the fibers resemble those of pristine $CsPbBr_3$ NC films for NC content up to $\sim$5% wt. For higher NC densities, a monotonic red-shift of the band-edge and

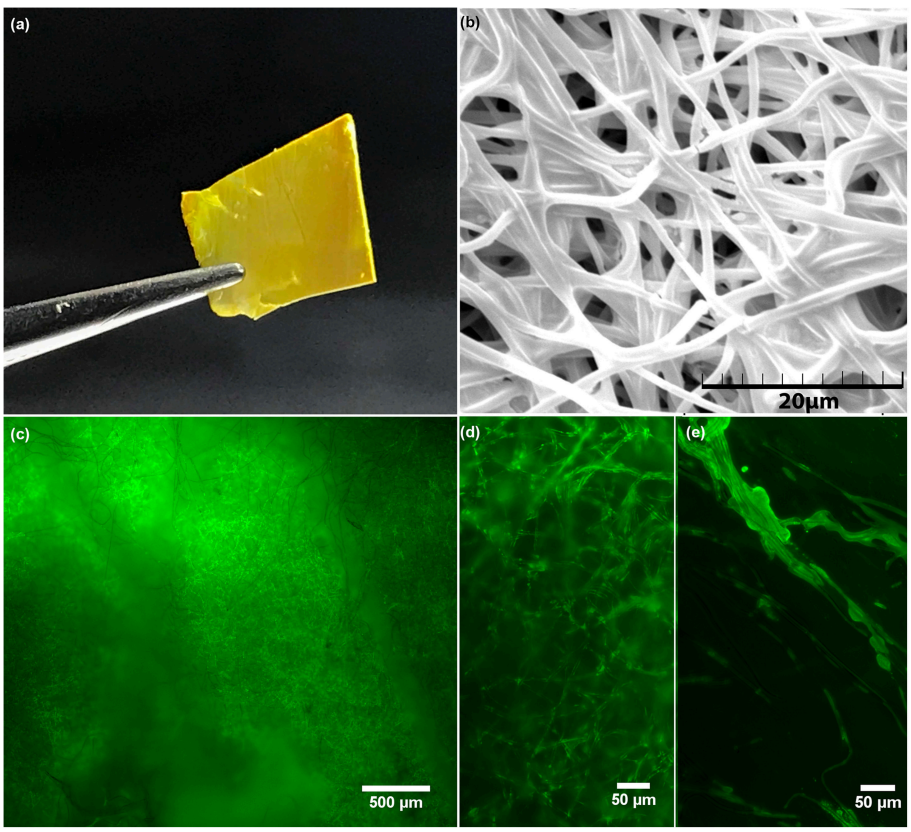

FIGURE 5 | (a) Photograph, **(b)** SEM, **(c–e)** Fluorescence microscopy images at different magnifications and different parts; i.e., **(c,d)** at the center, **(e)** at the edge of a $FAPbBr_3$ NC-PVP membrane with NC: polymer mass ratio of 50:100 (50%wt).

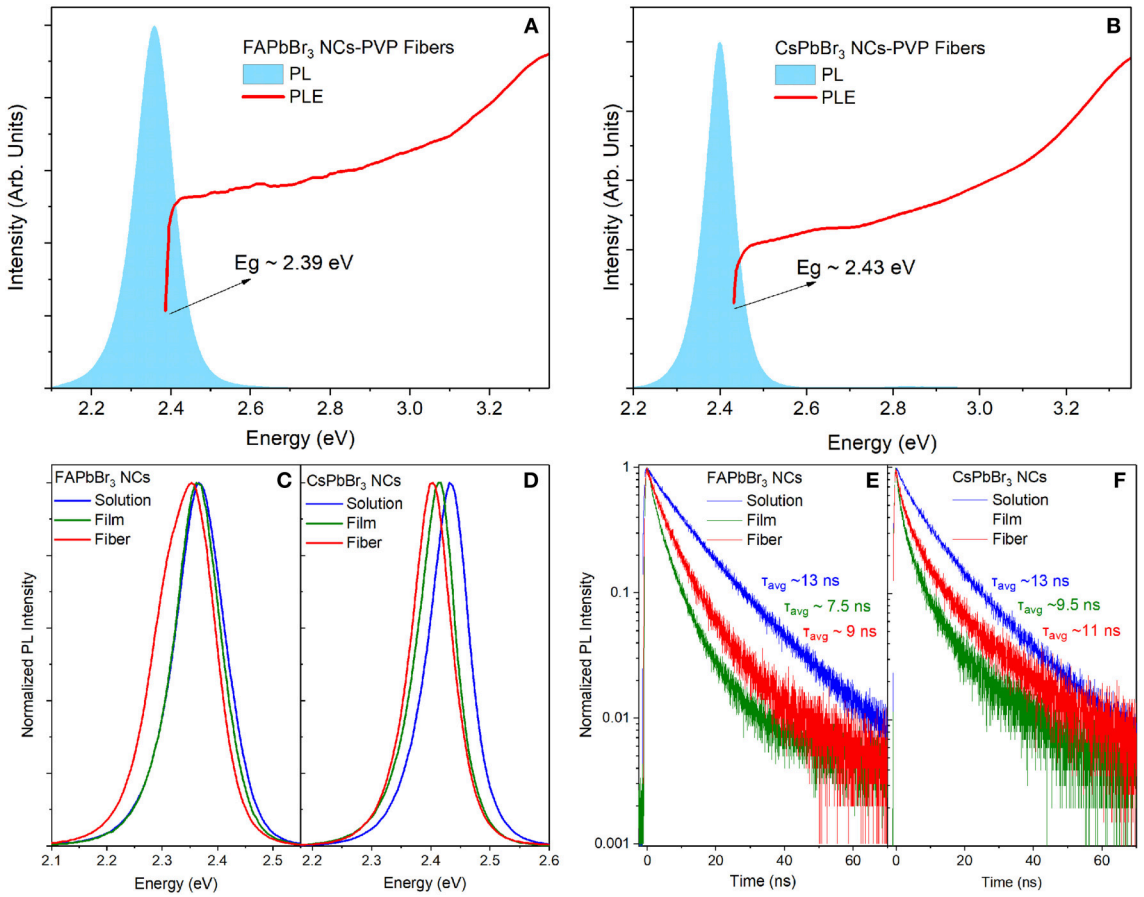

FIGURE 6 | PL and PLE spectra of 30% wt/wt NC:PMMA **(A)** $FAPbBr_3$, **(B)** $CsPbBr_3$. Continuous wave PL spectra at solution, solid and fibrous state **(C)** $FAPbBr_3$, **(D)** $CsPbBr_3$. TRPL decays at solution, solid and fibrous state **(E)** $FAPbBr_3$, **(F)** $CsPbBr_3$.

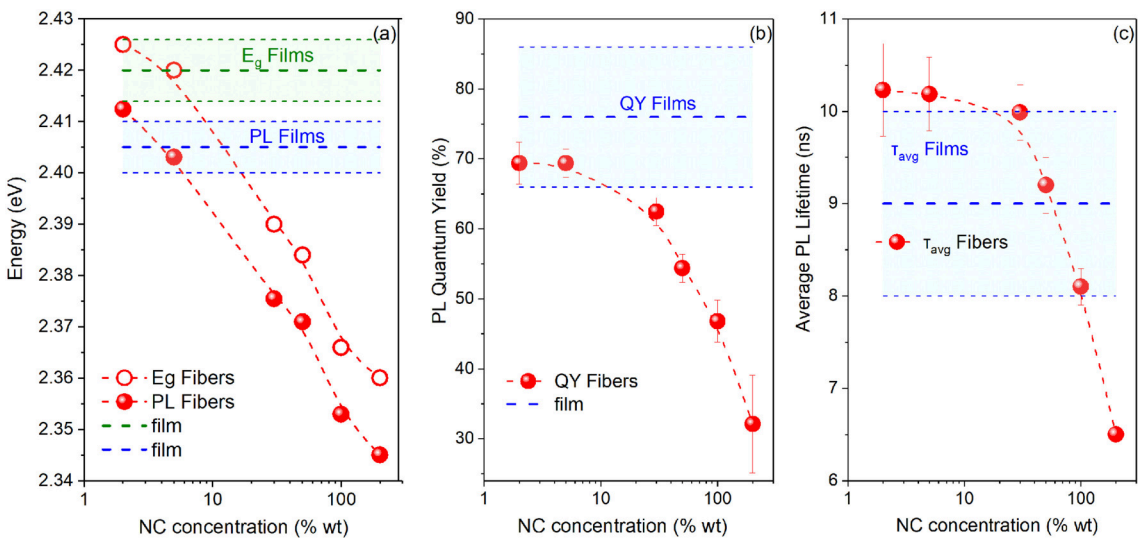

FIGURE 7 | (a) Energy gap (E_g) and PL Peak, **(b)** PL quantum yield and **(c)** PL lifetime vs. NC concentration for the PVP/$CsPbBr_3$ NC composite for a wide range of NC content (1–200% wt). Respective characteristics for reference pristine NC films are also displayed.

quenching of the PL QY and lifetime is observed. QY/Lifetime quenching appears to be promoted via the concentration-dependent shortening of the long decay PL channels and assigned to non-radiative quenching, that assume at low NC at low NC content values of ∼8–40 ns while suppressing to values as low as ∼3 ns, as the NC concentration increases to the maximum of 200% wt values probed. Based on the aforementioned discussion, we attribute the optical modifications in the PVP type of NC composites, to concentration-dependent aggregation of the NCs. The weak ligand binding into the lead halide perovskite NC surfaces can lead to partial ligand detachment of the ligands from the surface, allowing the NCs to pack and partly merge (Huang et al., 2017; Kovalenko et al., 2017; Akkerman et al., 2018; Zhao et al., 2018), forming larger perovskite nanostructures. It is reasonable to assume that the NC agglomeration effects become increasingly pronounced as NC concentration increases. NC aggregation is consistent with the broadening and red-shift of the band-edge due to the loss of confinement and the decrease of the PL quantum yield and lifetime due to increased non-radiative recombination, as merging of the NCs is known to lead to exciton quenching effects (Stadler et al., 2015; Papagiorgis et al., 2018).

Air and Water Stability Studies

As mentioned, a prerequisite for the realization of practical perovskite NC optoelectronics is the improvement of the nanocrystal structural, thermodynamic and optical stability under ambient conditions (Huang et al., 2017; Kovalenko et al., 2017; Akkerman et al., 2018; Zhao et al., 2018). **Table 1** lists PL QY results for a series of hybrid and inorganic NC fiber and film solids over a yearly period, stored at ambient dark conditions at temperature of ∼21°C and humidity levels varied within the 20–40% range through the year. The studied samples were produced out of two parent solutions, one containing $CsPbBr_3$ NCs and the other $FAPbBr_3$ NCs and their QY was measured at the day of fabrication and after a year under the same experimental conditions. For all samples studied, a moderate red-shift of the PL was observed after a year, while the QY quenching varied widely. In particular, the pristine films of the two NC types exhibit a significant deterioration of their emission efficiency, being more prominent for the $CsPbBr_3$ NC system in which emission QY dropped by more than one order of magnitude. In contrast, the QY of the NCs encapsulated with the PMMA fibers was found to quench by <10% of its original value, confirming the suppression of oxygen and moisture transmission to the NCs by the polymer matrix. NCs incorporated within the PVP cross-linked fiber membranes exhibit QY quenching in between the two other solid types, with the PVP-$FAPbBr_3$ NC composite exhibiting slightly better stability compared to the PVP-$CsPbBr_3$ NC, in agreement with the respective trend observed in the pristine films of the two NC materials. More detailed accelerated aging tests of the materials, at controlled relative humidity and blue-light flux conditions, relevant to industrial requirements for LCD lighting, are to be conducted soon.

Results on the temporal evolution of the NC-integrated luminescence under water soaking conditions for a period of a week (∼10^5 min) are displayed in **Figure 8**; the raw PL spectra are contained in **Figure S7**. Four types of samples have been included in the study, namely pristine NC films, PMMA:NC blend films and NC-sensitized PMMA and PVP fiber composites. NCs encapsulated during electrospinning into PMMA fibers exhibit by far the highest optical stability in a water environment, with their integrated emission dropping by <15% after a week of water immersion. Such results compare unfavorably to the highest reported water stability in perovskite NC-polymer fibers, exceeding a period of a month (Wang et al., 2017) but stand on a par (Wang et al., 2016; Tsai et al., 2018) with or even outperform (Liao et al., 2018; Lin et al., 2018) other reported work on the field. Interestingly, a small but reproducible improvement in PL efficiency is observed for the first 5–15 min of immersion for unknown reasons. NCs embedded within the PVP fibers exhibit stable emission over the first ∼10–30 min of water immersion with the emission quenching fully after a period of a day. On the other hand, the emission from the pristine NC films is water-suppressed fast, within 100 min of immersion. NCs at low content (1% wt) dispersed within a PMMA film are more efficiently protected by the matrix, with the emission quenching by 80–90% over the first 100 min of soaking, followed though by a much slower longer-term degradation.

TABLE 1 | Emission QY stability results for a series of samples in solid and fibrous phase.

Sample	PL QY (%) fresh	PL QY (%) 1 year old
$CsPbBr_3$ NCs film	86 ± 8	7 ± 1
$FAPbBr_3$ NCs film	83 ± 7	22 ± 4
PVP-$CsPbBr_3$ NC fibers (30% wt)	77 ± 6	27 ± 4
PVP-$FAPbBr_3$ NC fibers (30% wt)	75 ± 8	36 ± 5
PMMA-$FAPbBr_3$ NC fibers (1% wt)	76 ± 5	70 ± 5

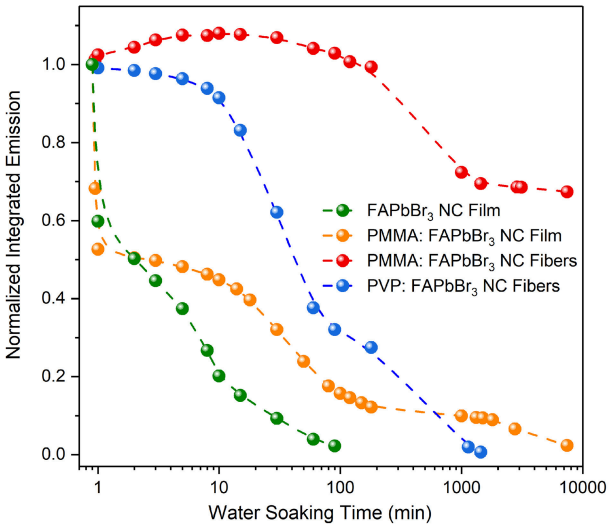

FIGURE 8 | Integrated emission vs. water soaking time for NCs embedded in films and fibers.

CONCLUSIONS

We demonstrate robust polymer-LHP NC fiber composite emitters via (i) encapsulation of the NCs into PMMA hydrophobic fibers using an electrospinning process and (ii) coating hydrophilic cross-linked polyvinylpyrrolidone (PVP) fibrous membranes with NCs via simple immersion and drying processes. For the larger range of the studied content, NCs embedded in the polymer fibers retain much of their narrow and high quantum yield emission, while degradation phenomena and aggregation effects result in the deterioration of the NC luminescence properties at the low/high limits of the concentration range probed for the PMMA-based and PVP-based emitters, respectively. Despite the quite different structural characteristics of the two composite types, we find that the NC sensitizers exhibit similar luminescence characteristics in terms of emission peak, lifetime and quantum yield within the intermediate, overlapping for the two composites NC density regime; furthermore, qualitatively similar concentration-dependent emission characteristics have been obtained in fiber composites employing NCs with oleic acid ligands that have not been subjected to the DDAB-treatment. The aforementioned statements further confirm the validity and generality of the reported studies. The long-term stability under ambient conditions and the short-term material robustness under harsh water-soaking conditions of the polymer-LHP NC fibers were also investigated. The studies confirm the demonstration of robust and bright polymer-fiber emitters with potential applications in backlighting for LCD displays and textile-based light emitting devices.

DATA AVAILABILITY

All datasets generated for this study are included in the manuscript and the supplementary files.

AUTHOR CONTRIBUTIONS

All authors listed have made a substantial, direct and intellectual contribution to the work, and approved it for publication.

ACKNOWLEDGMENTS

We would like to thank Dr. Triantafyllos Stylianopoulos (Cancer Biophysics Laboratory, Department of Mechanical and Manufacturing Engineering, University of Cyprus) for providing access to fluorescence microscopy and Ms. Myrofora Panagi for assistance with the fluoresence microscope measurements. GI acknowledges financial support from the Research Promotion Foundation of Cyprus, under the New Strategic Infrastructure Units—Young Scientists Programme (Grant Agreement No. INFRASTRUCTURES/1216/0004, Grant NANOSONICS).

SUPPLEMENTARY MATERIAL

The Supplementary Material for this article can be found online at: https://www.frontiersin.org/articles/10.3389/fchem.2019.00087/full#supplementary-material

REFERENCES

Akkerman, Q. A., Rainò, G., Kovalenko, M. V., and Manna, L. (2018). Genesis, challenges and opportunities for colloidal lead halide perovskite nanocrystals. *Nat. Mater.* 17, 394–405. doi: 10.1038/s41563-018-0018-4

Bodnarchuk, M. I., Boehme, S. C., Ten Brinck, S., Bernasconi, C., Shynkarenko, Y., Krieg, F., et al. (2019). Rationalizing and controlling the surface structure and electronic passivation of cesium lead halide nanocrystals. *ACS Energy Lett.* 4, 63–74. doi: 10.1021/acsenergylett.8b01669

Chronakis, I. S. (2015). Novel nanocomposites and nanoceramics based on polymer nanofibers using electrospinning process—A review. *J. Mater. Process. Technol.* 167, 283–293. doi: 10.1016/j.jmatprotec.2005.06.053

de Mello, J. C., Wittmann, H. F., and Friend, R. H. (1997). An improved experimental determination of external photoluminescence quantum efficiency. *Adv. Mater.* 9, 230–232. doi: 10.1002/adma.19970090308

De Roo, J., Ibáñez, M., Geiregat, P., Nedelcu, G., Walravens, W., Maes, J., et al. (2016). Highly dynamic ligand binding and light absorption coefficient of cesium lead bromide perovskite nanocrystals. *ACS Nano* 10, 2071–2081. doi: 10.1021/acsnano.5b06295

Demkiv, T. M., Myagkota, S. V., Malyi, T., Pushak, A. S., Vistovskyy, V. V., Yakibchuk, P. M., et al. (2018). Luminescence properties of $CsPbBr_3$ nanocrystals dispersed in a polymer matrix. *J. Luminesc.* 198, 103–107. doi: 10.1016/j.jlumin.2018.02.021

Hou, S., Guo, Y., Tang, Y., and Quan, Q. (2017). Synthesis and stabilization of colloidal perovskite nanocrystals by multidentate polymer micelles. *ACS Appl. Mater. Interfaces* 9, 18417–18422. doi: 10.1021/acsami.7b03445

Huang, H, Chen, B, Wang, Z, Hung, T. F., Susha, A. S., Zhong, H, et al. (2016). Water resistant $CsPbX_3$ nanocrystals coated with polyhedral oligomeric silsesquioxane and their use as solid state luminophores in all-perovskite white light-emitting devices. *Chem. Sci.* 7, 5699–5703. doi: 10.1039/C6SC01758D

Huang, H., Bodnarchuk, M. I., Kershaw, S. V., Kovalenko, M. V., and Rogach, A. L. (2017). Lead halide perovskite nanocrystals in the research spotlight: stability and defect tolerance. *ACS Energy Lett.* 2, 2071–2083. doi: 10.1021/acsenergylett.7b00547

Kovalenko, M. V., Protesescu, L., and Bodnarchuk, M. I. (2017). Properties and potential optoelectronic applications of lead halide perovskite nanocrystals. *Science* 358, 745–750. doi: 10.1126/science.aam7093

Liao, H., Guo, S., Cao, S., Wang, L., Gao, F., Yang, Z., et al. (2018). A general strategy for *in situ* growth of all-inorganic $CsPbX_3$ (X = Br, I, and Cl) perovskite nanocrystals in polymer fibers toward significantly enhanced water/thermal stabilities. *Adv. Opt. Mater.* 6:1800346. doi: 10.1002/adom.201800346

Lin, C. C., Jiang, D. H., Kuo, C. C., Cho, C. J., Tsai, Y. H., Satoh, T., et al. (2018). Water-resistant efficient stretchable perovskite-embedded fiber membranes for light-emitting diodes. *ACS Appl. Mater. Interfaces* 10, 2210–2215. doi: 10.1021/acsami.7b15989

Lu, W.-G., Wu, X.-G., Huang, S., Wang, L., Zhou, Q., Zou, B., et al. (2017). Strong polarized photoluminescence from stretched perovskite-nanocrystal-embedded polymer composite films. *Adv. Opt. Mater.* 5:1700594. doi: 10.1002/adom.201700594

Ma, K., Du X.-Y., Zhang Y.-W., and Chen, S. (2017). *In situ* fabrication of halide perovskite nanocrystals embedded in polymer composites via microfluidic spinning microreactors. *J. Mater. Chem. C* 5, 9398–9404. doi: 10.1039/C7TC02847D

Murphy, J. P., Andriolo, J. M., Sutton, N. J., Brockway, M. C., and Skinner, J. L. (2017). Coaxial hybrid perovskite fibers: synthesis and encapsulation *in situ* via electrospinning. *J. Vacuum Sci. Technol. B* 35, 06G402. doi: 10.1116/1.4991724

Papagiorgis, P., Manoli, A., Protesescu, L., Achilleos, C., Violaris, M., Nicolaides, K., et al. (2018). Efficient optical amplification in the nanosecond regime from formamidinium lead iodide nanocrystals. *ACS Photonics* 5, 907–917. doi: 10.1021/acsphotonics.7b01159

Persano, L., Camposeo, A., and Pisignano, D. (2013). Industrial upscaling of electrospinning and applications of polymer nanofibers: a review. *Macromol. Mater. Eng.* 298, 504–520. doi: 10.1002/mame.201200290

Protesescu, L., Yakunin, S., Bodnarchuk, M. I., Bertolotti, F., Masciocchi, N., Guagliardi, A., et al. (2016). Monodisperse formamidinium lead bromide nanocrystals with bright and stable green photoluminescence. *J. Am. Chem. Soc.* 138, 14202–14205. doi: 10.1021/jacs.6b08900

Protesescu, L., Yakunin, S., Bodnarchuk, M. I., Krieg, F., Caputo, R., Hendon, C. H., et al. (2015). Nanocrystals of cesium lead halide perovskites ($CsPbX_3$, X = Cl, Br, and I): novel optoelectronic materials showing bright emission with wide color gamut. *Nano Lett.* 15, 3692–3696. doi: 10.1021/nl5048779

Protesescu, L., Yakunin, S., Kumar, S., Bär, J., Bertolotti, F., Masciocchi, N., et al. (2017). Dismantling the "red wall" of colloidal perovskites: highly luminescent formamidinium and formamidinium/cesium lead iodide nanocrystals. *ACS Nano* 11, 3119–3134. doi: 10.1021/acsnano.7b00116

Raja, S. N., Bekenstein, Y., Koc, M. A., Fischer, S., Zhang, D., Lin, L., et al. (2016). Encapsulation of perovskite nanocrystals into macroscale polymer matrices: enhanced stability and polarization. *ACS Appl. Mater. Interfaces* 8, 35523–35533. doi: 10.1021/acsami.6b09443

Savva, I., and Krasia-Christoforou, T. (2018). "Encroachment of traditional electrospinning," in *Electrospinning—Basic Research to Commercialization*, eds S. Thomas, K. Ghosal, and E. Kny (London: Royal Society of Chemistry), 24–54.

Stadler, P., Mohamed, S. A., Gasiorowski, J., Sytnyk, M., Yakunin, S., Scharber, M. C., et al. (2015). Iodide-capped PbS Quantum dots: full optical characterization of a versatile absorber. *Adv. Mater.* 27, 1533–1539. doi: 10.1002/adma.201404921

Sutherland, B. R., and Sargent, E. H. (2016). Perovskite photonic sources. *Nat. Photonics*10, 295–302. doi: 10.1038/nphoton.2016.62

Sygletou, M., Kyriazi, M. E., Kanaras, A. G., and Stratakis, E. (2018). Anion exchange in inorganic perovskite nanocrystal polymer composites. *Chem. Sci.* 9, 8121–8126. doi: 10.1039/C8SC02830C

Takagahara, T. (1993). Effects of dielectric confinement and electron-hole exchange interaction on excitonic states in semiconductor quantum dots. *Phys. Rev. B* 47:4569. doi: 10.1103/PhysRevB.47.4569

Tsai, P. C., Chen, J. Y., Ercan, E., Chueh, C. C., Tung, S. H., and Chen, W. C. (2018). Uniform luminous perovskite nanofibers with color-tunability and improved stability prepared by one-step core/shell electrospinning. *Small* 14:1704379. doi: 10.1002/smll.201704379

Wang, Y., Zhu, Y., Huang, J., Cai, J., Zhu, J., Yang, X., et al. (2016). CsPbBr3 perovskite quantum dots-based monolithic electrospun fiber membrane as an ultrastable and ultrasensitive fluorescent sensor in aqueous medium. *J. Phys. Chem. Lett.* 7, 4253–4258. doi: 10.1021/acs.jpclett.6b02045

Wang, Y., Zhu, Y., Huang, J., Cai, J., Zhu, J., Yang, X., et al. (2017). Perovskite quantum dots encapsulated in electrospun fiber membranes as multifunctional supersensitive sensors for biomolecules, metal ions and pH. *Nanoscale Horizons* 2, 225–232. doi: 10.1039/C7NH00057J

Wong, Y.-C., Andrew Ng, J. D., and Tan, Z. K. (2018). Perovskite-initiated photopolymerization for singly dispersed luminescent nanocomposite. *Adv. Mater.* 30:1800774. doi: 10.1002/adma.201800774

Xin, Y., Zhao, H., and Zhang, J. (2018). Highly stable and luminescent perovskite-polymer composites from a convenient and universal strategy. *ACS Appl. Mater. Interfaces* 10, 4971–4980. doi: 10.1021/acsami.7b16442

Yakunin, S., Protesescu, L., Krieg, F., Bodnarchuk, M. I., Nedelcu, G., Humer, M., et al. (2015). Low-threshold amplified spontaneous emission and lasing from colloidal nanocrystals of caesium lead halide perovskites. *Nat. Commun.* 6:8056. doi: 10.1038/ncomms9056

Yang, M., Yu, J., Jiang, S., Zhang, C., Sun, Q., Wang, M., et al. (2018). High stability luminophores: fluorescent CsPbX3 (X = Cl, Br and I) nanofiber prepared by one-step electrospinning method. *Opt. Express* 26, 20649–20660. doi: 10.1364/OE.26.020649

Yang, S., Zhang, F., Tai, J., Li, Y., Yang, Y., Wang, H., et al. (2018). A detour strategy for colloidally stable block-copolymer grafted $MAPbBr_3$ quantum dots in water with long photoluminescence lifetime. *Nanoscale* 10, 5820–5826. doi: 10.1039/C8NR01493K

Yu, M., Dong R.-H., Yan, X., Yu G.-F., You M.-H., Ning, X., et al. (2017). Recent advances in needleless electrospinning of ultrathin fibers: from academia to industrial production. *Macromol. Mater. Eng.* 302:1700002. doi: 10.1002/mame.201700002

Zhang, M., Wang, M., Yang, Z., Li, J., and Qiu, H. (2018). Preparation of all-inorganic perovskite quantum dots-polymer composite for white LEDs application. *J. Alloys Compounds* 748, 537–545. doi: 10.1016/j.jallcom.2018.03.179

Zhao, X., Andrew Ng, J. D., Friend, R. H., and Tan, Z. K. (2018). Opportunities and challenges in perovskite light-emitting devices. *ACS Photonics*5, 3866–3875. doi: 10.1021/acsphotonics.8b00745

Zhu, J., Xie, Z., Sun, X., Zhang, S., Pan, G., Zhu, Y., et al. (2018). Highly efficient and stable inorganic perovskite quantum dots by embedding into a polymer matrix. *ChemNanoMat* 4, 1–7. doi: 10.1002/cnma.201800357

Conflict of Interest Statement: The authors declare that the research was conducted in the absence of any commercial or financial relationships that could be construed as a potential conflict of interest.

frontiers in Chemistry

ORIGINAL RESEARCH
published: 23 October 2018
doi: 10.3389/fchem.2018.00453

Water-Borne Perovskite Quantum Dot-Loaded, Polystyrene Latex Ink

Keke Huang[1], Lucheng Peng[1], Baijun Liu[2], Dongze Li[3], Qiang Ma[1], Mingyao Zhang[2], Renguo Xie[1], Dayang Wang[1] and Wensheng Yang[1]*

[1] State Key Laboratory of Inorganic Synthesis and Preparative Chemistry, College of Chemistry Jilin University, Changchun, China, [2] Engineering Research Center of Synthetic Resin and Special Fiber, Ministry of Education, Changchun University of Technology, Changchun, China, [3] China Star Optoelectronics Technology Co. Ltd, Shenzhen, China

Highly lipophilic nanocrystals (NCs) of cesium lead halides were successfully embedded in polystyrene (PS) particles by deliberately controlling the swelling of the PS particles in the mixtures of good and bad organic solvents. The resulting composite particles were readily transferred into water via simple stepwise solvent exchange, which yielded water-borne perovskite NC-based inks with outstanding structural and chemical stability in aqueous media. Minimal change in the photoluminescence (PL) of the NCs loaded in the PS particles was visible after 1 month of incubation of the composite particles in water in a broad pH range from 1 to 14, which could otherwise be hardly realized. Loading into the PS particles also made the NCs highly stable against polar organic solvents, such as ethanol, intense light irradiation, and heat. The NC PL intensity slightly changed after the composite particles were heated at 75°C and under irradiation of strong blue light (@365 nm) for 1 h. Furthermore, the PS matrices could effectively inhibit the exchange of halide anions between two differently sized perovskite NCs loaded therein, thereby offering a considerable technical advantage in the application of multiple perovskite NCs for multicolor display in the future.

Keywords: quantum dot, lead halide perovskites, luminescence, water-borne ink, polystyrene

OPEN ACCESS

Edited by:
Vladimir Lesnyak, Technische Universität Dresden, Germany

Reviewed by:
Sergii Yakunin, ETH Zürich, Switzerland
Nikolai Gaponik, Technische Universität Dresden, Germany
Loredana Protesescu, Massachusetts Institute of Technology, United States

****Correspondence:***
Renguo Xie
renguoxie@jlu.edu.cn

Specialty section:
This article was submitted to Nanoscience, a section of the journal Frontiers in Chemistry

Received: *05 May 2018*
Accepted: *13 September 2018*
Published: *23 October 2018*

Citation:
Huang K, Peng L, Liu B, Li D, Ma Q, Zhang M, Xie R, Wang D and Yang W (2018) Water-Borne Perovskite Quantum Dot-Loaded, Polystyrene Latex Ink. Front. Chem. 6:453. doi: 10.3389/fchem.2018.00453

INTRODUCTION

In recent decades, a paradigmatic shift has occurred in inkjet printing, from conventional printing of newspapers and photographs to innovative printing of microelectronic circuits and rapid prototyping, for example, of tissue implants and many other niche applications (Singh et al., 2010). Consequently, the spectrum of inks has been largely extended to a diversity of functional nanomaterials, such as metallic nanoparticles (Liang et al., 2016), semiconductor quantum dots (QDs) (Kim et al., 2011; Carey et al., 2015), and carbon nanotubes (Wang et al., 2012), to translate their peculiar functions into technological advances. In parallel, the awareness of environmental friendly manufacturing is prospering at present, and hence considerable attention is being given to the development of water-borne ink formulations. However, in most cases, high-quality nanomaterials are produced in organic media (Murray et al., 2000; Weller, 2003), and their designated functions are deteriorated after phase transfer into water to a considerable extent (Medintz et al., 2005; Jamieson et al., 2007). In this context, the present work aims to develop water-borne inks from perovskite QDs of $CsPbX_3$ (X = Cl, Br, and I) by taking advantage of their outstanding optical properties (Protesescu et al., 2015; Swarnkar et al., 2015; Tong et al., 2016; Liu et al., 2017), which, however, remains a daunting challenge as most of the currently available perovskite QDs readily incur severe degradation upon contact with water (Frost et al., 2014). Furthermore,

the anion-exchange reaction between different halide QD particles when used together remain a major issue that obstructs their practical applications (Akkerman et al., 2015; Nedelcu et al., 2015). To circumvent the challenge, we successfully incorporated preformed $CsPbX_3$ QDs into polystyrene (PS) latex particles via stepwise solvent exchange methodology. The resulting $CsPbX_3$ QD-loaded PS particles were able to disperse in aqueous media with outstanding chemical and structural stability. The photoluminescence (PL) behavior of the resulting composite particles in water is fairly comparable with the original QD dispersions in organic media. Anion exchange between the loaded QDs with different compositions was slightly visible.

Since the seminal work of Protesescu et al. (2015), $CsPbX_3$ QDs have rapidly emerged as promising candidates for optoelectronic applications, such as light-emitting diodes (LED), lasing, photodetection, and backlight display (Wang et al., 2015; Amgar et al., 2016; Li G. et al., 2016; Ling et al., 2016; Li X. et al., 2016; Palazon et al., 2016b; Rainò et al., 2016; Ramasamy et al., 2016; Swarnkar et al., 2016; Xu et al., 2016; Zhang et al., 2016; Li J. H. et al., 2017; Zhou et al., 2017) because of their high PL quantum yields (50–90%), extremely narrow full-width at half-maximum, and broad emission spectral tunability in visible-light region.(Protesescu et al., 2015) Nevertheless, the success of $CsPbX_3$ QDs in technical applications is largely bottlenecked by their high vulnerability to polar solvents, humidity, light, and temperature of the surrounding environment (Frost et al., 2014; Huang et al., 2016a; Wang et al., 2016a), in response to which the PL behavior of the perovskite QDs was severely deteriorated as a result of the QD degradation. To address this challenge, a number of efforts have been devoted to deliberately adjust the stabilizing ligands or the perovskite compositions to reduce the environmental vulnerability of the QDs derived thereof (Dirin et al., 2016; Huang et al., 2016; Palazon et al., 2016a; Sun et al., 2016; Wang et al., 2016b; Li Z. et al., 2017). Although the stability of QDs has been significantly improved, as-prepared QDs modified by inorganic materials or organic small molecules still show poor stability in polar solvent. Recently, polymer matrices have been utilized for *in situ* growth of perovskite QDs therein, leading to QD/polymer nanocomposites with substantially improved stability against water, heat, and light (Huang et al., 2016a,b; Meyns et al., 2016; Raja et al., 2016; Wang et al., 2016a; Hai et al., 2017). However, the preparation of QD–polymer composites by *in situ* growth or direct incorporation strategy cannot inhibit dynamic exchanges of anions between the growing perovskite QDs. This condition fails to incorporate the QDs with different compositions in polymer matrices. One of the merits of perovskite QDs is their flexibility to tune their PL characteristics based on the composition.

MATERIALS AND METHODS

Chemicals

Technical grade Octadecene (ODE, 90%) and Oleic acid (OA, 90%) were purchased from Alfa Aesar. Cesium carbonate (Cs_2CO_3, 99.9%), lead chloride ($PbCl_2$, 99.999%), lead bromide ($PbBr_2$, 99.999%), lead iodide (PbI_2, 99%), and Oleylamine (OLA, 70%) were purchased from Aldrich. Hexane and toluene were obtained from Beijing Chemical Reagent Ltd., China. All reagents were used as received without further experimental purification.

Preparation of Cs-Oleate Precursor

Cs_2CO_3 (0.652 g, 2 mmol), OA (2.5 mL, 7.5 mmol), and ODE (17.5 mL) were added into a 50 mL three-necked flask, dried for 1 h at 120°C, and then heated under N_2 to 150°C until Cs_2CO_3 reacted with OA. Since Cs-oleate precipitates out of ODE at room temperature, it must be preheated to 100°C before use.

Preparation of PbX_2 Stock Solution

Lead halide (0.2 mmol), Oleic acid (0.5 mL), and Oleylamine (0.5 mL) (Trioctylphosphine (0.5 mL) for lead chloride) were mixed with ODE (4.0 mL) in a 50 mL three-necked flask. The reaction mixtures were degassed under vacuum for 30 min and purged with argon. The flask was heated to 150°C until a clear solution was formed, and then cooled to the room temperature (25°C).

Synthesis of $CsPbBr_3$ Nanoparticles

In a typical synthesis of $CsPbBr_3$ nanocubes, ODE (5 mL) and $PbBr_2$ (0.2 mmol) were loaded into a 25 mL three-necked flask and dried under vacuum for 1 h at 120°C. Dried oleylamine (0.5 mL, OLA) and dried OA (0.5 mL) were injected at 120°C under N_2. After complete solubilization of a $PbBr_2$ salt, the temperature was raised to 170°C and Cs-oleate solution (0.2 mL, 0.2 M in ODE, prepared as described above) was quickly injected and 5 s later the reaction mixture was cooled in an ice-water bath. The aggregated nanocubes were then separated by centrifuging at 10,000 rpm for 10 min.

Anion-Exchange Reaction

Anion-exchange Reaction could happen between Cl-Br, Br-Cl, Br-I, and I-Br, and the PbX_2 stock solution was the anion source. In a typical anion-exchange reaction, such as $CsPbBr_3$ to $CsPb(Br/I)_3$, the whole reaction process was performed at room temperature with a certain amount of purified $CsPbBr_3$ nanocubes dispersed in toluene, followed by the drop-wise addition of PbI_2 stock solution to the sample, and after about 3 min, the reaction was completed.

Preparation of Polystyrene (PS) Microspheres

The preparation of mono-disperse, highly cross-linked, and re-dispersible polystyrene microspheres was carried out by seed swelling method. A typical seed swelling process for the preparation of highly cross-linked polystyrene particles with the size of several micrometer involves the following steps: 0.3 g of polystyrene seed particles (400 nm) and 100 g of SDS (0.25 wt% for water) were added into a three-necked round-bottom flask and subjected to ultrasonic dispersion (about 30 min). Then, 1 g cyclohexane was ultrasonically dispersed with 50 g SDS (0.25 wt% for water), wherein the dispersion time here was also 30 min. The dispersion of cyclohexane was placed in the bottom and the swelling of polystyrene seed was carried out as the first step. The swelling temperature was 30°C and the swelling time

was 10 h. After the first step of swelling, the system that 10 g styrene monomer, 5 g crosslinking agent vinyl benzene (DVB), 0.3 g initiator benzoyl peroxide (BPO) were disperse by 100 g SDS solution (0.25 wt%) under ultrasonic conditions and the dispersion time was 60 min. Afterwards, the system was added into the flask to carry out the second seed-swelling at 30°C for 8 h. After performing the swelling twice, 80 g polyvinyl alcohol solution at a concentration of 2.5 wt% and 0.02 g $CuCl_2$ were added to the flask, and the temperature was increased to 85°C with a reaction time of 12 h. Finally, the obtained slurry was centrifuged at 5,000 rpm for 10 min, and washed with ethanol, followed by washing with water for three times. The product was dried at 50°C under vacuum for 24 h.

Preparation of the NCs-PS Particles

The polystyrene particle dispersions (3 mL, $1*10^{-11}$ mol) were added into a 15 mL centrifugation tube. After centrifugation, the upper supernatant was decanted and the particle sediment was dispersed using ethanol. This centrifugation/decanting/re-dispersion cycle was repeated for three times and then the polystyrene particles were transferred from water into ethanol. Following the same procedure, the polystyrene particles were subsequently transferred from ethanol into hexane, thereby yielding the PS particle dispersion in hexane. Next, the dispersions of the PS in hexane (10 mL) were mixed with the dispersions of perovskite NCs in toluene (1 mL, $2*10^{-8}$ mol). After stirring for 2 h, the NCs-PS particles were separated from the organic media by centrifugation. The NCs-PS sample was then purified three times by centrifugation and re-dispersed into water for characterization.

Photooxidation During UV Light Irradiation

The photooxidation measurements of the colloidal perovskite NCs solution and NCs-PSP solution were analyzed using two bottom-transparent, airtight, quartz colorimetric cuvettes. At periodic intervals, the PL spectra of the colloidal perovskite NCs solution and NCs-PSP solution were recorded after illuminating with 365 nm LED light (8 Watt, 3UV^{TM}-38 UV Lamp, China).

CHARACTERIZATIONS

TEM observations were made using a JEOL 100CX transmission electron microscope with an acceleration voltage of 200 kV. Carbon-coated copper grids were dipped in the hexane solutions to deposit the NCs onto the films. The luminescent quantum efficiency was determined using an integrating sphere (150 mm diameter, BaSO4 coating) from the Edinburg FLS920 phosphor meter. Quantum yield is defined as the integrated intensity of the luminescence signal divided by the integrated intensity of the absorption signal. Absorption intensity was calculated by subtracting the integrated intensity of the light source with the sample in the integrating sphere from that of the light source with a blank sample in the integrating sphere. Dynamic light scattering (DLS) measurements were performed (based on the number of particles) using a particle size analyzer (BI-90 Plus, Brookhaven Instruments) with a scattering angle of 90°. UV-visible spectra were recorded on an HP8453 UV-visible spectrophotometer. PL spectra were recorded on an Edinburgh FLS920 spectrophotometer. Thermogravimetric analysis (TGA) measurements were performed using Pyris (PerkinElmer, Inc). The sample was purified for further use by centrifugation (Shanghai Luxiangyi centrifuge instrument TG16-WS). The lead ions from water were measured by means of inductively coupled plasma atomic emission spectroscopy (ICP-AES, Thermo Elemental IRIS1000). It should be noted that the sample was purified three times by centrifugation and redispersion in water. The detection limit was 17.8 ng/mL in our experiment.

Thermogravimetric Analysis (TGA)

Thermogravimetric analysis (TGA) was used to detect the amount of $CsPbBr_3$ nanocubes in a PSP. After purification, the sample was dried in a vacuum oven overnight at 50°C under reduced pressure (30 in. Hg), and the resulting sample was then scanned from 100 to 700°C with a heating rate of 5°C/min under N_2 atmosphere (**Figure S12**). Total mass of the sample was 10.344 mg before TGA and the residual mass was 0.036 mg after TGA. Hence, we assume that the mass of $CsPbBr_3$ nanocubes was 0.036 mg and the mass of PSP was 10.308 mg. The calculation was performed as follows:

$$V\ total\ psp = \frac{m\ total\ psp}{\rho psp} \tag{S1}$$

$$V\ total\ NCs = \frac{m\ total\ NCs}{\rho NCs} \tag{S2}$$

In Equations S1, S2, ρ_{psp} is 1.05 g/cm^3 and ρ_{NCs} is 4.94 g/cm^3.

$$V\ psp = \frac{4}{3}\pi R_{psp}^3 \tag{S3}$$

$$V\ NCs = \frac{4}{3}\pi R_{NCs}^3 \tag{S4}$$

In Equations S3, S4, R_{psp} is 1 μm and R_{NCs} is 8.4 nm.

$$N\ PSP = \frac{V\ total\ PSP}{V_{PSP}} \tag{S5}$$

$$N\ NCs = \frac{V\ total\ NCs}{V_{NCs}} \tag{S6}$$

$$N = \frac{N\ NCs}{N_{PSP}} \tag{S7}$$

The Equations S5, S6 could be determined using Equations S1–S4. According to the Equation S7, we could calculate that there are nearly 640 $CsPbBr_3$ nanocubes in one PS particle by assuming no liangds in polystyrene particles and the organic stabilizing ligands 700°C. It should be noted that the final mass for pure PS particles was almost zero after 700°C (**Figure S13**). Therefore, the final mass should be attributed to the incorporated NCs in PS particles.

RESULTS AND DISCUSSION

In the present work, we established a stepwise solvent exchange methodology to incorporate the prepared perovskite NCs into PS latex particles directly (**Figure 1A** and Experimental details in **Supporting Information**). On the basis of our previous success in loading hydrophobic CdSe NCs into hydrogel beads (Bai et al., 2010), we first transferred the commercially available or prepared PS particles from water to the dispersions of lipophilic $CsPbX_3$ NCs on hexane, which is a poor solvent for PS, via solvent exchange with the aid of ethanol as the intermediate solvent. Second, we added a small volume of toluene to the resulting hexane dispersions to deliberately stimulate the PS particles to swell and thus imbibe the NCs into the PS matrices, thereby yielding $CsPbX_3$ NC-loaded PS particles. Third, we collected the resulting composite particles via centrifugation and directly dispersed them in water after consecutively decanting the hexane/toluene supernatants and removing the residual organic solvents via evaporation in air. **Figure 1B** shows that the composite particles, which were derived from 11 nm $CsPbBr_3$ NCs (**Figure S1**) embedded in 1 μm PS particles (**Figure S2**), could well disperse in water and show strong green emission under irradiation of a UV lamp. As shown in **Figure 1C**, the green fluorescence came from the composite particles rather than the surrounding media, which showed the successful confinement of the $CsPbBr_3$ NCs in the particles. The loading efficiency of NCs into the PS particles was roughly estimated by thermogravimetric analysis to be 640 particles in one PS particle (see Experimental section). Notably, calculating the quantum yield of loaded NC in particles was difficult due to strong scattering from absorption spectra of samples. The average sizes and size distribution of the resulting composite particles slightly changed after 5 days on the basis of dynamic light scattering analysis, thereby indicating good stability of the composite particles in water (**Figure S3**). The emission spectra of the $CsPbBr_3$ NC-loaded PS particles in water were almost identical to those of the original dispersions of the $CsPbBr_3$ NCs in toluene (**Figure 1C**), which indicated minimal change in the NC sizes after loading into the PS particles and transferring into water. **Figure 1D** shows the NC-loaded PS particles after careful size selection under UV irradiation. Notably, the large aggregation from the composite particles during the solvent exchange and storage was removed by centrifugation, although the green emission from large composite particles was still observable in water, as shown **Figure S4**. In the current work, the optimal hexane-to-toluene (H/T) volume ratio in the organic dispersions of $CsPbBr_3$ NC-loaded PS particle mixtures was found to be ~10:1, at which the PS particles properly swelled so they could efficiently imbibe the $CsPbBr_3$ NCs from the surrounding and simultaneously retain the structural integrity (**Figure S5**B). Otherwise, the PS particles incurred noticeable decomposition at low H/T volume ratio (pure toluene; **Figure S5A**) or almost no NCs were loaded into the PS particles at high H/T volume ratio (pure hexane; **Figure S5C**). After transfer of the composite particles from water back into pure toluene solvent to liberate the $CsPbBr_3$ NCs, the NC size and morphology were almost identical to those of the original ones (**Figure S6**). This result was additional proof that the NC structures remained intact during loading into the PS particles and the subsequent phase transfer to water.

The stability of 11 nm $CsPbBr_3$ NCs loaded in 1 μm PS particles in aqueous media was further assessed by monitoring the temporal evolution of the PL intensity of the composite particles at different pH values and in the presence of ethanol in water. **Figure 2** shows that the PL of the NC dispersions in toluene suffered from rapid and severe deterioration upon being carefully placed in water, which was significantly expedited

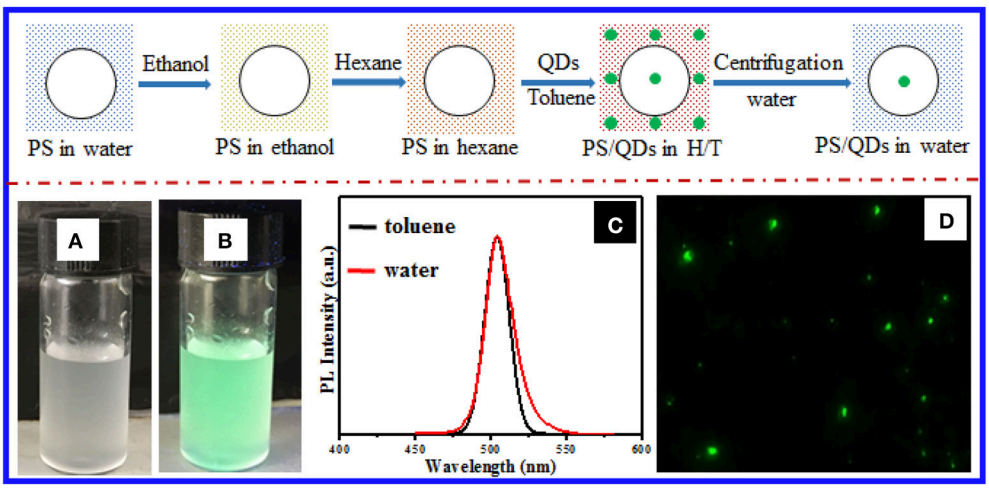

FIGURE 1 | (Top) Schematic of incorporating lipophilic perovskite NCs into the PS particles via solvent exchange, where the large circle represents the PS particles and the green dots signify the NCs. Photographs of the aqueous dispersions of composite particles bearing 11 nm $CsPbBr_3$ NCs loaded into 1 μm PS particles, shot **(A)** under sunlight and **(B)** UV irradiation (λ = 365 nm). **(C)** Emission spectra of the toluene dispersions of 11 nm $CsPbBr_3$ NCs (black curve) and the aqueous dispersions of the $CsPbBr_3$ NC-loaded PS composite particles. **(D)** Fluorescence micrograph of the $CsPbBr_3$ NC-loaded PS composite particles.

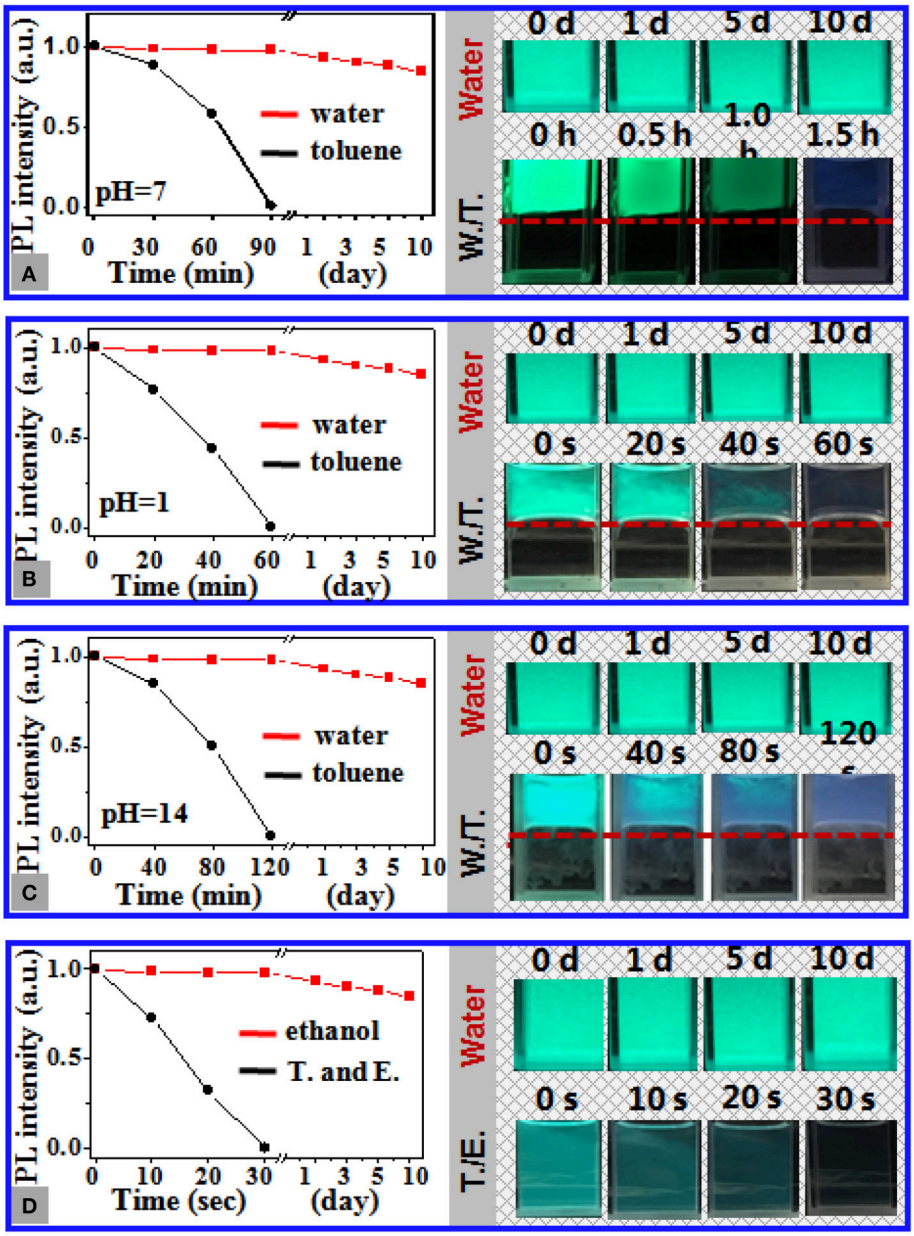

FIGURE 2 | (A–C) Temporal evolution of the PL intensity of the dispersions of 11 nm $CsPbBr_3$ NCs in toluene (black curves) and the aqueous dispersions of PS particles loaded with the same $CsPbBr_3$ NCs at pH of **(A)** 7, **(B)** 1, and **(C)** 14 (red curves). The insets show the photos of the aqueous dispersions of the NC-loaded PS composite particles during storage at the corresponding pH and those of the toluene dispersions of the NCs placed in water at the corresponding pH, in which the toluene/water interfaces are highlighted by the red dashed lines. **(D)** Temporal evolution of the PL intensity of the toluene dispersion of the $CsPbBr_3$ NCs (black curve) and the aqueous dispersions of the NC-loaded PS composite particles (red curve) in the presence of ethanol of the volume fraction of X vol. The photos of the corresponding dispersions are shown in the inset. The storage time is marked in the photos. The photos are shot under irradiation of UV light at 365 nm.

with the pH deviating from 7 or by adding ethanol into water (**Figures 2B-D**). The toluene dispersions of the NCs became slightly fluorescent after being in contact with neutral water (pH 7) for 1.5 h (**Figure 2A**). In contrast, minimal change in the PL of the NCs loaded in the PS particles was perceived after incubation of the composite particles in water for 10 days, regardless of the pH values and the presence of ethanol (**Figure S7**). The quantitative assessment revealed ∼15% reduction in the PL intensity of the aqueous dispersions of the composite particles after 10 days, which, however, showed slight dependence on the pH value and the presence of ethanol in water. The excellent chemical stability of the NCs loaded in the PS particles against water was further validated by the fact that lead ions were slightly detectable in the surrounding aqueous media of the

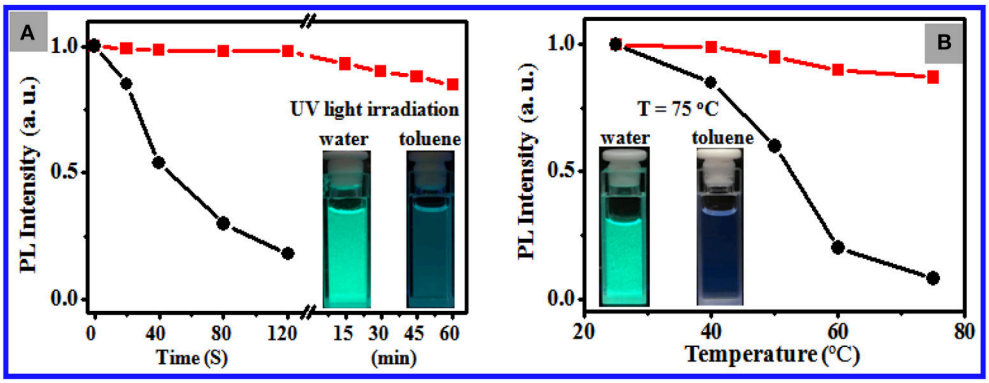

FIGURE 3 | (A) Temporal evolution of the PL intensity of the toluene dispersions of 11 nm $CsPbBr_3$ NCs (black curve) and the aqueous dispersion of the NC-loaded PS composite particles (red curve) under irradiation of light at 365 nm at a power of 8 W. The inset shows the photos of the corresponding composite particle dispersion in water after 30 min of irradiation (left panel) and the corresponding NC dispersions in toluene shot after 2 min of irradiation (right panel). **(B)** Plots of the PL intensity of the toluene dispersions of 11 nm $CsPbBr_3$ NCs (black curve) and the aqueous dispersion of the NC-loaded PS composite particles (red curve) vs. environmental temperature. The inset shows the photos of the corresponding composite particle dispersion in water (left panel) and the corresponding NC dispersions in toluene after being warmed up to 75°C.

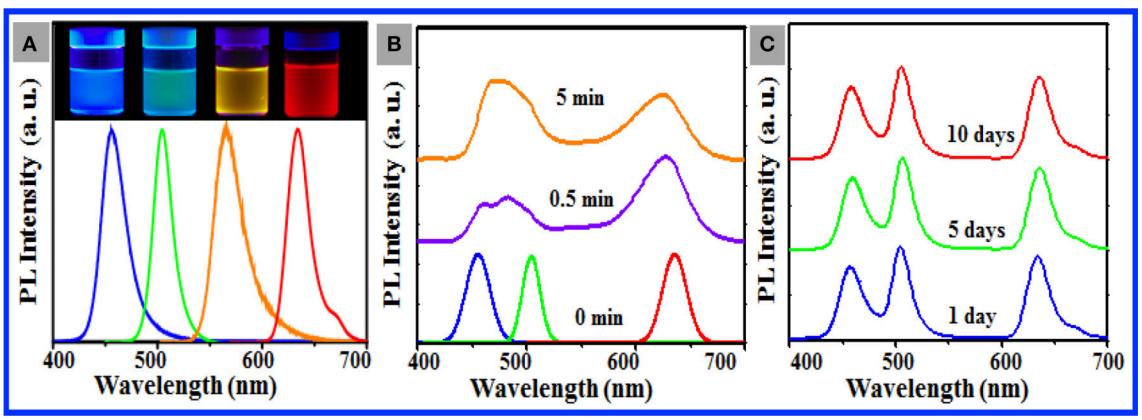

FIGURE 4 | (A) PL spectra of the aqueous dispersions of as-prepared composite particles consisting of 1 nm PS particles loaded with 10 nm $CsPb(Cl/Br)_3$ NCs (blue curve), 11 nm $CsPbBr_3$ NCs (green curve), 12 nm $CsPb(Br/I)_3$ NCs (orange curve), and 10 nm $CsPbI_3$ NCs (red curve). The photos of the corresponding dispersions shot under UV irradiation are shown in the inset. **(B)** PL spectra of the toluene dispersions of the ternary mixtures of $CsPb(Cl/Br)_3$ NCs, $CsPbBr_3$ NCs, and $CsPbI_3$ NCs recorded immediately after mixing for 30 s (purple curve) and incubated for 5 min under ambient condition (yellow line). For good comparison, the PL spectra (0 min) of these individual $CsPb(Cl/Br)_3$ NCs (blue curve), $CsPbBr_3$ NCs (green curve), and $CsPbI_3$ NCs (red curve) are shown in **(B)**. **(C)** PL spectra of the aqueous dispersions of the ternary mixtures of the composite particles comprising $CsPb(Cl/Br)_3$ NCs, $CsPbBr_3$ NCs, and $CsPbI_3$ NCs **(A)** during incubation under ambient condition for 1 day (blue curve), 5 days (green curve), and 10 days (red curve).

composite particles by means of inductively coupled atomic emission spectroscopy (**Table S1**).

Figure 3A shows that 2 min of exposure to strong UV light at 365 nm results in 95% reduction of PL intensity of 11 nm $CsPbBr_3$ NCs dispersed in toluene and ~6 nm blue shift as a result of photooxidation. By contrast, the NCs loaded in the PS particles retain 80% of their PL intensity after 30 min of irradiation, which indicated noticeably improved photostability (**Figure S8**). **Figure 3B** shows that the PL of the NCs dispersed in toluene significantly weakened with the increase in environmental temperature and was observed slightly at 75°C, whereas the NCs loaded in the PS particles in water maintained ~87% of the initial PL intensity at 75°C with minimal shift in emission position (**Figure S9**). Overall, these data endorse the excellent chemical and structural stability of the $CsPbBr_3$ NCs loaded in the PS particles in water against pH, temperature, light, and polar organic solvents.

Our stepwise solvent exchange methodology slightly depends on the nature of the target perovskite NCs, which enables us to load different $CsPbX_3$ NCs (**Figure S10**) into the PS particles [e.g., 10 nm $CsPb(Cl/Br)_3$ NCs with blue emission, 11 nm $CsPbBr_3$ NCs with green emission, 12 nm $CsPb(Br/I)_3$ NCs with yellow emission, and 12 nm $CsPbI_3$ NCs with red emission] to manufacture aqueous dispersions of various NC-loaded PS particles with single-emission colors (**Figure 4A**). The PL behavior of the resulting composite particles was fairly

comparable with that of the original NCs (**Figure S11**), whereas the slight NC aggregation in the PS particles may account for a tiny red shift of 1–2 nm observed for the composite particles and the appearance of a tiny emission shoulder at 650 nm for the $CsPbI_3$ NC-loaded particles (**Figure 4A**). As documented in the literature (Akkerman et al., 2015; Nedelcu et al., 2015), dynamic anion exchange occurs between perovskite NCs in multiple NC systems. This phenomenon is a serious technical shortcoming for the applicability of perovskite NCs in the field where multiple color display or luminescence is imperative. Our aforementioned success motivated us to intentionally mix the resulting composite particles loaded with 10 nm $CsPb(Cl/Br)_3$ NCs, 11 nm $CsPbBr_3$ NCs, and 12 nm $CsPbI_3$ NCs in water to test the anion exchange between the loaded NCs. **Figure 4B** shows noticeable broadening of the PL spectra of the ternary NC mixtures of the $CsPb(Cl/Br)_3$, $CsPbBr_3$, and $CsPbI_3$ NCs in toluene immediately upon mixing of these three QDs, with resulting noticeable spectral shifts of individual NCs. The PL spectra of the $CsPb(Cl/Br)_3$ and $CsPbBr_3$ NCs became slightly distinguishable after 5 min of incubation. In contrast, **Figure 4C** shows that after the three types of as-prepared composite particles were incubated in water for 5 days, the PL spectral profile of the individual particles remained slightly changed in the PL position and spectral profile, which indicated that minimal anion exchange occurred between the NCs loaded in the PS particles. This finding provides additional confirmation of the outstanding chemical stability of $CsPbX_3$ NCs loaded in PS particles in aqueous media. It should be noted that the lead toxicity raises concerns for the use of perovskites in many situations. To determine if lead escaped from the as-prepared sample (purified three times by centrifugation and redispersion) in water within 10 days, inductively coupled atomic emission spectroscopy (ICP-AES) was conducted. No lead ions in water could be observed for the sample washed three times, indicating that the polymers not only protect the perovskite NCs from the environment but also effectively protect the environment from the toxic lead.

In summary, we succeeded in manufacturing water-borne $CsPbX_3$ NC-embedded PS particles by directly incorporating prepared lipophilic perovskite NCs into the PS latex particles via solvent exchange with minimal alteration in the original structural and PL features of the NCs. Meanwhile, the hydrophilic surfaces of the PS host particles enabled excellent dispersion of the resulting composite particles in water. Their lipophilic dense interior matrices created excellent protection for vulnerable lipophilic perovskite NC guests against attack of acids, bases, and polar solvents, and also heat and light. This outstanding chemical and structural stability of the NCs loaded in the PS particles could minimize the release of toxic metallic ions (e.g., lead ions into aqueous media) and, more importantly, inhibit the anion exchange between the loaded NCs with different compositions to guarantee the color stability of the resulting composite particles. Overall, hydrophilic as-prepared perovskite NC-loaded PS particles would show promising prospects as innovative water-borne inks for printing of functional devices, such as wide color gamut LED backlight display. Furthermore, given that the present stepwise solvent exchange protocol is fairly trivial to operate and independent of the chemical nature of NC guests and latex hosts, it will enable us to adopt a broad spectrum of NCs and polymer particles to develop water-borne ink formulations in advanced inkjet printing.

AUTHOR CONTRIBUTIONS

KH, MZ, and LP contributed to the qunatum dots synthesis. BL, DL, and QM contributed to the PS particles and imaging of particles. RX, DW, and WY contributed to the idea and writing.

ACKNOWLEDGMENTS

This work was supported by the National Natural Science Foundation of China (21373097 and 51072067).

SUPPLEMENTARY MATERIAL

The Supplementary Material for this article can be found online at: https://www.frontiersin.org/articles/10.3389/fchem.2018.00453/full#supplementary-material

REFERENCES

Akkerman, Q. A., D'Innocenzo, V., Accornero, S., Scarpellini, A., Petrozza, A., Prato, M., et al. (2015). Tuning the optical properties of cesium lead halide perovskite nanocrystals by anion exchange reactions. *J. Am. Chem. Soc.* 137, 10276–10281. doi: 10.1021/jacs.5b05602

Amgar, D., Aharon, S., and Etgar, L. (2016). Inorganic and hybrid organo-metal perovskite nanostructures: synthesis, properties, and applications. *Adv. Funct. Mater.* 26, 8576–8593. doi: 10.1002/adfm.201603752

Bai, S., Nguyen, T. L., Mulvaney, P., and Wang, D. (2010). Using hydrogels to accommodate hydrophobic nanoparticles in aqueous media via solvent exchange. *Adv. Mater.* 22, 3247–3250. doi: 10.1002/adma.201000336

Carey, G. H., Abdelhady, A. L., Ning, Z., Thon, S. M., Bakr, O. M., and Sargent, E. H. (2015). Colloidal quantum dot solar cells. *Chem. Rev.* 115, 12732–12763. doi: 10.1021/acs.chemrev.5b00063

Dirin, D. N., Protesescu, L., Trummer, D., Kochetygov, I. V., Yakunin, S., Krumeich, F., et al. (2016). Harnessing defect-tolerance at the nanoscale: highly luminescent lead halide perovskite nanocrystals in mesoporous silica matrixes. *Nano Lett.* 16, 5866–5874. doi: 10.1021/acs.nanolett.6b02688

Frost, J. M., Butler, K. T., Brivio, F., Hendon, C. H., Schilfgaarde, M., and van Walsh, A. (2014). Atomistic origins of high-performance in hybrid halide perovskite solar cells. *Nano Lett.* 14, 2584–2590. doi: 10.1021/nl500390f

Hai, J., Li, H., Zhao, Y., Chen, F., Peng, Y., and Wang, B. (2017). Designing of blue, green, and red $CsPbX_3$ perovskite-codoped flexible films with water resistant property and elimination of anion-exchange for tunable white light emission. *Chem. Commun.* 53, 5400–5403. doi: 10.1039/C7CC01152K

Huang, H., Chen, B., Wang, Z., Hung, T. F., Susha, A. S., Zhong, H., et al. (2016a). Water resistant $CsPbX_3$ nanocrystals coated with polyhedral oligomeric silsesquioxane and their use as solid state luminophores in all-perovskite white light-emitting devices. *Chem. Sci.* 7, 5699–5703. doi: 10.1039/C6SC01758D

Huang, H., Lin, H., Kershaw, S. V., Susha, A. S., Choy, W. C., and Rogach, A. L. (2016b). Polyhedral oligomeric silsesquioxane enhances the brightness of perovskite nanocrystal-based green light-emitting devices. *J. Phys. Lett.* 7, 4398–4404. doi: 10.1021/acs.jpclett.6b02224

Huang, S., Li, Z., Kong, L., Zhu, N., Shan, A., and Li, L. (2016). Enhancing the stability of $CH_3NH_3PbBr_3$ quantum dots by embedding in silica spheres derived from tetramethyl orthosilicate in "waterless" toluene. *J. Am. Chem. Soc.* 138, 5749–5752. doi: 10.1021/jacs.5b13101

Jamieson, T., Bakhshi, R., Petrova, D., Pocock, R., Imani, M., and Seifalian, A. M. (2007). Biological applications of quantum dots. *Biomaterials* 28, 4717–4732. doi: 10.1016/j.biomaterials.2007.07.014

Kim, T. H., Lee, K. S., and Eun, E. K. (2011). Full-colour quantum dot displays fabricated by transfer printing. *Nat. Phot*. 5, 176–182. doi: 10.1038/nphoton.2011.12

Li, G., Rivarola, F. W., Davis, N. J., Bai, S., Jellicoe, T. C., and de la Peña, F., et al. (2016). Highly efficient perovskite nanocrystal light-emitting diodes enabled by a universal crosslinking method. *Adv. Mater.* 28, 3528–3534. doi: 10.1002/adma.201600064

Li, J., Xu, L., Wang, T., Song, J., Chen, J., Xue, J., et al. (2017). 50-Fold EQE improvement up to 6.27% of solution-processed all-inorganic perovskite $CsPbBr_3$ QLEDs via surface ligand density control. *Adv. Mater.* 29, 1603885–1603894. doi: 10.1002/adma.201603885

Li, X., Wu, Y., Zhang, S., Cai, B., Gu, Y., Song, J., et al. (2016). $CsPbX_3$ quantum dots for lighting and displays: room-temperature synthesis, photoluminescence superiorities, underlying origins and white light-emitting diodes. *Adv. Funct. Mater*. 26, 2435–2445. doi: 10.1002/adfm.201600109

Li, Z., Kong, L., Huang, S., and Li, L. (2017). Highly luminescent and ultrastable $CsPbBr_3$ perovskite quantum dots incorporated into a silica/alumina monolith. *Angew. Chem. Int. Ed.* 56, 8246–8250. doi: 10.1002/ange.201703264

Liang, J., Tong, K., and Pei, Q. (2016). A water-based silver-nanowire screen-print ink for the fabrication of stretchable conductors and wearable thin-film transistors. *Adv. Mater.* 28, 5986–5996. doi: 10.1002/adma.201600772

Ling, Y., Tian, Y., Wang, X., Wang, J. C., Knox, J. M., Perez-Orive, F., et al. (2016). Enhanced optical and electrical properties of polymer-assisted all-inorganic perovskites for light-emitting diodes. *Adv. Mater*. 28, 8983–8989. doi: 10.1002/adma.201602513

Liu, Z., Bekenstein, Y., Ye, X., Nguyen, S. C., Swabeck, J., Zhang, D. (2017). Ligand mediated transformation of cesium lead bromide perovskite nanocrystals to lead depleted Cs_4PbBr_6 nanocrystals. *J. Am. Chem. Soc.* 139, 5309–5312. doi: 10.1021/jacs.7b01409

Medintz, I. L., Uyeda, H. T., Goldman, E. R., and Mattoussi, H. (2005). Quantum dot bioconjugates for imaging, labelling and sensing. *Nat. Mater*. 4, 435–446. doi: 10.1038/nmat1390

Meyns, M., Perálvarez, M., Heuer-Jungemann, A., Hertog, W., Ibáñez, M., Nafria, R., et al. (2016). Polymer-enhanced stability of inorganic perovskite nanocrystals and their application in color conversion LEDs. *ACS Appl. Mater. Interfaces* 8, 19579–19586. doi: 10.1021/acsami.6b02529

Murray, C. B., Kagen, C. R., and Bawendi, M. G. (2000). Synthesis and characterization of monodisperse nanocrystals and close-packed nanocrystal assemblies. *Ann. Rev. Mater. Sci.* 30, 545–610. doi: 10.1146/annurev.matsci.30.1.545

Nedelcu, G., Protesescu, L., Yakunin, S., Bodnarchuk, M. I., Grotevent, M. J., and Kovalenko, M. V. (2015). Fast anion-exchange in highly luminescent nanocrystals of cesium lead halide perovskites ($CsPbX_3$, X = Cl, Br, I). *Nano Lett.* 15, 5635–5640. doi: 10.1021/acs.nanolett.5b02404

Palazon, F., Akkerman, Q. A., Prato, M., and Manna, L. (2016a). X-ray lithography on perovskite nanocrystals films: from patterning with anion-exchange reactions to enhanced stability in air and water. *ACS Nano* 10, 1224–1230. doi: 10.1021/acsnano.5b06536

Palazon, F., Di Stasio, F., Akkerman, Q. A., Krahne, R., Prato, M., and Mann, L. (2016b). Polymer-free films of inorganic halide perovskite nanocrystals as UV-to-white color-conversion layers in LEDs. *Chem. Mater.* 28, 2902–2906. doi: 10.1021/acs.chemmater.6b00954

Protesescu, L., Yakunin, S., Bodnarchuk, M. I., Krieg, F., Caputo, R., and Hendon, C. H., Et al. (2015). Nanocrystals of cesium lead halide perovskites ($CsPbX_3$, X= Cl, Br, and I): novel optoelectronic materials showing bright emission with wide color gamut. *Nano Lett*. 15, 3692–3696. doi: 10.1021/nl5048779

Rainò, G., Nedelcu, G., Protesescu, L., Bodnarchuk, M. I., Kovalenko, M. V., Mahrt, R. F., et al. (2016). Single cesium lead halide perovskite nanocrystals at low temperature: fast single-photon emission, reduced blinking, and exciton fine structure. *ACS Nano* 10, 2485–2490. doi: 10.1021/acsnano.5b07328

Raja, S. N., Bekenstein, Y., Koc, M. A., Fischer, S., Zhang, D., Lin, L., et al. (2016). Encapsulation of perovskite nanocrystals into macroscale polymer matrices: enhanced stability and polarization. *ACS Appl. Mater. Interfaces* 8, 35523–35533. doi: 10.1021/acsami.6b09443

Ramasamy, P., Lim, D. H., Kim, B., Lee, S. H., Lee, M. S., and Lee, J. S. (2016). All-inorganic cesium lead halide perovskite nanocrystals for photodetector applications. *Chem. Commun.* 52, 2067–2070. doi: 10.1039/C5CC08643D

Singh, M., Haverinen, H. M., Dhagat, P., and Jabbour, G. E. (2010). Inkjet printing-process and its applications. *Adv. Mater.* 22, 673–685. doi: 10.1002/adma.200901141

Sun, C., Zhang, Y., Ruan, C., Yin, C., Wang, X., Wang, Y., et al. (2016). Efficient and stable white LEDs with silica-coated inorganic perovskite quantum dots. *Adv. Mater*. 28, 10088–10094. doi: 10.1002/adma.201603081

Swarnkar, A., Chulliyil, R., Ravi, V. K., Irfanullah, M., Chowdhury, A., and Nag, A. (2015). Colloidal $CsPbBr_3$ perovskite nanocrystals: luminescence beyond traditional quantum dots. *Angew. Chem. Int. Ed.* 54, 15644–15648. doi: 10.1002/ange.201508276

Swarnkar, A., Marshall, A. R., Sanehira, E. M., Chernomordik, B. D., Moore, D. T., Christians, J. A., et al. (2016). Quantum dot–induced phase stabilization of α-$CsPbI_3$ perovskite for high-efficiency photovoltaics. *Science* 354, 92–95. doi: 10.1126/science.aag2700

Tong, Y., Bladt, E., Aygüler, M. F., Manzi, A., Milowska, K. Z., Hintermayr, V. A., et al. (2016). Highly luminescent cesium lead halide perovskite nanocrystals with tunable composition and thickness by ultrasonication. *Angew. Chem. Int. Ed.* 55, 13887–13892. doi: 10.1002/anie.201605909

Wang, H. C., Lin, S. Y., Tang, A. C., Singh, B. P., Tong, H. C., Chen, C. Y., et al. (2016a). Mesoporous silica particles integrated with all-inorganic $CsPbBr_3$ perovskite quantum-dot nanocomposites (MP-PQDs) with high stability and wide color gamut used for backlight display. *Angew. Chem., Int. Ed.* 55, 7924–7929. doi: 10.1002/anie.201603698

Wang, H. C., Lin, S. Y., Tang, A. C., Singh, B. P. Tong, H. C., Chen, C. Y., et al. (2016b). Enhancing the brightness of cesium lead halide perovskite nanocrystal based green light-emitting devices through the interface engineering with perfluorinated ionomer. *Angew. Chem. Int. Ed.* 55:7924.

Wang, J., Wang, C. F., and Chen, S. (2012). Amphiphilic egg-derived carbon dots: rapid plasma fabrication, pyrolysis process, and multicolor printing patterns. *Angew. Chem. Int. Ed.* 51, 9431–9435. doi: 10.1002/ange.201204381

Wang, Y., Li, X., Song, J., Xiao, L., Zeng, H., and Sun, H. (2015). All-inorganic colloidal perovskite quantum dots: a new class of lasing materials with favorable characteristics. *Adv. Mater*. 27, 7101–7108. doi: 10.1002/adma.201503573

Weller, H. (2003). Synthesis and self–assembly of colloidal nanoparticles. *Philos. Trans. R. Soc. Lond. A* 361, 229–240. doi: 10.1098/rsta.2002.1136

Xu, Y., Chen, Q., Zhang, C., Wang, R., Wu, H., Zhang, X., et al. (2016). Two-photon-pumped perovskite semiconductor nanocrystal lasers. *J. Am. Chem. Soc.* 138, 3761–3768. doi: 10.1021/jacs.5b12662

Zhang, X., Lin, H., Huang, H., Reckmeier, C., Zhang, Y., Choy, W. C., et al. (2016). Enhancing the brightness of cesium lead halide perovskite nanocrystal based green light-emitting devices through the interface engineering with perfluorinated ionomer. *Nano Lett*. 16, 1415–1420. doi: 10.1021/acs.nanolett.5b04959

Zhou, H., Yuan, S., Wang, X., Xu, T., Wang, X., Li, H., et al. (2017). Vapor growth and tunable lasing of band gap engineered cesium lead halide perovskite micro/nanorods with triangular cross section. *ACS Nano* 11, 1189–1195. doi: 10.1021/acsnano.6b07374

Conflict of Interest Statement: DL was employed by China Star Optoelectronics Technology Co. Ltd.

The remaining authors declare that the research was conducted in the absence of any commercial or financial relationships that could be construed as a potential conflict of interest.

The reviewer NG and handling Editor declared their shared affiliation.

frontiers in Chemistry

MINI REVIEW
published: 15 August 2018
doi: 10.3389/fchem.2018.00353

Challenges and Prospects of Photocatalytic Applications Utilizing Semiconductor Nanocrystals

Pavel Moroz[1,2], *Anthony Boddy*[3] *and Mikhail Zamkov*[1,2]*

[1] The Center for Photochemical Sciences, Bowling Green State University, Bowling Green, OH, United States, [2] Department of Physics and Astronomy, Bowling Green State University, Bowling Green, OH, United States, [3] Department of Biological Sciences, Bowling Green State University, Bowling Green, OH, United States

Photocatalytic systems based on colloidal semiconductor nanocrystals have gained considerable attention owing to potential benefits that include a visible-range light extinction and a low spatial overlap of photoinduced charges. When coupled to metal catalysts, nanocrystal sensitizers have demonstrated a compelling performance in homogenous photoreduction reactions, including the degradation of organic dyes and hydrogen generation. Going beyond half-cycle reactions, however, the progress in the field of nanocrystal photocatalysis has been rather limited. Here, we review some of the challenges associated with photocatalytic applications of colloidal semiconductor nanocrystals and highlight possible directions aimed toward their resolution. A particular emphasis was made on new paradigms in this field, including the possibility of harvesting triplet excitons and utilizing nanocrystal assemblies to accumulate multiple charges at the reaction site.

Keywords: photocatalysis, nanocrystals (NC), exciton dynamics, heterostructures, triplet sensitization

OPEN ACCESS

Edited by:
Maksym Yarema,
ETH Zürich, Switzerland

Reviewed by:
Adam Slabon,
RWTH Aachen Universität, Germany
Benjamin T. Diroll,
Argonne National Laboratory (DOE), United States

***Correspondence:**
Mikhail Zamkov
zamkovm@bgsu.edu

Specialty section:
This article was submitted to Nanoscience, a section of the journal Frontiers in Chemistry

Received: *12 June 2018*
Accepted: *25 July 2018*
Published: *15 August 2018*

Citation:
Moroz P, Boddy A and Zamkov M (2018) Challenges and Prospects of Photocatalytic Applications Utilizing Semiconductor Nanocrystals. Front. Chem. 6:353. doi: 10.3389/fchem.2018.00353

The prospect of employing colloidal semiconductor nanocrystals (NCs) in photocatalytic applications is inspired by unique advantages of quantum confined semiconductors over more traditional systems based on transition metal oxides (Schultz and Yoon, 2014) and precious metal coordination compounds (Concepcion et al., 2009). The benefit of inorganic nanocrystal catalysts lies in the combination of tunable redox energies and a large density of states across the visible spectrum, which gives rise to the energetic feasibility for overall water splitting (e.g., CdS, CdSe). While the photooxidation of water by semiconductor colloids has not yet been realized at a meaningful performance level, the photoreduction half-cycle reactions were shown to reach turnover numbers (TONs) in excess of 10^5, which was attributed to an efficient charge separation between the semiconductor domain and an appended metal catalyst [Ni (Simon et al., 2014; Chai et al., 2016), Pt (Bao et al., 2008; Berr et al., 2010), Pd (Raza et al., 2017), or Au (Costi et al., 2008)]. Such metal-semiconductor assemblies were also deemed cost effective as most semiconductor colloids contained no precious metals with several architectures featuring heavy metal-free compositions [$CuInS_2$ (Zhou et al., 2017), Cu_2ZnSnS_4 (Yu et al., 2014a), $CuIn_{1-x}Ga_xS_2$ (Yu et al., 2014b) NCs].

One of the early successful demonstrations of nanocrystal-based photocatalytic systems represents a heterostructured combination of a CdS nanocrystal sensitizer coupled to a Pt reduction co-catalyst. This architecture was shown to be up to 60% efficient in catalyzing the sacrificial reduction of protons (Costi et al., 2008; Zhou et al., 2017), and organic molecules (Brown et al., 2016; Jensen et al., 2016) under visible radiation ($\lambda \approx 450$ nm).

A compelling performance of the CdS/Pt assembly was attributed to the two key aspects of this hybrid architecture: (i) the fast removal of photocorrosive holes from the CdS domain (Acharya et al., 2011), aided by electron-donating surface ligands, and (ii) a significant driving force for the electron injection into the metal catalyst (Khon et al., 2011). Further increases in the proton reduction quantum yield were made possible by employing heterostructured CdSe/CdS and ZnSe/CdS nano-interfaces within the sensitizer component (Zhu et al., 2012; Kalisman et al., 2016), which allowed increasing the spatial extent of the photoinduced charge separation between hole-rich (CdSe, ZnSe) and electron-rich (Pt) domains (see **Figures 1a–c**; Hewa-Kasakarage et al., 2009; O'Connor et al., 2012; Kalisman et al., 2016).

While Pt remains to be the most efficient co-catalyst, other compounds have also been explored in combination with semiconductor colloids to drive sacrificial reduction reactions. For instance, Ni-based heterostructures comprising a CdS sensitizer have enabled up to 50% of the H_2 production internal efficiency (Simon et al., 2014; Zhukovskyi et al., 2015). Non-noble metal co-catalysts, including Ni_2P, Co_2P, FePt metal phosphides, and bimetallic compounds appended to CdS nanocrystals, have also been investigated as an alternative to Pt (Cao et al., 2014, 2015; Cheng et al., 2016). Regarding the sensitizer component, attempts to reduce the Cd content have led to its partial replacement by Cu in $Cu_{1.94}S$–$Zn_xCd_{1-x}S$ heteronanorods (Chen et al., 2016), or a complete removal of Cd in CZTS/Pt heterostructures (see **Figure 1e**). Photocatalytic applications of

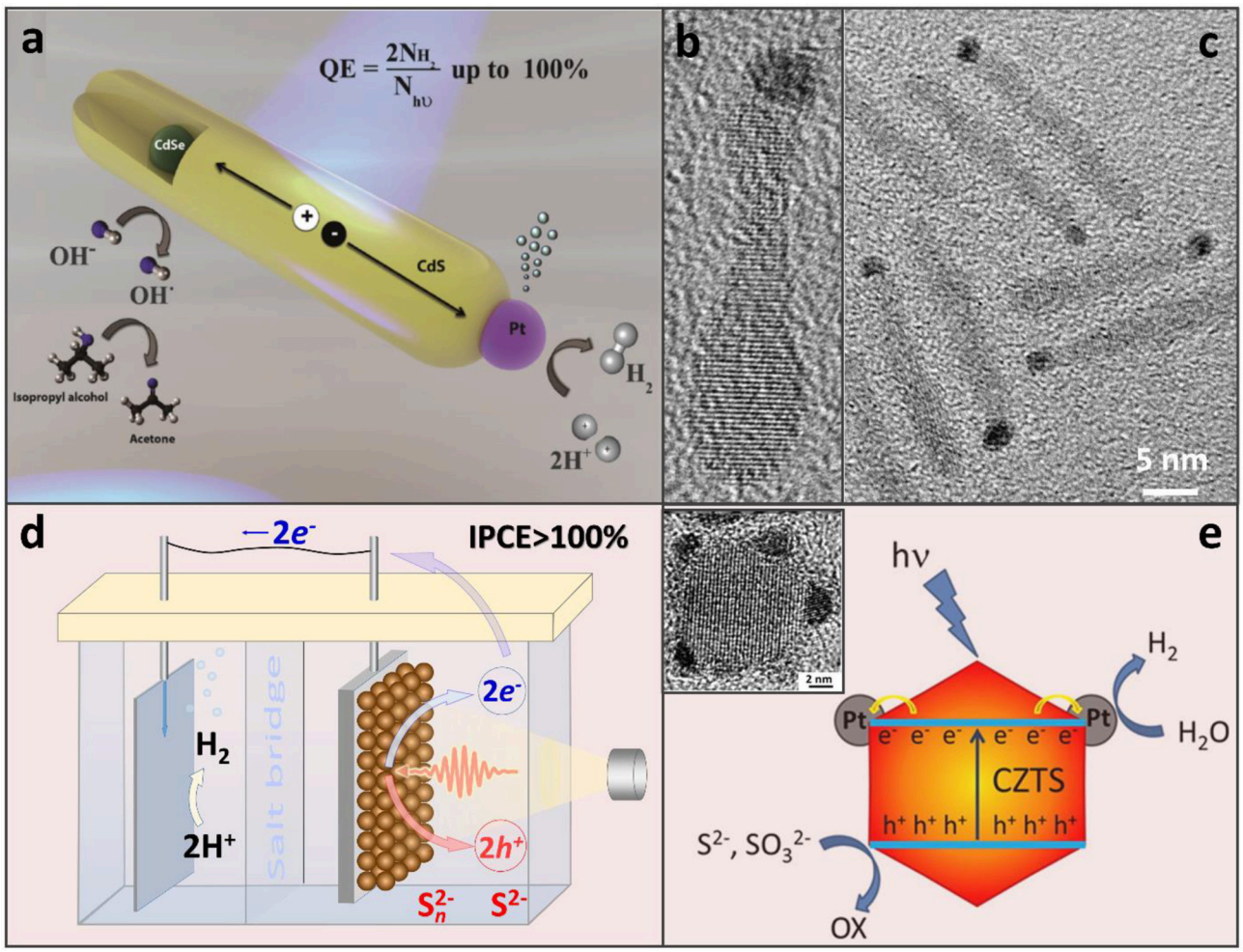

FIGURE 1 | (a) CdSe/CdS nanorods appended with a Pt co-catalyst that serves the role of an electron sink for the accumulation of photoinduced electrons at a single reductive site. Adapted with permission from Kalisman et al. (2016). Copyright 2016 American Chemical Society. **(b,c)** TEM images of CdSe/CdS nanorods selectively tipped with a Pt catalyst on one side. Based on the location of the CdSe bulb, Pt appears to grow on an opposite end. Adapted with permission from Khon et al. (2013). Copyright 2016 American Chemical Society. **(d)** Photoelectrochemical hydrogen evolution from aqueous Na_2S solution with over 100% of incident photon-to-current efficiency (IPCE). PbS NC-based active region of the working electrode (right, brown spheres) where one photon may be converted into two electron-hole pairs via MEG (Yang et al., 2014). Energized electrons are then transferred to the dark electrode (left) for H_2 production and sulfide ions are oxidized by the holes. **(d)** Illustration of the H_2 evolution on CZTS-Pt heterostructured nanoparticles in the presence of S^{2-} and SO_3^{2-} hole scavengers. Adapted with permission from Yu et al. (2014a).

semiconductor nanocrystal assemblies have been attempted as well (Warren et al., 2013; Yang et al., 2014). As an interesting example of an emerging paradigm, photoelectrodes comprising PbS semiconductor nanocrystal solids were shown to generate multiple photoinduced electrons-hole pairs from a single UV exciton, a phenomenon known as the multiple exciton generation (MEG) (Yan et al., 2017; Zamkov, 2017). A particular advantage of the MEG effect in photoelectrochemical cells over the same phenomenon in photovoltaic devices (Beard et al., 2013) was the reverse anode architecture that did not filter the excitation light through the oxide hole-blocking layer (Yan et al., 2017).

Many years of extensive research on photocatalytic applications of semiconductor nanocrystals has identified the key performance-limiting factors of these systems, most of which could be traced to the instability of inorganic semiconductors under catalytic conditions. Depending on a particular material, the catalytic performance of corresponding nanocrystals was shown to suffer from such issues as photocorrosion, a short excited state lifetime, poor colloidal stability in acidic solutions, or a limited ability to convey the photoinduced charges to active catalytic sites.

Photocorrosion of the semiconductor material due to the accumulation of photoinduced holes represents one of the most significant issues impeding photocatalytic applications of colloidal nanocrystals. Since chalcogenides are readily oxidized (Kamat et al., 2014), nanocrystal catalysts comprising CdS, CdSe, CZTS, or PbS semiconductors eventually undergo some degree of the chemical degradation, particularly when positive charges are not regenerated quickly. Even if the timely regeneration of holes is achieved via sacrificial agents, the photooxidizing energy could still be transferred to surface ligands triggering their desorption and the subsequent nanoparticle aggregation (Acharya et al., 2011; Hines and Kamat, 2014). For instance, commonly used mercaptopropionic (MPA) or mercaptoundecanoic (MUA) acids ligands are readily oxidized by scavenged holes resulting in the formation of disulfides. Consequently, these thiolates need to be continuously replaced in order to sustain the reduction half-cycle rate. One effective strategy is to use an abundant concentration of the scavenger moiety in solution (e.g., ascorbic acid) (Han et al., 2012) that quickly relieves the nanocrystal-ligand system of a positive charge.

Semiconductor photocorrosion could also be the result of defective surfaces that tend to localize positive charges at potential energy minima (Utterback et al., 2016). It was shown that holes diffuse through such defects by hopping, thus creating hot spots for chalcogenide oxidation and other side reactions. The localization of holes inside the nanocrystal sensitizer was also shown to reduce the ensuing catalytic activity due to a low sacrificial regeneration rate (Utterback et al., 2016). For instance, such a confinement of holes may be responsible for a relatively low photocatalytic activity of $CuInS_2$ NCs where these charges become trapped on Cu^+ ions within the lattice structure (Leach and Macdonald, 2016; Fuhr et al., 2017).

In addition to photocorrosion, the performance of nanocrystal-based photocatalytic systems could, in some cases, be limited by short lifetimes of singlet excitons. Indeed, homogenous systems utilizing organometallic dyes benefit from an effective way of storing the photon energy through a rapid intersystem crossing into a triplet state (McCusker and Castellano, 2016; Twilton et al., 2017), which lifetime can extend into hundreds of microseconds [e.g., the triplet state of $Ir(ppy)_3$] (Hofbeck and Yersin, 2010). The radiative lifetimes of singlet excitons in cadmium chalcogenide nanocrystals, on the other hand, are in the 10–100 ns range, which requires the dissociation of excitons on a faster time scale. In practice, the temporal window for a photoinduced charge transfer to a catalyst is even shorter due to competing pathways of non-radiative exciton dissociation at trap states, caused by the increased density of dangling bonds in aqueous environments.

The task of increasing excited state lifetimes of colloidal nanocrystals could be accomplished both by extending radiative lifetimes and reducing the density of charge-localizing trap states. In regard to the former condition, some groups have employed a heterojunction of the two semiconductor materials exhibiting a type II band edge alignment at the interface, which increases the spatial separation of photoinduced charges (Amirav and Alivisatos, 2010). The benefits of this strategy were demonstrated through the observation of a nearly 100% quantum yield (QY) for MV^{2+} photo reduction in Pt-tipped CdSe/CdS nanorods (Zhu et al., 2012) vs. a 60% QY observed for in Pt-tipped CdS structures (Bao et al., 2008). In addition to CdSe/CdS semiconductor combination, type II heterojunctions utilizing ZnSe/CdS (O'Connor et al., 2012) and $Cu_{1.94}S–Zn_x/Cd_{1-x}S$ (Chen et al., 2016) semiconductors have also been shown to enhance excited state lifetimes beyond those of single-phase nanocrystals. One potential issue with employing such type II interfaces in photocatalytic applications concerns the fact that one of the separated charges resides in the enclosed domain, which is shielded from the external environment by the other material (e.g., a core/shell or dot-in-a-rod geometry) (Perera et al., 2012). As a result, the confined carrier cannot be efficiently regenerated. In order to expose both semiconductor domains of a type II heterostructure to a redox environment, chemical etching could be employed. It was shown that etching of spatially-asymmetric CdSe/CdS nanorods results in the formation dimer-like structures where both donor and acceptor components are in direct contact with the external environment, resulting in the increased catalytic activity (Khon et al., 2013).

One emerging strategy for enhancing radiative lifetimes of excitons in nanocrystal-based photocatalytic systems relies on doping of semiconductors with transition metal ions. Lattice incorporated Mn^{2+} or Cu^+ can serve as hole trap sites promoting exciton localization in the bulk of the nanocrystal. In colloidal solutions, this strategy can allow extending excited state lifetimes into a microsecond range for Ag^+- and Cu^+-doped CdSe NCs (Kholmicheva et al., 2017; Nelson et al., 2017), or even a millisecond range for Mn^{2+}-doped ZnSe/ZnS core/shell (Pu et al., 2016) and CdS QDs (Knowles et al., 2015). The photocatalytic applications of doped semiconductor nanocrystals, however, have not yet been explored. A potentially adverse aspect of this architecture concerns the slow regeneration of photoinduced holes localized at dopant sites. Another possible strategy for increasing the nanocrystal excited state lifetime is based on reducing the density of surface traps.

The two approaches that were shown successful in this regard have employed either exciton-delocalizing ligands or a defect-passivating semiconductor shell (Grenland et al., 2017). The former strategy was recently demonstrated through the employment of hole-accepting ligand molecules that were covalently linked to nanocrystals *via* a thiolate binding group (Ding et al., 2015; Olshansky et al., 2015). By using ferrocene ligands with different alkyl chain lengths it was possible to find an optimal driving force for hole removal. As a result, existing surface traps could be mitigated without compromising the ability to extract photoinduced charges. Similarly, surface defects can be neutralized through the use of exciton delocalizing PZT ligands that were shown to scavenge holes on a picosecond to nanosecond time scale in CdS and CdSe NCs (Wu et al., 2015; Lian et al., 2016).

An important prerequisite of any photocatalytic system is the ability to accumulate photoinduced charges at an active site. This is particularly relevant in the case of multi-electron reactions where charges need to be collected onto a single catalytic domain. In regard to semiconductor sensitizers, this aspect was experimentally confirmed through the observation of a diminishing hydrogen production efficiency in Pt-decorated CdSe@CdS rods with the increasing number of appended Pt catalysts (Nakibli et al., 2015). In particular, nanorods tipped with a single Pt domain showed ∼1.6 times the efficiency for the H_2 production as compared to nanorods containing two Pt domains. This result was attributed to the competition of the two metal tips for photoinduced electrons absorbed by a shared semiconductor domain. The importance of funneling the absorbed energy to a catalytic site was also illustrated by an earlier study (Amirav and Alivisatos, 2010) showing an increased H_2 production rate by Pt-tipped CdS nanorods with an increasing CdS length.

The above mentioned benefits and drawbacks of nanocrystal-based photocatalytic systems, identified and investigated by the community over the course of many years, allow formulating design principles for the future development in this field. The key challenges to be addressed include the suppression of photocorrosion by photoinduced holes, the reduction of the trap states' effect, maintaining a suitable pH balance to prevent aggregation in acidic buffers, and funneling the excitation energy to an active reaction site (Aldana et al., 2005). Below we would like to discuss the design of the two emerging nanocrystal photocatalytic platforms that show strong potential for overcoming the aforementioned challenges. The first is based on a recently demonstrated ability of semiconductor nanocrystals to harvest triplet excitons through the Dexter energy transfer to coordination compounds exhibiting long-lived excited states. The second approach utilizes closed-coupled nanocrystal assemblies to funnel the absorbed energy to a catalytic site. Below we described the two paradigms in more detail.

The demonstrated ability of semiconductor nanocrystals to harvest triplet excitons (Mongin et al., 2016) offers new opportunities in light sensitization of photoinduced redox reactions (**Figure 2a**). By engaging in the Dexter energy transfer with molecular photoredox catalysts, such as $[Ru(bpy)_3]^{2+}$ or $Ir(ppy)_3$ coordination compounds (Arias-Rotondo and McCusker, 2016), nanocrystal energy could be transformed into a long lived state with minimal energy losses. While such energy transfer has been demonstrated for simple molecules, such as ruberene (Wu et al., 2016) or 9-anthracenecarboxylic acid (ACA) (Mongin et al., 2016), sensitizations of triplet excited states of photoredox coordination compounds is imminent. Of a particular interest are metal polypyridyl complexes, which exhibit excellent oxidizing and reducing properties. For instance photoexcited $[Ru(bpy)_3]^{3+}$ can oxidize water into O_2 and protons *via* a metal oxide catalyst (Hara et al., 2000), while, $[Ru(bpy)_3]^{2+*}$ triplet states can be utilized for reducing methylviologen (via ligands), a recyclable carrier of electrons.

Employing semiconductor nanocrystals as triplet sensitizers of photoredox coordination compounds would allow avoiding many aforementioned issues of nanocrystal photocatalytic materials related to photocorrosion, hole regeneration, and

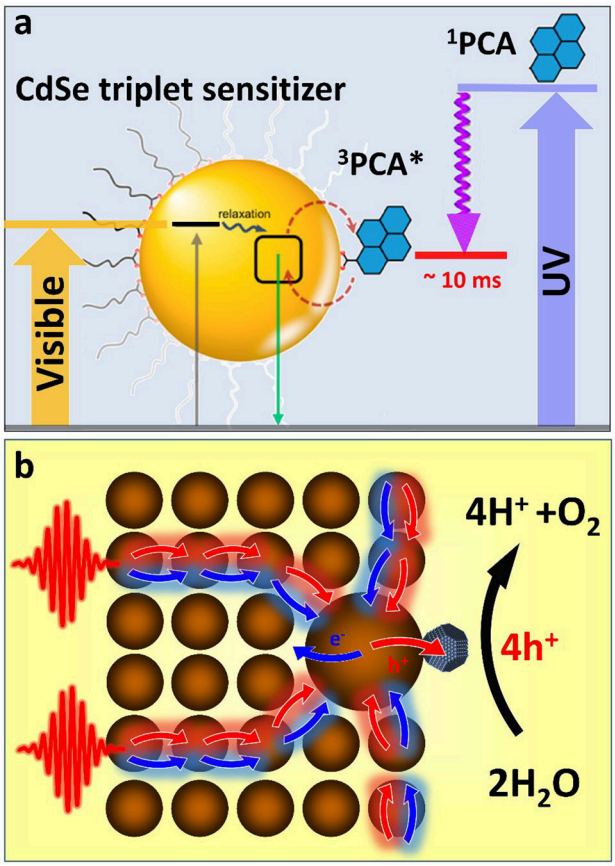

FIGURE 2 | (a) Triplet sensitization of 1-pyrenecarboxylic acid (PCA) molecular acceptor by CdSe NCs via photoinduced triplet–triplet energy transfer (TTET). Close to 90% of photons absorbed by the semiconductor QD could be stored in form of long-lived triplet states of ^{3}PCA*. The associated exciton energy loss resulting from TTET is less than 20%, which compares favorably with a >50% energy loss accompanying ^{1}PCA→ ^{3}PCA intersystem crossing. Adapted with permission from Garakyaraghi and Castellano (2018). Copyright 2016 American Chemical Society. **(b)** A proposed scheme for funneling the photoinduced energy in assemblies of semiconductor nanocrystals via the diffusion toward the low-energy gap reaction center. This strategy benefits multi-electron catalytic processes by increasing the probability of multiple charges to be collected on the same catalytic site.

short singlet lifetime. On the other hand, coupling nanocrystal sensitizers to organometallic catalysts will extend the usable portion of the solar spectrum into the visible range. This is because the excitation of a triplet state undergoes *via* a photon absorption into a singlet metal-ligand charge transfer state (^{1}MLCT) followed by a rapid intersystem crossing to a ^{3}MLCT state, which is commonly accompanied by an ∼1 eV energy loss (due to large splitting of singlet and triplet states). Since such singlet-triplet splitting in semiconductor nanocrystals is usually much smaller (within thermal kT ∼ 30 meV), the associated energy loss will be reduced. Furthermore, a molar absorptivity of CdSe at 400–450 nm is 20 times greater (Yu et al., 2003) than that of the ^{1}MLCT transition in $[Ru(bpy)_3]^{2+}$ (∼13,000 M^{-1} cm^{-1}in acetonitrile). Considering that the efficiency of triplet exciton transfer from CdSe to organic acceptors, such as ACA is over 90% (Mongin et al., 2016), there is an expected benefit in employing semiconductor nanocrystals for sensitizing redox reactions.

Like any excitonic system, an assembly of semiconductor nanocrystals can be designed to transfer the photoinduced energy from the excitation site toward the potential energy minima through the process of exciton diffusion. Such funneling of the photoinduced energy is often utilized by biological systems as a mechanism to drive multiple carriers to the reaction center where multielectron catalytic reactions can subsequently take place. For instance during the oxygenic photosynthesis in plants, light is absorbed by hundreds of pigments (e.g., chlorophylls) that transfer the photoinduced energy to a small number of special pigments (P680), which are capable of charge separation (Blankenship, 2013). P680 will then share a photoinduced hole with a water-oxidizing complex (WOC) (Najafpour et al., 2017). After four oxidizing equivalents have been stored at the WOC site, it obtains four electrons from water molecules causing H_2O splitting. We expect that nanocrystal assemblies could be employed in a similar manner in order to drive multielectron catalytic processes, such as water oxidation or hydrogen production. For instance, the diffusion of excitons in a nanocrystal solid to a nanoparticle with the smallest band gap (Kholmicheva et al., 2015) (an equivalent of the P680 pigment in PSII) can be used to collect multiple excitons in the same spot. The accepting dot could be appended with a catalyst that would assist the charge separation to store photoinduced charges. The presence of an electron- (or hole-) accepting catalysis would also allow avoiding the multiexciton populations on a single nanocrystal, which are subject to a rapid decay through Auger recombination. Such nanocrystal assembly could be incorporated into a photoelectrochemical cell (see **Figure 1d**) or even harnessed within an "artificial leaf" platform (Liu et al., 2016). The key advantage of this architecture lies in the sequential collection of multiple charges within the same catalytic complex (**Figure 2b**). Zero-dimensional nanocrystals in these assemblies could be substituted with either one- or two-dimensional nanostructures in order to increase the energy transfer efficiency and reduce Auger recombination rates. Notably, without such an energy "antenna," nanocrystal-based water splitting systems would exhibit very low efficiencies (Kalisman et al., 2015) even when designed with a robust corrosion suppression mechanism.

In summary, the prospect of employing semiconductor nanocrystals in photocatalysis offers a number of unique benefits related to a spatially-extended charge separation and visible-range light absorption, which have been confirmed through a compelling performance in reduction half-reactions. In order for such systems to become practical, however, additional challenges need to be resolved. These pertain to the semiconductor photocorrosion, short excited state lifetimes, and poor control over energy transfer to catalytic sites. To resolve these issues, several emerging strategies have been proposed and discussed. Among potential solutions, harnessing nanocrystals as triplet sensitizers of photoredox coordination compounds is expected to enhance the absorption characteristics of the latter while decreasing the damage of the semiconductor. Assemblies of inorganic colloids can also be used for funneling the photoinduced energy to reactive sites in a manner analogs to the action of chlorophylls in PSII. This geometry could inspire a cascade like design of photosynthetic assemblies for water oxidation.

AUTHOR CONTRIBUTIONS

All authors have contributed equally to preparing the review article.

ACKNOWLEDGMENTS

We gratefully acknowledge OBOR Material Networks program and NSF Award CHE-1465052 for financial support.

REFERENCES

Acharya, K. P., Khnayzer, R. S., O'Connor, T., Diederich, G., Kirsanova, M., Klinkova, A., et al. (2011). The role of hole localization in sacrificial hydrogen production by semiconductor–metal heterostructured nanocrystals. *Nano Lett.* 11, 2919–2926. doi: 10.1021/nl201388c

Aldana, J., Lavelle, N., Wang, Y., and Peng, X. (2005). Size-dependent dissociation pH of thiolate ligands from cadmium chalcogenide nanocrystals. *J. Am. Chem. Soc.* 127, 2496–2504. doi: 10.1021/ja047000+

Amirav, L., and Alivisatos, A. P. (2010). Photocatalytic hydrogen production with tunable nanorod heterostructures. *J. Phys. Chem. Lett.* 1, 1051–1054. doi: 10.1021/jz100075c

Arias-Rotondo, D. M., and McCusker, J. K. (2016). The photophysics of photoredox catalysis: a roadmap for catalyst design. *Chem. Soc. Rev.* 45, 5803–5820. doi: 10.1039/C6CS00526H

Bao, N., Shen, L., Takata, T., and Domen, K. (2008). Self-templated synthesis of nanoporous CdS nanostructures for highly efficient photocatalytic hydrogen production under visible light. *Chem. Mater.* 20, 110–117. doi: 10.1021/cm7029344

Beard, M. C., Luther, J. M., Semonin, O. E., and Nozik, A. J. (2013). Third generation photovoltaics based on multiple exciton generation in quantum confined semiconductors. *Acc. Chem. Res.* 46, 1252–1260. doi: 10.1021/ar3001958

Berr, M., Vaneski, A., Susha, A. S., Rodríguez-Fernández, J., Döblinger, M., Jäckel, F., et al. (2010). Colloidal CdS nanorods decorated with subnanometer sized

Pt clusters for photocatalytic hydrogen generation. *Appl. Phys. Lett.* 97:093108. doi: 10.1063/1.3480613

Blankenship, R. E. (2013). *Molecular Mechanisms of Photosynthesis*. Malden, MA; Oxford: Blackwell Science.

Brown, K. A., Harris, D. F., Wilker, M. B., Rasmussen, A., Khadka, N., Hamby, H., et al. (2016). Light-driven dinitrogen reduction catalyzed by a CdS:nitrogenase MoFe protein biohybrid. *Science* 352, 448–450. doi: 10.1126/science.aaf2091

Cao, S., Chen, Y., Hou, C. C., Lv, X. J., and Fu, W. F. (2015). Cobalt phosphide as a highly active non-precious metal cocatalyst for photocatalytic hydrogen production under visible light irradiation. *J. Mater. Chem. A* 3:6096–6101. doi: 10.1039/C4TA07149B

Cao, S., Chen, Y., Wang, C. J., He, P., and Fu, W. F. (2014). Highly efficient photocatalytic hydrogen evolution by nickel phosphide nanoparticles from aqueous solution. *Chem. Commun.* 50, 10427–10429. doi: 10.1039/C4CC05026F

Chai, Z., Zeng, T. T., Li, Q., Lu, L. Q., Xiao, W. J., and Xu, D. (2016). Efficient visible light-driven splitting of alcohols into hydrogen and corresponding carbonyl compounds over a Ni-modified CdS photocatalyst. *J. Am. Chem. Soc.* 138, 10128–10131. doi: 10.1021/jacs.6b06860

Chen, Y., Zhao, S., Wang, X., Peng, Q., Lin, R., Wang, Y., et al. (2016). Synergetic integration of $Cu_{1.94}S$–$Zn_xCd_{1-x}S$ heteronanorods for enhanced visible-light-driven photocatalytic hydrogen production. *J. Am. Chem. Soc.* 138, 4286–4289. doi: 10.1021/jacs.5b12666

Cheng, H., Lv, X. J., Cao, S., Zhao, Z. Y., Chen, Y., and Fu, W. F. (2016). Robustly photogenerating H_2 in water using FeP/CdS catalyst under solar irradiation. *Sci. Rep.* 6:19846. doi: 10.1038/srep19846

Concepcion, J. J., Jurss, J. W., Brennaman, M. K., Hoertz, P. G., Patrocinio, A. O., Iha, N. Y. M., et al. (2009). Making oxygen with ruthenium complexes. *Acc. Chem. Res.* 42, 1954–1965. doi: 10.1021/ar9001526

Costi, R., Saunders, A. E., Elmalem, E., Salant, A., and Banin, U. (2008). Visible light-induced charge retention and photocatalysis with hybrid CdSe–Au nanodumbbells. *Nano Lett.* 8, 637–641. doi: 10.1021/nl0730514

Ding, T. X., Olshansky, J. H., Leone, S. R., and Alivisatos, A. P. (2015). Efficiency of hole transfer from photoexcited quantum dots to covalently linked molecular species. *J. Am. Chem. Soc.* 137, 2021–2029. doi: 10.1021/ja512278a

Fuhr, A. S., Yun, H. J., Makarov, N. S., Li, H., McDaniel, H., and Klimov, V. I. (2017). Light emission mechanisms in $CuInS_2$ quantum dots evaluated by spectral electrochemistry. *ACS Photonics* 4, 2425–2435. doi: 10.1021/acsphotonics.7b00560

Garakyaraghi, S., and Castellano, F. N. (2018). Nanocrystals for triplet sensitization: molecular behavior from quantum-confined materials. *Inorg. Chem.* 57, 2351–2359. doi: 10.1021/acs.inorgchem.7b03219

Grenland, J. J., Maddux, C. J. A., Kelley, D. F., and Kelley, A. M. (2017). Charge trapping versus exciton delocalization in CdSe quantum dots. *J. Phys. Chem. Lett.* 8, 5113–5118. doi: 10.1021/acs.jpclett.7b02242

Han, Z., Qiu, F., Eisenberg, R., Holland, P. L., and Krauss, T. D. (2012). Robust photogeneration of H_2 in water using semiconductor nanocrystals and a nickel catalyst. *Science* 338, 1321–1324. doi: 10.1126/science.1227775

Hara, M., Waraksa, C. C., Lean, J. T., Lewis, B. A., and Mallouk, T. E. (2000). Photocatalytic water oxidation in a buffered tris(2,2'-bipyridyl)ruthenium complex-colloidal IrO_2 system. *J. Phys. Chem. A* 104, 5275–5280. doi: 10.1021/jp000321x

Hewa-Kasakarage, N. N., Kirsanova, M., Nemchinov, A., Schmall, N., El-Khoury, P. Z., Tarnovsky, A. N., et al. (2009). Radiative recombination of spatially extended excitons in (ZnSe/CdS)/CdS heterostructured nanorods. *J. Am. Chem. Soc.* 131, 1328–1334. doi: 10.1021/ja8082895

Hines, D. A., and Kamat, P. V. (2014). Recent advances in quantum dot surface chemistry. *ACS Appl. Mater. Interfaces* 6, 3041–3057. doi: 10.1021/am405196u

Hofbeck, T., and Yersin, H. (2010). The triplet state of fac-Ir$(ppy)_3$. *Inorg. Chem.* 49, 9290–9299. doi: 10.1021/ic100872w

Jensen, S. C., Bettis Homan, S., and Weiss, E. A. (2016). Photocatalytic conversion of nitrobenzene to aniline through sequential proton-coupled one-electron transfers from a cadmium sulfide quantum dot. *J. Am. Chem. Soc.* 138, 1591–1600. doi: 10.1021/jacs.5b11353

Kalisman, P., Kauffmann, Y., and Amirav, L. (2015). Photochemical oxidation on nanorod photocatalysts. *J. Mater. Chem. A* 7, 3261–3265. doi: 10.1039/C4TA06164K

Kalisman, P., Nakibli, Y., and Amirav, L. (2016). Perfect photon-to- hydrogen conversion efficiency. *Nano Lett.* 16, 1776–1781. doi: 10.1021/acs.nanolett.5b04813

Kamat, P. V., Christians, J. A., and Radich, J. G. (2014). Quantum dot solar cells: hole transfer as a limiting factor in boosting the photoconversion efficiency. *Langmuir* 30, 5716–5725. doi: 10.1021/la500555w

Kholmicheva, N., Moroz, P., Bastola, E., Razgoniaeva, N., Bocanegra, J., Shaughnessy, M., et al. (2015). Mapping the exciton diffusion in semiconductor nanocrystal solids. *ACS Nano* 9, 2926–2937. doi: 10.1021/nn507322y

Kholmicheva, N., Razgoniaeva, N., Yadav, P., Lahey, A., Erickson, C., Moroz, P., et al. (2017). Enhanced emission of nanocrystal solids featuring slowly diffusive excitons. *J. Phys. Chem. C* 121, 1477–1487. doi: 10.1021/acs.jpcc.6b10994

Khon, E., Lambright, K., Khnayzer, R. S., Moroz, P., Perera, D. N., Butaeva, E., et al. (2013). Improving the catalytic activity of semiconductor nanocrystals through selective domain etching. *Nano Lett.* 13, 2016–2023. doi: 10.1021/nl400715n

Khon, E., Mereshchenko, A., Tarnovsky, A. N., Acharya, K., Klinkova, A., Hewa-Kasakarage, N. N., et al. (2011). Suppression of the plasmon resonance in Au/CdS colloidal nanocomposites. *Nano Lett.* 11, 1792–1799. doi: 10.1021/nl200409x

Knowles, K. E., Nelson, H. D., Kilburn, T. B., and Gamelin, D. R. (2015). Singlet–triplet splittings in the luminescent excited states of colloidal Cu^+:CdSe, Cu^+:InP, and $CuInS_2$ nanocrystals: charge transfer configurations and self-trapped excitons. *J. Am. Chem. Soc.* 137, 13138–13147. doi: 10.1021/jacs.5b08547

Leach, A. D. P., and Macdonald, J. E. (2016). Optoelectronic properties of $CuInS_2$ nanocrystals and their origin. *J. Phys. Chem. Lett.* 7, 572–583. doi: 10.1021/acs.jpclett.5b02211

Lian, S., Weinberg, D. J., Harris, R. D., Mohamad, S., Kodaimati, M. S., and Weiss, E. A. (2016). Subpicosecond photoinduced hole transfer from a CdS quantum dot to a molecular acceptor bound through an exciton-delocalizing ligand. *ACS Nano* 10, 6372–6382. doi: 10.1021/acsnano.6b02814

Liu, C., Colon, B. C., Ziesack, M., Silver, P. A., and Nocera, D. G. (2016). Water splitting–biosynthetic system with CO_2 reduction efficiencies exceeding photosynthesis. *Science* 352, 1210–1213. doi: 10.1126/science.aaf5039

McCusker, C. E., and Castellano, F. N. (2016). Materials integrating photochemical upconversion. *Top. Curr. Chem.* 374, 1–25. doi: 10.1007/s41061-016-0021-7

Mongin, C., Garakyaraghi, S., Razgoniaeva, N., Zamkov, M., and Castellano, F. N. (2016). Direct observation of triplet energy transfer from semiconductor nanocrystals. *Science* 351, 369–372. doi: 10.1126/science.aad6378

Najafpour, M. M., Heidari, S., Balaghi, S. E., Hołynska, M., Sadr, M. H., Soltani, B., et al. (2017). Proposed mechanisms for water oxidation by Photosystem II and nanosized manganese oxides. *Biochim. Biophys. Acta Bioenerg.* 1858, 156–174. doi: 10.1016/j.bbabio.2016.11.007

Nakibli, Y., Kalisman, P., and Amirav, L. (2015). Less is more: the case of metal cocatalysts. *J. Phys. Chem. Lett.* 6, 2265–2268. doi: 10.1021/acs.jpclett.5b00872

Nelson, H. D., Hinterding, S. O. M., Fainblat, R., Creutz, S. E., Li, X., and Gamelin, D. R. (2017). Mid-gap states and normal vs inverted bonding in luminescent Cu^+- and Ag^+-doped CdSe nanocrystals. *J. Am. Chem. Soc.* 139, 6411–6421. doi: 10.1021/jacs.7b01924

O'Connor, T., Panov, M. S., Mereshchenko, A., Tarnovsky, A. N., Lorek, R., Perera, D., et al. (2012). The effect of the charge-separating interface on exciton dynamics in photocatalytic colloidal heteronanocrystals. *ACS Nano* 6, 8156–8165. doi: 10.1021/nn302810y

Olshansky, J. H., Ding, T. X., Lee, Y. V., Leone, S. R., and Alivisatos, A. P. (2015). Hole transfer from photoexcited quantum dots: the relationship between driving force and rate. *J. Am. Chem. Soc.* 137, 15567–15575. doi: 10.1021/jacs.5b10856

Perera, D., Lorek, R., Khnayzer, R. S., Moroz, P., O'Connor, T., Khon, D., et al. (2012). Photocatalytic activity of core/shell semiconductor nanocrystals featuring spatial separation of charges. *J. Phys. Chem. C* 116, 22786–22793. doi: 10.1021/jp308921s

Pu, C., Ma, J., Qin, H., Yan, M., Fu, T., Niu, Y., et al. (2016). Doped semiconductor-nanocrystal emitters with optimal photoluminescence decay dynamics in microsecond to millisecond range: synthesis and applications. *ACS Cent. Sci.* 2, 32–39. doi: 10.1021/acscentsci.5b00327

Raza, F., Yim, D., Park, J. H., Kim, H. I., Jeon, S. J., and Kim, J. H. (2017). Structuring Pd nanoparticles on 2H-WS2 nanosheets induces excellent

photocatalytic activity for cross-coupling reactions under visible light. *J. Am. Chem. Soc.* 139, 14767–14774. doi: 10.1021/jacs.7b08619

Schultz, D. M., and Yoon, T. P. (2014). Solar synthesis: prospects in visible light photocatalysis. *Science* 343:1239176. doi: 10.1126/science.1239176

Simon, T., Bouchonville, N., Berr, M. J., Vaneski, A., Adrović, A., and Volbers, D., et al. (2014). Redox shuttle mechanism enhances photocatalytic H2 generation on Ni-decorated CdS nanorods. *Nat. Mater* 13, 1013–1018. doi: 10.1038/nmat4049

Twilton, J., Le, C., Zhang, P., Shaw, M. H., Evans, R. W., and MacMillan, D. W. C. (2017). The merger of transition metal and photocatalysis. *Nat. Rev. Chem.* 1:0052. doi: 10.1038/s41570-017-0052

Utterback, J. K., Grennell, A. N., Wilker, M. B., Pearce, O., Eaves, J. D., and Dukovic, G. (2016). Observation of trapped-hole diffusion on the surfaces of CdS nanorods. *Nat. Chem.* 8, 1061–1066. doi: 10.1038/nchem.2566

Warren, S. C., Voïtchovsky, K., Dotan, H., Leroy, C. M., Cornuz, M., Stellacci, F., et al. (2013). Identifying champion nanostructures for solar water-splitting. *Nat. Mater.* 12, 842–849. doi: 10.1038/nmat3684

Wu, K., Du, Y., Tang, H., Chen, Z., and Lian, T. (2015). Efficient extraction of trapped holes from colloidal CdS nanorods. *J. Am. Chem. Soc.* 137, 10224–10230. doi: 10.1021/jacs.5b04564

Wu, M., Congreve, D. N., Wilson, M. W. B., Jean, J., Geva, N., Welborn, M., et al. (2016). Solid-state infrared-to-visible upconversion sensitized by colloidal nanocrystals. *Nat. Photon.* 10, 31–34. doi: 10.1038/nphoton.2015.226

Yan, Y., Crisp, R., Gu, J., Chernomordik, B., Pach, G., Marshall, A., et al. (2017). Multiple exciton generation for photoelectrochemical hydrogen evolution reactions with quantum yields exceeding 100%. *Nat. Energy* 2:17052. doi: 10.1038/nenergy.2017.52

Yang, H. B., Miao, J., Hung, S. F., Huo, F., Chen, H. M., and Liu, B. (2014). Stable quantum dot photoelectrolysis cell for unassisted visible light solar water splitting. *ACS Nano* 8, 10403–10413. doi: 10.1021/nn503751s

Yu, W. W., Qu, L., Guo, W., and Peng, X. (2003). Experimental determination of the extinction coefficient of CdTe, CdSe, and CdS nanocrystals. *Chem. Mater.* 15, 854–2860. doi: 10.1021/cm034081k

Yu, X., An, X., Shavel, A., Ibáñez, M., and Cabot, A. (2014b). The effect of the Ga content on the photocatalytic hydrogen evolution of $CuIn_{1-x}Ga_xS_2$ nanocrystals. *J. Mater. Chem. A* 2, 12317–12322. doi: 10.1039/C4TA01315H

Yu, X., Shavel, A., An, X., Luo, Z., Ibáñez, M., and Cabot, A. (2014a). Cu_2ZnSnS_4-Pt and Cu_2ZnSnS_4-Au heterostructured nanoparticles for photocatalytic water splitting and pollutant degradation. *J. Am. Chem. Soc.* 136, 9236–9239. doi: 10.1021/ja502076b

Zamkov, M. (2017). Solar hydrogen generation: exceeding 100% efficiency. *Nat. Energy* 2:17072. doi: 10.1038/nenergy.2017.72

Zhou, Y., Hu, W., Ludwig, J., and Huang, J. (2017). Exceptionally robust $CuInS_2$/ZnS nanoparticles as single component photocatalysts for H2 evolution. *J. Phys. Chem. C* 121, 19031–19035. doi: 10.1021/acs.jpcc.7b05241

Zhu, H., Song, N., Lv, H., Hill, C. L., and Lian, T. (2012). Near unity quantum yield of light-driven redox mediator reduction and efficient H_2 generation using colloidal nanorod heterostructures. *J. Am. Chem. Soc.* 134, 11701–11708. doi: 10.1021/ja303698e

Zhukovskyi, M., Tongying, P., Yashan, H., Wang, Y., and Kuno, M. (2015). Efficient photocatalytic hydrogen generation from Ni nanoparticle decorated CdS nanosheets. *ACS Catal.* 5, 6615–6623. doi: 10.1021/acscatal.5b01812

Conflict of Interest Statement: The authors declare that the research was conducted in the absence of any commercial or financial relationships that could be construed as a potential conflict of interest.

frontiers in Chemistry

ORIGINAL RESEARCH
published: 22 January 2019
doi: 10.3389/fchem.2018.00672

Impact of Crystal Structure and Particles Shape on the Photoluminescence Intensity of CdSe/CdS Core/Shell Nanocrystals

Lukas Ludescher[1], *Dmity N. Dirin*[2,3], *Maksym V. Kovalenko*[2,3], *Michael Sztucki*[4], *Peter Boesecke*[4] *and Rainer T. Lechner*[1]*

[1] Institute of Physics, Montanuniversitaet Leoben, Leoben, Austria, [2] Department of Chemistry and Applied Biosciences, ETH Zurich, Zurich, Switzerland, [3] Empa - Swiss Federal Laboratories for Materials Science and Technology, Duebendorf, Switzerland, [4] European Synchrotron Radiation Facility, Grenoble, France

To study the influence of the chemical and crystalline composition of core/shell NCs on their photoluminescence (PL) the mean structural profile of a large ensemble of NCs has to be retrieved in atomic resolution. This can be achieved by retrieving the chemical profile of core/shell NCs using anomalous small angle x-ray scattering (ASAXS) in combination with the analysis of powder diffraction data recorded by wide angle x-ray scattering (WAXS). In the current synchrotron based study, we investigate CdSe/CdS core/shell NCs with different core dimensions by recording simultaneously ASAXS and WAXS spectra. The CdS shells are grown epitaxial on nominal spherical CdSe cores with core diameters from around 3.5–5.5 nm. Three different CdSe shell thicknesses are realized by depositing around 4, 6, and 8 monolayers (MLs) of CdSe. We reveal that the epitaxial core/shell structure depicts a chemical sharp interface, even after a post growth annealing step. With increasing NC diameter, however, the CdSe/CdS NCs deviate significantly from a spherical shape. Instead an elliptical particle shape with pronounced surface facets for the larger core/shell NCs is found. In combination with the powder diffraction data we could relate this anisotropic shape to a mixture of crystal phases within the CdSe core. The smallest CdSe cores exhibit a pure hexagonal wurtzite crystal structure, whereas the larger ones also possess a cubic zincblende phase fraction. This mixed crystal phase fractions lead to a non-spherical shell growth with different thicknesses along specific crystallographic directions: The long axes are terminated by basal crystal faces parallel either to the *a*- or *c*-axis, the short axes by "tilted" pyramidal planes. By combining these structural data with the measured PL quantum yield values, we can clearly connect the optical output of the NCs to their shape and to their shell thickness. Above 6 ML CdS shell-thickness no further increase of the PL can be observed, but for large aspect ratio values the PL is significantly decreased. The gained understanding of the internal crystal structure on CdSe/CdS NCs is general applicable for a precise tuning of the optical properties of crystalline core/shell NCs.

Keywords: core/shell nanocrystals, CdSe/CdS, photoluminescence, SAXS, WAXS

OPEN ACCESS

Edited by:
Vladimir Lesnyak,
Technische Universität Dresden, Germany

Reviewed by:
Vladimir Sayevich,
Los Alamos National Laboratory (DOE), United States
Soong Ju Oh,
Korea University, Japan

***Correspondence:**
Rainer T. Lechner
rainer.lechner@unileoben.ac.at

Specialty section:
This article was submitted to Nanoscience, a section of the journal Frontiers in Chemistry

Received: *08 November 2018*
Accepted: *24 December 2018*
Published: *22 January 2019*

Citation:
Ludescher L, Dirin DN, Kovalenko MV, Sztucki M, Boesecke P and Lechner RT (2019) Impact of Crystal Structure and Particles Shape on the Photoluminescence Intensity of CdSe/CdS Core/Shell Nanocrystals. Front. Chem. 6:672. doi: 10.3389/fchem.2018.00672

1. INTRODUCTION

The wet-chemical synthesis of colloidal nanocrystals (NCs) is a well established method providing highly monodisperse quantum dots (Murray et al., 2000; Sun and Xia, 2002; Kovalenko et al., 2015) with unique optical (Klimov and Bawendi, 2001; Yin and Alivisatos, 2005; Achermann et al., 2006; Talapin, 2012) or magnetic properties (Park et al., 2004; Kovalenko et al., 2007; Laurent et al., 2008; Yoo et al., 2011). The additional growth of an *epitatxial shell* around the core allows, e.g., to tune the magnetic properties (Kovalenko et al., 2007) or enhance the photoluminescence (PL) quantum yield (QY) (Hines and Guyot-Sionnest, 1996; Reiss et al., 2009). Two typical methods for growing a protective shell atop a core are: Either epitaxially on top of the initial core (Hines and Guyot-Sionnest, 1996; Reiss et al., 2009; Yarema et al., 2011), or by replacing elements in the core's shell using galvanic replacements for metallic NCs (Sun and Xia, 2002; Chen et al., 2005) or cation exchange reactions (Son et al., 2004; Pietryga et al., 2008; Kovalenko et al., 2012; Sytnyk et al., 2013; Lechner et al., 2014). Beside the chemical stabilization of the optically active core, the shell enables a significantly enhanced PL-QY due to electron-hole confinement by choosing a wider band gap material for the shell as for the core (Talapin et al., 2001; Pietryga et al., 2004; Reiss et al., 2009; Kovalenko et al., 2012; Lechner et al., 2014). This PL enhancement, however, levels off when the shell thickness exceeds a critical shell thickness. This was related to defect formation caused by the strain impact of the core on the thick shell or vice versa due to the lattice mismatch between the core and the shell (Pietryga et al., 2008; Zhao et al., 2011). Additional influence on the whole core/shell structure is found, when the core and the shell crystal structure differs. For the case where the shell is grown by cationic exchange reaction, e.g., for PbS/CdS NCs, the shell keeps in the beginning the *rocksalt* structure of the PbS core, and only with growing shell thickness the transition to the equilibrium *zincblende* phase of the CdS shell occurs (Lechner et al., 2014).

To avoid problems with different core/shell crystal structures, in this study we investigate the growth of CdSe/CdS core/shell NCs and the PL ouput of these NCs. By following the wet chemical synthesis described in Chen et al. (2013) we realize CdSe cores in the hexagonal *wurtzite* crystal structure ($P6_3m$, a = 4.30 Å, c = 7.00 Å) and grow slowly CdS (a = 4.14 Å, c = 6.75 Å) epitaxially on top. Thus, core/shell NCs with a uniform crystal structure can be achieved. The lattice mismatch between core and shell of around 3.8 % will imply a certain *tensile* strain on the shell material.

To study the influence of increasing CdS shell thicknesses and of different CdSe core diameters, we have realized three series of CdSe NCs with 3.6, 4.4, and 5.7 nm diameter (D_{core}), denoted as *small*, *medium* and *large* NCs (see **Figures 1A,B**). The sizes derived from TEM are 3.1, 3.9, and 4.7 nm respectively, which is significantly lower than the SAXS derived core sizes. This might be due to a potential anisotropoy of the particles, as discussed later in Section 4, which may lead to a preferred orientation of the nanocrystals in the closed packing observed in transmission electron microscopy (TEM). On these cores we intended to grow a CdS shell of 4 monolayers (MLs), 6 and 8 MLs thickness. In **Figure 1C** for all *three* samples series an increasing PL-QY for increasing shell thickness is evidenced. (For the single PL spectra see **Figure S1**) Up to 6 MLs the PL increases, above 6 MLs the QY-increase remains quite constant. If this is related to a higher stacking fault concentration within the shell, an optional annealing step can improve again the crystalline quality and hence the PL ouput (Chen et al., 2013). To prove this hypothesis for the thickest shell of 8 ML, corresponding to ∼ 2.8 nm CdS, we performed for the *medium* and *large* samples an additional annealing step at 310°C , but *no* real increase in the PL-QY could be observed. The small increase after annealing for the medium

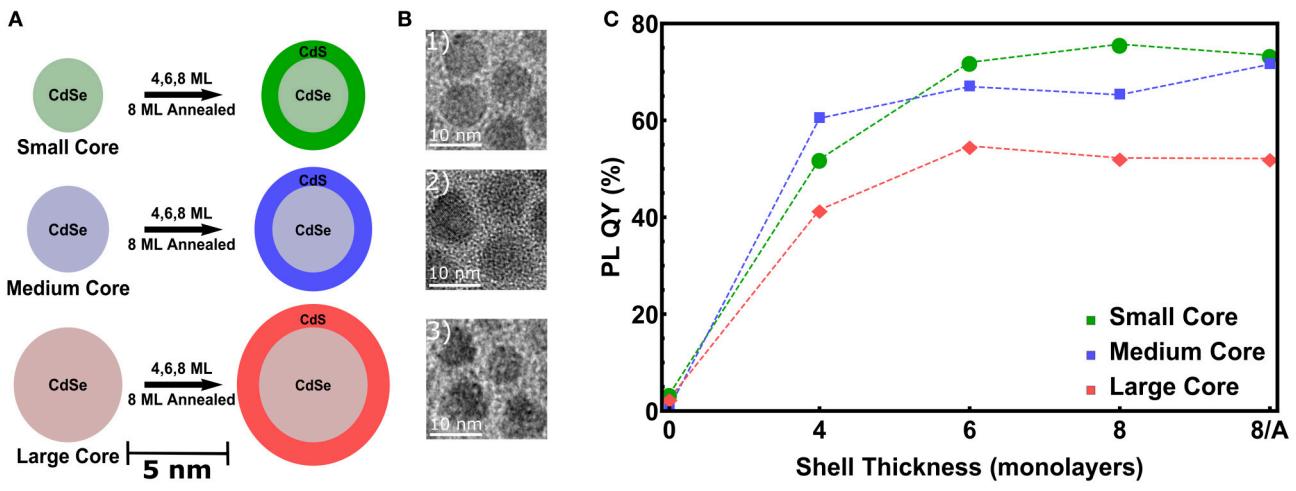

FIGURE 1 | (A) Scheme of the used CdSe cores dimensions denoted as *small* (D_{core} = 3.6 nm), *medium* (D_{core} = 4.4 nm) and *large* (D_{core} = 5.7 nm). On top of these cores 4, 6, and 8 ML of CdS are grown. For the thickest shell an additional annealing step at 310°C is performed for the *medium* and *large* samples. **(B)** TEM images of the CdSe/CdS core/shell NCs with the thickest shell of 8 ML. **(C)** Photoluminescence quantum yield (PL-QY) as a function of the intended shell thickness for all three sample series.

sized core/shell sample is close to the error band. Remarkable, however, is the fact that the PL enhancement for the *largest* core/shell sample series is significantly lower as compared to the *small* and *medium* sized NCs (see **Figure 1C**).

To now relate the observed optical behavior to the chemical and crystalline profile of the core/shell NCs we have to derive the *averaged* structural parameter of the NC-batches, because also the PL data are probed from a large ensemble of individual NCs. With small angle x-ray scattering (SAXS) techniques in combination with the analysis of powder diffraction data retrieved by wide angle x-ray scattering (WAXS) we can probe the colloidal CdSe/CdS core/shell NCs directly in solution (toluene). Thus, we obtain structural information on the 3D shape of around 10^8–10^{10} NCs, a number that is comparable to that used for optical characterizations.

The NCs' mean size and size distribution, their shape and—especially—the core diameter and shell thickness values are important parameters to explain the observed PL performance. Especially the question, if the intended ML-coverage of the CdSe core is reached for all samples homogeneously is an important question. For local sensitive microscopy techniques alone, like TEM based techniques analysing 2D images of NCs deposited on a TEM-grid, it is not easy to resolve single ML steps in the shell thickness (see **Figure 1B**). Even in combination with energy dispersive x-ray spectroscopy (EDX), the chemical profile of a rather small number of single core/shell NCs may be probed. Especially after the applied annealing step the question, if the core/shell NCs keep a chemically stable CdSe/CdS interface, is of importance. From the analysis of the diffraction peaks derived by WAXS we can obtain the crystalline structure and size of the NCs, but the averaged chemical profile can be revealed by anomalous SAXS (ASAXS).

Thus, synchrotron based ASAXS and WAXS measurements will be combined with TEM to reveal quantitative values of the above discussed structural parameter of the NCs. These data will be related to the measured PL output to explain the observed behavior of the PL-QY.

2. CHEMICAL SYNTHESIS OF CDSE/CDS NCS

The CdSe cores were synthesized via the following procedure (Chen et al., 2013; Gollner et al., 2015). 240 mg (1.872 mmol) of CdO (Aldrich, 99.99%), 1.12 g (3.344 mmol) of octadecylphosphonic acid (ODPA, PCI synthesis, 99%) and 12 g of trioctylphosphine oxide (TOPO, Strem, 99%) were mixed in 3-neck flask and subsequently degassed for 1 h at 150°C . Afterwards, under a nitrogen flow, the temperature was elevated up to 320°C to form a colorless solution, upon which 4 mL trioctylphosphine (TOP, ABCR, 97%) was injected. The temperature was further increased to 355–390°C depending on the desired size of CdSe cores. At this point solution of 240 mg Se (Aldrich, 99.99%) in 2 mL TOP was swiftly injected. After 30–120 s the growth was stopped by rapid cooling with air flow and water bath. The resulting CdSe particles were diluted by 10 mL toluene and precipitated by 30 mL of acetone. The pellet was re-dissolved in a mixture of 8 mL hexane, 6 mL of nonanoic acid, 6 mL of octylamine and immediately precipitated by minimum amount (20–25 mL) of ethanol and the obtained powder finally dispersed in hexane. Size and concentration of CdSe cores have been estimated from absorption spectra by using previously reported calibration curves (Jasieniak et al., 2009). The epitaxial CdS shells were grown by loading the hexane solution containing 100 nmol CdSe NCs in a mixture of 3 mL 1-octadecene (ODE, Aldrich, 90%) and 3 mL oleylamine (OLAm, Aldrich, 70%). The reaction solution was degassed afterwards at room temperature under vacuum for 1 h and subsequently for 20 minutes at 120°C . The solution was again heated up to 310°C with a heating rate of 20°C /min, with nitrogen flow and magnetic stirring. Upon reaching 240°C a desired amount of shell-forming cadmium (II) oleate and octanethiol (ABCR, 98%) solutions in 6 mL ODE were injected dropwise at ca. 3 ml/h via two syringe pumps. Cadmium oleate solution in ODE was obtained by direct reaction and degassing of cadmium oxide with 2 equivalents of oleic acid in ODE at 120°C over 1 h. Amounts of shell-forming precursors were calculated from CdSe core NCs size and concentration in order to grow 8 monolayers of CdS shell. After the desired amount was injected 1 mL of degassed oleic acid (Aldrich, 90%) was introduced and the solution was further annealed at 310°C for an hour. Aliquots were extracted when shell thicknesses of around 4, 6, and 8 MLs of CdS has been achieved under the assumption that for the different core diameters the shell growth has the same efficiency (Chen et al., 2013). The resulting particles were washed with hexane/ethanol and finally dissolved in toluene, since this solvent has the best fitting x-ray transmission value within quartz capillaries with 1.5 mm in diameter as used for the planned ASAXS experiments.

3. CHEMICAL PROFILING USING ASAXS

In extension to SAXS, ASAXS (Stuhrmann, 1985; Goerigk et al., 2003) allows element specific contrast variation (Sztucki et al., 2010; Raghuwanshi et al., 2012) and hence the possibility to determine the chemical compositions of the core and the shell with high accuracy in an macroscopic ensemble of NCs (Lechner et al., 2014; Yarema et al., 2017). The contrast variation in ASAXS is due to the energy dependency of the atomic scattering factor $f(Z, E)$, in particular, in the vicinity of x-ray absorption edges, where E is the x-ray energy and Z the atomic number. The non-resonant scattering term depends only on the total electron density within a material related to the overall elementary composition and the bulk density, whereas the resonant scattering term depends on E. By tuning the x-ray energy close to the Se-K-edge at 12.66 keV the contribution of Se ($Z = 34e^-$) as a unique core element to the total scattering amplitude $f(Z, E)$ and hence to the total scattered intensity $I(q, E)$ can be varied significantly. The length of the scattering vector $\boldsymbol{q}$ is derived by $q = 4\pi \sin\theta/\lambda$, where λ is the x-ray wavelength and 2θ the scattering angle. From a minimum set of 3 ASAXS spectra measured at different energies we can separate independently the total electron density from the Se-electron density inside the core/shell NCs. This was achieved by applying a step-like

spherical core/shell model to fit all scattering curves (for the used form factor see Equation S1 in the **Supplementary Material** and Lechner et al., 2014 for a detailed description of the used ASAXS method).

In **Figure 2A** 5 experimental scattering curves are shown together with their model fits for the *small* core/shell NC sample with the 8 ML thick CdS shell on top. (For an example of ASAXS data of the *medium* core series, see **Figure S2**) Up to four pronounced minima in the SAXS curve directly evidence the narrow size distribution of the NC-ensemble, whereas from the position of the first minimum a fast calculation results in an outer diameter of around 11 nm. The energy dependent effect in the 5 ASAXS curves is visible in the small, but significant shift of the q-position of the first minimum in the shape function.

For a quantitative analysis, all 5 curves were fitted with the same unique spherical core/shell model with the following fitting parameter: The inner diameter D_{core}, the shell thickness t_{shell}, the resonant $\nu_{core,shell}$ and non-resonant $\rho_{core,shell}$ electron density differences between the nanocrystal and the solvent, as well as the total size distribution σ of the spherical core/shell NC. The correspondence between data and fit is excellent, smaller deviations are only visible at larger q-values, where we also expected to find an influence of a faceted nanocrystal surface, even for an isotropic NC-dimension (Burian et al., 2015, 2018). (In this region, however, the error band of the scattering data is getting larger and the minima of the fit do not fully follow the experimental minima).

The fitting results are summarized in **Figure 2B**, where the density profile of the *small* CdSe core with the nominal 8 ML CdS shell samples is shown. On the left and right axis the Se-electron density and the total electron (e^-) density as a function of the distance from the center of the spherical fit model is shown. The abrupt drop of the Se-concentration from 17.5 ± 0.7 Se-atoms/nm^3 to 0 at 1.8 ± 0.05 nm reflects the radius of the CdSe core. The theoretical value of 17.9 Se-atoms/nm^3 for CdSe in the wurtzite structure is within the error band of our measurement, thus proving a pure CdSe core. Also the value of the total e^--density with 1120 ± 50 e^-/nm^3 matches the expected value of 1180 e^-/nm^3 for CdSe. In the shell region between 1.8 nm and 5.2 nm the e^--density drops to $\Delta\rho_{shell} = 940 \pm 50$ e^-/nm^3 revealing a pure CdS shell with a theoretical density value of 980 e^-/nm^3.

This results in a shell thickness t_{shell} of 3.4 ± 0.05 nm, which is a above the expected value of 2.8 nm for 8 MLs of CdS by assuming an averaged ML-thickness (along all crystallographic directions) of 0.35 nm/ML for bulk CdS. The difference is around 2 ML for the intended 8 and 6 ML shell, for the 4 ML shell we receive only a 1 ML thicker CdS shell as is summarized in **Table 1**, where all derived core/shell parameters for the *small* and *medium* samples are shown. In contrast, the shell thickness values of the *medium* sized NCs hit the intended ML values within an accuracy of below 0.5 MLs. Only the annealed shell is ∼ 1 ML thicker (see **Table 1**). We explain the larger CdS shell thickness for the *small* nanocrystals by an inaccuracy in estimation of their concentration. We found, indeed, that on average all three *small* shells before annealing are a factor of 1.2 thicker as compared to the *medium* shells (see **Table 1**).

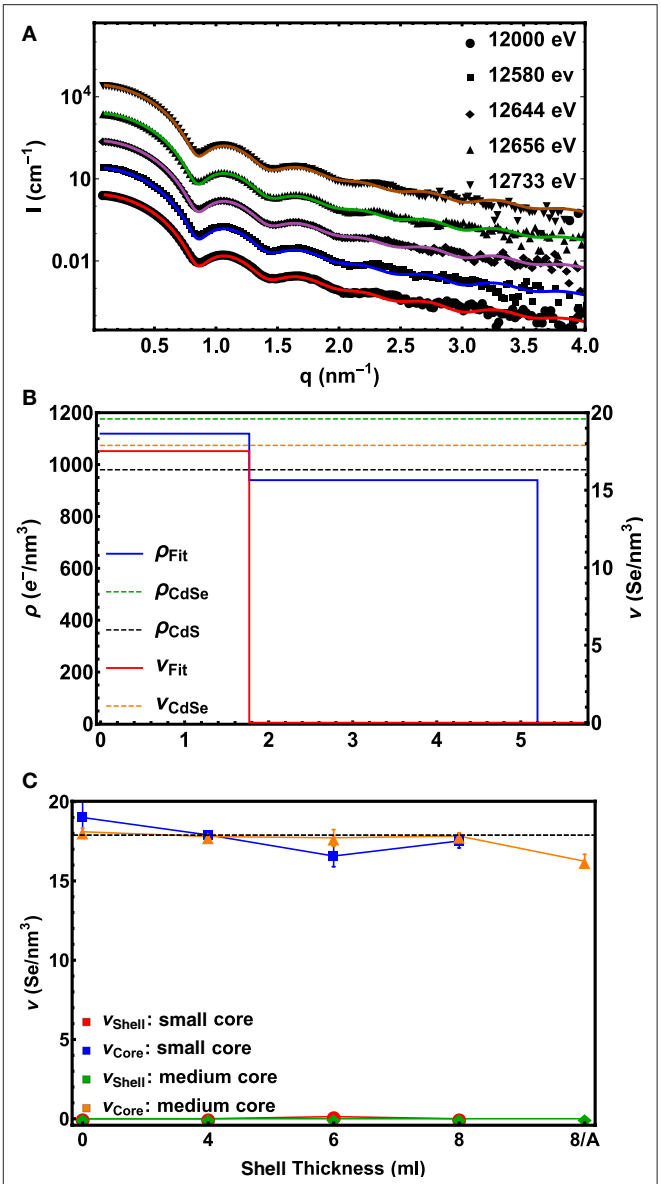

FIGURE 2 | (A) Experimental ASAXS curves (symbols) fitted with a unique spherical core/shell model (lines) for the *small* core/shell CdSe/CdS NC-sample with the 8 ML CdS shell. The scattering cross section $I(q, E)$ plotted over the scattering vector q were recorded at 5 different x-ray energies around the Se-K-edge. The scans are shifted vertically for clarity. The lowest curve is plotted in absolute units, whereas the scattering curves above are each scaled by a factor of 10. **(B)** The resulting density profile for the sample in **(A)** s depicted. The Se-density ν (red line) is plotted on the right axis and the total electron density ρ (blue line) on the left axis as a function of the distance from the centre of the sphere. The dashed lines mark the theoretical density values found in bulk materials. **(C)** The Se-concentration ν in the core and the shell as a function of shell thickness is shown. The dashed lines mark the theoretical values for pure CdSe and CdS, respectively. Note that "0" denotes the initial pure CdSe NC and "8/A" the 8 ML thick shell sample after annealing. For the annealed *small* core/shell sample we have no ASAXS data.

This indicates that the concentration of CdSe cores has been overestimated by a factor of 1.73 (≈ 1.2^3), which is not surprising given that extinction coefficients vary by a factor of 2 for CdSe

TABLE 1 | Listing of the fitting parameters for the spherical core shell model applied to the *small* and *medium* core series.

	Small Core				Medium Core				
Series	**Core**	**4 ML**	**6 ML**	**8 ML**	**Core**	**4 ML**	**6 ML**	**8 ML**	**8 ML Annealed**
$r_{core}(nm)$	1.79	1.77	1.77	1.77	2.09	2.17	2.16	2.17	2.25
$t_{shell}(nm)$	–	1.82	2.73	3.43	–	1.56	2.18	2.94	3.12
$Se_{core}(n/nm^{-3})$	19	18	17	18	18	17	18	18	16
$\rho_{core}(e^-/nm^{-3})$	1163.53	1111	1149	1119	1168	1085	1220	1165	1156
$\rho_{shell}(e^-/nm^{-3})$	–	1049	1072	940	–	1034	1056	943	981

r_{core} denotes the radius of the core, t_{shell} the thickness of the shell. Se_{core} is the atomic density of Selenium in the core, where as ρ_{core} and ρ_{shell} describe the electron densities in the core and the shell respectively.

nanocrystals of such small sizes. Overestimated concentration of cores leads to larger amount of shell precursors per nanocrystal and therefore thicker shell. For the large core/shell NC series this effect will be discussed further below. If we relate the found shell thicknesses with the PL data presented in **Figure 1B**, we can conclude that shell thicknesses between 6 and 9 MLs give the highest PL quantum yield, especially for the *small* CdSe core samples.

Remarkably, in none of the *small* and *medium* core/shell samples a significant amount of Se could be found in the shell. This is also reflected in the constant averaged Se concentration in the cores of 17.7 Se-atoms/nm^3 at least within $\pm$1 Se-atoms/nm^3 measurement and analysis accuracy. This is shown in **Figure 2C**. Even after the 1 h annealing step, no diffusion profile could be deduced from our analysis for the medium sized samples. We tried several diffusion profiles, but all resulted in a larger deviation between fit and experimental data. From this we conclude on a chemical sharp interface between CdSe core and CdS shell. Moreover, the chemical composition as well as the core diameter remains constant during the shell growth with a mean D_{core} value of 3.6 $\pm$ 0.02 nm for the *small* and of 4.4 $\pm$ 0.13 nm for the *medium* sized sample series.

4. 3D SHAPE RETRIEVAL FROM SAXS

The same accurate, straightforward ASAXS analysis is not possible for the *large* NC series. The ASAXS fitting procedures give stable and rather unambiguous results for the case of *spherical*, polydisperse core/shell NCs. As shown in **Figure 3A**, this spherical model can not describe the measured SAXS curve of the *large* CdSe cores sufficiently well. Only the position of the first minimum can be reproduced, but especially around the minima the spherical model deviates drastically from the experimental curve. This position in q would correspond to a sphere with around 5.6 nm in diameter. Improved accordance between data and fit up to the 2. minimum at around 3 nm^{-1} in q is achieved using a homogeneous ellipsoid of revolution as model, with two long axes and one short axis of 5.6 and 6 nm, respectively (see **Figure 3A**). The size distribution now is only around 6–8 vol%, but also this fit can not fully reproduce the SAXS curve: The initial slope as well as the depth of the minima cannot be represented satisfactorily by polydisperse ellipsoids of revolution. In both cases -for spheres and ellipsoids- low polydispersity is needed to fit the small q-region ($<$1.5 nm^{-1}), but the smeared minima deceptively point to large polydispersity. The aspect ratio in the ellipsoidal model artificially smears the minima, but again the actual minima as well as the initial slope cannot be fit simultaneously.

To gain further information on the shape of the *large* NC series crystals, we employed the ab-initio shape retrieval software DAMMIN (Franke et al., 2017), which has been applied successfully by Burian et al. (2015, 2018) on similar colloidal nanocrystal samples. So-called dummy atoms, arranged randomly in a starting volume, are removed and shifted via simulated annealing until an approximate shape is achieved, which fits the recorded scattering curve excellently (see **Figure 3A**). Because the resulting dummy atom models are one of several possible configurations, averaging over several, repeating minimization runs is performed. In our case we used five runs, resulting in the faceted real space structure shown in **Figure 3B**. The interval in q used to fit the real space structure was chosen from 0.07 to 3.85 nm^{-1}, due to the increased noise in higher q-values. When compared to recorded nanocrystal shapes by 2D TEM in **Figure 3C**, we can see that the CdSe/CdS nanocrystals achieved by hot synthesis show strong faceting of the surface and somewhat irregular crystal shapes. The irregularities of the shape in TEM (see also **Figures S3**, **S4**) is due to the nature of the technique, in which only 2 dimensional cuts through individual nanocrystals are observable. Similarly, highly faceted shapes can be reconstructed for any sample of the *large* core series achieving similar qualities of fit.

The same procedure was performed for the *small* and *medium* sized core series, in which no aspect ratio in the range of the large core series, but significant faceting was observed. (Partly visible also in the TEM image shown in **Figures S3**, **S4** . High-resolution electron microscopy images were collected on a FEI Talos F200X microscope operated at 200 kV). This is also represented in the fit quality of the *small* core series with the simplified, spherical core shell model. The shape of the initial slope and the first two minima of the NC form factor are quite well reproduced, but higher order minima are not fit satisfactorily. This is mainly due to the additional smearing and slight deviation from the purely spherical shape due to faceting. (This will be topic of a future study).

Although recent studies seem to point to the fact that the probability to find a dummy atom at a certain position as

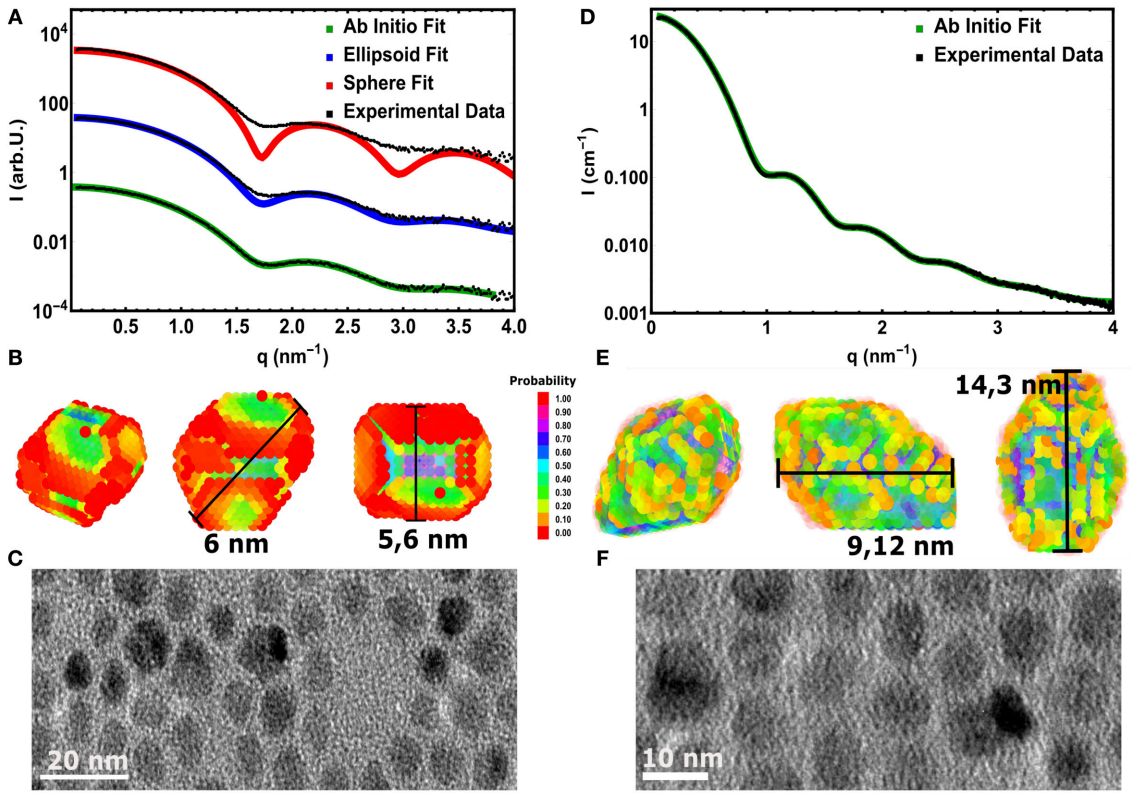

FIGURE 3 | (A) Experimental SAXS curve (symbols) of the *large* core CdSe NC-sample fitted with a spherical (red line) and an elliptical (blue lines) polydisperse shape model. The third fitting result (green line) is derived by a assumption free shape retrieval method using freely moveable dummy atoms with 0.5 nm in diameter (see **B**). The line symbolizes the average of 5 independent fitting runs. **(B)** The resulting 3D mean shape as derived from the fits shown in **(A)**. The color represents the probability to find a single dummy atom at the same position after averaging 5 single shapes. The measurement bars show the found longest and shortest axes. **(C)** TEM image of the *large* CdSe cores revealing the surface facets in 2D projections. **(D)** Data (symbols) and fit (line) using the 3D shape retrieval for the *large* core/shell sample with the thickest shell. **(E)** The resulting 3D mean shape as derived from the fits shown in **(D)**, presenting pronounced surface facets and an elliptical shape with an aspect ratio of 1.7. **(F)** 2D TEM images of the *large* core/shell NCs measured in **(D)**.

shown in **Figure 3B** is related to the electron density (Burian et al., 2015) of the particle, we refrain from examining the resulting structures in such a way to differentiate between core and shell. Due to the uncertainty of the shape retrieval method itself, the lowered probability in the outer regions can also be associated with irregularities between the individually retrieved shapes, which are being smeared out by the averaging of the individual results. Consequently one cannot definitively expect the retrieved model in **Figure 3B** to accurately represent the actual shape of a single nanocrystal. It is rather a mean 3D shape of the whole NC ensemble, including typical features such as the general size, the aspect ratio or the existence of faceted surfaces. The resulting characteristic size parameters of the *large* core series are listed in **Table 2**.

Here it can be nicely seen that we started with a nearly isotropic CdSe core with a very small aspect ratio of 1.07, close to our resolution limit. The aspect ratio between short and long axis increases, however, very strongly with increasing shell thickness from about 1.2 up to 1.7 for the thickest shell. After annealing the shell is still slightly growing but also shows indications of surface restructuring,which is reflected in the lowered aspect ratio of 1.6 as can be seen in **Figure 3E**. We can retrieve now the shell thickness values along the short and long axis by subtracting the core axes from the total diameter values. In general, for all samples both shell directions are getting thicker with increasing ML coverage, but the increase is not so homogeneous with growth time as observed for the *small* and *medium* sized NCs. From the nominal 6–8 ML growth step the short shell thickness actually decreases. Because this is not possible in systems which

TABLE 2 | The size parameters of the retrieved 3 dimensional dummy atom models for the *large* core series.

Particle	Short axis (nm)	Long axis (nm)	Aspect ratio (/)	Equation diameter (nm)
Core	5.60	6.00	1.07	5.7
4 ML	6.90	8.50	1.23	7.4
6 ML	9.50	11.20	1.20	10.0
8 ML	7.70	13.40	1.74	9.3
8 ML annealed	9.12	14.30	1.56	10.5

The equivalent diameter corresponds to a spherical particle with the same volume as the ellipsoids of revolution, with long and short axes.

are not precursor deficient, on reason could be the limited amount of structural information retrievable from scattering techniques. Because the overall number of Shannon Channels is set at 8 for this sample, we probably cannot fully retrieve the actual shape in full detail due the strong anisotropy and faceting of the nanocrystals. What one gets from averaging several shapes retrieved by ab-initio approaches like DAMMIN is a most likely representation, featuring the most dominant characteristics of the shape of the sample under investigation. This is shown in **Figures 3B,C,E,F**, where facets, both in the TEM images and the reconstructed shapes, can be seen. The overall size and structure is mostly determined by the minima of the SAXS-patterns in **Figures 3A,D**, whereas the smeared nature of the minima indicates faceting and anisotropy in the shape. However, one clear overall trend can be observed: The shell growth along the short axis is clearly below the intended ML thickness values, whereas along the long axes the t_{shell} values are up to 2 ML thicker as intended. The results of the 3D shape analysis allows the conclusion that some of the core facets enables better CdS growth than others. These pronounced surface facets are certainly induced by the crystal structure of the NCs, but from the SAXS based 3D shape analysis alone we can not conclude on the crystallographic direction of the crystal faces. Taking the detailed TEM studies on CdSe/CdS NCs into account one would expect to find the anistropy axes axis parallel the hexagonal *a*– and *c*-axis Peng et al. (1997).

The combination of both techniques -ASAXS and 3D shape retrieval- delivers many parameters of the internal structure of the core/shell NCs. From ASAXS we get reliable information on the internal chemical core/shell profile and from the shape retrieval method on the outer NC shape. Although we were only able to get full information on the chemical composition of the *small* and *medium* core series, both of which exhibit a chemically sharp boundary between core and shell, we are confident to assume the same for the *large* core series. So two open questions remain: First, what is the physical reason that the *large* NCs develop the revealed pronounced elliptical shape and large surface facets? The facet formation should be driven by the *wurtzite* crystal structure of CdSe and CdS. This leads to the second question: Which is the crystallographic direction of the short and long axis? These questions may be answered by analysing the powder x-ray diffraction data (XRD) measured simultaneously with the ASAXS data by recording the wide angle x-ray scattering (WAXS) pattern in transmission geometry.

5. WIDE ANGLE SCATTERING ANALYSIS

In **Figure 4A** the WAXS data of the whole *small* NC series are shown. The dashed lines mark the theoretical Bragg peak positions for bulk CdS (a = 4.14 Å, c = 6.75 Å) as well as the expected intensity ratios (black sticks). The lowest diffraction peaks has clearly the small core CdSe NCs. With increasing shell thickness and thus increasing total diameter the peak intensity increases, as the diffracted intensity is proportional to the particle volume square. (The total XRD intensity depends also on the NC concentration within the solvent toluene. The annealed sample depict the highest NC concentration). Furthermore the width of the peaks decreases with increasing NC-diameter as is

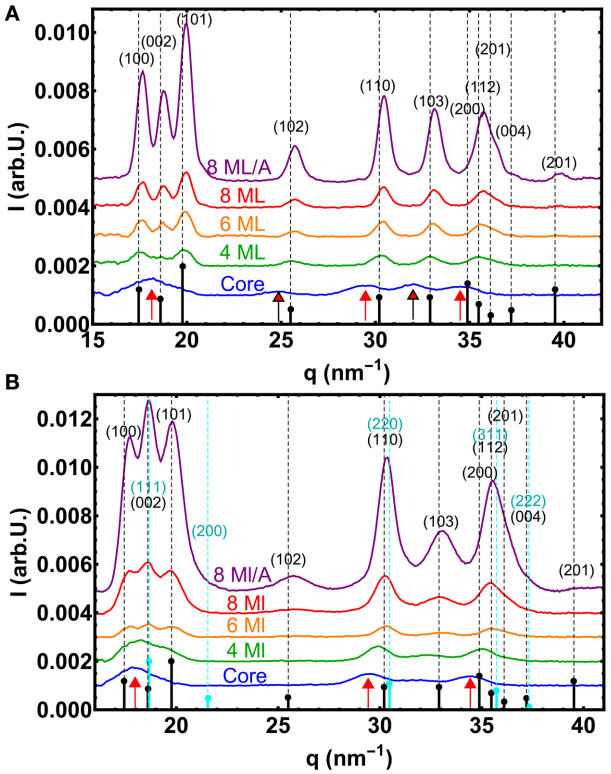

FIGURE 4 | (A) WAXS curves of the *small* core/shell NC series. The vertical dashed lines mark the theoretical positions of the Bragg peaks for unstrained bulk CdS in the hexagonal *wurtzite* phase. The theoretical relative intensities are symbolized by small black sticks, whereas the red arrows mark the theoretical positions for *wurtzite* CdSe. **(B)** The same for the *large* core/shell NC series, but now also with the marked positions and intensities the for cubic *zincblende* CdS phase (cyan). Here the red arrows mark the positions of cubic *zincblende* CdSe.

expected for an increasing crystalline particle sizes. From fitting the powder diffraction data with Gaussian peaks on a splined background, we derive the full width at half maximum FWHM (Δq) of the Bragg peaks along specific crystallographic directions. From Δq one can calculate the crystallite size D_{hkl} using the Scherrer equation with $D_{hkl} = F \cdot 2\pi/\Delta q$, where F is a constant with values close to 1, but depends on crystallographic direction or particles shape (Als-Nielsen and McMorrow, 2011).

The positions of the peaks are determined by the crystalline structure and the chemical composition, but also by all influences that changes the d-spacing within the atomic lattice, such as internal strains or external applied pressures. As an overall trend one can observe that the peaks shift from the initial CdSe position (marked by red arrows) toward the CdS positions, as the CdS shell forms the major part of the core/shell scattering volume when the shell thickness reaches 4 ML (see **Figure 4A**). (The core/shell volume ratio for the 4 ML shell is around 1/7 resulting in an about 1/50 XRD intensity ratio).

For the CdS shells above 4 ML thickness all peak positions are, however, at larger q-positions as the theoretical values. Larger q-values mean smaller lattice spacings and thus the nanocrystal structure is under *compressive* strain. As the peak

shift along all crystallographic directions is roughly the same, a hydrosatic pressure caused by a surface relaxation due to the high surface/volume ratio for small sized NCs can be the reason. A hydrostatic decrease in lattice spacing was also found for other NCs with comparable elastic constants, like ZnS, but only for diameters below 5 nm (Rath et al., 2008). The total diameter of our CdSe/CdS NCs would exceed this limits for the thicker shells, but it was reported especially for 2 nm CdS shells around PbS cores that also the shell alone can be compressed (Lechner et al., 2014).

Also a new polytype of the CdS crystal structure or even a non-periodic lattice within a closed packed nanocrystal can result in shifted or vanishing peaks as shown for CdS-NCs (Rempel and Magerl, 2010). In our measurements two pronounced peak triples, the (100)-(002)-(101) and the (110)-(103)-(112) triple, are visible that are characteristic for the hexagonal *wurtzite* structure as is shown in **Figure 4A**. For the smallest core sample the first peak triple cannot be easily resolved due to overlapping of three broad peaks. (Within the second triple the (112) peak consists in fact again of three individual peaks). Furthermore, the peak intensity ratios of the first triple nicely follow the theoretical values for *wurtzite* CdSe. When we additionally analyse now the width Δq of all visible diffraction peaks and calculate the total crystalline diameter D_{hkl}, we derive an rather isotropic size for the whole *small* core/shell series (see **Table 3**), with rather small deviations in Δq. (Here we neglect in a first approximation the peak broadening due to stacking faults and other crystal defects. As we calculate mainly the chord length of "hollow" CdS spheres we use the Scherrer constant $F = 1$). The largest difference in size we found not along the hexagonal [100] and [001] directions, but between "straight" and "tilted" surface facets. The *straight* planes are either fully parallel to the hexagonal *a*- or *c*-axis. The corresponding size $D_{||,\perp}$ is related to the crystalline particle dimension that are terminated by the $\{h00\}, \{00l\}$ and $\{hh0\}$ lattice planes. The $D_{||,\perp}$ values are derived by averaging the sizes obtained by the (100), (002), and (110) peak widths. The *tilted* plane values D_{tilt} are related to planes containing *a*- and *c*-axis components and thus having $\{h0l\}$ Miller indices. The D_{tilt} values are calculated from the widths of the (101), (102), and (103) peaks. All absolute D_{hkl} values are always smaller as the diameters derived by ASAXS. This can be related to additional peak broadening by lattice defects or by not fully perfect crystalline top most surface layers (see **Table 3**). For spherical core/shell NCs, however, we have to take an additional effect into account. For thick CdS shells, where the CdSe core can be neglected, the width of the CdS peaks originate from hollow CdS sphere with a certain shell thickness. With XRD we hence probe rather the*weighted chord lenght* (Gille, 2000) of the CdS shell instead of directly the shell thickness or even the total NC diameter. For spherical NCs the shell thickness or diameter can be calculated, but for strongly anisotropic and faceted shapes absolute structural parameter can not be easily deduced.

For a first comparison between SAXS and WAXS data we calculate the chord length values for the different CdS-shell thicknesses for the *small* and *large* series. For the *large* core/shell NCs we use the derived spherical equivalent diameters as listed in **Table 2**. All these value are compared to the derived crystallite sizes as listed in **Table S1** (see **Supplementary Material**) and proves a really good accordance between overall dimensions and crystallite sizes.

TABLE 3 | The crystallite sizes of the *small* and *large* core/shell series as derived from the analysis of the WAXS pattern shown in **Figure 4**.

	$D_{||,\perp}$ (nm)	D_{tilt} (nm)	Aspect ratio
SMALL CORE			
Core	3.3	–	1
4 ML	6.2	6	1.05
6 ML	6.9	7	0.99
8 ML	8.1	7.3	1.10
8 ML/A	7.6	7.4	1.03
LARGE CORE			
Core	4.5	–	–
4 ML	5.2	–	–
6 ML	6.3	5.3	1.20
8 ML	7.9	5.6	1.42
8 ML/A	8.4	5.8	1.46

$D_{||,\perp}$ denoted the crystallite size parallel to the straight planes, D_{tilt} parallel to the tilted planes. The relative size accuracy is ± 0.1 *nm.*

We can also calculate an crystalline aspect ratio between $D_{||,\perp}$ and D_{tilt} as listed in **Table 3**. For the *small* CdSe core sample we could not derive all peak-width values due to overlapping peaks. But where it can be calculated we derive an isotropic crystal size of around 3.3 nm. But also all other aspect ratio values are below 1.1, which is close to our resolution limit, indicating an isotropic core/shell shape.

To summarize the XRD analysis of the *small* NC series, we can conclude that both, CdSe core and CdS shell, keep their hexagonal *wurtzite* crystal structure, but the thicker shell samples depict an compressive strain between 0.6 and 1%. The found crystallite size reflect again the rather isotropic shape of these NCs as already evidenced independently by the ASAXS analysis (compare **Table 1**). An analysis of the *medium* core series was also conducted, but it is not necessary to illustrate the effects discussed in this paper. The corresponding WAXS pattern is depicted in the Supplementary Material (see **Figure S4**).

A rather different picture results from the analysis of the WAXS data of the *large* core/shell series as shown in **Figure 4B**. The first directly visible effect is the changed intensity ratios of the first peak triple, the (100)-(002)-(101) peaks: Here the middle peak—the hexagonal (002) peak—is the strongest peak of the three, clearly visible for the samples with CdS shells. The first triple is not visible for the *large* core CdSe sample, but in contrast the middle peak of the second triple—the (103)–vanished. Also the (102) peak around 25 nm^{-1} is no longer visible. This can be explained by the fact that the CdSe core now has a changed crystal structure, i.e., the cubic *zincblende* structure ($F\bar{4}3m$), with the equivalent cubic lattice constant of 5.832 Å. The unstrained *q*-positions for the new CdSe core phase are additionally marked in **Figure 4B** by the three red arrows, whereas the positions and relative intensities of cubic *zincblende* CdS are marked by cyan dashed lines and sticks.

This XRD pattern, missing *wurtzite* (102) and (103) peaks, but increased (002), is also visible for the 4 and 6 ML shell sample. For the case of the 4 ML CdS sample this could be explained by a cubic *zincblende* CdSe core with an *wurtzite* CdS on top, because for this shell thickness the scattering volumes of core and shell are comparable. By reaching shell thicknesses equal and larger of 6 ML the shell-volume clearly exceeds the core-volume and thus the main diffraction contributions originates from the shell's crystal structure. Indeed, the *wurtzite* (103) peak appears again, but really faintly making a fitting rather ambiguous. Within the first peak triple, however, the central (002) peak is still the strongest peak. The same behavior can be observed for the thickest shell, where additionally the (102) peak is back again and now also the (103) peak is clearly visible indicating a larger *wurtzite* phase fraction within the CdS shell. The intensity ratios of the whole XRD pattern, however, can be only explained by a *considerable* amount of a cubic *zincblende* phase fraction within a hexagonal CdS shell. The additionally cubic (111) Bragg peak at the position of the hexagonal (002) causes the increased central peak by adding up both peak intensities. For spherical core/shell particles it would be possible to simulate the diffraction patterns for the different crystal structures and hence determine quantitative values of the amount of *zincblende* phase fraction within core and shell as shown (e.g., in Lechner et al., 2014). For the strong anisotropic and faceted NC-shape these simulations are not so straight forward and will be topic of an upcoming study.

5.1. WAXS-SAXS-PL

For further insight we analyse the FWHM of the peaks to derive the crystallite sizes $D_{||,\perp}$ and D_{tilt} perpendicular to the *straight* and *tilted* planes and thus calculate the aspect ratio between these directions. This analysis is, however, not fully possible for the *large* CdSe core sample and for the shells up to 6 MLs, because especially the {*h*0*l*} peaks are not visible, or can not be resolved within merged triple peaks (see **Figure 4**). For the 6 ML sample the three straight peaks and only one tilted, the (101) could be resolved. The derived chord length values (listed in **Table 3**) clearly increase with growing shell thickness and are only around 10% below the values as estimated from the core/shell parameters derived from SAXS.

For the two 8 ML large core/shell sample we can analyse three *straight* peaks ({*h*00}, {*hh*0}, {00*l*}) and three tilted peaks ({*h*0*l*}).The 8 ML annealed sample show clearly increased D_{hkl} values in both directions with respect to the 8 ML shell sample without annealing. This indicates that during annealing the crystalline shell part growths, or that the shell's crystal quality is improved also resulting in a narrower peak. For the 6 ML and both 8 ML samples the found crystalline aspect ratio values are listed in **Table 3** and ranges from 1.2 to 1.5. These values are very close to the values derived from the SAXS based 3D shape analysis, where we are not sensitive to the crystal structure (see **Table 2**).

The accordance between these two independent data sets allow now to relate the found long NC axes to the *straight* crystal planes ({*h*00}, {00*l*}, and {*hh*0}) and the short axes to the *tilted* planes ({*h*0*l*}).

This result has some physical evidence as the CdS shell growth on the tilted CdSe planes is not so efficient as on straight planes, because for the shell growth on planes with {*h*0*l*} Miller indices additional monolayer steps has to be introduced. As this effect is not observed for the *small* NC series and only partly for the *medium* sized series (not discussed in this paper), the presented explanation is not sufficient for explaining the derived experimentally derived NC-parameters.

We found, however, already a mixed cubic/hexagonal phase fraction within the large CdSe core that result in increased crystal defects within specific surface facets. These defects will result again in increased stacking faults within the subsequent CdS shell and may enable more effective shell growth parallel to the *straight* crystal planes. An increased number of lattice defects or stacking faults, however, should result in strain relaxation within the CdS shell (Wickham et al., 2000; Zaziski et al., 2004). This is indeed observed in **Figure 4**, where NCs of the *large* series with the thicker shells exhibit less compressive strain (below 0.01%) as compared to the *small* NC series.

For further insight, the overall mechanism of deformation for hexagonal systems has to be discussed shortly. The overall criterion for the type of deformation in hexagonal lattices is the c/a ratio, which is slightly above 1.63 for CdS. For any hexagonal material, deformation for c/a ratios below 1.63 is found on basal, pyramidal and prismatic lattice planes, above 1.63 only in basal planes and above 1.73 through conformal movement via twinning (Gottstein, 2013). Twinning can also be found in materials with c/a ratios close to 1.63, but only in the context of polycrystalline materials. In these cases at least 5 glide systems need to be active to ensure deformation. For crystals with free surfaces and a c/a ratio at 1.63, the three glide systems provided by glide on the basal plane are enough to ensure sufficient deformation to relieve strain, hence we do not expect deformation by twinning.

We expect so called Shockley dislocations, i.e., two partial dislocations (Gottstein, 2013), to form on the basal plane to reduce the line energy connected to the length of the associated burgers vector (Berghezan et al., 1961). These dislocations extend through the crystal on the (001) plane, which coincides with the (111) plane of the fcc *zincblende* lattice upon dislocation movement and consequent change in stacking order from *ABAB* to *ABCA* (Berghezan et al., 1961). Consequently, we can expect crystals, which are able to release stresses via dislocation glide forming stacking faults perpendicular to the basal plane, changing the stacking order locally from hexagonal to face centered cubic. With these observations we think we can explain the fact that the cores exhibit increasingly *zincblende* structure with increasing core size. In the case of large core particles, the overall structure seems to be *zincblende* for the core and increasingly more *wurtzite* phase seems to exist in the nanocrystals with increasing shell thickness. Similar mechanisms can be responsible for the phase transition from *zincblende* to *wurtzite*. The dominant glide system in *fcc* materials are directions situated on the (111) plane, on which the Burgers vector can split into two partial dislocations to minimize its line energy (Gottstein, 2013). The stacking is then also changed, but this time from *ABC ABC* to *ABC BCA*, meaning we get small but

extended *wurtzite* domains inside the *zincblende* structure due to the fact that the respective (111) and (001) planes coincide. Indeed, we see some streak-like features in some nanocrystals of the *large* core series with 8 ML shell and annealing and can distinguish stacking faults (see **Figure S3**). These defects in the CdS shell should be reflected in a reduced PL emission due to a partial extension of the exciton wavefunction into the shell material (Reiss et al., 2009). Indeed, the *large* core/shell NCs with pronounced shape anisotropy and surface facets show an at least 20% lower PL-QY as compared to the *small* and *medium* sized samples (see **Figure 1C**). A possible reason for this pronounced difference might simply be the size difference between both series. The *large* core size of 5.8 nm simply offers enough space for creating dislocations to compensate strain (Peierls, 1940; Demortiere et al., 2018) and trigger the phase transition from *wurtzite* to *zincblende*. Coherently, the *small* core series exhibits a single, but strained, *wurtzite* structure in contrast to the predominately *zincblende* phase fraction within the *large* core series.

5.2. Conclusion and Outlook

A more detailed analysis of all WAXS data in combination with atomistic simulations of the XRD patterns in a future study will give more quantitative results on, e.g., dislocation densities along specific crystallographic directions. This will allow to follow the transition from smaller, isotropic NCs with a single hexagonal *wurtzite* crystal structure to larger anisotropic NCs with a mixed hexagonal and cubic *zincblende* phase, especially by analysing the data of the *medium* sized CdSe/CdS samples.

The size change from the initial *small* CdSe core from 3.6 nm, over the *medium* sized core with 4.4 nm to the *large* core of 5.7 nm corresponds to *only* 3 ML more CdSe on top of the *small* core. The combined (A)SAXS/WAXS measurements and analyses allow to resolve such small changes in the NC dimension on a large ensemble of NCs that is needed in optical applications. It clearly shows the drastic change to an anisotropic shape, when the a bit larger core exhibit a mixed crystal phase fraction. Annealing at 310°C does not affect the chemical sharp CdSe/CdS core shell interface and slightly reduces the large aspect ratio for the largest core/shell NCs derived from SAXS, but not the crystallite aspect ratio as derived from WAXS. This can be explained by an exclusively reordering of the amorphous (or partly crystalline) top most shell layer not affecting the main part of the CdS shell. This would also explain why the photoluminescence output after annealing is not significantly increased.

When we summarize all structural and optical derived NC parameters presented in this study on CdSe/CdS, we can conclude the following: An initial difference in the CdSe core dimension of only 2 MLs finally results in a 20% decreased PL output. Especially for high efficiency CdSe/CdS NCs with QYs above 90% (Chen et al., 2013) such changes has to be understood and—finally—has to be controlled. That means during synthesis of optical active NCs, the NCs' size has to be controlled in monolayer accuracy *and* that the applied characterization techniques has to deliver an even better accuracy in the range of atomic resolution. This resolution in 3D should be obtained for both, the chemical and crystalline profile of core/shell NCs.

DATA AVAILABILITY STATEMENT

Raw data were generated at the large-scale synchrotron radiation facility ESRF. Processed data are available from the corresponding author RTL on request.

AUTHOR CONTRIBUTIONS

LL, RTL, MS, and PB conducted the anomalous small angle and wide angle x-ray scattering (ASAXS/WAXS) experiments. LL and RTL performed the ASAXS/WAXS data evaluation. DND and MVK synthesized and prepared samples and performed TEM as well as PL measurements. LL and RTL wrote the manuscript, RTL envisioned, planed and supervised the research.

FUNDING

MVK acknowledges financial support from European Union (FP7 ERC Starting Grant 2012, GA No. 306733); DND was funded by European Union via a Marie Curie Fellowship (PIIF-GA-2012-330524).

ACKNOWLEDGMENTS

The ASAXS/WAXS experiments have been performed at the beamline ID02 at the synchrotron ESRF. Electron microscopy was carried out by Frank Krumeich at the Scientific Center for Optical and Electron Microscopy (ScopeM) at ETH Zurich.

SUPPLEMENTARY MATERIAL

The Supplementary Material for this article can be found online at: https://www.frontiersin.org/articles/10.3389/fchem.2018.00672/full#supplementary-material

REFERENCES

Achermann, M., Petruska, M. A., Koleske, D. D., Crawford, M. H., and Klimov, V. I. (2006). Nanocrystal-based light-emitting diodes utilizing high-efficiency nonradiative energy transfer for color conversion. *Nano Lett.* 6, 1396–1400. doi: 10.1021/nl060392t

Als-Nielsen, J., and McMorrow, D. (2011). *Elements of Modern X-ray Physics*. Hoboken, NJ: Wiley.

Berghezan, A., Fourdeux, A., and Amelinckx, S. (1961). Transmission electron microscopy studies of dislocations and stacking faults in a hexagonal metal: Zinc. *Acta Metallurg.* 9, 464–490.

Burian, M., Fritz-Popovski, G., He, M., Kovalenko, M. V., Paris, O., and Lechner, R. T. (2015). Considerations on the model-free shape retrieval of inorganic nanocrystals from small-angle scattering data. *J. Appl. Cryst.* 48, 857–868. doi: 10.1107/S1600576715006846

Burian, M., Karner, C., Yarema, M., Heiss, W., Amenitsch, H., Dellago, C., et al. (2018). A shape-induced orientation phase Within 3D nanocrystal solids. *Adv. Mater.* 30:1802078. doi: 10.1002/adma.201802078

Chen, J., Wiley, B., McLellan, J., Xiong, Y., Li, Z., and Xia, Y. (2005). Optical properties of Pd-Ag and Pt-Ag nanoboxes synthesized via galvanic replacement reactions. *Nano Lett.* 5, 2058–2062. doi: 10.1021/nl051652u

Chen, O., Zhao, J., Chauhan, V. P., Cui, J., Wong, C., Harris, D. K., et al. (2013). Compact high-quality CdSe-CdS core-shell nanocrystals with narrow emission linewidths and suppressed blinking. *Nat. Mater.* 12, 445–451. doi: 10.1038/nmat3539

Demortiere, A., Leonard, D. N., Petkov, V., Chapman, K., Chattopadhyay, S., She, C., et al. (2018). Strain-Driven Stacking Faults in CdSe/CdS Core/Shell Nanorods. *J. Phys. Chem. Lett.* 9, 1900–1906. doi: 10.1021/acs.jpclett.8b00914

Franke, D., Petoukhov, M. V., Konarev, P. V., Panjkovich, A., Tuukkanen, A., Mertens, H. D. T., et al. (2017). *ATSAS 2.8*: a comprehensive data analysis suite for small-angle scattering from macromolecular solutions. *J. Appl. Cryst.* 50, 1212–1225. doi: 10.1107/S1600576717007786

Gille, W. (2000). Chord length distributions and small-angle scattering. *Eur. Phys.J. B.* 17, 371–383. doi: 10.1007/s100510070116

Goerigk, G., Haubold, H.-G., Lyon, O., and Simon, J.-P. (2003). Anomalous small-angle X-ray scattering in materials science. *J. Appl. Cryst.* 36(3 Pt 1), 425–429. doi: 10.1107/S0021889803000542

Gollner, C., Ziegler, J., Protesescu, L., Dirin, D. N., Lechner, R. T., Fritz-Popovski, G., et al. (2015). Random lasing with systematic threshold behavior in films of CdSe/CdS Core/Thick-Shell colloidal quantum dots. *ACS Nano* 9, 9792–9801. doi: 10.1021/acsnano.5b02739

Gottstein, G. (2013). *Physical Foundations of Materials Science*. Heidelberg: Springer Science & Business Media.

Hines, M. A., and Guyot-Sionnest, P. (1996). Synthesis and characterization of strongly luminescing ZnS-capped CdSe nanocrystals. *J. Phys. Chem.* 100, 468–471.

Jasieniak, J., Smith, L., Van Embden, J., Mulvaney, P., and Califano, M. (2009). Re-examination of the size-dependent absorption properties of CdSe quantum dots. *J. Phy. Chem. C* 113, 19468–19474.

Klimov, V., and Bawendi, M. (2001). Ultrafast carrier dynamics, optical amplification, and lasing in nanocrystal quantum dots. *MRS Bull.* 26, 998–1004. doi: 10.1557/mrs2001.256

Kovalenko, M. V., Bodnarchuk, M. I., Lechner, R. T., Hesser, G., Schäffler, F., and Heiss, W. (2007). Fatty acid salts as stabilizers in size- and shape-controlled nanocrystal synthesis: the case of inverse spinel iron oxide. *J. Am. Chem. Soc.* 129, 6352–6353. doi: 10.1021/ja0692478

Kovalenko, M. V., Manna, L., Cabot, A., Hens, Z., Talapin, D. V., Kagan, C. R., et al. (2015). Prospects of nanoscience with nanocrystals. *ACS Nano* 9, 1012–1057. doi: 10.1021/nn506223h

Kovalenko, M. V., Schaller, R. D., Jarzab, D., Loi, M. A., and Talapin, D. V. (2012). Inorganically functionalized PbS-CdS colloidal nanocrystals: integration into amorphous chalcogenide glass and luminescent properties. *J. Am. Chem. Soc.* 134, 2457–2460. doi: 10.1021/ja2087689

Laurent, S., Forge, D., Port, M., Roch, A., Robic, C., Vander Elst, L., et al. (2008). Magnetic iron oxide nanoparticles: synthesis, stabilization, vectorization, physicochemical characterizations, and biological applications. *Chem. Rev.* 108, 2064–2110. doi: 10.1021/cr068445e

Lechner, R. T., Fritz-Popovski, G., Yarema, M., Heiss, W., Hoell, A., Schülli, T. U., et al. (2014). Crystal phase transitions in the shell of PbS/CdS Core/Shell nanocrystals influences photoluminescence intensity. *Chem. Mater.* 26, 5914–5922. doi: 10.1021/cm502521q

Murray, C. B., Kagan, C. R., and Bawendi, M. G. (2000). Synthesis and characterization of monodisperse nanocrystals and close-packed nanocrystal assemblies. *Ann. Rev. Mater. Sci.* 30, 545–610. doi: 10.1146/annurev.matsci.30.1.545

Park, J., An, K., Hwang, Y., Park, J. G., Noh, H. J., Kim, J. Y., et al. (2004). Ultra-large-scale syntheses of monodisperse nanocrystals. *Nat. Mater.* 3, 891–895. doi: 10.1038/nmat1251

Peierls, R. (1940). The size of a dislocation. *Proc. Phys. Soc.* 52:34. doi: 10.1088/0959-5309/52/1/305

Peng, X., Schlamp, M. C., Kadavanich, A. V., and Alivisatos, A. P. (1997). Epitaxial growth of highly luminescent CdSe/CdS core/shell nanocrystals with photostability and electronic accessibility. *J. Am. Chem. Soc.* 119, 7019–7029. doi: 10.1021/ja970754m

Pietryga, J. M., Schaller, R. D., Werder, D., Stewart, M. H., Klimov, V. I., and Hollingsworth, J. A. (2004). Pushing the band gap envelope: mid-infrared emitting colloidal PbSe quantum dots. *J. Am. Chem. Soc.* 126, 11752–11753. doi: 10.1021/ja047659f

Pietryga, J. M., Werder, D. J., Williams, D. J., Casson, J. L., Schaller, R. D., Klimov, V. I., et al. (2008). Utilizing the lability of lead selenide to produce heterostructured nanocrystals with bright, stable infrared emission. *J. Am. Chem. Soc.* 130, 4879–4885. doi: 10.1021/ja710437r

Raghuwanshi, V. S., Tatchev, D., Haas, S., Harizanova, R., Gugov, I., Ruessel, C., and Hoell, A. (2012). Structural analysis of magnetic nanocrystals embedded in silicate glasses by anomalous small-angle X-ray scattering. *J. Appl. Cryst.* 45, 644–651. doi: 10.1107/S002188981202064X

Rath, T., Kunert, B., Resel, R., Fritz-Popovski, G., Saf, R., and Trimmel, G. (2008). Investigation of primary crystallite sizes in nanocrystalline ZnS powders: comparison of microwave assisted with conventional synthesis routes. *Inorg. Chem.* 47, 3014–3022. doi: 10.1021/ic7017715

Reiss, P., Protiere, M., and Li, L. (2009). Core/shell semiconductor nanocrystals. *Small* 5, 154–168. doi: 10.1002/smll.200800841

Rempel, A. and Magerl, A. (2010). Non-periodicity in nanoparticles with close-packed structures. *Acta Crystallogr. A Found. Crystallogr.* 66, 479–483. doi: 10.1107/S010876731001250X

Son, D., Hughes, S., Yin, Y., and Alivisatos, A. (2004). Cation exchange reactions-in ionic nanocrystals. *Science* 306, 1009–1012. doi: 10.1126/science.1103755

Stuhrmann, H. (1985). Resonance scattering in macromolecular structure research. *Adv. Polym. Sci.* 67, 123–163. doi: 10.1007/BFb0016608

Sun, Y., and Xia, Y. (2002). Shape-controlled synthesis of gold and silver nanoparticles. *Science* 298, 2176–2179. doi: 10.1126/science.1077229

Sytnyk, M., Kirchschlager, R., Bodnarchuk, M. I., Primetzhofer, D., Kriegner, D., Enser, H., et al. (2013). Tuning the magnetic properties of metal oxide nanocrystal heterostructures by cation exchange. *Nano Lett.* 13, 586–593. doi: 10.1021/nl304115r

Sztucki, M., Di Cola, E., and Narayanan, T. (2010). Instrumental developments for anomalous small-angle X-ray scattering from soft matter systems. *J. Appl. Cryst.* 43, 1479–1487. doi: 10.1107/S002188981003298X

Talapin, D., Rogach, A., Kornowski, A., Haase, M., and Weller, H. (2001). Highly luminescent monodisperse CdSe and CdSe/ZnS nanocrystals synthesized in a hexadecylamine-trioctylphosphine oxide-trioctylphospine mixture. *Nano Lett.* 1, 207–211. doi: 10.1021/nl0155126

Talapin, D. V. (2012). Nanocrystal solids: a modular approach to materials design. *MRS Bull.* 37, 63–71. doi: 10.1557/mrs.2011.337

Wickham, Herhold, and Alivisatos (2000). Shape change as an indicator of mechanism in the high-pressure structural transformations of CdSe nanocrystals. *Phys. Rev. Lett.* 84, 923–926. doi: 10.1103/PhysRevLett.84.923

Yarema, M., Pichler, S., Sytnyk, M., Seyrkammer, R., Lechner, R. T., Fritz-Popovski, G., et al. (2011). Infrared emitting and photoconducting colloidal silver chalcogenide nanocrystal quantum dots from a silylamide-promoted synthesis. *ACS Nano* 5, 3758–3765. doi: 10.1021/nn2001118

Yarema, M., Xing, Y., Lechner, R. T., Ludescher, L., Dordevic, N., Lin, W. M., et al. (2017). Mapping the atomistic structure of graded Core/Shell colloidal nanocrystals. *Sci. Rep.* 7:11718. doi: 10.1038/s41598-017-11996-2

Yin, Y., and Alivisatos, A. (2005). Colloidal nanocrystal synthesis and the organic-inorganic interface. *Nature* 437, 664–670. doi: 10.1038/nature04165

Yoo, D., Lee, J. H., Shin, T. H., and Cheon, J. (2011). Theranostic magnetic nanoparticles. *Accounts Chem. Res.* 44, 863–874. doi: 10.1021/ar200085c

Zaziski, D., Prilliman, S., Scher, E., Casula, M., Wickham, J., Clark, S., et al. (2004). Critical size for fracture during Solid-Solid phase transformations. *Nano Lett.* 4, 943–946. doi: 10.1021/nl049537r

Zhao, H., Chaker, M., and Ma, D. (2011). Effect of CdS shell thickness on the optical properties of water-soluble, amphiphilic polymer-encapsulated PbS/CdS core/shell quantum dots. *J. Mater. Chem.* 21, 17483–17491. doi: 10.1039/c1jm12864g

Conflict of Interest Statement: The authors declare that the research was conducted in the absence of any commercial or financial relationships that could be construed as a potential conflict of interest.

frontiers in Chemistry

REVIEW
published: 17 April 2019
doi: 10.3389/fchem.2019.00252

Quantum Dots Synthesis Through Direct Laser Patterning: A Review

Francesco Antolini[1]* *and Leonardo Orazi*[2]

[1] *Photonics Micro and Nanostructures Laboratory, Physical Technologies for Safety and Health Division, Fusion and Technologies for Nuclear Safety and Security Department, ENEA, Frascati, Italy,* [2] *Department of Sciences and Methods for Engineering, University of Modena and Reggio Emilia, Reggio Emilia, Italy*

In this brief review the advances on Direct Laser Patterning (DLP) for the synthesis of photo-luminescent semiconductor quantum dots (QDs) belonging to II-VI groups, especially in solid state using laser-assisted conversion are reported and commented. The chemistry of the precursor synthesis is illustrated because it is a crucial step for the development of the direct laser patterning of QDs. In particular, the analysis of cadmium (bis)thiolate and cadmium xanthates precursors after thermal and laser treatment is examined, with a special focus on the optical properties of the formed QDs. The second part of the review examines how the laser parameters such as the wavelength and pulse duration may regulate the properties of the patterned QDs. The DLP technique does not require complex laser systems or the use of dangerous chemical post treatments, so it can be introduced as a potential method for the patterning of pixels in quantum dot light emitting diodes (QD-LEDs) for display manufacturing.

Keywords: semiconductor quantum dots (QDs), precursors, direct laser patterning (DLP), QD-LEDs, display

OPEN ACCESS

Edited by:
Tianyou Zhai,
Huazhong University of Science and Technology, China

Reviewed by:
Xian Chen,
Shenzhen University, China
Ayaskanta Sahu,
New York University, United States

***Correspondence:**
Francesco Antolini
francesco.antolini@enea.it

Specialty section:
This article was submitted to Nanoscience, a section of the journal Frontiers in Chemistry

Received: *26 October 2018*
Accepted: *29 March 2019*
Published: *17 April 2019*

Citation:
Antolini F and Orazi L (2019) Quantum Dots Synthesis Through Direct Laser Patterning: A Review. Front. Chem. 7:252. doi: 10.3389/fchem.2019.00252

SEMICONDUCTOR QUANTUM DOTS (QDs) SYNTHESIS AND PROPERTIES

Colloidal photoluminescent semiconductor nano-crystals, also referred to as quantum dots (QDs) (Grim et al., 2015; Panfil et al., 2018), have received considerable interest both from the point of view of fundamental materials research and in terms of industrial needs especially in photonics application. The growing interest in this field is due to the unique optical and electronic properties of QDs including narrow emission, broad absorption, and high photo-stability compared with the corresponding bulk materials. Accordingly, QDs have great potential for several industrial applications, such as optoelectronic devices, LEDs (Yang et al., 2015), photovoltaics (Yang et al., 2017), lasers (Supran et al., 2013), sensors (Cho et al., 2015), and bio-labeling (Woo et al., 2013).

The optical properties of this material are determined by the mobility of hole and electrons confined in nanosized structures (Rossetti et al., 1984; Brus, 1986), and this phenomenon is called quantum size effect. Due to this effect it is possible to modulate the QDs optical properties by changing their size and/or shape, and it is possible in principle to get any color of the visible spectrum by tuning the particles to the right size. This means that by controlling the condition of the synthesis it is possible to control the absorption and emission spectra of the QDs.

Various chemical synthetic routes for semiconducting quantum dots have been previously reported: in organic solvents (Yu and Peng, 2002), in aqueous media (Lesnyak et al., 2013), the "one pot mixture" more suitable for the preparation of large amounts of QDs (Williamson et al., 2015) or even in polymers (Xu et al., 2015).

In the synthesis of QDs, a very important role is played by the passivation of the QDs core. Indeed the efficient confinement of the exciton (separation of hole and electron) within the core of the QDs and the absence of non-radiative phenomena is achieved only if the surface of the QDs is well-passivated (Klimov, 2010). Effective passivation can be achieved by controlling the surface chemistry of the QDs by over-coating the QD's surface with organic or inorganic shells it is possible to obtain luminescent quantum yield higher than 80% with narrow emission spectra (Hines and Kamat, 2014). The QDs stability, both over the time and under external conditions (light, oxygen, and moisture), can also be improved by modifying their surface properties through the introduction of organic ligands or inorganic "shells" to the structures.

With the advances in synthetic procedures, coupled with the development of surface modification techniques, the optical properties of QDs has improved to the point where they are now attracting significant interest for light-emitting applications (Shirasaki et al., 2013; Supran et al., 2013; Talapin and Steckel, 2013; Kathirgamanathan et al., 2015). The main optical properties showed by the QDs can be summarized in the following concepts: color purity, color tunability, bright emission, and stability.

Color purity and tunability are a consequence of the size quantization effect, which means that the nanocrystals show different absorption and emission spectra as a function of size and shape. The possibility to control their band-gap in a wide range gives rise to the tunability of color emission. The perception of color purity of the nanocrystals is related to the width of the emission spectra, which in turn is a function of the QDs size distribution. As the variance of QD's size distribution decreases, the full width at half-maximum (FWHM) of the emission band narrows. The typical values of the FWHM of a QD solution are 20–35 nm, resulting in luminescent sources with saturated emission colors (high color purity).

Another interesting feature of QDs is that their absorption gradually increases at shorter wavelengths. Such absorption spectra allow for simultaneous excitation of QDs with different emission color using a single blue pumping light. For these reasons QDs have found application in several fields including LEDs (Talapin and Steckel, 2013), solar cells (Jun et al., 2013), field-effect transistors (Choi et al., 2016), and for *in vivo* and *in vitro* imaging sensing and labeling techniques (Valizadeh et al., 2012), where their narrow emission linewidth, efficient luminescence, and broad absorption spectra give them an advantage over organic dyes.

PATTERNING STRATEGIES OF QDs

The low-energy solution-based synthesis of QDs enables their scalability and incorporation into devices (processability) (Kathirgamanathan et al., 2015). Owing to colloidal stability and the ability to make films without disrupting the physical integrity of the crystals, the use of QDs in electroluminescent devices has become possible. Deposition techniques such as spin-coating, micro-contact printing, ink-jet printing, can be exploited to manufacture optoelectronic devices such as light emitting diodes (LEDs) and displays onto rigid or flexible substrates.

The manufacturing of displays in particular needs to pattern red-green-blue emitting QDs side-by-side at high spatial resolution. Commercial displays are formed by a matrix of a Red, Green, and Blue (RGB) areas, forming a pixel, that consecutively form the screens we are using in many devices. Therefore the industrial development of a QDs based display needs the development of an efficient way to pattern the QDs into an RGB matrix (Wang et al., 2017).

The laboratory fabrication of patterned quantum dot light emitting diodes (QD-LEDs) is mainly achieved by using spin-coating, which has some drawbacks for industrial applications. Indeed the material loss during the process is large at more than 90% (Haverinen et al., 2010) and the process cannot be used to make a multicolour pattern on a single substrate, which is a key step to developing a display.

For QD-LED displays to be commercialized, it is therefore necessary to develop manufacturing techniques to pattern different QDs based materials with (i) high spatial resolution and overall accuracy, (ii) high homogeneity, and (iii) high production rate for large scale production.

Currently several techniques can be used to pattern QDs over different substrates and can be grouped in three main classes (**Figure 1**):

1. Photolithography (PLG)
2. Contact Transfer (CT)
3. Inkjet Printing (IJP).

Photolithography (Mack, 2008) is the dominant manufacturing approach for inorganic electronics and optoelectronics. The photolithography technique for QDs display manufacturing has been shown by Ji et al. (2018) and Park et al. (2016) (**Figure 1A**). In both works the photolithographic process is the same but the difference is that Ji deposited the QDs by spin coating while Park et al. used the layer by layer deposition at micron resolution. **Table 1** summarizes the main characteristics of the photolithography.

A similar approach based on the use of mask elements for QD-LED manufacturing is the mist deposition (Pickering et al., 2012). In this technique the QDs of different colors are deposited by dispersing the liquid in small droplets that pass through different registered shallow masks obtaining a matrix of alternating pixels (Zhu et al., 2008). This method allows the deposition of QDs solutions without damaging the previously deposited layers obtaining close packed pixels in the micron range.

Displays can be realized also by using Contact Transfer (CT) patterning (Cho et al., 2015; Dai et al., 2017). This technique is also called as molding or stamp printing. Here the basic idea is to use soft elastomeric stamps to replicate patterns generated by photolithography or other patterning techniques (**Figure 1B**). The process is obtained in two stages: in the first one the solution containing the QDs is deposited onto a substrate (the donor) obtaining a film. The film is then transferred from the donor substrate to a poly-dimethylsiloxane (PDMS) structured stamp (receiver) by pressing. The QDs are finally transferred from the PDMS stamp to the device. The mold can be used to create structures or to print organic materials over different substrates

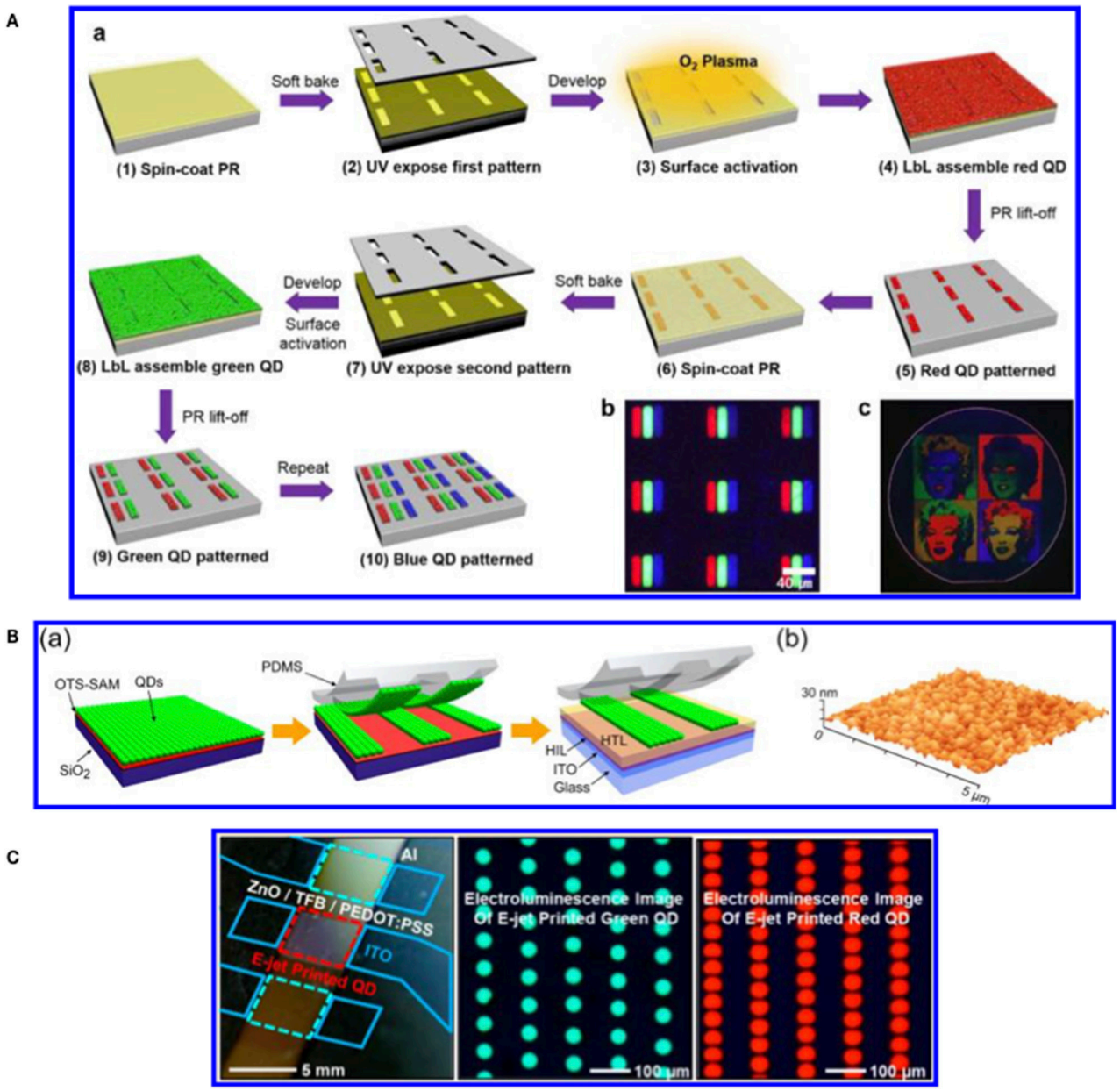

FIGURE 1 | (A) Scheme of the photolithography steps for the realization of QDs display reprinted with permission from Park et al. (2016) copyright 2016 American Chemical Society. **(B)** Diagram of the CT steps for the realization of patterning on a QD-LED reprinted with permission from Cho et al. (2015) copyright 2015 American Chemical Society. **(C)** Ink Jet Printed green and red QDs for QD-LED realization reprinted with permission from Kim et al. (2015) copyright 2015 American Chemical Society.

without using different solvents or particular functionalisation of materials (Dai et al., 2017). The molding methods have a good resolution (below 100 nm) however they need several steps in stamp preparation and chemicals to obtain the final device (**Table 1**).

The patterning by printing means that the active materials are deposited by physical contact through the use of nozzles (e.g., inkjet printheads, Wood et al., 2009; Haverinen et al., 2010; Teichler et al., 2013). The main characteristics of the printing methodology are (i) very low materials waste and (ii) easy modification of the desired pattern via software. Both characteristics contribute to lower the production costs especially for small batches. On the other side the challenges faced by ink jet printing rely on the development of suitable inks that avoid the nozzle clogging, the solvent evaporation (coffee ring effect) (Jiang et al., 2016) and improve the adhesion to the substrate (Cobas et al., 2015). The IJP is a simpler technology with respect to contact transfer and photolithography but on the other side its resolution is poorer (10–20 μm) (Menard et al., 2007) (**Table 1**). A recent development in IJP has been the introduction

TABLE 1 | Resolution and characteristics of the most common patterning techniques.

Patterning technique	Resolution	Pro	Cons
Photolithography	<100 nm	Well-established, good resolution	Many preparation steps
Molding	<100 nm	Deposition on different substrates, good resolution	Many preparation steps
Ink jet	10–20 μm	Single step, large area	Low resolution

of electro-dynamic ink jet printing (Park et al., 2010). This improved method does not require any chemical or physical pre-patterning of the substrate, and can achieve a level of lateral and vertical resolution at the submicron level. By using this variant of the IJP, the Rogers's team (Kim et al., 2015) reported the deposition of red and green QDs dispersed in organic solvents and the manufacturing of a QD-LED.

The IJP method is technologically appealing indeed JOLED (Japan OLED) in 2017 announced the production of 21.1″ 4K OLED monitors panels with Ink Jet Printing technology (https://www.oled-info.com/joled, accessed October 2018).

DIRECT LASER PATTERNING OF QDs

A potential alternative to lithographic and printing techniques is the direct fabrication or direct patterning of QDs by means of a laser. The direct laser patterning (or laser writing) refers to the ability to produce arbitrary and programmable patterns of materials in a single step (or as a few as possible) by using a laser, with a medium resolution (<5 μm) and with an easy implementation in an industrial environment (Hocheng et al., 2014).

Lasers are unique tools that can be used to modify the morphological, physical, or chemical properties of surfaces without any mechanical contact. Lasers are widely used in the industry because they can clean or sinter the surfaces, ablate (drill, cut) and print. Laser printing has been introduced to transfer the active materials from a sacrificial layer to a substrate and can be considered as a particular printing method called Laser Induced Forward Transfer (LIFT) (Wolk et al., 2004; Feinaeugle et al., 2012).

Here the Direct Laser Patterning (DLP) is referred to the use of a laser as a tool to induce a chemical reaction, thus forming the desired product onto the substrate. This use is the one that is reported in the following sections and in particular for the synthesis of QDs and their surface modification.

Materials for Direct Laser Patterning of QDs

The exploitation of laser direct patterning technology for the synthesis of QDs in solid state needs the development of suitable materials. Indeed, the molecules have to pick up the energy coming from the laser source and reorganize their structure to form QDs.

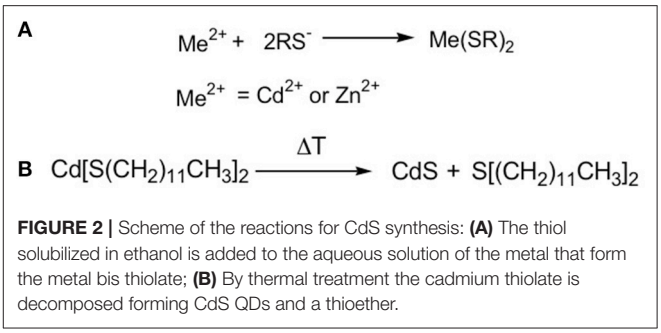

FIGURE 2 | Scheme of the reactions for CdS synthesis: **(A)** The thiol solubilized in ethanol is added to the aqueous solution of the metal that form the metal bis thiolate; **(B)** By thermal treatment the cadmium thiolate is decomposed forming CdS QDs and a thioether.

The type of molecules that can be used for laser direct patterning are the single source precursors (SSPs) that were successfully employed in the fabrication of crystalline and stable nanoparticles (Malik et al., 2010). These molecules are good candidates for direct laser patterning because the preformed bonds between the metal atom and the chalcogenide lead to the formation of nano-crystals with fewer defects. In addition, considering that the process takes place in solid state and the mobility of the atoms is reduced, in SSP the atoms are already "close" to their final position and the QDs growth can be facilitated.

In recent years raised the idea that molecules which in solid states give the nanocomposites by effect of their thermal decomposition could give QDs by the effect of laser (Antolini et al., 2006). This area of research was explored to study the formation of the II-VI QDs by several authors (Fragouli et al., 2010a; Resta et al., 2012; Agareva et al., 2015; Bansal et al., 2015).

The general approach for the evaluation of a precursor as possible candidate for laser patterning is its capacity to form QDs by thermal decomposition in solution or, better, in solid state. Some of the SSPs used for laser patterning were first evaluated for the generation of the QDs in solid state within a matrix by thermal decomposition (Antolini et al., 2005; Leventis et al., 2010; Resta et al., 2010; Dowland et al., 2011; Bansal et al., 2016), which is a common process to obtain nanocomposites.

The first molecule studied as precursor of CdS QDs under laser treatment was a chalcogenolate complex of cadmium, namely the cadmium (*bis*)dodecanthiol (**Figure 2**). This molecule was used to obtain CdS nanocomposite when dispersed in polystyrene (Antolini et al., 2005) and was selected due to its relatively easy chemical synthesis and stability in normal ambient conditions. The synthesis of this precursor, described in the literature (Rees and Kräuter, 1996), consists of a single step process: the metal salt is mixed in water/ethanol solution then the dodecanthiol, dissolved in ethanol, is added and the desired metal thiolate is formed as white precipitate (**Figure 2A**). This compound, once added to the polymer and heated at the proper time and temperature (300°C 10–15 min), produces the CdS QDs (Antolini et al., 2007, 2012) according with the reaction reported in **Figure 2B**.

When the loaded polystyrene film is treated with a laser at the wavelength of 1,064 nm, it is possible to observe the

formation of a yellow area, like in the case of thermal treatment, which is characterized by the presence of the CdS QDs (Antolini et al., 2006). Here the effect of the laser beam is an increase of the temperature within the polystyrene film, caused by the absorption of a small fraction of the energy of the 1,064 nm laser source (see next paragraph). The formation of the QDs was revealed by the typical PL emission and absorption spectra. The PL linewidth, however, is quite large suggesting the presence of many surface defects as in the case of thermal treatment of the composite (Antolini et al., 2007).

The Athanassiou research group treated the same compound with two different laser sources at 266 nm and 355 nm, because these wavelengths match the absorption spectrum of the compound, so that the laser energy can be adsorbed directly by the precursor (Fragouli et al., 2010b). In these works Fragouli et al. (2010b) showed the importance of the choice of laser wavelength for the QDs formation in a PMMA matrix. Indeed, by using a laser source at 266 nm the resulting PL spectrum shows a broad emission centered at about 560 nm, while in the case of a similar treatment carried out with a laser source at 355 nm, it displays a sharper emission at about 500 nm. The emission broadening suggests the presence of many surface defects when the 266 nm laser source is used. The formation of the defects over the CdS QDs is caused by the higher reactivity of the PMMA under the 266 nm radiation. Indeed, the PMMA is damaged by the 266 nm wavelength and its decomposition products react with the growing QDs stimulating the formation of the QDs surface defects. When the used laser is at 355 nm, where the PMMA is transparent, the decomposition compounds are not created and the PL emission of the CdS QDs is sharper (Fragouli et al., 2010b). The effect of the presence of the PMMA, under 266 nm laser (15 ns pulse) treatment, was studied by the Bityurin group. Agareva et al. (2015) observed that without the PMMA the PL emission of the generated CdS QDs was always centered at about 600 nm independently from the number of pulses (from 1 to 50) and laser fluence (from 150 to 290 mJ/cm^2). On the contrary when the laser treatment was carried out on PMMA loaded with the precursor the PL maxima of the formed QDs are blue shifted (from 600 nm to about 500 nm) from low to higher laser fluences (from 150 to 290 mJ/cm^2). This suggests that the presence of a matrix influences the amount of the defects during the QDs growth.

The effect of both wavelength is not only the formation of the QDs but also their size modulation. Indeed Fragouli et al. (2009) observed that in both conditions the PL emission is red shifted by increasing the number of pulses. This observation suggests that enhancing the deposited energy the QDs size increases. The main difference between the two laser wavelengths is that at 266 nm the QDs are formed faster than at 355 nm. This effect is due to the different level of absorption of the radiation from the precursors that at 266 nm is high while at 355 nm is low.

However, the main drawback of this Cd-based system lies in the chemistry of the precursor, because it is insoluble. Its insolubility is a critical point for the practical application of the laser patterning of QDs, because the QDs formation and their optical properties would be not homogeneous through the film itself and then the spatial resolution of the patterning would be

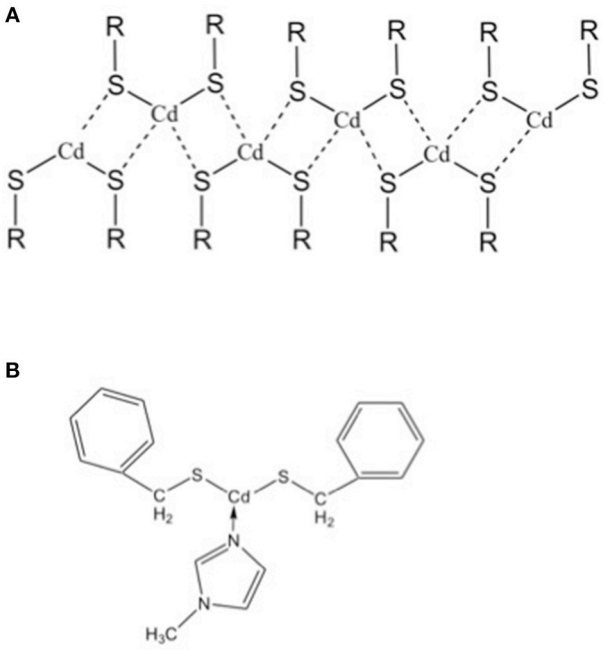

FIGURE 3 | (A) Inorganic polymer structure of cadmium bis-thiolate. **(B)** Molecular formula of cadmium bis benzilthiolate functionalised with the 1-N-methylimidazole that avoid the formation of the inorganic polymer showed in "a," because it blocks the free orbitals for the coordination with sulfur atoms of the neighboring molecules.

decreased. The insolubility of the cadmium *bis*(dodecathiolate) is due to the formation of inorganic polymeric structures of the precursor, as a consequence of the strong bonds between the Cd atom and the lone pairs of sulfur atoms of the neighbor molecule (**Figure 3A**) (Dance, 1986). In general, these inorganic chains can be broken blocking the cadmium free orbitals using suitable ligands. In the particular case of the cadmium (*bis*)thiolates this issue was solved from the group of Tapfer (Resta et al., 2010) by introducing a new cadmium bis thiolate molecule, namely cadmium *bis*(benzilthiolate), functionalised with the 1-N-methylimidazole (MI). The role of the MI ligand is to block the free Cd orbitals with the nitrogen lone pairs beard by the MI so that the molecule cannot coordinate with its neighbors (**Figure 3B**). The molecule inside the polymer will interact only by weak chemical interactions such as Van der Waals forces, that can be broken by the organic solvents.

This precursor was successfully used by the Tapfer group to study more deeply the correlation between the energy deposited by the laser on the polymer/precursor film and the nanoparticle defects within the PMMA matrix (Resta et al., 2012). In this work the sample is treated with a 355 nm laser source changing in a systematic way the laser fluence and number of pulses. The results showed that the laser fluence drives the number of QDs while the number of pulses regulates the broadening in the size distribution. The laser fluence can be regarded as the temperature of annealing that determines the nucleation of the QDs while the total number of pulses modifies the size and shape distribution. Indeed, at higher fluencies the

PL signal at about 395 nm is more intense, suggesting the presence of a higher number of QDs. When the number of pulses are increased under the same lasing conditions, the low energy emission band at about 500 nm increases, suggesting the defect formation.

A clear correlation between the laser energy deposited in the film and the particle size modulation was reported in the work of Camposeo et al. (2012). In this work a femtosecond laser source operating at around 800 nm was used and the energy delivery to the sample was mediated by a multi-photon process. Here it is shown that the PL emission is red shifted by increasing the fluence of the laser treatment. The PL emission of the QDs is formed by two contributions: the band edge emission centered at about 450 nm and the defects emission between 550 and 600 nm (shallow defects and deep trap states). Starting from the red shift of the band edge emission it is possible to calculate the size of the QDs as a function of the fluence: it was found that the QDs size changes from 5 to 8.5 nm varying the fluence from 0.15 to 0.45 J/cm^2.

The solubility of the precursors is not the only chemical parameter to take into account in view of their application for a device manufacturing; indeed the decomposition temperature is another key parameter. The cadmium *bis*-dodecanthiol has a decomposition temperature of about 300°C that is too high when the decomposition is carried out within a polymer, because the organic matrix can decompose or be damaged. In addition, if the thermal/laser treatment has to be carried out in an electrical-driven multi-layer device, severe treatment conditions can damage the overall system. So it is necessary to explore other classes of molecules that decompose at lower temperatures as possible candidates for laser patterning.

The xanthate molecules are another class of molecules that could be exploited for laser patterning because they can be easily solubilised in organic solvents and have decomposition temperatures below 200°C (**Figure 4A**) (Stroea et al., 2015). The use of xanthate molecules for QDs production has been proposed by Pradhan et al. (2003). The xanthates are characterized by the bond between the oxygen and the carbon which in turn is linked to the sulfur that coordinates the Cd atom. In the case of cadmium ethylxanthate, the bipyridil molecule is added to improve its solubility. The use of longer alkyl chains, like the buthyl chains, improves the solubility of the xanthates, that are preferred to form CdS QDs (**Figure 4B**) (Stroea et al., 2015).

These molecules present another interesting advantage: indeed their thermal decomposition gives rise to CdS QDs, while the reaction products undergo to fragmentation with the final formation of volatile compounds (**Figure 5**) (Pradhan et al., 2003).

This behavior is important, because in the case of QDs formation within a matrix or a device, no other compounds apart QDs should be present in the medium. In **Figure 5** the OCS molecule and the olefin are the volatiles compounds leaving the matrix (Chugaev mechanism) during the heating.

The xanthate molecules were tested as materials for laser patterning and the preliminary results showed the formation of QDs from cadmium dibuthyl xanthate (Račiukaitis et al., 2013). In this case, by changing the energy dose of the laser, it is possible to modulate the color of the precursors from faint yellow to deep yellow suggesting that the QD's size can be modulated by the deposited energy. (**Figure 6A**). However, the CdS QDs are not the best candidates for the luminescent emission even when produced by solvothermal methods due to the presence of many surface defects (broadening of PL emission spectrum) and low emission in the visible range. The CdSe QDs were therefore explored as new candidates, because they show better optical properties, including less surface defects and a wider spectrum of emission in the visible spectral range (Regulacio and Han, 2010). These characteristics enable their use in light emitting devices like QD-LEDs.

The criteria for the selection of the precursors of CdSe QDs were the same as for CdS QDs: (i) solubility in organic solvents, (ii) decomposition temperature below 300°C, and (iii) a relatively easy protocol of synthesis and compound stability. This condition will be an important factor for cost reduction in case of industrial applications. A single source CdSe QDs precursor, which combines all these characteristics, is the cadmium 2-(N,N′ dimethylamino) ethylselenolate (CdDMASe, **Figure 7**) (Kedarnath et al., 2006).

This precursor has been successfully used for the laser induced synthesis of QDs alone (Račiukaitis et al., 2013) and in combination with a small organic molecule like TPBI (Bansal et al., 2015). Račiukaitis et al. showed a correlation between the laser energy dose and the average size of the QDs. The first qualitative evidence was the formation of different colors under laser treatment at 266 nm when the CdMASe is deposited as a neat film. As the laser power increases the color of the film becomes darker: the more reddish/brown color is correlated with a higher amount/size of the CdSe QDs (**Figure 6B**). The change of the QDs size as a function of the laser energy was revealed by TEM measurement when CdSe QDs were grown in combination with a polyfluorene like film. **Table 2** shows that the CdSe QDs grown by laser form clusters containing 10–20 QDs and their size increases from 6 to 10 nm when the delivered energy is enhanced, as expected.

The Samuel research group used the same precursor coupled with electroluminescent polymers, such as polyfluorene and TPBI, to study the CdSe QDs growth after thermal (Bansal et al., 2014) and laser (Bansal et al., 2015) treatment. The study of the PL spectra from the polyfluorene/CdSe QDs and of the polyfluorene/CdS QDs showed that the PL emission is strongly dependent from the arrangement of the HOMO-LUMO levels of the polymer and the nanocrystals (Todescato et al., 2016). In particular the CdSe/polyfluorene system (Bansal et al., 2014) is photoluminescent, but its CdS counterpart is not emissive. This behavior is due to the arrangement of the HOMO-LUMO energy levels of the polyfluorene/CdSe, that allows the exciton shift from the polymer to the QDs (Type I system) with the emission of one photon (**Figure 8A**). On the contrary the polyfluorene/CdS system did not show any QDs emission because the HOMO-LUMO levels are arranged like a Type II system, where the hole and electron are displaced in two different materials so that the charge recombination cannot take place (**Figure 8B**).

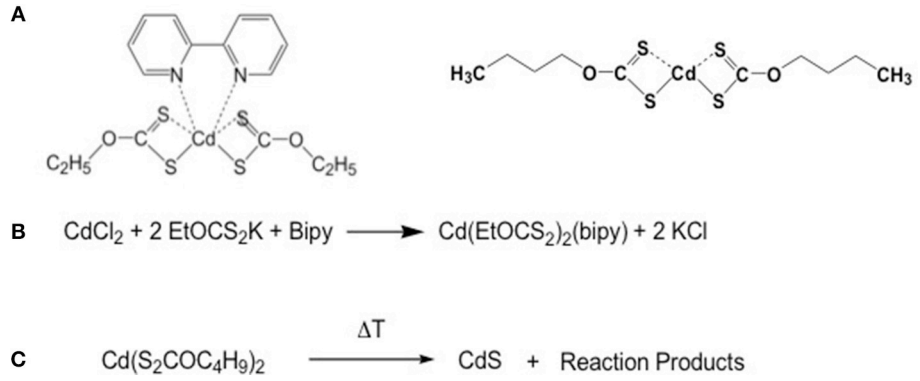

FIGURE 4 | (A) Structural formula of cadmium diethylxantahte and dibuthylxanthate; **(B)** Scheme of the synthesis of cadmium diethyl xanthate; **(C)** Decomposition scheme of the cadmium diethylxanthate.

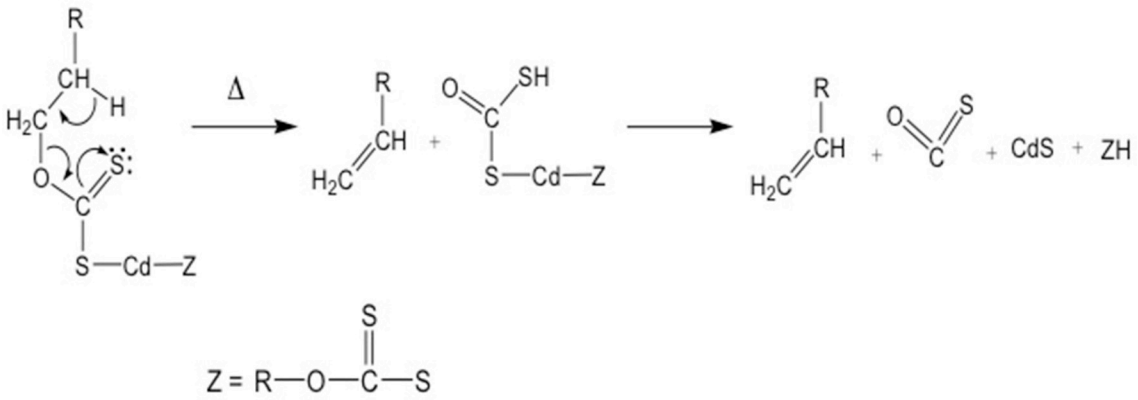

FIGURE 5 | Decomposition path of the xanthate metallorganic compounds following the Chugaev mechanism.

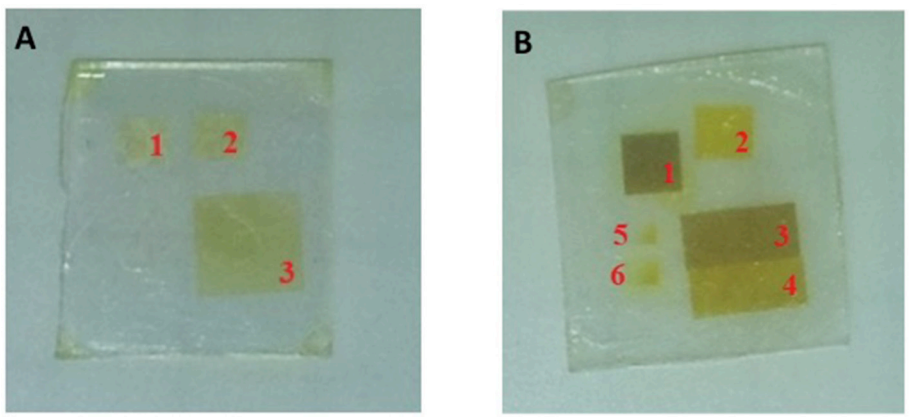

FIGURE 6 | (A) Cadmium dibuthylxanthate film irradiated with a 266 nm, 10 ps, 100 kHz laser source at different average power: 1–25, 2–30, 3–35 mW. **(B)** CdMASe film irradiated with a 266 nm, 10 ps, 100 KHz laser source at different average power: 1–20, 2–8, 3–15, 4–10 mW, 5-6 dot matrix tests.

This evidence is even more pronounced when the TPBI matrix is used instead of polyfluorene, as shown by Bansal et al. (2015). In this case the distribution of the HOMO-LUMO levels of CdSe QDs and the organic matrix is still more favorable for the energy transfer between TPBI and CdSe. In this matrix the photo-luminescent quantum yield (PLQY) of

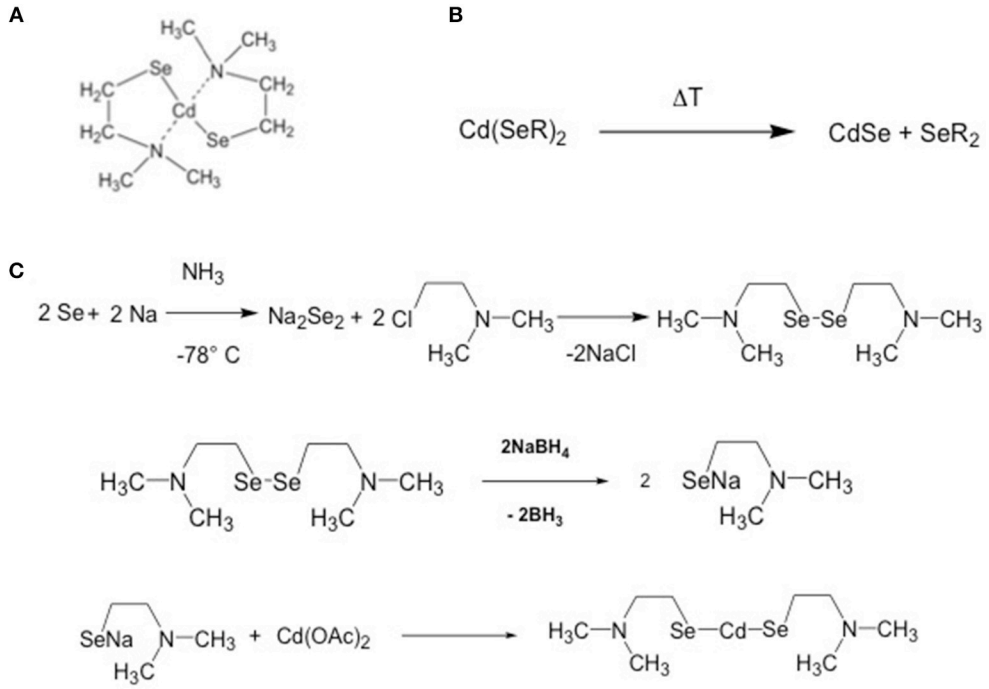

FIGURE 7 | (A) chemical structure of the CdDMASe **(B)** formation of the CdSe QDs after backing; **(C)** scheme of the synthesis of the CdDMASe.

TABLE 2 | QDs parameters in Polyfluorene derived polymer/CdDMASe film after ps-laser treatment at 266 nm (With permission of Račiukaitis et al., 2013).

Power (mW)	Scan speed (mm/s)	Cluster size (number of QDs)	QDs size (nm)
20	1.0	10–20	6.0 ± 1.1
35	1.0	10–30	10.2 ± 4.4

the CdSe QDs increases up to 15.5% (annealing at 160°C for 15 min). With this new system finally it was possible to obtain the visible PL emission from the laser patterned QDs (**Figure 9**). The best laser patterning conditions were found on the basis of the PL response. This was done by building a matrix of pulse energy vs. number of pulses (**Figure 9A**), then selecting the best speed of patterning (**Figure 9B**) and finally drawing the logo (**Figure 9C**). The emission properties of the patterned areas are similar to the ones obtained with backing.

The mechanism of the QDs formation is still under investigation. However, the use of UV laser (266 nm and 355 nm) radiation, that is absorbed by the CdS and CdSe precursors, points toward a photochemical breaking of the carbon and chalcogenide bonds and then favors the reorganization of the atoms to form the nanocrystal. The Bityurin group (Smirnov et al., 2018) has recently deeply investigated the mechanism of formation of the CdS QDs from a precursor under thermal or photochemical activation. Here a dithiobiuret complex of cadmium embedded in the PMMA matrix is decomposed under a UV light treatment at different temperatures. The UV radiation helps the formation of the QDs and the lack of results under furnace treatments at the same temperature suggests that the QDs growth is mainly a photochemical process rather than a thermal process. This means that the UV lasers can affect the synthesis also by the interaction of the energetic photons directly on the precursor.

Recent results about QDs synthesis by using a 532 nm laser has been presented by Morselli et al. (2016). Here the used precursor is the zinc acetate for the production of zinc oxide after laser treatment. The authors reported the formation of the ZnO QDs with unknown volatile compounds being formed as a by-product, but the chemistry of the process is still not clarified.

Another strategy to pattern QDs using lasers is to modify the adhesion characteristic of the substrate with respect to the QDs (Chen et al., 2017b). A two stage process was demonstrated by selectively patterning perovskite based QDs on glass surface. The process involved a 405 nm UV continuous laser and a following washing step to remove, by dissolution, the untreated QDs and obtaining patterned regions. However, in this approach, the QDs are prepared "*ex situ*" and deposited over a substrate and the role of the laser is to modify only the adhesion of the QDs over the substrate and not their synthesis. Indeed, the laser action removes the organic ligands around the QDs surface modifying their ability to bind the surface. In general, the effect of the laser is 2-fold: first it decreases the PL emission with respect to the untreated perovskite QDs and, secondly, the laser fluence causes also the QDs size modification.

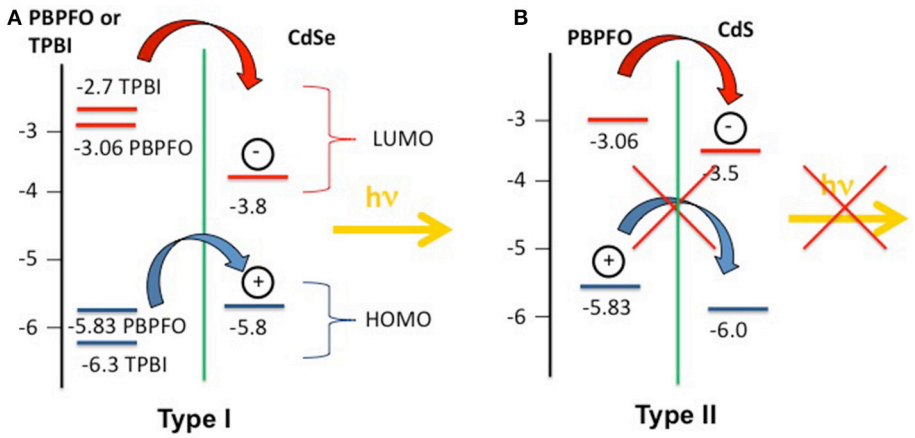

FIGURE 8 | (A) The type I system formed by PBPFO and CdSe and TPBI/CdSe energy levels. In the so called Type I configuration the HOMO-LUMO levels of the CdSe QDs are encompassed by the HOMO-LUMO levels of the PBPFO or TPBI. **(B)** The type II system formed by PBPFO and CdS energy levels. When the HOMO-LUMO levels of the CdS and PBPFO are staggered the resulting system belong to the so called Type II system.

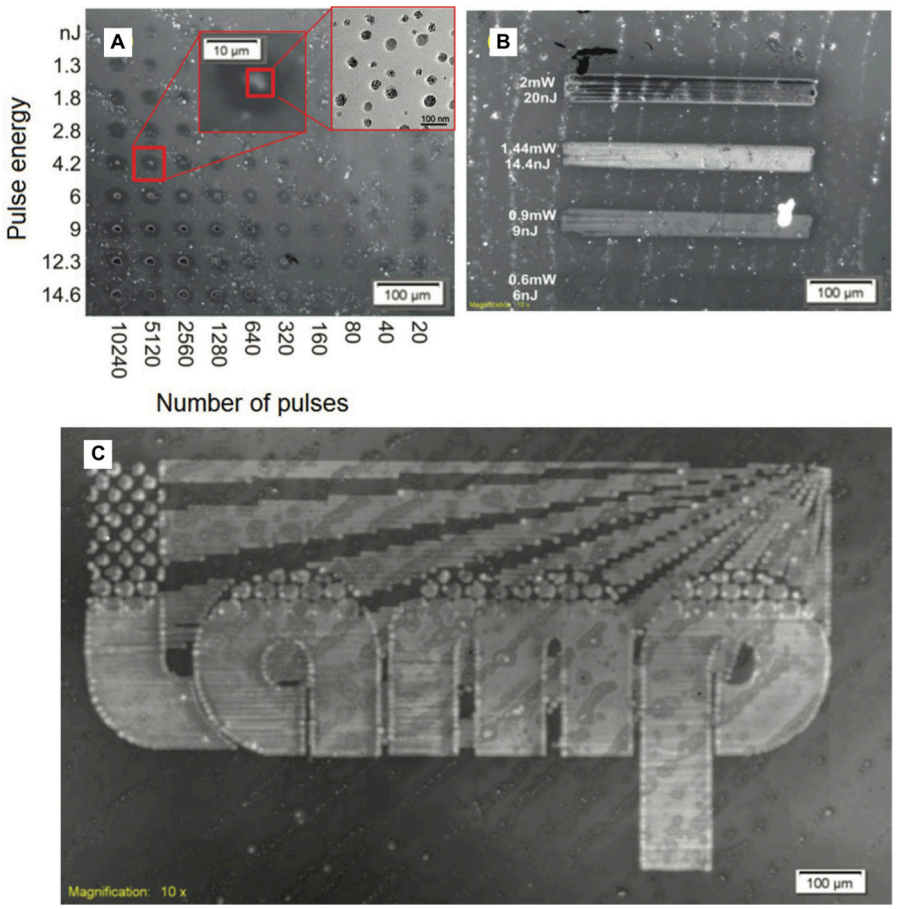

FIGURE 9 | Laser fluorescence image of **(A)** dot matrix to find the optimal conditions of the laser source; **(B)** laser scanning at different mean power, and **(C)** scanning of a logo by using 1.05 mW average power, 100 KHz, 10.5 nJ, and a speed of 0.75 mm/s laser parameter (Bansal et al., 2015).

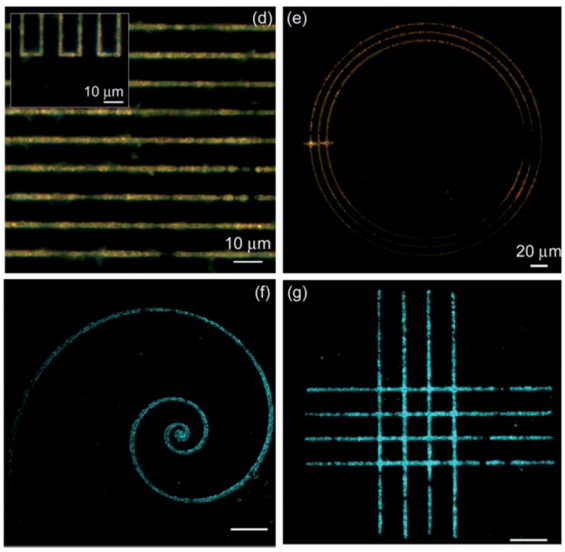

FIGURE 10 | Different geometric patterns obtained by Camposeo et al. (2012) scanning at 0.2 mm/s with an incident fluence of 0.2 J cm^{-2} (With permission of Camposeo et al., 2012).

Laser Patterning of QDs: the Effect of the Pulse Duration and Wavelength

The examples in literature to induce QDs formation/modification by laser can be categorized by time operating regime: from continuous wave to the femtosecond range, and by laser wavelength: from near infrared (NIR) solid state laser to fourth harmonic UV laser. This broad range of patterning methods suggest that different physical phenomena drive the process, from thermal annealing to "cold" photochemical process.

About wavelength, the first example of QDs generation was obtained with a high power Nd:YAG using 10 to 50 ms pulses with an estimated fluence of about 16 kW/cm^2 (Antolini et al., 2006). Such high fluence had to cause the complete degradation of the polymer film; in order to explain the reported successful results, the very low absorptivity of polystyrene matrix at the 1,064 nm wavelength of Nd:YAG laser should be taken in account. Moreover, the used NIR laser can be considered as a local heating source and the process is essentially a thermal one, like in Hu and Wu (2013).

Another example of the use of near IR lasers is presented in Camposeo et al. (2012), where a 200 femtoseconds laser operating at about 800 nm is used. In this case the absorption of precursors in the near IR is almost negligible and authors suggest that a multiphoton absorption mechanism take part in the growth of QDs. In any case, the use of an ultrashort laser avoids thermal effects and permits, thanks to the use of an oil-immersion large aperture objective, the ability to generate very fine and detailed patterns with micrometric resolutions (**Figure 10**).

An example of the use of a second harmonic continuous Nd:YAG laser to generate QDs in solution is presented in Lin et al. (2005). In this work, high-quality CdSe QDs were prepared by irradiating an aqueous solution at 532 nm, the same wavelength was used in Morselli et al. (2016) to synthesize ZnO nanoparticles in PMMA/$Zn(OAc)_2$ films. Even though these nanoparticles were not generated to operate as QDs, the results demonstrates the possibility to pattern a film with a laser operating at 532 nm, as already shown in Qayyum et al. (2016).

Račiukaitis et al. (2013) and Singh et al. (2018) operated in the UV range. In particular Račiukaitis et al. (2013) investigated the effects of the 266 nm fourth harmonic UV picosecond laser patterning of polymer/precursor blends, obtaining color change in the laser treated areas of precursors and QDs size modulation as function of laser fluence as discussed in the previous paragraph.

In (Singh et al., 2018) QDs are generated in TGA capped CdTe using the second harmonic of a Ti-sapphire laser. The authors described the QDs generation as a thermal process, but in this case the medium is liquid and QDs generation is strictly connected with the use of the laser wavelength in the UV range (380–415 nm), while no effects were measured using the first harmonic (800 nm). This behavior suggests the presence of a photochemical phenomenon rather than a thermal one.

Laser induced QDs generation in a different matrix was demonstrated in Voznesenskiy et al. (2015) in which CdS QDs in porous silica was successfully modified changing their dimensions by agglomeration when irradiated at fluence higher than 0.1 J/cm^2 at 405.9 nm. The process effectiveness depends on the right choice of laser parameters. Moving to other semiconductors, in Qayyum et al. (2016) authors show the generation of uniformly distributed Ge/Si QDs by laser patterning of a Ge coated Si substrate with the second harmonic at 532 nm of a Nd:YAG laser with a pulse duration of 10 ns. In this case the higher absorptivity of Ge compared to Si at this wavelength opens an operating window between 92 and 115 mJ/cm^2 in which very uniform and densely distributed QDs are generated with mean diameters between 20 and 40 nm and height between 4 and 10 nm, (**Figure 11**). The authors proposed a simple phenomenological model of the QDs formation under these experimental conditions.

Pulse Duration

About the time distribution of the laser intensity, modern laser sources permit operation from the continuous regime to Q-switched pulsing (ns regime) to mode locking (ps and fs regimes). All these operating regimes can be used to generate QDs.

Continuous Regime

Continuous regimes as in Lin et al. (2005) and long pulses regime as in Antolini et al. (2006) for QDs generation in aqueous solutions and for the generation of QDs starting from precursors embedded in thick polymer films, respectively, are examples of laser induced thermal activation. In these cases, the temperature is locally raised by heating the material, thanks to the absorption of the laser intensity in the film thickness. The absorption, assuming that the laser scattering is negligible, will follow the

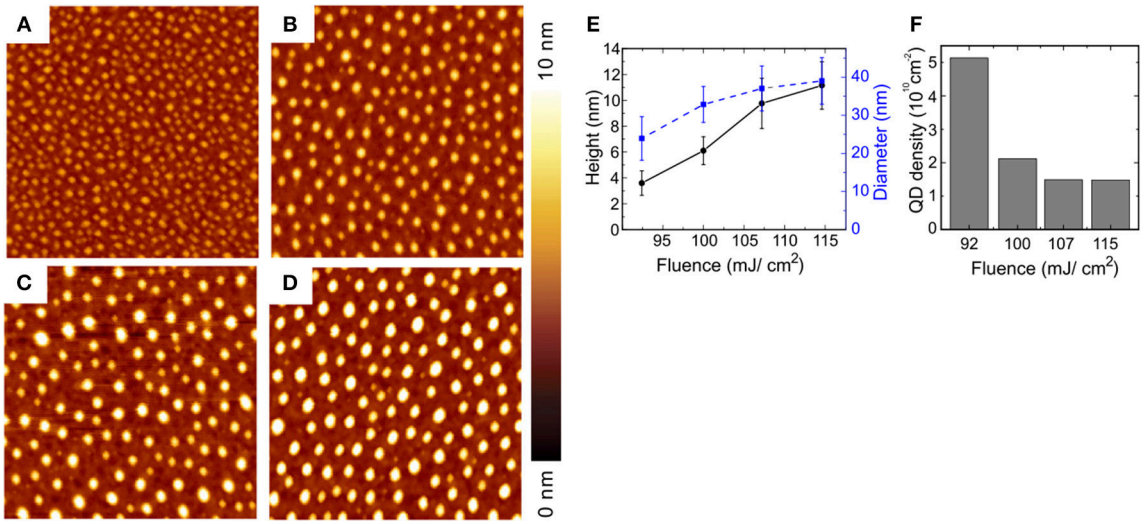

FIGURE 11 | Laser induced Ge/Si QDs obtained by patterning a thin (0.9 nm) Ge coating on Silicon substrate with different fluences, **(A)** 92 mJ/cm^2, **(B)** 100 mJ/cm^2, **(C)** 107 mJ/cm^2, **(D)** 115 mJ/cm^2. The dimension of AFM maps is 1 × 1 μm (With permission of Qayyum et al., 2016).

general formula:

$$I\left(x,y,z,t\right) = (1-R)\ I_0(x,y,t)\ \left(1-e^{-\alpha z}\right)$$

where $I_0(x, y, t)$ is the laser intensity spatial and temporal distribution on the material surface expressed in W/m^2, z is the depth in the polymer thickness in m, R is the film reflectivity at the laser wavelength and α is the material absorptivity expressed in m^{-1}.

The heat flux absorbed by the material under patterning is distributed by conduction, following the usual Fourier equation:

$$C_P\ \rho\ \frac{\partial T}{\partial t} = \frac{\partial}{\partial x}\left(K\frac{\partial T}{\partial x}\right) + \frac{\partial}{\partial y}\left(K\frac{\partial T}{\partial y}\right) + \frac{\partial}{\partial z}\left(K\frac{\partial T}{\partial z}\right) + \alpha\ I(t)$$

in which C_P is the specific heat in $J\ kg^{-1}\ K^{-1}$, ρ is the material density in kg/m^3, K is the thermal conductivity in $W\ m^{-1}\ K^{-1}$ and $\alpha\ I$ is the heat source in W/m^3.

Selective patterning with long pulses or in continuous wave mode is strongly influenced by thermal diffusivity and under these regimes fine details cannot be obtained.

Q Switched Regimes

Short pulses in the ns range can be obtained with Q-switch modulated laser. In Athanassiou et al. (2007) CdS QDs in TOPAS are generated by the use of XeCl excimer laser at 308 nm, pulse duration of 30 ns, fluence of 100 mJ/cm^2, and a repetition rate of 1 Hz. A strong correlation between the number of irradiation pulses and PL emission (from 490 to 501 nm) was observe and confirmed that larger QDs size growth when the deposited energy is increased. The correlation observed also between the total number of pulses and the PL intensity indicated that the increase of the pulses number enhances the emission broadening and the surface defects.

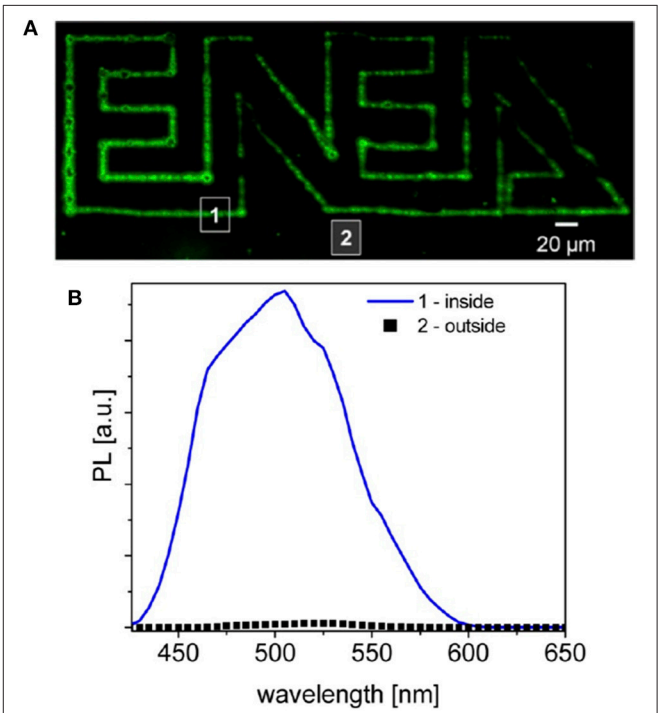

FIGURE 12 | Resta et al. (2012) Laser processing of $[Cd(SBz)_2]_2$·MI/PMMA with a fluence of ∼ 700 mJ/cm^2. In **(A)** the fluorescence emission of the patterned polymer under excitation at 405 nm. In **(B)** the spectral emission (With permission of Resta et al., 2012).

Fragouli et al. investigated both the effects of polymer matrix (Fragouli et al., 2010a) and laser wavelength (Fragouli et al., 2010b) on the formation of CdS nanocrystals in PMMA and TOPAS matrix. In particular, an 8

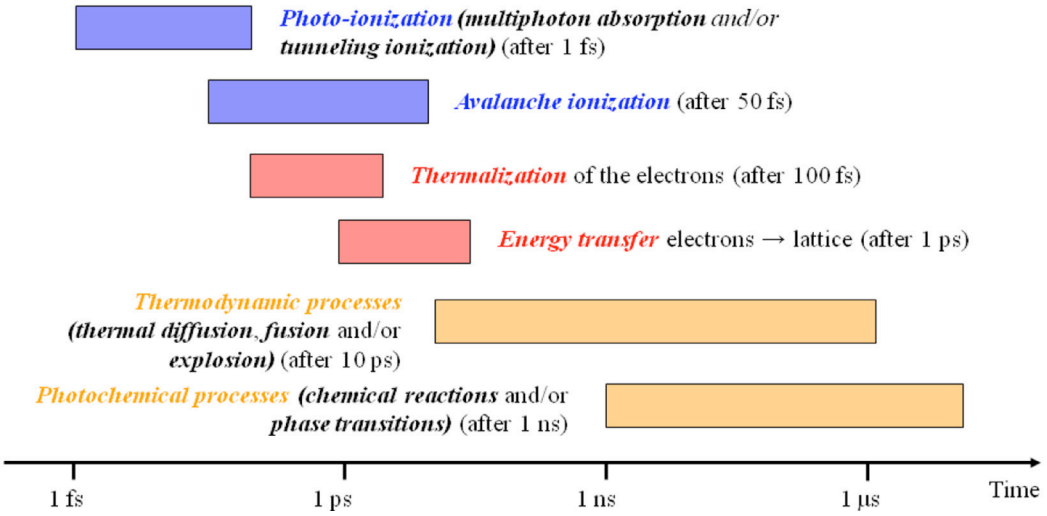

FIGURE 13 | Timescales in laser matter interaction, adapted from Royon et al. (2011) (With permission of the authors).

ns pulsed Nd:YAG laser operating at third (355 nm) and fourth harmonic (266 nm) was implemented, cumulating pulses to tune the QDs emission as already discussed (section Materials for direct laser patterning of QDs).

The use of laser induced generation of nanoparticles was investigated also in Onwudiwe et al. (2014a) for ZnS in polyvinylpyrrolidone and in Onwudiwe et al. (2014b) for CdS in PVA.

While in the previous works the accuracy and the resolution attainable by using short pulsed laser were not investigated by operating in liquid phase, in Resta et al. (2012) a PMMA polymeric film with CdS precursor was selectively patterned with a third harmonic laser ($\lambda = 355$ nm, $\tau = 10$ ns) and a minimum focused spot of 10 µm (**Figure 12**).

Mode Locking Regimes

In recent years the ultrafast lasers operating in mode-locking has become cheaper, more compact, more reliable and highly operable, thus opening a broad range of scientific, industrial, and medical applications recognized also by the 2018 Nobel prize in physics (The Nobel Prize in Physics, 2018).

Laser sources with pulse duration shorter than few picoseconds are currently available for both scientific and industrial applications. Under this operating regime light/matter interaction is completely different from what is seen in continuous or short pulse lasers. A scheme of the laser/matter interaction at the different timescales is presented in **Figure 13**, from Royon et al. (2011) below 1 ps no energy is transferred from ionized/thermalized electrons to the molecules in the solid lattice, and thermal diffusion only starts to operate after about 10 ps. Until this point, the temperature of electrons and the lattice are different and hence the system must be described by the so-called two temperature model (Anisimov et al., 1974).

$$C_e \frac{\partial T_e}{t} = \frac{\partial}{\partial x}\left(K_e \frac{\partial T_e}{\partial x}\right) + \frac{\partial}{\partial y}\left(K_e \frac{\partial T_e}{\partial y}\right) + \frac{\partial}{\partial z}\left(K_e \frac{\partial T_e}{\partial z}\right) + \Gamma\,(T_l - T_e) + \alpha\, I\,(t)$$

$$C_l \frac{\partial T_l}{\partial t} = \frac{\partial}{\partial x}\left(K_l \frac{\partial T_l}{\partial x}\right) + \frac{\partial}{\partial y}\left(K_l \frac{\partial T_l}{\partial y}\right) + \frac{\partial}{\partial z}\left(K_l \frac{\partial T_l}{\partial z}\right) + \Gamma\,(T_l - T_e)$$

In this model the laser source $\alpha\ I$ interacts with electrons, the temperature T_e of the electrons and T_l of the lattice will depend by the respective conductivities K_e and K_l and by $\Gamma\ (T_l - T_e)$, the electron-lattice coupling term that describe the heat flux between electrons and lattice. In this classical model the conduction in lattice can be normally neglected compared to electrons $K_e \gg K_l$. The pulse duration of 10 ps can be considered a general threshold for the ultrashort pulsed regime, in which both physical and chemical effects on molecules take part after the end of the irradiation, and the normal pulsed regime, where molecules and lattice transformations occur during the pulse duration. By operating below this pulse duration, it is possible to obtain a high spatial accuracy, theoretically below the diffraction limit if the process threshold is close to the maximum intensity in the center of the laser spot.

As already cited (Camposeo et al., 2012) proposed the use of a very short 180 fs laser at 800 nm to achieve direct laser writing of high resolution patterns of CdS QDs in TOPAS®-C12 films. Three-dimensional silver nanostructures with dimensions of nanometers have also been patterned by Vora et al. (2012) in polyvinylpyrrolidone with the use of a 50 fs Ti:sapphire laser operating in the first harmonic.

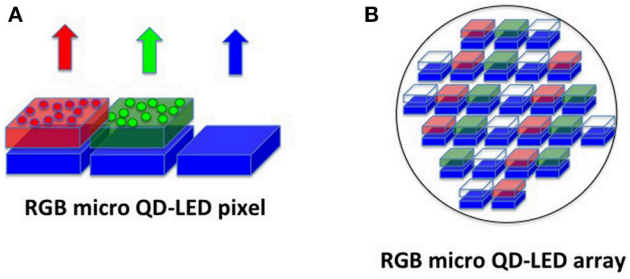

FIGURE 14 | Illustration of the principle for the formation of a RGB pixel driven by three blue micro-LED/OLEDs covered with red and green QDs **(A)**. The manufacturing of a matrix of a large number of blue micro-LED/OLEDs patterned with red and green QDs form a display **(B)**.

Račiukaitis et al. (2013) operated with the IV harmonic at 266 nm, 10 ps pulse, of a .Nd:YAG laser generating QDs in electroluminescent polyfluorene like polymers films, and they were able to determine the relationship between QDs size and laser parameters using TEM (see section Materials for direct laser patterning of QDs).

CONCLUDING REMARKS

The direct laser patterning of QDs has a great technological potential because it combines three main concepts:

i) Laser light can stimulate growth of QDs in the solid state in selected areas of the irradiated materials;
ii) The laser light can be suitably modulated (wavelength, pulse energy, repetition rate etc) to tune the particle size;
iii) The QDs modify their chemical-physical properties as a function of their size/shape.

These three concepts: the "possibility to drive the position of photons," the "possibility to modulate the energy distribution of the photons," typical of laser writing process and the "possibility to modulate the photophysical properties of the QDs as a function of their size," typical of the nanomaterials can be exploited in several fields of the science and technology and in this review is envisaged its possible application in the manufacturing of QD-based displays.

Indeed, in display technologies it is necessary to pattern in selected areas of a surface the red, green, and blue subpixels in order to obtain a RGB matrix that can be realized by using the suitable precursors and laser parameters. In this case the QDs would be conveniently used as color converter materials, as already reported for displays application (Steckel et al., 2015; Chen et al., 2017a).

A further step ahead can be done considering that recently micro-LED sources become available so that they can be used as RGB pixels in a display (Wu et al., 2018). However, this technology suffers from several disadvantages for mass production, because the main difficulty is to produce green and red micro-LED efficiently and at low prices in the same substrate. A possible solution to cover this so-called "green gap" is to employ a blue micro-LED array and to pattern over it the red and green color converters, constituted by QDs (Han et al., 2015; Lin et al., 2017) generated directly by the laser writing process with high precision and resolution (**Figure 14**).

These basic concepts, such as blue micro-displays and laser patterning of QDs, are nowadays implemented by the EU project MILEDI, (www.miledi-h2020.eu) for a display manufacturing by using lasers.

It is worth-noting that in this review the direct laser patterning and its technological exploitation was discussed in terms of Cd based QDs because they are the best-developed and well-characterized materials, and their optoelectronic properties cover the entire visible spectrum. Indeed the Cd based QDs benefit from a well-known synthesis route, that allows a PLQY almost at unity with a quite narrow FWHM (20–30 nm) (Christodoulou et al., 2014).

However, the main drawback of these materials is their content of heavy metals, that has been limited by recent regulation, as, for example the EU Directive 2002/95/EC 2003. This limitation was also considered in the recent project MILEDI taking into account, as an alternative to the heavy metal based QDs, the ternary alloys like $CuIn(S, Se)_2$ and $AgIn(S, Se)_2$, that provide light emission extending in all the visible spectrum up to the NIR.

Finally Scalbi et al. (2017) studied the environmental impact, by means of the Lyfe Cycle Assessment methodology, of a QD-LED including the CdS QDs made by laser and embedded in a electroluminescent polymer like polyfluorene. Surprisingly the final results showed that the hotspots for the environmental impact are the polymer synthesis and ITO electrode manufacturing. Indeed, the use of catalysers such as Palladium and of solvents like the hexane for the synthesis of polyfluorene have a major environmental impact on device life.

These results are encouraging for a further exploration of this approach for display manufacturing by using direct laser patterning methodology and QDs even containing heavy metals.

AUTHOR CONTRIBUTIONS

FA is the coordinator of the work and involved LO for the laser patterning section.

FUNDING

This work is part of the MILEDI project funded by one of the calls (H2020-ICT-2017-1) under the Photonics Public Private Partnership (PPP). European Commission H2020 project Grant number 779373.

ACKNOWLEDGMENTS

This paper is supported by European Union Horizon 2020 research and innovation programme under Grant Agreement in 779373, project MILEDI (MIcro quantum dot Light Emitting diode and organic LEDs DIrect patterning). The authors thank Dr. R.M Montereali, Prof. I.D.W. Samuel for their useful suggestions. and Dr. Jonathon Harwell for his support on manuscript revision.

REFERENCES

Agareva, N., Smirnov, A. A., Afanasiev, A., Sologubov, S., Markin, A., Salomatina, E., et al. (2015). Properties of Cadmium-(bis)dodecylthiolate and polymeric composites based on it. *Materials* 8, 8691–8700. doi: 10.3390/ma8125487

Anisimov, S. I., Kapeliovich, B. L., and Perelman, T. L. (1974). Electron emission from metal surfaces exposed to ultrashort laser pulses. *J. Exp. Theoret. Phys.* 39:375.

Antolini, F., Burresi, E., Stroea, L., Morandi, V., Ortolani, L., Accorsi, G., et al. (2012). Time and temperature dependence of CdS nanoparticles grown in a polystyrene matrix. *J. Nanomater.* 2012:815696. doi: 10.1155/2012/815696

Antolini, F., Ghezelbash, A., Esposito, C., Trave, E., Tapfer, L., and Korgel, B. A. (2006). Laser-induced nanocomposite formation for printed nanoelectronics. *Mater. Lett.* 60, 1095–1098. doi: 10.1016/j.matlet.2005.10.093

Antolini, F., Luccio, T. D., Laera, A. M., Mirenghi, L., Piscopiello, E., Re, M., et al. (2007). Direct synthesis of II–VI compound nanocrystals in polymer matrix. *Phys. Status Solid.* 244, 2768–2781. doi: 10.1002/pssb.200675608

Antolini, F., Pentimalli, M., Di Luccio, T., Terzi, R., Schioppa, M., Re, M., et al. (2005). Structural characterization of CdS nanoparticles grown in polystyrene matrix by thermolytic synthesis. *Mater. Lett.* 59, 3181–3187. doi: 10.1016/j.matlet.2005.05.047

Athanassiou, A., Cingolani, R., Tsiranidou, E., Fotakis, C., Laera, A. M., Piscopiello, E., et al. (2007). Photon-induced formation of CdS nanocrystals in selected areas of polymer matrices. *Appl. Phys. Lett.* 91:153108. doi: 10.1063/1.2790484

Bansal, A. K., Antolini, F., Sajjad, M. T., Stroea, L., Mazzaro, R., Ramkumar, S. G., et al. (2014). Photophysical and structural characterisation of *in situ* formed quantum dots. *Phys. Chem. Chem. Phys.* 16, 9556–9564. doi: 10.1039/C4CP00727A

Bansal, A. K., Antolini, F., Zhang, S., Stroea, L., Ortolani, L., Lanzi, M., et al. (2016). Highly Luminescent colloidal CdS quantum dots with efficient near-infrared electroluminescence in light-emitting diodes. *J. Phys. Chem. C* 120, 1871–1880. doi: 10.1021/acs.jpcc.5b09109

Bansal, A. K., Sajjad, M. T., Antolini, F., Stroea, L., Gečys, P., Raciukaitis, G., et al. (2015). *In situ* formation and photo patterning of emissive quantum dots in small organic molecules. *Nanoscale* 7, 11163–11172. doi: 10.1039/C5NR01401H

Brus, L. (1986). Electronic wave functions in semiconductor clusters: experiment and theory. *J. Phys. Chem.* 90, 2555–2560. doi: 10.1021/j100403a003

Camposeo, A., Polo, M., Neves, A. A. R., Fragouli, D., Persano, L., Molle, S., et al. (2012). Multi-photon in situ synthesis and patterning of polymer-embedded nanocrystals. *J. Mater. Chem.* 22, 9787–9793. doi: 10.1039/c2jm16625a

Chen, H., He, J., and Wu, S.-T. (2017a). Recent advances on quantum-dot-enhanced liquid-crystal displays. *IEEE J. Select. Top. Quant. Electron.* 23, 1–11. doi: 10.1109/JSTQE.2017.2649466

Chen, J., Wu, Y., Li, X., Cao, F., Gu, Y., Liu, K., et al. (2017b). Simple and fast patterning process by laser direct writing for perovskite quantum dots. *Adv. Mater. Tech.* 2:1700132. doi: 10.1002/admt.201700132

Cho, H., Kwak, J., Lim, J., Park, M., Lee, D., Bae, W. K., et al. (2015). Soft contact transplanted nanocrystal quantum dots for light-emitting diodes: effect of surface energy on device performance. *ACS Appl. Mater. Interfaces* 7, 10828–10833. doi: 10.1021/acsami.5b01738

Choi, J. H., Wang, H., Oh, S. J., Paik, T., Jo, P. S., Sung, J., et al. (2016). Exploiting the colloidal nanocrystal library to construct electronic devices. *Science* 352, 205–208. doi: 10.1126/science.aad0371

Christodoulou, S., Vaccaro, G., Pinchetti, V., Donato, F. D., Grim, J. Q., Casu, A., et al. (2014). Synthesis of highly luminescent wurtzite CdSe/CdS giant-shell nanocrystals using a fast continuous injection route. *J. Mater. Chem. C* 2, 3439–3447. doi: 10.1039/c4tc00280f

Cobas, R., Muñoz-Pérez, S., Cadogan, S., Ridgway, M. C., and Obradors, X. (2015). Surface charge reversal method for high-resolution inkjet printing of functional water-based inks. *Adv. Func. Mater.* 25, 768–775. doi: 10.1002/adfm.201401638

Dai, X., Deng, Y., Peng, X., and Jin, Y. (2017). Quantum-dot light-emitting diodes for large-area displays: towards the dawn of commercialization. *Adv. Mater.* 29:1607022. doi: 10.1002/adma.201607022

Dance, I. G. (1986). The structural chemistry of metal thiolate complexes. *Polyhedron* 5, 1037–1104. doi: 10.1016/S0277-5387(00)84307-7

Dowland, S., Lutz, T., Ward, A., King, S. P., Sudlow, A., Hill, M. S., et al. (2011). Direct growth of metal sulfide nanoparticle networks in solid-state polymer films for hybrid inorganic-organic solar cells. *Adv. Mater. Weinheim* 23, 2739–2744. doi: 10.1002/adma.201100625

Feinaeugle, M., Alloncle, A. P., Delaporte, P., Sones, C. L., and Eason, R. W. (2012). Time-resolved shadowgraph imaging of femtosecond laser-induced forward transfer of solid materials. *Appl. Surf. Sci.* 258, 8475–8483. doi: 10.1016/j.apsusc.2012.04.101

Fragouli, D., Laera, A. M., Caputo, G., Resta, V., Pompa, P. P., Tapfer, L., et al. (2010a). The Effect of polymer matrices in the *in-situ* CdS formation under UV irradiation of precursor-polymer films. *J. Nanosci. Nanotechnol.* 10, 1267–1272. doi: 10.1166/jnn.2010.1861

Fragouli, D., Laera, A. M., Pompa, P. P., Caputo, G., Resta, V., Allione, M., et al. (2009). Localized formation and size tuning of CdS nanocrystals upon irradiation of metal precursors embedded in polymer matrices. *Microelectr. Eng.* 86, 816–819. doi: 10.1016/j.mee.2008.12.050

Fragouli, D., Pompa, P. P., Kalyva, M., Caputo, G., Tapfer, L., Cingolani, R., et al. (2010b). The effect of irradiation wavelength on the quality of CdS nanocrystals formed directly into PMMA matrix. *J. Phys. Chem. C* 114, 13985–13990. doi: 10.1021/jp103387a

Grim, J. Q., Manna, L., and Moreels, I. (2015). A sustainable future for photonic colloidal nanocrystals. *Chem. Soc. Rev.* 44, 5897–5914. doi: 10.1039/C5CS00285K

Han, H. V., Lin, H. Y., Lin, C. C., Chong, W. C., Li, J. R., Chen, K. J., et al. (2015). Resonant-enhanced full-color emission of quantum-dot-based micro LED display technology. *Opt. Exp.* 23, 32504–32515. doi: 10.1364/OE.23.032504

Haverinen, H. M., Myllyla, R. A., and Jabbour, G. E. (2010). Inkjet printed RGB quantum dot-hybrid LED. *J. Display Tech.* 6, 87–89. doi: 10.1109/JDT.2009.2039019

Hines, D. A., and Kamat, P. V. (2014). Recent advances in quantum dot surface chemistry. *ACS Appl. Mater. Interfaces* 6, 3041–3057. doi: 10.1021/am405196u

Hocheng, H., Tsai, H. Y., Jadhav, U. U., Wang, K. Y., and Lin, T. C. (2014). "9.05 - Laser Surface Patterning," in *Comprehensive Materials Processing*, eds S. Hashmi, G. F. Batalha, C. J. Van Tyne, and B. Yilbas (Oxford: Elsevier), 75–113.

Hu, L., and Wu, H. (2013). Annealing-induced bimodal size distribution of small CdSe quantum dots with white-light emission. *Phys. Status Solid.* 210, 1726–1733. doi: 10.1002/pssa.201228872

Ji, T., Jin, S., Zhang, H., Chen, S., and Sun, X. W. (2018). Full color quantum dot light-emitting diodes patterned by photolithography technology. *J. Soc. Inform. Display* 26, 121–127. doi: 10.1002/jsid.640

Jiang, C., Zhong, Z., Liu, B., He, Z., Zou, J., Wang, L., et al. (2016). Coffee-ring-free quantum dot thin film using inkjet printing from a mixed-solvent system on modified ZnO transport layer for light-emitting devices. *ACS Appl. Mater. Interfaces* 8, 26162–26168. doi: 10.1021/acsami.6b08679

Jun, H. K., Careem, M. A., and Arof, A. K. (2013). Quantum dot-sensitized solar cells-perspective and recent developments: a review of Cd chalcogenide quantum dots as sensitizers. *Renew. Sust. Energ. Rev.* 22, 148–167. doi: 10.1016/j.rser.2013.01.030

Kathirgamanathan, P., Bushby, L. M., Kumaraverl, M., Ravichandran, S., and Surendrakumar, S. (2015). Electroluminescent organic and quantum dot LEDs: the state of the art. *J. Display Tech.* 11, 480–493. doi: 10.1109/JDT.2015.2418279

Kedarnath, G., Dey, S., Jain, V. K., Dey, G. K., and Varghese, B. (2006). 2-(N,N-Dimethylamino)ethylselenolates of cadmium(II): syntheses, structure of [Cd3(OAc)2(SeCH2CH2NMe2)4] and their use as single source precursors for the preparation of CdSe nanoparticles. *Polyhedron* 25, 2383–2391. doi: 10.1016/j.poly.2006.02.011

Kim, B. H., Onses, M. S., Lim, J. B., Nam, S., Oh, N., Kim, H., et al. (2015). High-resolution patterns of quantum dots formed by electrohydrodynamic jet printing for light-emitting diodes. *Nano Lett.* 15, 969–973. doi: 10.1021/nl503779e

Klimov, V. I. (2010). Nanocrystal Quantum Dots. CRC Press. Available online at: https://www.crcpress.com/Nanocrystal-Quantum-Dots/Klimov/p/book/9781420079265 (accessed October 24, 2018).

Lesnyak, V., Gaponik, N., and Eychmüller, A. (2013). Colloidal semiconductor nanocrystals: the aqueous approach. *Chem. Soc. Rev.* 42, 2905–2929. doi: 10.1039/C2CS35285K

Leventis, H. C., King, S. P., Sudlow, A., Hill, M. S., Molloy, K. C., and Haque, S. A. (2010). Nanostructured hybrid polymer-inorganic solar cell active layers formed by controllable in situ growth of semiconducting sulfide networks. *Nano Lett.* 10, 1253–1258. doi: 10.1021/nl903787j

Lin, H. Y., Sher, C. W., Hsieh, D. H., Chen, X. Y., Chen, H. M. P., Chen, T. M., et al. (2017). Optical cross-talk reduction in a quantum-dot-based full-color micro-light-emitting-diode display by a lithographic-fabricated photoresist mold. *Photon. Res. PRJ* 5, 411–416. doi: 10.1364/PRJ.5.000411

Lin, Y. W., Hsieh, M. M., Liu, C. P., and Chang, H. T. (2005). Photoassisted Synthesis of CdSe and core–shell CdSe/CdS quantum dots. *Langmuir* 21, 728–734. doi: 10.1021/la049489q

Mack, C. (2008). *Fundamental Principles of Optical Lithography: The Science of Microfabrication*. Wiley.com. Available online at: https://www.wiley.com/en-us/Fundamental$+$Principles$+$of$+$Optical$+$Lithography%3A$+$The$+$Science$+$of$+$Microfabrication-p-9780470018934 (accessed October 26, 2018).

Malik, M. A., Afzaal, M., and O'Brien, P. (2010). Precursor chemistry for main group elements in semiconducting materials. *Chem. Rev.* 110, 4417–4446. doi: 10.1021/cr900406f

Menard, E., Meitl, M. A., Sun, Y., Park, J. U., Shir, D. J. L., Nam, Y. S., et al. (2007). Micro- and nanopatterning techniques for organic electronic and optoelectronic systems. *Chem. Rev.* 107, 1117–1160. doi: 10.1021/cr050139y

Morselli, D., Scarpellini, A., Athanassiou, A., and Fragouli, D. (2016). Single step in situ formation of porous zinc oxide/PMMA nanocomposites by pulsed laser irradiation: kinetic aspects and mechanisms. *RSC Adv.* 6, 11412–11418. doi: 10.1039/C5RA23125F

Onwudiwe, D. C., Krüger, T. P. J., Jordaan, A., and Strydom, C. A. (2014a). Laser-assisted synthesis, and structural and thermal properties of ZnS nanoparticles stabilised in polyvinylpyrrolidone. *Appl. Surf. Sci.* 321, 197–204. doi: 10.1016/j.apsusc.2014.10.022

Onwudiwe, D. C., Krüger, T. P. J., Oluwatobi, O. S., and Strydom, C. A. (2014b). Nanosecond laser irradiation synthesis of CdS nanoparticles in a PVA system. *Appl. Surf. Sci.* 290, 18–26. doi: 10.1016/j.apsusc.2013.10.165

Panfil, Y. E., Oded, M., and Banin, U. (2018). Colloidal quantum nanostructures: emerging materials for display applications. *Angew. Chem. Int. Edn.* 57, 4274–4295. doi: 10.1002/anie.201708510

Park, J. S., Kyhm, J., Kim, H. H., Jeong, S., Kang, J., Lee, S., et al. (2016). Alternative patterning process for realization of large-area, full-color, active quantum dot display. *Nano Lett.* 16, 6946–6953. doi: 10.1021/acs.nanolett.6b03007

Park, J. U., Lee, S., Unarunotai, S., Sun, Y., Dunham, S., Song, T., et al. (2010). Nanoscale, electrified liquid jets for high-resolution printing of charge. *Nano Lett.* 10, 584–591. doi: 10.1021/nl903495f

Pickering, S., Kshirsagar, A., Ruzyllo, J., and Xu, J. (2012). Patterned mist deposition of tri-colour CdSe/ZnS quantum dot films toward RGB LED devices. *Opto-Electron. Rev.* 20, 148–152. doi: 10.2478/s11772-012-0019-9

Pradhan, N., Katz, B., and Efrima, S. (2003). Synthesis of high-quality metal sulfide nanoparticles from Alkyl Xanthate single precursors in alkylamine solvents. *J. Phys. Chem. B* 107, 13843–13854. doi: 10.1021/jp035795l

Qayyum, H., Lu, C. H., Chuang, Y. H., Lin, J. Y., and Chen, S. (2016). Formation of uniform high-density and small-size Ge/Si quantum dots by scanning pulsed laser annealing of pre-deposited Ge/Si film. *AIP Adv.* 6:055323. doi: 10.1063/1.4953057

Račiukaitis, G., Gečys, P., Antolini, F., Stroea, L., Bansal, A. K., Samuel, I. D. W., et al. (2013). "Formation of quantum dots from precursors in polymeric films by ps-laser," in *Proceedings Volume 8607, Laser Applications in Microelectronic and Optoelectronic Manufacturing (LAMOM) XVIII; 860702 (2013), SPIE LASE, 2013*, eds X. Xu, G. Hennig, Y. Nakata, and S. W. Roth (San Francisco, CA)., doi: 10.1117/12.2004086

Rees, W. S., and Kräuter, G. (1996). Preparation and characterization of several group 12 element (Zn, Cd)-bis(thiolate) complexes and evaluation of their potential as precursors for 12–16 semiconducting materials. *J. Mater. Res.* 11, 3005–3016. doi: 10.1557/JMR.1996.0382

Regulacio, M. D., and Han, M. Y. (2010). Composition-tunable alloyed semiconductor nanocrystals. *Accounts Chem. Res.* 43, 621–630. doi: 10.1021/ar900242r

Resta, V., Laera, A. M., Camposeo, A., Piscopiello, E., Persano, L., Pisignano, D., et al. (2012). Spatially confined CdS NCs *in situ* synthesis through laser irradiation of suitable unimolecular precursor-doped polymer. *J. Phys. Chem. C* 116, 25119–25125. doi: 10.1021/jp3090759

Resta, V., Laera, A. M., Piscopiello, E., Schioppa, M., and Tapfer, L. (2010). Highly efficient precursors for direct synthesis of tailored CdS nanocrystals in organic polymers. *J. Phys. Chem. C* 114, 17311–17317. doi: 10.1021/jp104097w

Rossetti, R., Ellison, J. L., Gibson, J. M., and Brus, L. E. (1984). Size effects in the excited electronic states of small colloidal CdS crystallites. *J. Chem. Phys.* 80, 4464–4469. doi: 10.1063/1.447228

Royon, A., Petit, Y., Papon, G., Richardson, M., and Canioni, L. (2011). Femtosecond laser induced photochemistry in materials tailored with photosensitive agents [Invited]. *Optical Mater. Exp.* 1:866. doi: 10.1364/OME.1.000866

Scalbi, S., Fantin, V., and Antolini, F. (2017). Environmental assessment of new technologies: production of a quantum dots-light emitting diode. *J. Cleaner Produc.* 142, 3702–3718. doi: 10.1016/j.jclepro.2016.10.098

Shirasaki, Y., Supran, G. J., Bawendi, M. G., and Bulović, V. (2013). Emergence of colloidal quantum-dot light-emitting technologies. *Nat. Photon.* 7, 13–23. doi: 10.1038/nphoton.2012.328

Singh, A., Jayabalan, J., Khan, S., and Chari, R. (2018). Femtosecond laser induced photoluminescence enhancement of TGA-capped CdTe quantum dots. *J. Luminesci.* 194, 45–49. doi: 10.1016/j.jlumin.2017.10.009

Smirnov, A. A., Afanasiev, A., Gusev, S., Tatarskiy, D., Ermolaev, N., and Bityurin, N. (2018). Exposure dependence of the UV initiated optical absorption increase in polymer films with a soluble CdS precursor and its relation to the photoinduced nanoparticle growth. *Opt. Mater. Exp. OME* 8, 1603–1612. doi: 10.1364/OME.8.001603

Steckel, J. S., Ho, J., Hamilton, C., Xi, J., Breen, C., Liu, W., et al. (2015). Quantum dots: the ultimate down-conversion material for LCD displays. *J. Soc. Inform. Display* 23, 294–305. doi: 10.1002/jsid.313

Stroea, L., Bansal, A. K., Samuel, I. D. W., Kowalski, S., Allard, S., Scherf, U., et al. (2015). Growth of photoluminescent cadmium sulphide quantum dots from soluble single source precursors in solution and in film. *Sci. Adv. Mater.* 7, 1–4. doi: 10.1166/sam.2015.2002

Supran, G. J., Shirasaki, Y., Song, K. W., Caruge, J. M., Kazlas, P. T., Coe-Sullivan, S., et al. (2013). QLEDs for displays and solid-state lighting. *MRS Bull.* 38, 703–711. doi: 10.1557/mrs.2013.181

Talapin, D. V., and Steckel, J. (2013). Quantum dot light-emitting devices. *MRS Bull.* 38, 685–691. doi: 10.1557/mrs.2013.204

Teichler, A., Perelaer, J., and Schubert, U. S. (2013). Inkjet printing of organic electronics – comparison of deposition techniques and state-of-the-art developments. *J. Mater. Chem. C* 1, 1910–1925. doi: 10.1039/c2tc00255h

The Nobel Prize in Physics (2018). *NobelPrize.org.* Available at: https://www.nobelprize.org/prizes/physics/2018/summary/ (accessed October 19, 2018).

Todescato, F., Fortunati, I., Minotto, A., Signorini, R., Jasieniak, J., Bozio, R., et al. (2016). Engineering of semiconductor nanocrystals for light emitting applications. *Materials* 9:672. doi: 10.3390/ma9080672

Valizadeh, A., Mikaeili, H., Samiei, M., Farkhani, S. M., Zarghami, N., Kouhi, M., et al. (2012). Quantum dots: synthesis, bioapplications, and toxicity. *Nanoscale Res. Lett.* 7:l480. doi: 10.1186/1556-276X-7-480

Vora, K., Kang, S., Shukla, S., and Mazur, E. (2012). Fabrication of disconnected three-dimensional silver nanostructures in a polymer matrix. *Appl. Phys. Lett.* 100:063120. doi: 10.1063/1.3684277

Voznesenskiy, S. S., Sergeev, A. A., Postnova, I. V., Galkina, A. N., Shchipunov, Y. A., and Kulchin, Y. N. (2015). Dynamic laser-induced effects in nanocomposite systems based on the cadmium sulfide quantum dots in a silicate matrix. *Opt. Exp. OE* 23, 4415–4420. doi: 10.1364/OE.23.004415

Wang, P., Zhang, Y., Ruan, C., Su, L., Cui, H., and Yu, W. W. (2017). A few key technologies of quantum dot light-emitting diodes for display. *IEEE J. Select. Top. Quantum Electron.* 23, 1–12. doi: 10.1109/JSTQE.2017.2665779

Williamson, C. B., Nevers, D. R., Hanrath, T., and Robinson, R. D. (2015). Prodigious effects of concentration intensification on nanoparticle synthesis: a high-quality, scalable approach. *J. Am. Chem. Soc.* 137, 15843–15851. doi: 10.1021/jacs.5b10006

Wolk, M. B., Baetzold, J. P., Bellmann, E., Hoffend, T. R., Lamansky, S., Li, Y., et al. (2004). "Laser thermal patterning of OLED materials," in *Organic Light-Emitting Materials and Devices VIII* (International Society for Optics and Photonics) (Denver, Co), 12–24. doi: 10.1117/12.563872

Woo, H., Lim, J., Lee, Y., Sung, J., Shin, H., Oh, J. M., et al. (2013). Robust, processable, and bright quantum dot/organosilicate hybrid films with uniform QD distribution based on thiol-containing organosilicate ligands. *J. Mater. Chem. C* 1, 1983–1989. doi: 10.1039/c3tc00719g

Wood, V., Panzer, M. J., Chen, J., Bradley, M. S., Halpert, J. E., Bawendi, M. G., et al. (2009). Inkjet-printed quantum dot–polymer compositesfor full-

color AC-driven displays. *Adv. Mater.* 21, 2151–2155. doi: 10.1002/adma.200803256

Wu, T., Sher, C. W., Lin, Y., Lee, C. F., Liang, S., Lu, Y., et al. (2018). Mini-LED and micro-LED: promising candidates for the next generation display technology. *Appl. Sci.* 8:1557. doi: 10.3390/app8091557

Xu, H., Pang, X., He, Y., He, M., Jung, J., Xia, H., et al. (2015). An Unconventional route to monodisperse and intimately contacted semiconducting organic–inorganic nanocomposites. *Angew. Chem.* 127, 4719–4723. doi: 10.1002/ange.201500763

Yang, Y., Zheng, Y., Cao, W., Titov, A., Hyvonen, J., Manders, J. R., et al. (2015). High-efficiency light-emitting devices based on quantum dots with tailored nanostructures. *Nat. Photon.* 9, 259–266. doi: 10.1038/nphoton.2015.36

Yang, Z., Fan, J. Z., Proppe, A. H., Arquer, F. P. G., de, Rossouw, D., Voznyy, O., et al. (2017). Mixed-quantum-dot solar cells. *Nat. Commun.* 8:1325. doi: 10.1038/s41467-017-01362-1

Yu, W. W., and Peng, X. (2002). Formation of high-quality CdS and other II–VI semiconductor nanocrystals in noncoordinating solvents: tunable reactivity of monomers. *Angew. Chem. Int. Edn.* 41, 2368–2371. doi: 10.1002/1521-3773(20020703)41:13<2368::AID-ANIE2368>3.0.CO;2-G

Zhu, T., Shanmugasundaram, K., Price, S. C., Ruzyllo, J., Zhang, F., Xu, J., et al. (2008). Mist fabrication of light emitting diodes with colloidal nanocrystal quantum dots. *Appl. Phys. Lett.* 92:023111. doi: 10.1063/1.2834734

Conflict of Interest Statement: The authors declare that the research was conducted in the absence of any commercial or financial relationships that could be construed as a potential conflict of interest.

frontiers in Chemistry

ORIGINAL RESEARCH
published: 10 April 2019
doi: 10.3389/fchem.2019.00207

Photoluminescence Lifetime Based Investigations of Linker Mediated Electronic Connectivity Between Substrate and Nanoparticle

Jan F. Miethe, Franziska Lübkemann, Nadja C. Bigall and Dirk Dorfs**

Institute of Physical Chemistry and Electrochemistry, Leibniz Universität Hannover, Hannover, Germany

The evolution of systems based on nanoparticles as the main component seems to be a self-accelerating process during the last five decades. Hence, an overview across this field gets more and more challenging. It is sometimes rewarding to focus on the fundamental physical phenomenon of the electronic interconnection between the different building blocks of the obtained devices. Therefore, the investigation of charge transport among the utilized particles and their substrate is one of the mandatory steps in the development of semiconductor nanoparticle based devices like e.g., sensors and LEDs. The investigation of the influence of tunneling barriers on the properties of nanoparticle-functionalized surfaces is a challenging task. The different basic influences on the charge transport dynamics are often difficult to separate from each other. Non-invasive and easily viable experiments are still required to resolve the charge distributing mechanisms in the systems. In the presented work, we want to focus on thin and transparent indium tin oxide (ITO) layers covered glass slides since this substrate is frequently utilized in nanoelectronics. CdSe/CdS nanorods (NRs) are applied as an optically addressable probe for the electronic surface states of the conductive glass. The presented experimental design provides the proof of electronic interconnections in ITO coated glass/linker/NR electrodes via easy reproducible functionalization and polishing experiments. UV/Vis absorption and photoluminescence (PL) lifetime measurements revealed changes in the optical properties caused by differences in the charge carrier dynamics between the system. Our work is focused on the modification of charge carrier dynamics due to the application of linker molecules with different functional groups like (3-mercaptopropyl)methoxysilane (MPTMS) and (3-aminopropyl)trimethoxysilane (APTMS). The presented observations are explained with a simple kinetic model.

Keywords: nanoparticles, photoluminescence, substrate, quenching, charge carrier dynamics

OPEN ACCESS

Edited by:
Maksym Yarema,
ETH Zürich, Switzerland

Reviewed by:
Ayaskanta Sahu,
New York University, United States
Xian Chen,
Shenzhen University, China

****Correspondence:***
Nadja C. Bigall
nadja.bigall@pci.uni-hannover.de
Dirk Dorfs
dirk.dorfs@pci.uni-hannover.de

Specialty section:
This article was submitted to Nanoscience, a section of the journal Frontiers in Chemistry

Received: *17 December 2018*
Accepted: *18 March 2019*
Published: *10 April 2019*

Citation:
Miethe JF, Lübkemann F, Bigall NC and Dorfs D (2019) Photoluminescence Lifetime Based Investigations of Linker Mediated Electronic Connectivity Between Substrate and Nanoparticle. Front. Chem. 7:207. doi: 10.3389/fchem.2019.00207

INTRODUCTION

Indium tin oxide coated glass is one of the most common substrates in the field of nanoscience, since it is a transparent material with high electronic conductivity. The ITO coated glass slide is employed as typical nanoparticle carrying substrate in case of photoelectrochemical sensing applications (Wang and Wang, 2004a; Yue et al., 2013; Zhang, 2013), solar cells

(Yaacobi-gross, 2011; Poppe et al., 2014), and screen technology. The application related improvement of this material is still ongoing (Savu and Joanni, 2006; Taniguchi et al., 2011). ITO is the composition of two oxides with the classical stoichiometric distribution of $(In_2O_3)_{0.9}) \cdot (SnO_2)_{0.1}$. ITO is chemically relatively inert and needs to be activated and functionalized in order to be integrated in devices (Kern and Puotinen, 1970). The functionalization of distinct surfaces like titania, silica, indium tin oxide (ITO), iron oxide, silicon and copper with silanes via silanization is a widely known and implemented process. Such modifications allow to obtain chemical surface characteristics, which are far away from the ones of the pristine substrates (Zhang et al., 2004; Ballarin et al., 2008; Yang D. et al., 2011; Lin et al., 2012; Liu et al., 2013; Poppe et al., 2013). Two of the most applied reagents to achieve the functionalization of surfaces are the silanes (3-aminopropyl)trimethoxysilane (Kern and Puotinen, 1970; Zhang, 2013) and (3-mercaptopropyl)methoxysilane (Doron et al., 1995; Miethe et al., 2018). This molecules are not only enabling the fixation of metal and semiconductor nanoparticles but also the implementation of novel technical processes like inkjet printing (Pavlovic et al., 2003; Xiao et al., 2005; Lübkemann et al., 2017). It is obvious, that the main difference of the mentioned linkers is their functional group. Thiol groups (MPTMS) are more acidic than their alcohol equivalents and form in this perspective a counterpart to amine groups (APTMS), which are the classical basic building block in organic chemistry (Cao et al., 2013). The nucleophilic character of deprotonated thiols leads to the chemisorption of subvalent and metal rich surfaces of semiconductor nanoparticles. Another factor is the sulfur affinity of metals like gold, which can be linked well to thiols (Zhang et al., 2004; Ballarin et al., 2008; Pensa et al., 2012). APTMS is widely known for its linking capabilities of metal nanoparticles. (Wang and Wang, 2004b; Zhang, 2013) The silanes 11-mercaptoundecyltrimethoxysilane (11-thiol) and N^1-(3-trimethoxysilylpropyl)diethylenetriamine (3-amine) were applied as reference systems with longer carbon chains. The utilization of these molecules allows to investigate the influence of the carbon chain length on the probability of electron tunneling. However, a lower expected electronic interaction might be the reason, why these longer chained linkers are rarely utilized. Nonetheless, both molecules are suitable reference systems, since they show in principle the same chemical linking behavior to the ITO substrate and to the nanoparticles as their shorter chained analogous.

In the presented work a simple and easily producible ITO coated glass/linker/nanoparticle system was chosen out of the manifold of possibilities provided by literature (Hickey et al., 2000; Zhang et al., 2004; Chen et al., 2014; Miethe et al., 2018). PL lifetime measurements are utilized to reveal the electronic interconnection between the ITO and the semiconductor nanoparticles, which are linked to it via the above mentioned linker molecules. The stepwise preparation of the slides is based on (i) activation of ITO, (ii) functionalization of ITO, (iii) linking of nanoparticles to ITO, and (iv) finally polishing one of the two sides (either glass side or ITO side) of the substrate. To understand the electronic properties of an ITO/linker/nanoparticle electrode the optical properties of the system after every step of preparation were investigated and compared. Apparently, the results gained by our scientific study could not be obtained under consideration of solely the final system. Since the silanization of the soda lime glass side and the ITO side of the substrates was always realized simultaneously and thereby under the same conditions, the comparison of the functionalization process of both substrate surfaces was possible in case of all four linkers (short and long chained amino and thiol silanes). This allows the investigation of the influence of parameters like functional group and chain length of the linker molecule on the charge carrier dynamics. Furthermore, the effect of the surface modification of the particle as well as the electronic linking of the particle to ITO can be separated. A key point is to consider the polishing of one side of the slide, even when it is not an interesting chemical reaction, as a main step in the preparation process. Polishing excludes 50% of the nanoparticles in the system. This leads to the effective separation of effects from the linker itself and those caused by the linking to a conductive surface.

In detail the ITO coated glass/linker/nanoparticle system is based on one dimensional CdSe/CdS nanorods, which are known from the work of Carbone et al. (2007). This material is the result of a two-step synthesis. In the first step CdSe cores are obtained and in a second step applied as seeds to grow a rod shaped CdS shell around them. Accordingly, the direct semiconductor heterostructure shows a band structure, which is known as a pseudo-type II or type I in dependence of the core size (Eshet et al., 2013). CdSe/CdS nanorods were considered as a suitable material for the experiment since the PL quantum yield (QY) of the particles is high enough to guarantee results in an acceptable experimental timescale of minutes. Furthermore, the radiative lifetime of the particles is commonly much higher than in other direct semiconductor nanoparticles without heterostructure (Crooker et al., 2003; Tessier et al., 2012; Eshet et al., 2013). Another benefit of the chosen nanoparticles is their high surface per particle in comparison to dots of the same atom number. The latter fact might facilitate the particle linking to the substrate. The PL wavelength of the chosen nanoparticles is in the orange/red regime and thus far away from the wavelength of the excitation beam of 420 nm. There is no reported fluorescence of bulk ITO, as applied in our case, in contrast to ITO nanoparticles (Ma et al., 1995; Yang H. et al., 2011; Liang and Liu, 2018).

Overall it was possible to show a significant difference in the contribution of thiol silanes (MPTMS, 11-thiol) and amine silanes (APTMS and 3-amine) to the electronic interconnection of nanoparticles to their substrates. This effect can be related to electronic states caused by chemisorption of thiol or amine groups to the nanoparticle surface.

EXPERIMENTAL SECTION

Materials

Tin doped indium oxide coated unpolished soda lime float glass with a surface resistance of 12 ohms/sq (ITO slides) and 1.1 mm thickness were purchased from VisionTek.

Cadmium oxide (CdO, 99.99%) and selenium (Se, 99.99%) were acquired from Alfa Aesar. Hexylphosphonic acid (HPA, ≥ 99%) and octadecylphosphonic acid (ODPA, ≥ 99%) were purchased from PCI synthesis. Toluene (99,7%), ammonium hydroxide (NH_4OH, 28–30%), hydrogen peroxide (H_2O_2, 30%), sulfur (99.98%), (3-aminopropyl)trimethoxysilane (APTMS, 97%), (3-mercaptopropyl)trimethoxysilane (MPTMS, 95%) and N^1-(3-trimethoxysilylpropyl)diethylenetriamine (3-amine, technical) were bought from Sigma-Aldrich. 11-mercaptoundecyltrimethoxysilane (11-thiol, 95%) was purchased from Gelest Inc. Tri-*n*-octylphosphine oxide (TOPO, 99%) and tri-*n*-octylphosphine (TOP, 97%) were obtained from abcr. 2-Propanol was purchased from Carl Roth.

Instruments

UV/Vis absorption spectra of the CdSe/CdS nanorod solutions and the nanoparticle decorated substrates were measured with an Agilent Cary 5000 absorption spectrophotometer equipped with an Agilent DRA-2500 integrating sphere in center mount position. Emission spectra and the PL lifetime of the solution and the prepared ITO samples were recorded with a Fluoromax-4 spectrometer from Horiba equipped with a time correlated single photon counting (TCSPC) accessory. All presented absorption spectra of the ITO/linker/nanoparticle electrodes are obtained under the subtraction of the spectrum of a blank ITO slide from the ones of nanoparticle decorated slides. The non-corrected absorption of a NR decorated substrate and the spectrum of a blank ITO slide are matching well at wavelengths were the particles are not optical absorbing (**SI Figure 1**).

Synthesis of CdSe Dots

CdSe dots were synthesized by using a slightly modified procedure developed by Carbone et al. (2007). 0.06 g CdO, 3 g TOPO and 1.7 g ODPA were placed in a 25 mL three-neck flask. The mixture was heated up to 150°C under vacuum and degassed for 1 h. Subsequently, the reaction mixture was heated up to 300°C under an argon atmosphere before 1.8 mL TOP were injected. After a temperature increase to 380°C, which leads to a clear solution, 1.8 mL TOP:Se (0.058 g Se in 1.8 mL TOP) solution were quickly injected. After recovering of the temperature the reaction was quenched with 6 mL ODE and the heating mantel was removed. The reaction mixture cooled down, before 5 mL toluene were added at 70°C and the CdSe dots were precipitated by the addition of 5 mL methanol. All nanoparticles were precipitated via centrifugation for 10 min (3.885 RCF). The precipitate was purified by adding 5 mL of toluene and 5 mL of methanol, subsequent centrifugation for 10 min (3.885 RCF), and dissolution in 5 mL of toluene. This process was repeated one time. The CdSe dots were stored in 6 mL toluene. TEM micrographs of the synthesized CdSe dots were measured (**SI Figure 2**).

Synthesis of Dot-in-Rod CdSe/CdS NRs

The CdS shell growth was adapted from Carbone et al. (2007). In a synthesis 0.06 g CdO, 3 g TOPO, 0.16 g ODPA, and 0.08 g HPA were placed in a 25 mL three-neck flask, heated up to 150°C and degassed for 1 h. The temperature was increased to 300°C under an argon atmosphere. After the desired temperature was reached, 1.8 mL TOP were injected followed by an increase of the temperature to 380°C. At this temperature 1.8 mL TOP:S (2.21 mmol) containing 400 μM of CdSe dots [the concentration was determined by UV/Vis spectroscopy and calculation according the work of Yu et al. (2003)] were injected and the reaction mixture was heated for 8 min. After the reaction mixture was cooled down, 5 mL toluene were added at 70°C and the CdSe/CdS NRs were precipitated by the same procedure as the CdSe seeds and stored in 5 mL toluene. TEM images of the synthesized nanorods are displayed (**SI Figure 2**).

Pre-silanization Preparation of ITO Slide

The ITO slides were cleaned via a modification of the common known RCA (Radio Corporation of America) cleaning procedure (Kern and Puotinen, 1970). The slides were cut into pieces with the lateral dimensions of 1.5 × 3.0 cm. The slides were placed in a polytetrafluoroethylene (PTFE) holder, which is equipped with a stirring bar. The holder was placed in a beaker. Volume parts of H_2O_2 (30%), NH_3 (28–30%) and H_2O were mixed in the composition 1:1:5. The ITO slides were completely covered with the solution, which was stirred and heated to a temperature of 70°C for at least 2 h. After the cleaning the slides were rinsed with deionized water and dried under air stream.

Functionalization of ITO Slides With Linker Molecules

After the cleaning process the cleaned slides were placed in a PTFE holder equipped with a stirring bar and covered with a specific amount of toluene. The system was heated to 60°C and stirred. A volume of the silane linker molecule (1.0 mL MPTMS, 0.2 mL APTMS, 1.5 mL 11-thiol, or 0.3 mL 3-amine) was pipetted into the toluene. After 24 h, the reaction was stopped by removing the slides from the functionalization solution and dipping them into pure toluene to remove residual not bound silane molecules.

Decoration of ITO/Linker System With CdSe/CdS Nanorods

The silane functionalized slides were immersed into 10 mL of a solution of CdSe/CdS nanorods in toluene with a Cd-concentration of 15.2 mmol/L. The screw cap vial is placed in a shaker and shacked for 24 h with a velocity of 250 rpm. After this process the functionalization is stopped by removing the ITO slide from the coating solution and immersing it for 2 min in pure toluene. The last step is necessary to remove unbound NRs, which could otherwise form agglomerates on the slide surface during the final drying process. The introduced mechanism is presented as a scheme in **Figure 1**.

After linking of CdSe/CdS NRs to the slides and a second cleaning step the slides appear slightly yellowish. A comparison of the UV/Vis absorption spectra of pristine nanoparticles in solution and the prepared CdSe/CdS decorated ITO glass slides (under subtraction of the ITO absorption) shows the same optical band edge of CdS at ca. 460 nm, but slight differences at lower wavelengths (**SI Figure 3**). These differences are probably caused by interferences, which are the result of the glass/ITO/linker/NR layer stacking. The emission maximum of the particles in

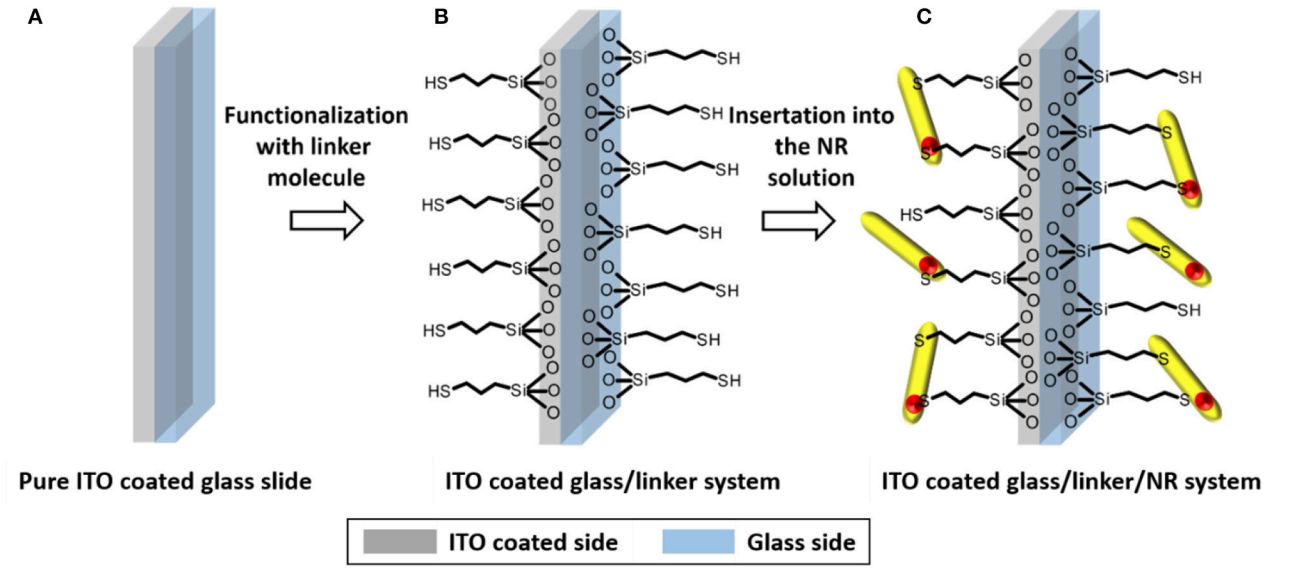

FIGURE 1 | Scheme of the first two steps of substrate preparation. The example of the functionalization of a **(A)** cleaned and surface activated slide **(B)** via MPTMS and the subsequent decoration of the resulting surface via **(C)** CdSe/CdS NR is shown.

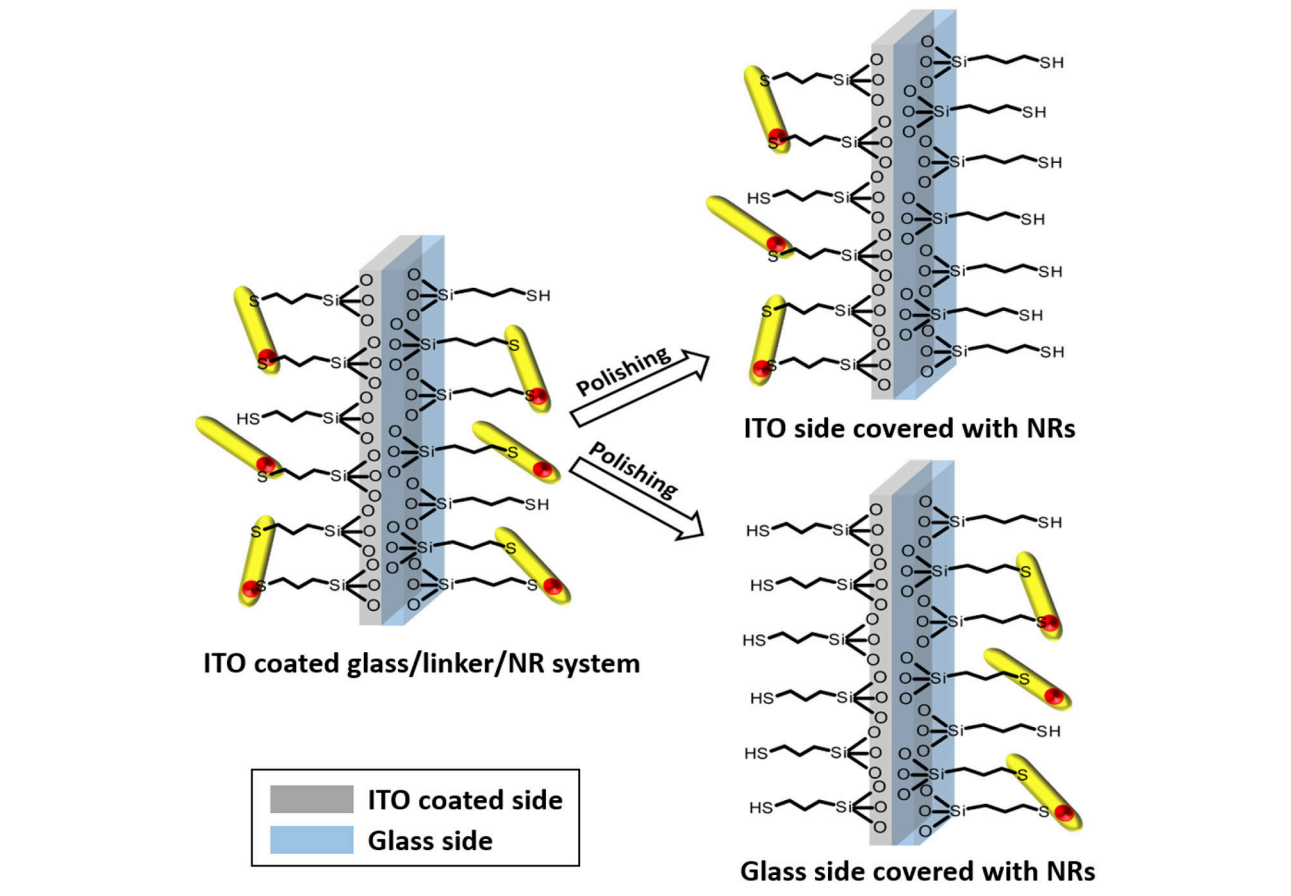

FIGURE 2 | Schematic illustration of the selective polishing of the different sides of the substrate. The result of this process are two comparable systems with completely different electronic interconnections, namely between NR and ITO or NR and glass.

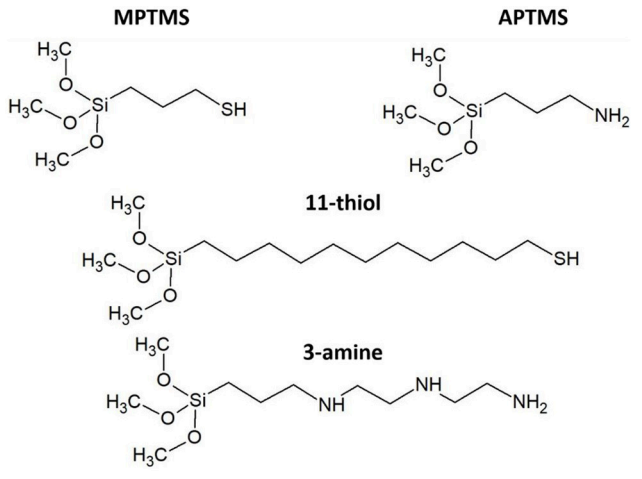

FIGURE 3 | The four different applied silane molecules are based on two thiols (MPTMS and 11-thiol) and two amines (APTMS and 3-amine).

solution and on the substrate differs by 3 nm, which is probably caused by the appearance of further electronic surface states by linking (**SI Figure 4**).

Polishing of ITO Coated Glass/Linker/NR System

A lint–free paper towel soaked with 2-propanol was applied to polish the desired side of the substrate. Steady wiping for 5 min polished the slide. The effect of polishing is immediately visible under UV-irradiation. The paper towel starts to fluorescence in the same color as the nanoparticles. An overview of the polishing process is delivered in a scheme (**Figure 2**).

RESULTS AND DISCUSSION

A perfect homogeneous molecular layer of the applied silane molecule (**Figure 1**) was considered as the target of the silanization reaction. This is elementary for our experiments, since in a monolayer of particles every linked nanoparticle should show similar electronic interconnection with the substrate (**Figure 2**). The applied thiol and amino silanes are well-known to yield particle monolayers (Brust et al., 1998; Su et al., 2007; Yokota et al., 2012) (**Figure 3**). Thick multilayers, which are known by literature, would circumvent the required electronic equality of particles connected to the same surface (Wang and Wang, 2004a; Howarter et al., 2006; Kannan and John, 2010). The reaction parameters of the silanization via mercaptosilane and aminosilane linkers have to be modified in different ways, to achieve a monolayer in each case. Aminosilanes form under the same conditions much thicker layers than their thiol counterparts since the amine group is auto catalyzing the hydrolysis of the methoxy groups of the silanes (Sunkara and Cho, 2012). In our experiments the same concentration of aminosilanes and mercaptosilanes in the functionalization step leads to turbid and sometimes opalescent substrates in case of the aminosilanes. The amine based systems showed in this case an inhomogeneous lateral distribution of nanorods, which was even visible by bar eye. Attention was paid to this fact by using a lower concentration of aminosilanes for the functionalization.

The presence of a monolayer was verified by UV/Vis spectroscopy in all cases as demonstrated by us in an earlier work (see SI for details, **SI Tables 1**, **2**). SEM micrographs of a pristine ITO coated glass substrate and an ITO/MPTMS/NR substrate are displaying remarkable differences between the systems. In case of a decorated substrate the rough ITO is covered with small white spots. This spots have an elongated shape and can be identified as nanorods (see **SI Figure 5**).

By recording absorption spectra before and after polishing the nanorod related percentage of absorbed photons of particle decorated slides can be calculated (**Figures 4**, **5**).

The calculated values of the decorated and undecorated particles differ by a factor of two (**Figures 4**, **5**). The explanation for this observation is the existence of approximately the same degree of coating at both surfaces of the slides, which is one of the fundamentals of the later performed fluorescence analysis of the slides.

The absorption of the NRs at polished substrate is always lower than 5%. This is in fact in good agreement with calculations in our previous work (Miethe et al., 2018). This calculations lead to the interpretation that the optical density is caused by a nanorod coverage in the monolayer regime (Miethe et al., 2018). The similar chemical behavior of both sides of the slide suggests a similar degree of functionalization of the soda lime glass and the ITO. The same behavior is found for every of the four applied linkers (**Figure 3**).

Photoluminescence spectra of the pristine NRs in solution as well as of the slides show a PL at 612 nm (**SI Figure 4**). A simple comparison of PL lifetime measurements of samples with one polished ITO or glass side with the spectrum of exactly the same slide before polishing shows a remarkable difference in the decay signal. In case of the thiol based linkers MPTMS and 11-thiol a shorter lifetime for NRs connected to ITO can be found in relation to unpolished systems (**Figures 6**, **7**), whereas the glass connected NRs exhibit a higher PL lifetime compared to the unpolished system. More details of the PL lieftime measurements are given in the supporting information of this paper.

In case of amine linked CdSe/CdS particles it was more challenging to find any difference between the PL decay curves of the glass and ITO connected particles (**Figures 6**, **7**). Here, the effect of polishing on the glass and ITO connected particles is small.

This major observation was at least three times repeated with three samples for every unpolished, glass polished and ITO polished substrate functionalized with one of the four utilized linker molecules. This leads to a data collection, which provides a standard deviation in every measurement point. The basis of the following kinetical PL description of samples is given by the simple determination of the kinetic constant of fluorescence quenching processes in NRs in solution k_s. This kinetic constant is derived from equation 1.

$$I = I_{mono} \cdot e^{-k_s t} \tag{1}$$

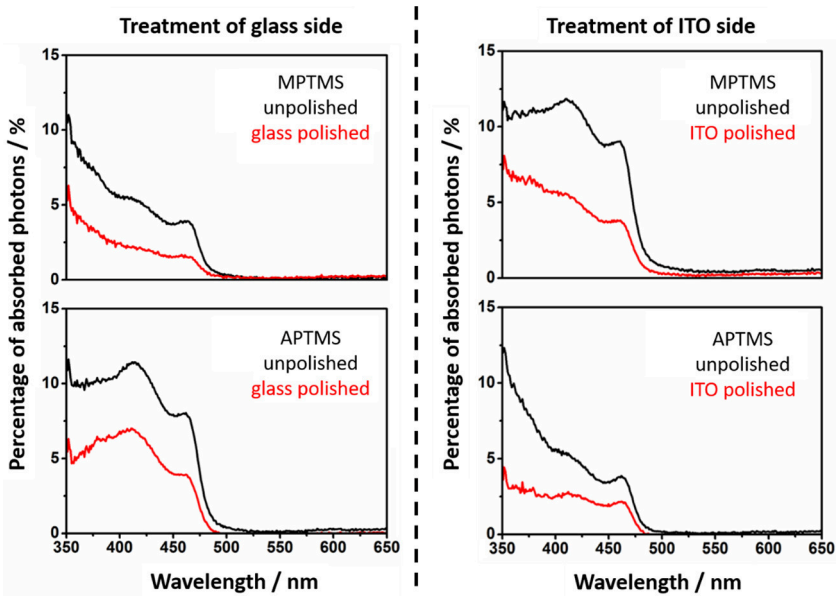

FIGURE 4 | Absorption spectra of the MPTMS and APTMS functionalized substrates with NR decoration. The spectra of unpolished slides are given in black. The absorption spectra of polished slides are red. It is always mentioned if the glass or ITO side is polished. The shape of the NR based absorption differs slightly from sample to sample since interference effects are present.

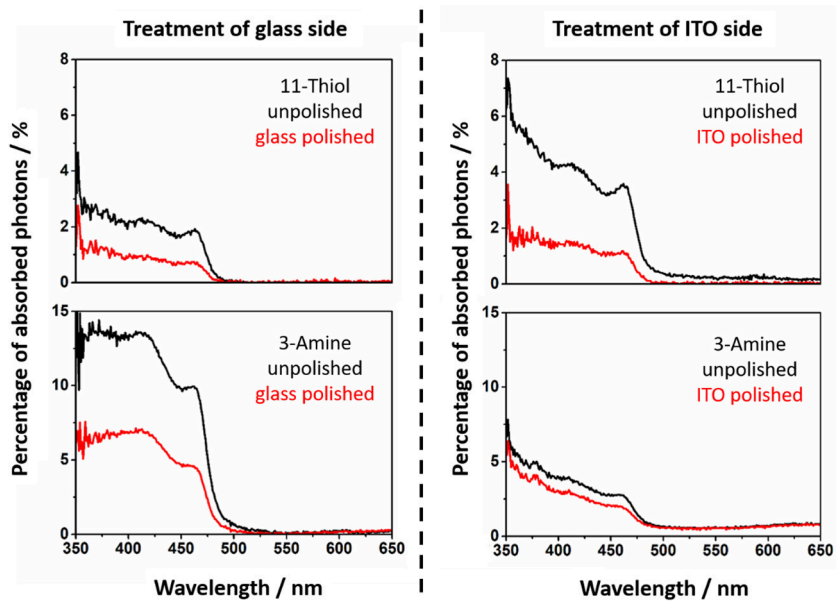

FIGURE 5 | The absorption of NRs at 11-thiol and 3-amine functionalized substrates is shown. The spectra of unpolished slides are presented (black). The absorption of polished slides are red.

The pristine tri-*n*-octylphosphine and tri-*n*-octylphosphine oxid covered CdSe/CdS NRs in toluene solution exhibit a PL lifetime of 24 ns and decay constant k_s, which is caused by the sum of all non-radiative and radiative processes of $41 \bullet 10^6$ s^{-1}.

PL lifetimes of the NR covered substrates were obtained via mono or biexponential fitting. Particle monolayers with homogenous nanoparticle-surface connectivity should be describable via a monoexponential decay function. This function (Equation 2 and Equation 3) was applied to describe the additional kinetic influence of trap states created by linking k_g in case of every polished sample. Whereby only the NRs linked to ITO develop additional ITO related quenching kinetics k_I. The

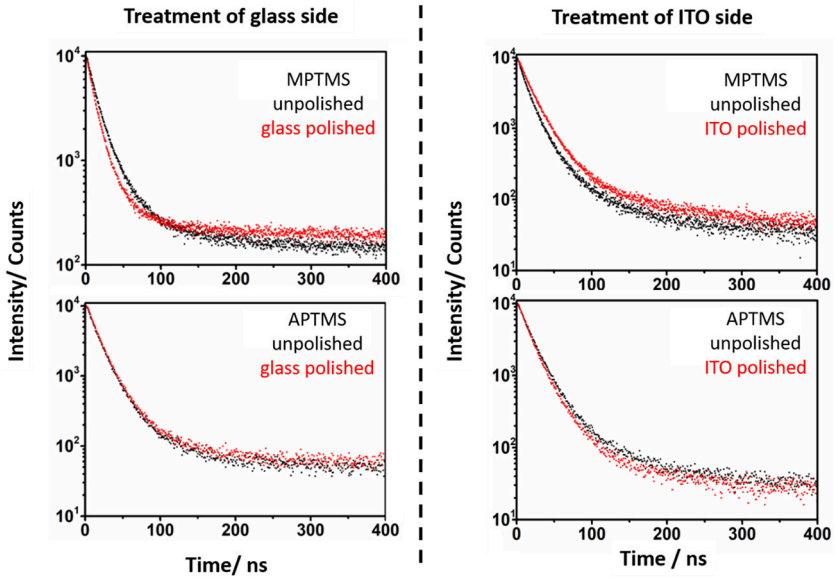

FIGURE 6 | Photoluminescence lifetime spectra of the MPTMS and APTMS based systems before (black) and after polishing (red). The specific side, which is polished is mentioned in the spectra. It is obvious, that the polishing of the glass side of MPTMS based systems decreases the PL lifetime. In contrast to this, a polishing of the ITO side increases the PL lifetime.

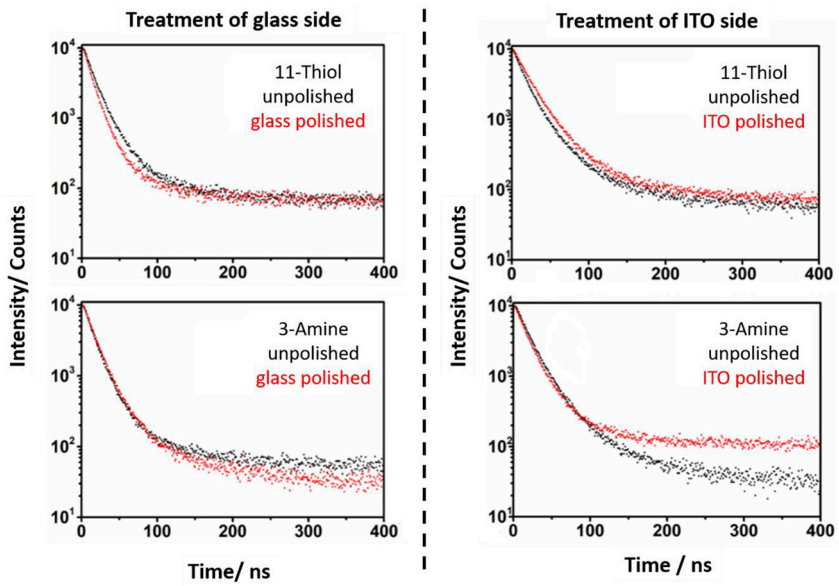

FIGURE 7 | The PL lifetime of NR, which are linked to substrates via 11-thiol and 3-amine, is measured. The spectra of unpolished (black) and polished (red) slides is shown. The lifetimes of unpolished and polished slides vary strongly in case of 11-thiol but not in their 3-amine counterparts.

existing kinetic mechanisms are described in **Figure 8**.

$$I = I_{mono} \cdot e^{-(k_s+k_g)t} \quad (2)$$

$$I = I_{mono} \cdot e^{-(k_s+k_g+k_I)t} \quad (3)$$

PL decays of unpolished NR decorated ITO slides (**Figures 6**, **7**) were fitted with a biexponential decay function (Equation 4). This fitting protocol is justifiable by the circumstance that two ensembles of emitting nanoparticles exist on an unpolished slide. One at each side.

$$I = I_{bi} \cdot e^{-(k_s+k_g)t} + I_{bi} \cdot e^{-(k_s+k_g+k_I)t} \quad (4)$$

Since the contribution to the total signal of every side to the system should be 50% the factor I_{bi} was assumed to be only

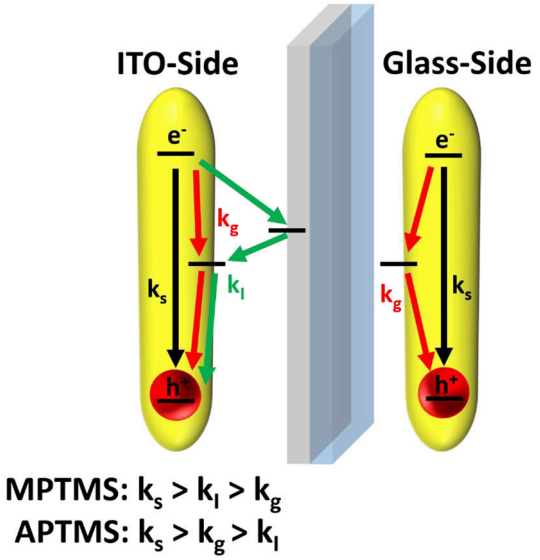

FIGURE 8 | A scheme of the described exciton quenching is based on three different mechanisms. The phenomenological kinetic constant k_S describes all quenching mechanisms, which are existing in case of NRs in free solutions. The by linking molecules introduced trap state related quenching processes are described by the kinetic constant k_g. Only excitons of NRs linked to the ITO side of the slide can undergo a quenching process, which is related to an interconnection between them and the free charge carriers of ITO (accounted for by the kinetic constant k_I).

TABLE 1 | The calculated kinetic constants of slide/linker/NR system are shown for the four applied linkers.

	Kinetic Constant/$10^6 s^{-1}$			
	Polished system		Unpolished system	
	Monoexponential fit		Biexponential fit	
Applied linker	k_I	k_g	k_I	k_g
MPTMS	24 ± 5	4 ± 2	39 ± 8	1 ± 6
APTMS	3 ± 3	17 ± 3	4 ± 6	17 ± 14
11-thiol	44 ± 2	2 ± 1	38 ± 31	1 ± 10
3-amine	7 ± 7	20 ± 10	3 ± 20	24 ± 7

The values of unpolished systems were derived from biexponential fits. The values of k_g are derived from monoexponential fits of ITO polished samples. Monoexponential fits of glass polished samples lead under consideration of K_g to k_I.

half of the factor I_{mono} for every term of the biexponential fit (Equation 5).

$$I_{mono} = 2 \cdot I_{bi} \tag{5}$$

An overview of the values of the kinetic constant of the non-radiative decay components is given in **Table 1**. An overview of the PL lifetime of the measured samples, which are obtained by mono and biexponential fits is shown in the supporting information (**SI Figure 6** and **SI Table 3**).

The kinetic constant k_g is only relevant in case of aminosilane linkers (**Table 1**). NRs that are connected by mercaptosilane linkers to ITO are the only system, which show an ITO related quenching process. This process is described by the constant k_I. The biexponential fit of unpolished slides is required to verify the kinetic constants (Equation 4 and **Table 1**). In case of polished slides, the same kind of constant is derived from monoexponential fits (Equation 2 and 3, **Table 1**). Note that the standard deviation of the kinetic constants calculated in two different ways at glass and ITO are confirming the validity of our approach. This is a good indication that the measured biexponetial behavior of the unpolished samples is indeed a simple superposition of the two sides of the sample.

The simple linking of thiol groups to the particle surface does not change their PL kinetics. This is proven by the same PL lifetimes for unlinked CdSe/CdS NRs and NRs linked to the glass side (**SI Figure 6** and **SI Table 3**).

Thus, the obtained results show that the lifetime of nanorods decreases more by a chemisorption of amine groups than by thiol groups. Nearly no noticeable decrease of the PL lifetime is recognizable when NRs are connected via aminosilanes to the conductive ITO side of the slide. This finding can be explained either by a much weaker interaction between ITO and nanoparticles when amine linkers are employed, or possibly also by a thicker layer of aminosilane formed. The latter effect is less likely since much lower amounts of aminosilanes were employed during functionalization. A connection between particle and slide via mercaptosilanes instead leads to a strong decay via an additional particle-ITO interaction (represented by k_I).

One of the major questions, which arises by studying this spectroscopic phenomenon, is how ITO can shorten the PL kinetics and why the effects depends more on the functional group of the linker than its length. The literature gives answers to this question. The Fermi energy of ITO has a potential, which is placed in the band gap of the semiconductor (Tang et al., 2007; Zillner et al., 2012). An arrangement of energy levels like this and the multiple times higher amount of free charge carriers in ITO than in the nanoparticles lead to an injection of electrons from the ITO into unoccupied electronic states in the energy levels of the photoexcited metal chalcogenide semiconductor. The injection of electrons is responsible for the faster quenching of holes obtained by photoexcitation of the metal chalcogenide particles. Holes are often trapped at subvalent sulfur atoms at the particle surface. The amount of the trapped charge on nanoparticles of metal chalcogenides is investigated by Fengler et al. (2013). The whole charge transport is describable by the kinetic constant k_I.

It is assumed in the work of Grandhi et al. that the chemisorption of amines at the NR surface leads to a quenching of hole traps at the NR (Grandhi et al., 2016). This would also lead to a short PL lifetime, which can be verified by the obtained measurements in **Table 1**. On the other hand, there are no holes available for quenching by injection from ITO. Under these conditions there seems to be no influence of ITO on the PL kinetics (Cooper et al., 2011; Zeng and Kelley, 2016). This mechanism can be described by the kinetic constant k_g.

In summary both types of linkers enable a quenching of PL kinetics. The aminosilane linker under direct hole quenching and the mercaptosilane linker via indirect charge injection from ITO. Literature shows that the described PL influencing processes are

also strongly interconnected to the population of electronic states in the slide (Wehrenberg and Guyot-Sionnest, 2003; Gooding et al., 2008; Li et al., 2017).

CONCLUSION

In the presented work, we showed an experimental setup, which relays on the comparison of classical prepared CdSe/CdS nanorod decorated ITO coated glass substrates with unusual reference samples. The samples consist of a slide at which a soda lime glass side and a ITO coated side are covered with the same particles. The absorption spectroscopy of the products proves that all four applied silane linker molecules (APTMS, MPTMS, 11-thiol, 3-amine) are applicable to form monolayers of particles. Even though the silanization behavior of the linker molecules is extremely different, all of them have in common that they show no specific difference in affinity to the soda lime or the ITO side of the glass substrate. This is the fundamental experimental condition to describe the PL decay with a biexponential fit representing the two different species in the system. The evaluation of the differences between the PL decay of pristine NRs, glass connected and ITO connected NRs yields kinetic constants, which describe the influence of the electronic coupling in the system. The way of interaction of ITO with particles is clearly depending on the functional group of the applied linker molecule. Mercaptosilanes are forming hole trap states at the surface of the NRs, which enable the injection of electrons from the ITO and by this a faster PL quenching mechanism. On the other hand, there seems to be only a small influence of this trap states on the PL in the absence of ITO. In case of aminosilanes functionalized substrates, a strong decrease of the PL lifetime of the connected NRs can be observed. The electronic interconnection of ITO and NRs, which is initialized via APTMS and related to the decrease of the PL lifetime however is very weak. The PL quenching effects and their linker related differences can be understood as a possibility to use the experimental setup reported in our work to create approaches for an analytical differentiation between various linker molecules.

The collected results lead to the conclusion that the electronic connection of photoluminescent nanoparticles to the electronic states of the ITO can be proven via contact free measurements of the PL lifetime of the particles. Since there is a growing interest in ITO surfaces for sensing applications and the possibility to utilize specific linker molecules as sensor interface, PL lifetime measurements could be applied as a productive tool of analysis.

The presented work might be the basis for more advanced investigations, which could reveal the influence of the semiconductor heterostructure and by association the effect of the occupation of electronic states in transparent conductive oxides. Even the influence of both kinds of investigated molecules in mixed linker systems could be interesting.

In summary there should be strong motivation to consider the obtained mechanisms of charge transport in case of applications like photoelectrochemical sensing and energy harvesting in order to amplify the desired performance.

AUTHOR CONTRIBUTIONS

JM has conducted all electrochemical measurements and has drafted the manuscript. FL has synthesized the investigated nanocrystals. DD and NB have supervised the project and were involved in all data interpretation as well as in writing and correcting the manuscript.

ACKNOWLEGMENTS

The authors are grateful for financial support from the German Federal Ministry of Education and Research (BMBF) within the framework of the program NanoMatFutur, support code 03X5525. Furthermore, the project leading to these results has received funding from the European Research Council (ERC) under the European Unions Horizon 2020 research and innovation program (Grant Agreement No. 714429). DD and FL thank the Volkswagen foundation (lower Saxony/Israel cooperation, Grant ZN2916), DD thanks the DFG (research Grant 1580/2-1 and 1580/5-1) for funding. NB thanks the DFG (research grant BI 1708/4-1). The authors thank the Laboratory of Nano and Quantum Engineering (LNQE) for support. The authors thank Prof. Caro and Prof. Feldhoff for access to a scanning electron microscope and Frank Steinbach for the SEM measurements.

SUPPLEMENTARY MATERIAL

The Supplementary Material for this article can be found online at: https://www.frontiersin.org/articles/10.3389/fchem.2019.00207/full#supplementary-material

REFERENCES

Ballarin, B., Cassani, M. C., Scavetta, E., and Tonelli, D. (2008). Self-assembled gold nanoparticles modified ITO electrodes: the monolayer binder molecule effect. *Electrochim. Acta* 53, 8034–8044. doi: 10.1016/j.electacta.2008.06.020

Brust, M., Bethell, D., Kiely, C. J., and Schiffrin, D. J. (1998). Self-assembled gold nanoparticle thin films with nonmetallic optical and electronic properties. *Langmuir* 14, 5425–5429. doi: 10.1021/la980557g

Cao, Y., Xie, J., Liu, B., Han, L., and Che, S. (2013). Synthesis and characterization of multi-helical DNA-silica fibers. *Chem. Commun.* 49, 1097–1099. doi: 10.1039/c2cc37470f

Carbone, L., Nobile, C., De Giorgi, M., Sala, F., Della Morello, G., Pompa, P., et al. (2007). Synthesis and micrometer-scale assembly of colloidal CdSe/CdS nanorods prepared by a seeded growth approach. *Nano Lett.* 7, 2942–2950. doi: 10.1021/nl0717661

Chen, W., Tseng, Y., Hsieh, S., Liu, W., Hsieh, C.-W., Wu, C.-W., et al. (2014). Silanization of solid surfaces via mercaptopropylsilatrane : a new approach of constructing gold colloid monolayers. *RCS Adv.* 4, 46527–46535. doi: 10.1039/C4RA05583G

Cooper, J. K., Franco, A. M., Gul, S., Corrado, C., and Zhang, J. Z. (2011). Characterization of primary amine capped CdSe, ZnSe, and ZnS Quantum dots by FT-IR: determination of surface bonding interaction and identification of selective desorption. *Langmuir* 27, 8486–8493. doi: 10.1021/la201273x

Crooker, S. A., Barrick, T., Hollingsworth, J. A., and Klimov, V. I. (2003). Multiple temperature regimes of radiative decay in CdSe nanocrystal quantum dots: intrinsic limits to the dark-exciton lifetime. *Appl. Phys. Lett.* 82, 2793–2795. doi: 10.1063/1.1570923

Doron, A., Katz, E., and Willner, I. (1995). Organization of Au colloids as monolayer films onto ITO glass surfaces: application of the metal colloid films as base interfaces to construct redox-active monolayers. *Langmuir* 11, 1313–1317. doi: 10.1021/la00004a044

Eshet, H., Grünwald, M., and Rabani, E. (2013). The electronic structure of CdSe/CdS core/shell seeded nanorods: type-I or Quasi-Type-II? *Nano Lett.* 13, 5880–5885. doi: 10.1021/nl402722n

Fengler, S., Zillner, E., and Dittrich, T. (2013). Density of surface states at CdSe quantum dots by fitting of temperature-dependent surface photovoltage transients with random walk simulations. *J. Phys. Chem. C* 117, 6462–6468. doi: 10.1021/jp4002687

Gooding, A. K., Gómez, D. E., and Mulvaney, P. (2008). The effects ofelectron and hole injection on the photoluminescence of CdSe/CdS/ZnS nanocrystal monolayers. *ACS Nano* 2, 669–676. doi: 10.1021/nn7003469

Grandhi, G. K., Arunkumar, M., and Viswanatha, R. (2016). Understanding the role of surface capping ligands in passivating the quantum dots using copper dopants as internal sensor. *J. Phys. Chem. C* 120, 19785–19795. doi: 10.1021/acs.jpcc.6b04060

Hickey, S. G., Riley, D. J., and Tull, E. J. (2000). Photoelectrochemical Studies of CdS nanoparticle modified electrodes: absorption and photocurrent investigations. *J. Phys. Chem. B* 104, 7623–7626. doi: 10.1021/jp993858n

Howarter, J. A., Youngblood, J. P., May, R. V., Final, I., and September, F. (2006). Optimization of silica silanization by 3-aminopropyltriethoxysilane. *Langmuir* 22, 11142–11147. doi: 10.1021/la061240g

Kannan, P., and John, S. A. (2010). Highly sensitive electrochemical determination of nitric oxide using fused spherical gold nanoparticles modified ITO electrode. *Electrochim. Acta* 55, 3497–3503. doi: 10.1016/j.electacta.2010.01.084

Kern, W., and Puotinen, D. A. (1970). Cleaning solutions based on hydrogen peroxide for use in silicone semiconductor technolog. *RCA Rev.* 31:187.

Li, B., Lu, M., Liu, W., Zhu, X., He, X., Yang, Y., et al. (2017). Reversible Electrochemical control over photoexcited luminescence of core/Shell CdSe/ZnS quantum dot film. *Nanoscale Res. Lett.* 12:626. doi: 10.1186/s11671-017-2398-9

Liang, F., and Liu, J.-X. (2018). Photoluminescence properties of hexagonal indium tin oxide nanopowders prepared by solvothermal method. *Rare Met.* 37, 47–53. doi: 10.1007/s12598-016-0831-3

Lin, S. P., Chi, T. Y., Lai, T. Y., and Liu, M. C. (2012). Investigation into the effect of varied functional biointerfaces on silicon nanowire MOSFETs. *Sensors* 12, 16867–16878. doi: 10.3390/s121216867

Liu, Y., Li, Y., Li, X., and He, T. (2013). Kinetics of (3-Aminopropyl)triethoxylsilane (APTES) silanization of superparamagnetic iron oxide nanoparticles. *Langmuir* 29, 15275–15282. doi: 10.1021/la403269u

Lübkemann, F., Anselmann, R., Kodanek, T., and Bigall, N. C. (2017). Inkjet printing of aqueous photoluminescent CdSe/CdS nanorods on solid substrates. *Chemie Ing. Tech.* 89, 807–813. doi: 10.1002/cite.201600086

Ma, H. L., Zhang, D. H., Ma, P., Win, S. Z., and Li, S. Y. (1995). Preparation and properties of transparent conducting indium tin oxide films deposited by reactive evaporation. *Thin Solid Films* 263, 105–110. doi: 10.1016/0040-6090(95)06554-7

Miethe, J. F., Lübkemann, F., Poppe, J., Steinbach, F., Dorfs, D., and Bigall, N. C. (2018). Spectroelectrochemical investigation of the charge carrier kinetics of gold-decorated cadmium chalcogenide nanorods. *ChemElectroChem* 5, 175–186. doi: 10.1002/celc.201700798

Pavlovic, E., Quist, A. P., Nyholm, L., Pallin, A., Gelius, U., and Oscarsson, S. (2003). Patterned generation of reactive thiolsulfinates/thiolsulfonates on silicon oxide by electrooxidation using electromicrocontact printing. *Langmuir* 19, 10267–10270. doi: 10.1021/la035434x

Pensa, E., Cortés, E., Corthey, G., Carro, P., Vericat, C., Fonticelli, M. H., et al. (2012). The chemistry of the sulfur-gold interface: in search of a unified model. *Acc. Chem. Res.* 45, 1183–1192. doi: 10.1021/ar200260p

Poppe, J., Gabriel, S., Liebscher, L., and Hickey, S. G. (2013). A versatile approach for coating oxidic surfaces with a range of nanoparticulate materials. *J. Mater. Chem. C* 1, 1515–1524. doi: 10.1039/C2TC00863G

Poppe, J., Hickey, S. G., and Eychmüller, A. (2014). Photoelectrochemical investigations of semiconductor nanoparticles and their application to solar cells. *J. Phys. Chem. C* 118, 17123–17141. doi: 10.1021/jp5016092

Savu, R., and Joanni, E. (2006). Low-temperature, self-nucleated growth of indium-tin oxide nanostructures by pulsed laser deposition on amorphous substrates. *Scr. Mater.* 55, 979–981. doi: 10.1016/j.scriptamat.2006.08.022

Su, Y. H., Lai, W. H., Teoh, L. G., Hon, M. H., and Huang, J. L. (2007). Layer-by-layer Au nanoparticles as a schottky barrier in a water-based dye-sensitized solar cell. *Appl. Phys.* 178, 173–178. doi: 10.1007/s00339-007-3988-7

Sunkara, V., and Cho, Y. K. (2012). Investigation on the mechanism of aminosilane-mediated bonding of thermoplastics and poly(Dimethylsiloxane). *ACS Appl. Mater. Interf.* 4, 6537–6544. doi: 10.1021/am3015923

Tang, A. W., Teng, F., Xiong, S., Gao, Y. H., Liang, C. J., and Hou, Y. B. (2007). Electroluminescence from organic/inorganic heterostructure device based on blends of PVK and water-Sol CdSe nanocrystals. *J. Photochem. Photobiol. Chem.* 192, 1–7. doi: 10.1016/j.jphotochem.2007.04.029

Taniguchi, S., Yokozeki, M., Ikeda, M., and Suzuki, T. (2011). Transparent oxide thin-film transistors using n-(In 2 O 3) 0.9 (SnO 2) 0.1 /InGaZnO 4 modulation-doped heterostructures. *Jpn. J. Appl. Phys.* 50:04DF11. doi: 10.7567/JJAP.50.04DF11

Tessier, M. D., Javaux, C., Maksimovic, I., Loriette, V., and Dubertret, B. (2012). Spectroscopy of single CdSe nanoplatelets. *ACS Nano* 6, 6751–6758. doi: 10.1021/nn3014855

Wang, L., and Wang, E. (2004a). Direct electron transfer between cytochrome c and a gold nanoparticles modified electrode. *Electrochem. Commun.* 6, 49–54. doi: 10.1016/j.elecom.2003.10.004

Wang, L., and Wang, E. (2004b). A novel hydrogen peroxide sensor based on horseradish peroxidase immobilized on colloidal au modified ITO electrode. *Electrochem. Commun.* 6, 225–229. doi: 10.1016/j.elecom.2003.12.004

Wehrenberg, B. L., and Guyot-Sionnest, P. (2003). Electron and hole injection in PbSe quantum dot films. *J. Am. Chem. Soc.* 125, 7806–7807. doi: 10.1021/ja035369d

Xiao, C. W., Chi, L. F., and Fuchs, H. (2005). Patterning of semiconductor nanoparticles via microcontact printing. *Eur. J. Inorg. Chem.* 3729–3733. doi: 10.1002/ejic.200500520

Yaacobi-gross, N. (2011). Field and its application to CdSe-based solar cells. *Nat. Mater.* 10, 974–979. doi: 10.1038/nmat3133

Yang, D., Chen, G., Wang, L., Zou, Y., Sheng, X., Liu, H., et al. (2011). CdSe quantum dots sensitized mesoporous TiO2solar cells with CuSCN as solid-state electrolyte. *J. Nanomater.* 2011:269591. doi: 10.1155/2011/269591

Yang, H., Liu, L., Liang, H., Wei, J., and Yang, Y. (2011). Phase-controlled synthesis of monodispersed porous In2O3nanospheres via an Organic acid-assisted hydrothermal process. *CrystEngComm* 13, 5011–5016. doi: 10.1039/c1ce05274h

Yokota, H., Shimura, K., Nakayama, M., and Kim, D. (2012). Optical Properties of self-assembled monolayer of CdSe quantum dots. *Phys. Status Solid. C* 9, 2465–2468. doi: 10.1002/pssc.201200261

Yu, W. W., Qu, L., Guo, W., and Peng, X. (2003). Experimental Determination of the extinction coefficient of CdTe, CdSe, and CdS nanocrystals. *Chem. Mater.* 15, 2854–2860. doi: 10.1021/cm034081k

Yue, Z., Lisdat, F., Parak, W. J., Hickey, S. G., Tu, L., Sabir, N., et al. (2013). Quantum-dot-based photoelectrochemical sensors for chemical and biological detection. *ACS Appl. Mater. Interf.* 5, 2800–2814. doi: 10.1021/am3028662

Zeng, Y., and Kelley, D. F. (2016). Excited hole photochemistry of CdSe/CdS quantum dots. *J. Phys. Chem. C* 120, 17853–17862. doi: 10.1021/acs.jpcc.6b06282

Zhang, J., Kambayashi, M., and Oyama, M. (2004). A novel electrode surface fabricated by directly attaching gold nanospheres and nanorods onto indium tin oxide substrate with a seed mediated growth process. *Electrochem. Commun.* 6, 683–688. doi: 10.1016/j.elecom.2004.05.006

Zhang, L. (2013). Self-assembly ag nanoparticle monolayer film as SERS substrate for pesticide detection. *Appl. Surf. Sci.* 270, 292–294. doi: 10.1016/j.apsusc.2013.01.014

Zillner, E., Kavalakkatt, J., Eckhardt, B., Dittrich, T., Ennaoui, A., and Lux-Steiner, M. (2012). Formation of a heterojunction by electrophoretic deposition of CdTe/CdSe nanoparticles from an exhaustible source. *Thin Solid Films* 520, 5500–5503. doi: 10.1016/j.tsf.2012.05.002

Conflict of Interest Statement: The authors declare that the research was conducted in the absence of any commercial or financial relationships that could be construed as a potential conflict of interest.

frontiers in Chemistry

REVIEW
published: 28 November 2018
doi: 10.3389/fchem.2018.00575

Road Map for Nanocrystal Based Infrared Photodetectors

*Clément Livache, Bertille Martinez, Nicolas Goubet, Julien Ramade and Emmanuel Lhuillier**

Sorbonne Université, CNRS, Institut des NanoSciences de Paris, INSP, Paris, France

Infrared (IR) sensors based on epitaxially grown semiconductors face two main challenges which are their prohibitive cost and the difficulty to rise the operating temperature. The quest for alternative technologies which will tackle these two difficulties requires the development of new IR active materials. Over the past decade, significant progresses have been achieved. In this perspective, we summarize the current state of the art relative to nanocrystal based IR sensing and stress the main materials, devices and industrial challenges which will have to be addressed over the 5 next years.

Keywords: infrared, nanocrystals, photodetection, device, interband, intraband

OPEN ACCESS

Edited by:
Maksym Yarema,
ETH Zürich, Switzerland

Reviewed by:
Dmitry Aldakov,
CEA Grenoble, France
Maria Ibáñez,
Institute of Science and Technology Austria (IST Austria), Austria

***Correspondence:**
Emmanuel Lhuillier
el@insp.upmc.fr

Specialty section:
This article was submitted to Nanoscience, a section of the journal Frontiers in Chemistry

Received: *13 September 2018*
Accepted: *05 November 2018*
Published: *28 November 2018*

Citation:
Livache C, Martinez B, Goubet N, Ramade J and Lhuillier E (2018) Road Map for Nanocrystal Based Infrared Photodetectors. Front. Chem. 6:575. doi: 10.3389/fchem.2018.00575

INTRODUCTION

Over the recent years, colloidal quantum dots (CQDs) have reached a first mass market application with their use as light sources for displays. This application brought even more interest for CQDs both at the academic and industrial levels. Among emerging applications, infrared (IR) photodetection (Kershaw et al., 2013; Lhuillier and Guyot-Sionnest, 2017) is a field where colloidal materials have a strong potential to bring cost disruption, especially because organic semiconductors, often seen as the low-cost alternative to conventional semiconductors, are ineffective in this range of wavelengths.

IR detection currently relies on two types of sensors. Quantum detectors are based on photon-absorbing semiconductor materials. These can either be narrow band gap semiconductors (InGaAs in the short-wave IR, InSb in the mid-wave and HgCdTe for both mid- and long-wave IR) or semiconductor heterostructures (GaAs/AlGaAs, used in Quantum Well Infrared Photodetector or QWIP, and InAs/GaSb in type II superlattices). These technologies are mature, present high performances (i.e., high quantum efficiency, relatively low dark current, high uniformity, fast time response), but suffer from an excessive cost (a typical IR camera costs 30 k−100 k€) and a low operating temperature. As a result, access to this type of technologies remains restricted to defense and scientific applications (mostly astronomy).

The second class of IR detectors is thermal detectors, sensitive to energy flux rather than photon flux. Materials used for this kind of detectors see one of their physical property (typically, their electrical resistance) changing upon absorption of IR radiation. Typical technologies are bolometers and pyrometers. Their operation principles make them intrinsically slower than quantum devices, and they present lower detectivity (signal to noise ratio) than their quantum detector counterpart. On the other hand, they can be operated at room temperature and their cost is significantly lower, ranging from 100 € to few k€ per focal plane array (FPA) and 1 to 10 k€ for camera.

To bring IR detection to a mass market level, a technology combining both the performances of quantum detector and the low cost of thermal detector needs to emerge. CQDs appear as promising candidates to reach this goal. Beyond their tunable absorption from the near IR to the THz range

(Goubet et al., 2018a), several significant proofs of concepts such as mid-IR photoconduction (Keuleyan et al., 2011), background limited photodiode (Guyot-Sionnest and Roberts, 2015) and investigation of stability issues (Jagtap et al., 2018a) have brought CQDs to a technological readiness level (TRL) above 3 which is critical for the industry to start considering an emerging technology.

The focus of this paper is intentionally limited to IR detection, which means that we have excluded from the scope of this review any solar cell application (Sargent, 2012). In this perspective, we propose a road map of the main challenges that have to be addressed by the community in order to transfer the IR CQD technology to the industrial level.

DISCUSSION

Basic of IR Detection Using Nanocrystals as Active Material

To start, we would like to discuss the basics of the transformation of a colloidal nanocrystal solution into an IR sensor. Two type of geometries have been explored: planar and vertical geometry, see **Figures 1A,C**. The planar geometry is certainly the easiest to implement, because this geometry is far less sensitive to the film quality (i.e., film roughness and cracks do not lead to electrical shorts in the device). The success of this geometry also relates to the possibility to add a gate for the design of field effect (photo)transistor (Talapin and Murray, 2005). Typically, electrodes are prepared on a conventional substrate (Si/SiO_2 typically). Interdigitated electrodes have been widely used as a strategy to enhance the current magnitude. The film of CQD is deposited on this substrate using methods such as spin coating, dropcasting, dip coating or spray coating (Cryer and Halpert, 2018). As is, the film of nanocrystal is insulating and a ligand exchange step is necessary to increase the CQD electronic coupling and achieve photoconduction. IR exposition is obtained by top side illumination. Typical I-V curve from such planar photoconductive device is shown in **Figure 1B**. The photosignal relates to the modulation of the I-V curve slope. Field effect transistor configuration (Lhuillier et al., 2014b) is interesting to tune the majority carrier current and possibly enhance the signal to noise ratio. The gating is typically obtained through the use of the dielectric layer from the substrate or through the deposition of a top side dielectric (Chung et al., 2012) or electrolyte (Lhuillier et al., 2014b).

The second type of detector geometry that has been widely explored is based on a vertical geometry. The typical stack of layers relies on a transparent substrate (glass in the near infrared) on top of which a transparent conductive layer is deposited. ITO (indium tin oxide) and FTO (fluoride doped tin oxide) are the most used material. An electron transport layer (ETL) is then deposited: the most used material for CQD based device are inorganic layers made of ZnO or TiO_2. This layer generally needs to be annealed at high temperature, which makes that it is highly desirable to process it as a bottom layer (i.e., before the CQD deposition). On the top of the ETL, the CQD layer is deposited. The typical thickness of this layer range from 200 to 400 nm. This value is a trade-off: thicker layer might be desirable to absorb more light since only 10–30 % of the light are absorbed in those conditions (Cademartiri et al., 2006; Hens and Moreels, 2012). However, thicker layers are difficult to build due to the multiplication of deposition and ligand exchange steps. Moreover, the short transport diffusion length makes that photocarriers might not be collected in thicker layers. On the top of the QD layer, a hole transport layer can be deposited. MoO_3 has been intensively used in the case of CQD (Gao et al., 2011; Chuang et al., 2014). Finally, a top metallic contact is deposited. There are many possible alternative configurations to the one described above with inverted geometry, as the combination of a n and p type layer (Chuang et al., 2014) or graded band gap configuration (Kramer et al., 2011) to funnel charges to the contacts. In this vertical configuration, illumination is made through the substrate, bottom contact and ETL. A typical IV curve of such photodiode is shown in **Figure 1D**. The key advantage of this configuration is to be able to operate the device close to zero bias to reduce the dark current, by taking advantage of the built-in electric field of the diode.

Now that the basic of CQD based IR detector design being established, it is of utmost importance to remind the main figures of merit relative to IR sensing (Rosencher, 2002). Responsivity (in A/W) is the first figure of merit which translates the ability of the active layer to transform a light signal into an electrical signal. This quantity directly relates to the external quantum efficiency (efficiency to convert incident photons into electrical current) and to internal quantum efficiency (efficiency to convert absorbed photons into electrical current, in other word the external quantum efficiency normalized by the device absorption). One of the key specificities of IR is the limited signal-to-noise ratio. Indeed, because of the narrow energy transition involved in the IR, thermal activation competes with photon activation of the carriers. This results in a dark current which can be a significant fraction of the total current. The relevant contribution of the dark current to noise is its spectral distribution (in $A.Hz^{-1/2}$), Hence, the quantity involved in the ultimate figure of merit of an IR detector is the detectivity (signal to noise ratio expressed in $cm.Hz^{1/2}.W^{-1}$ or Jones). Currently, all convincing reports relative to the measurement of noise in nanocrystal arrays have led to *1/f* noise as the prevailing contribution (Lai et al., 2014; Liu et al., 2014; De Iacovo et al., 2017). It is a very common habit to observe detectivity value reported assuming that noise is shot noise limited (mostly because there is an analytical expression for shot noise and none for *1/f* noise), however this leads to a huge overestimation of the device detectivity. Finally, another important figure of merit which differentiates detectors from solar cells is the device time response. To take full advantage of photon detectors, faster time responses that the ones reported for thermal detectors ($\approx$10 ms) are highly desirable. In the following we discuss state of the art results and expected performance targets for SWIR, MWIR, and LWIR range of wavelengths. We will now discuss the main challenges to address in order to bring the CQD technology to the industrial level. We have sorted those in three main categories: (i) material, (ii) device and (iii) camera integration challenges, see **Figure 2**.

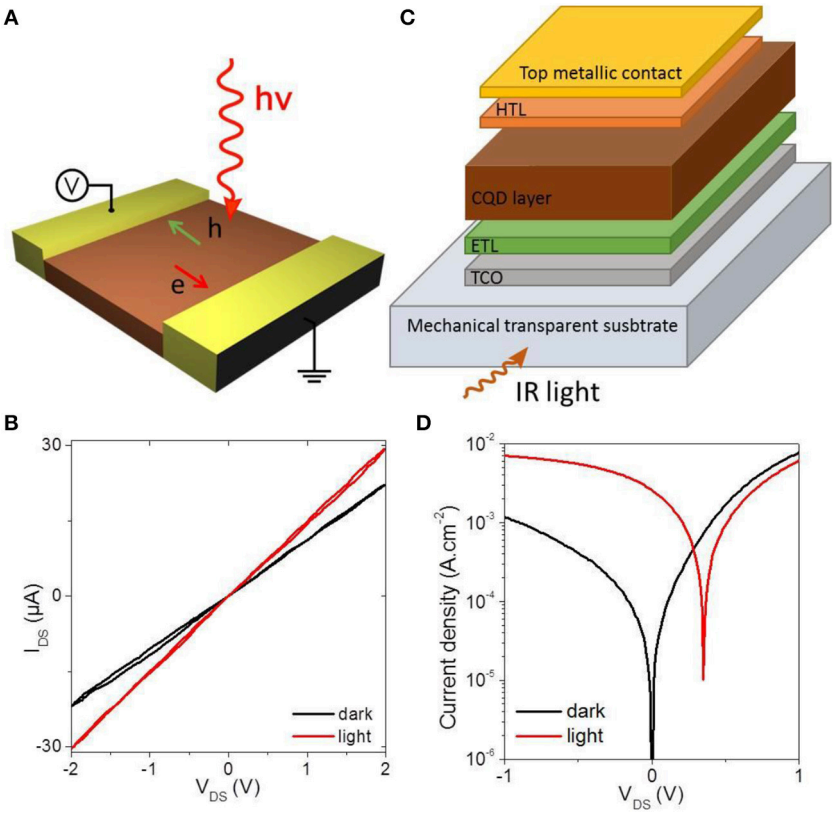

FIGURE 1 | (A) Scheme of a photoconductive device in planar geometry. **(B)** I-V curve of a photoconductive device under dark condition and under illumination. **(C)** Scheme of a photodiode in vertical geometry. TCO, ETL and HTL stands respectively, for transparent conductive oxide, electron transport layer and hole transport layer. **(D)** I-V curve of a photodiode under dark condition and under illumination.

Material Challenges

IR Absorption: Interband vs. Intraband Transitions

Among all criteria to build an IR detector, design IR absorption appears as the first challenge to tackle. Three wavelength bands appear promising for applications: short-, mid- and long-wave infrared.

Short-Wave Infrared (SWIR) extends from 800 nm to 1.7 µm, and up to 2.5 µm for extended SWIR. In this range, the objective for CQD-based detectors is to offer an alternative to InGaAs. As stated earlier, these technologies offer top-level performances. However, their cost, without being prohibitive, remains far above comparable technologies in the visible range. Moreover, the perspectives of cost disruption are limited for such a mature technology. In this range of wavelengths, applications are typically active imaging, night glow assisted imaging and tissues imaging. Among possible colloidal materials to be used in this range of wavelengths, two materials have reached a large enough maturity: lead chalcogenides (Sargent, 2008) (PbS and PbSe, mostly) and HgTe (Kovalenko et al., 2006; Keuleyan et al., 2011; Green and Mirzai, 2018). In those materials, IR absorption is obtained through interband transitions, see **Figure 3A**.

In the Mid-Wave Infrared (MWIR: 3–5 µm), blackbody emission of room-temperature objects starts to prevail over reflection of other light sources, hence opening the field of thermal imaging. In this range, HgTe is by far the most investigated material (Kovalenko et al., 2006; Keuleyan et al., 2011; Tang et al., 2016) thanks to its tunable interband IR transition, see **Figure 3D**. Another strategy to achieve low-energy transition in the MWIR is to use intraband transitions (see **Figure 3B**; Deng et al., 2014; Jagtap et al., 2018b; Kim et al., 2018). In this case, the transition occurs in the first levels of the conduction band, hence doped semiconductors are necessary. Again, mercury chalcogenides are the most investigated materials for photodetection thanks to self-doping (Deng et al., 2014; Jagtap et al., 2018b; Kim et al., 2018).

Long-Wave Infrared (LWIR: 5–30 µm) is the optimal range to perform thermal imaging of room-temperature objects since their blackbody emission maximum lies around 10 µm. Addressing such low energy with interband transitions is extremely challenging since the confinement energy needs to be so small that the required size of nanocrystals becomes incompatible with colloidal stability or monodispersity. Intraband (Park et al., 2018) and plasmonic transitions (Luther et al., 2011; Agrawal et al., 2017; Coughlan et al., 2017; Askari et al., 2018; Liu et al., 2018) (achieved at a higher doping level) in doped nanocrystals, see **Figure 3C**, are interesting for two reasons: (i) addressing long wavelengths from the MWIR to the

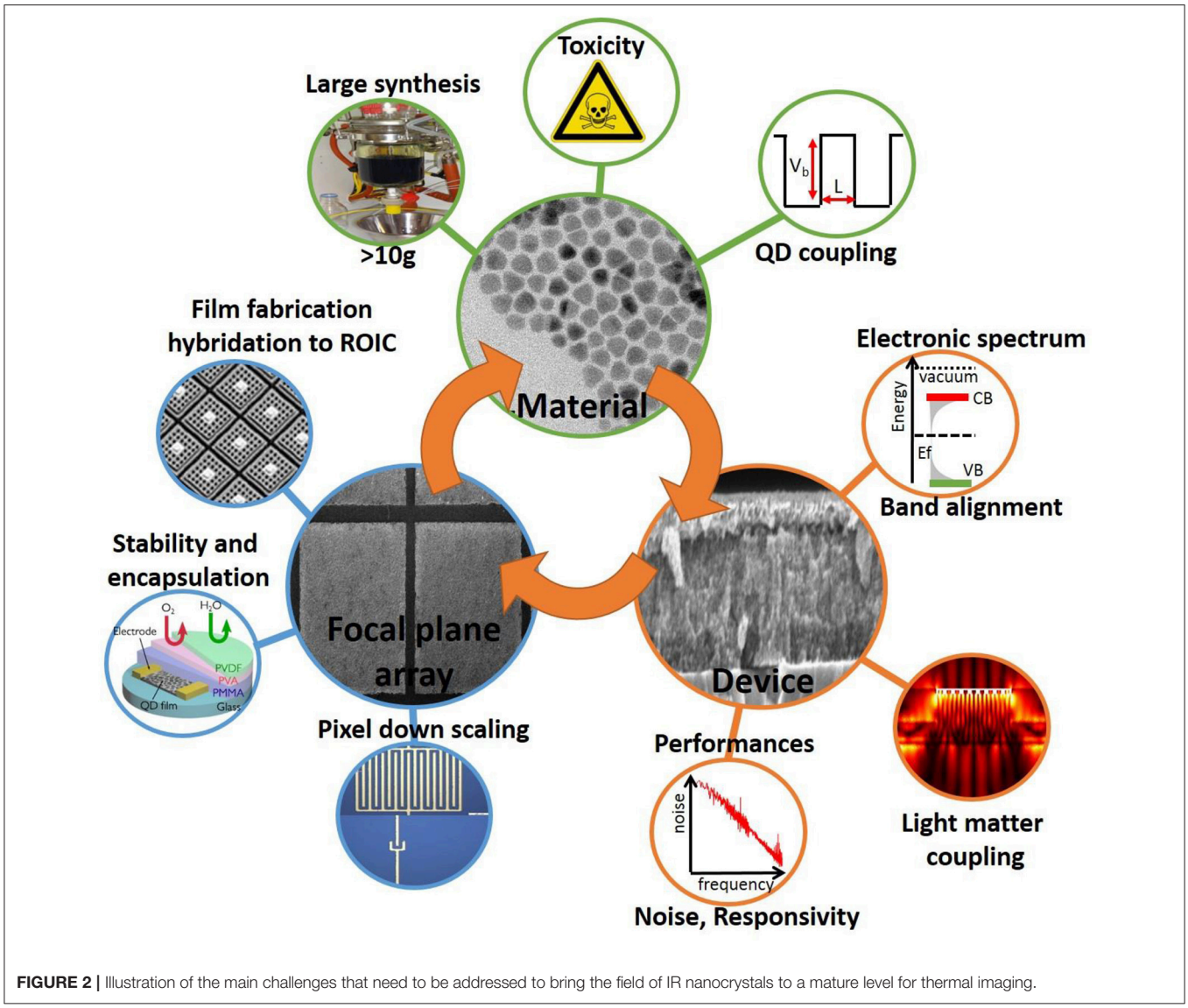

FIGURE 2 | Illustration of the main challenges that need to be addressed to bring the field of IR nanocrystals to a mature level for thermal imaging.

THz range while keeping the colloidal stability of the material and (ii) because doping of nanocrystals might not be limited to toxic material.

Surface Chemistry

Beyond the nanocrystal synthesis, the control of surface chemistry is a critical step toward the design of photoconductive thin films. Initial long capping ligands, which ensure the nanometer size growth and preserve the colloidal stability, need to be stripped from the surface to increase the inter-CQD coupling (i.e., to reduce the inter CQD tunnel barrier) and obtain reasonable carrier mobility. For most of the reported devices the ligand exchange remains based on a solid state ligand exchange (i.e., performed on the film), typically using ethanedithiol as capping ligand (Lhuillier et al., 2013). This undoubtedly limits the carrier mobility in the 10^{-3} $cm^2V^{-1}s^{-1}$ range and likely the associated photoresponse. Introduction of inorganic ligands such as As_2S_3 appears as an interesting path to obtain higher film mobility (Lhuillier et al., 2013; Yakunin et al., 2014; Tang et al., 2016; Cryer and Halpert, 2018). It is nevertheless as important to boost mobility as preserving a good CQD surface passivation, especially for the design of photodiode, and more work needs to be done in this direction. In the case of ink preparation, CQD ends up being ligand-exchanged and suspended in polar solvent with high boiling point, raising some questions relative to the film preparation. Indeed, most of the devices are currently prepared using dropcasting (Tang et al., 2018) or spin coating. The latter method is difficult to implement using high boiling point solvent, in addition to a dramatically low efficiency (i.e., 90% of the material is wasted). Among alternative methods, dip coating (Chernomordik et al., 2017) and spray coating (Chen et al., 2013; Wang et al., 2015; Cryer and Halpert, 2018) have also been reported. The choice for a given method also impacts the preparation of the QD ink: low concentrations are used for dropcasting (10 mg/mL), while higher concentrations (50

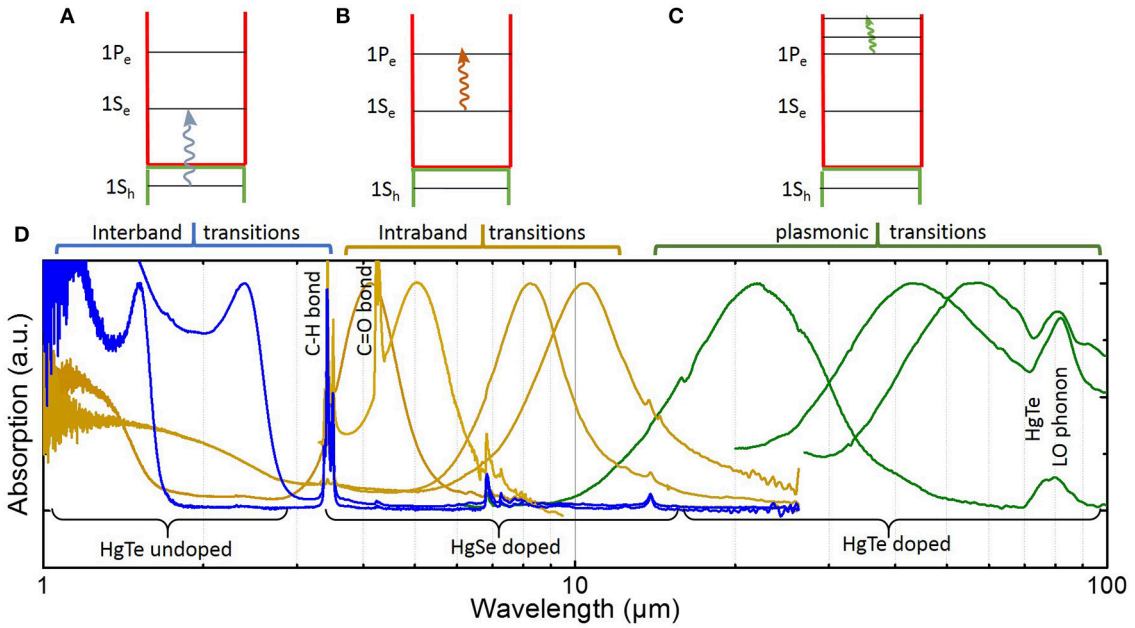

FIGURE 3 | (A–C) are respectively, the scheme for interband, intraband, and plasmonic transitions in nanocrystals. **(D)** Absorption spectra for mercury chalcogenide (HgSe and HgTe) nanocrystals of various sizes.

mg/mL) are used for spin coating in non-polar solvent and even higher in the case of spin coating from polar solvent. There is probably no perfect method for deposition and each involved team has to pay the price of time-consuming optimization for this step.

Another main challenge relative to the use of mercury chalcogenides relates to the softness of the material. As a result, any annealing step (to boost the mobility or as part of a lithography process) leads to sintering of the nanocrystal film. This induces an increase of the CQD effective radius which broadens the absorption cut-off and, even worse, dramatically increases the dark current (through a reduction of the effective band gap). Thus, core-shell objects with an external material which is able to sustain temperatures around 160°C (i.e., typical baking temperature of lithography resist such as polymethyl methacrylate) without aggregation will be of utmost interest. Introduction of core-shell structure may also lead to longer living photocarriers which is highly desirable for photodetection. A first study has been done in this direction by coupling HgTe and HgSe materials in heterostructured nanocrystals (Goubet et al., 2018b). However, growing such shell remains quite challenging because HgX compounds are grown at low temperature (100°C typically), while conventional shell materials are synthetized at high temperature (200°C and more). Currently all reported HgX based core-shell materials remain based on the room temperature Colloidal-Atomic Layer Deposition (C-ALD) process (Robin et al., 2016; Shen and Guyot-Sionnest, 2016; Sagar et al., 2017), which appears to be suboptimal procedure (Lhuillier et al., 2014a). Shell growth method specific to soft materials will have to be developed.

Material Toxicity

Material toxicity is probably one of the most difficult issues to address. As stated previously, the field remains driven by lead and mercury chalcogenides, which are actually the same material as the ones used in current IR detection technologies. For sure, the introduction of low toxicity compounds will be a breakthrough in the field. In the visible range of wavelengths, a large effort has been devoted to the synthesis of InP as an alternative to CdSe as light source for display. On the other hand, colloidal narrow band gap III-V materials (InAs Franke et al., 2016; Grigel et al., 2016; Srivastava et al., 2018 and InSb Maurice et al., 2013; Chang et al., 2014) remain poorly mature with a too limited amount of reports and none dedicated to IR detection further than the SWIR. First issue is due to the more covalent character of III-V materials with respect to II-VI materials. As a result, more reactive precursors need to be used which leads to a higher degree of synthesis complexity. Second, the availability of stable pnictogen precursors is decreasing for narrow band gap materials mostly due to their atomic radius increasing.

Narrow band gap interband transitions are more likely to be observed using heavy elements (higher Z value comes with a denser density of states, which are more likely to present a narrow band gap in the vicinity of the Fermi level). However, materials in the bottom part of the periodic table are also toxic. Certainly, a switch toward intraband transition is the promising path to achieve heavy metal free IR detection. This strategy is nevertheless currently limited to the MWIR and LWIR and the level of performance is by far not as good as their interband counterparts. Ag_2Se, thanks to its spectral vicinity with HgSe has recently generated some interest for MWIR detection (Sahu et al., 2012; Park et al., 2018; Qu et al., 2018), although detection

performances remain for now several orders of magnitude below than what have been reported with HgX compounds.

Another class of material that may appears as promising to achieve infrared absorption are strongly-doped semiconductors with plasmonic absorption in the infrared. This is typically the case of copper chalcogenides (Dorfs et al., 2011; Kriegel et al., 2012; Coughlan et al., 2017), oxide nanoparticles (Kanehara et al., 2009; Buonsanti et al., 2011; Della Gaspera et al., 2013; Ghosh et al., 2014; Schimpf et al., 2015; Runnerstrom et al., 2016; Tandon et al., 2017) or doped silicon (Gresback et al., 2014; Zhang et al., 2017). Plasmonic nanoparticles tend to have a much higher cross section ($\approx 10^{-13}$ cm^{-2}/particle) that the one associated with interband or intraband transitions (10^{-15}-10^{-14} cm^{-2}/particle range). However, their very short living photocarrier (<1 ps) might strongly balance the absorption enhancement. The investigation of (photo)transport properties in those materials needs to be pushed further.

Scale-up for Production

When it comes to mass market application, a first question to consider is how much material will be necessary. Let's assume that the objective is to provide to every car sold in Europe (≈20 million unit per year) an IR sensor dedicated to night-driving assistance. Typical device will have a 1 cm^2 size for a thickness of a few hundreds of nm (400 nm for the calculation). Let's assume further a density of 10 for the material with a film filling of 0.64, corresponding to a randomly close-packed film. Moreover, we can account for the poor efficiency of deposition method such as spin coating where 90% of the material is wasted. A single device thus requires 2.6 mg of active material. This means that around 50 kg of HgTe will be necessary to saturate the targeted market. It is worth pointing that this amount is actually quite small and material supply is not an issue. This strongly contrasts with solar cell applications, where much larger devices (m^2) are necessary and where consequently material supplying (in particular Te, for which supply short fall is expected 10 years from now) and toxicity become critical issues.

Large scale synthesis of quantum dots (Protière et al., 2011) and more particularly mercury chalcogenides at the 10 g scale has already been reported (Lhuillier et al., 2016). Thus, to reach an annual production of 50 kg, batches reaching a few 100 of g will be needed. This is probably a step where small and medium size companies producing nanocrystals should be involved to take advantage of the know-how developed for wide band gap materials (i.e., CdSe and InP).

Regarding the material production cost, it was recently evaluated by (Jean et al., 2018) that PbS CQDs present a fabrication cost in the 10 to 60 $/g range. Thus, even assuming that for HgTe the fabrication cost will be in the upper range of this estimation, the cost of active material per device remains extremely low (0.15 $). We can conclude that contrary to solar cells, the material cost is here not a limiting factor.

Device Challenges

Electronic Structure and Band Alignment

As stated earlier, the most promising colloidal materials for IR detection are lead and mercury chalcogenides. Knowledge of the electronic structure of these material remains limited compared to the one reached for silicon and III-V semiconductors, and most electronic structure parameters are known within a limited accuracy, even for the bulk. Once under colloidal form, we add on the top of that quantum confinement, dependence of the electronic spectrum with surface chemistry and surface traps. As a result, the electrical landscape of our active material remains quite blurry. It is consequently difficult to design device with carefully-optimized band alignments and ohmic contacts. A significant effort will have to be done to provide to the community data relative to the electronic structure of the infrared colloidal materials in a quite systematic way (material, size, surface chemistry). First results in this direction have been reported using combination of IR spectroscopy and electrochemistry (Chen and Guyot-Sionnest, 2017) or photoemission measurements (Martinez et al., 2017), but more will be needed.

As critical is the investigation of carrier dynamics in these narrow band gap materials especially for the understanding of current performances limitations. Methods based on time-resolved optical spectroscopy are difficult to transfer in the IR due to an intrinsically low PL efficiency of IR nanocrystals and due to less advanced optical setups in the IR. Development of alternative methods will be required. Again, some preliminary results in this direction have been obtained using time resolved photoluminescence (Keuleyan et al., 2014b), transient absorption (Melnychuk and Guyot-Sionnest, 2018), time resolved photoemission (Spencer et al., 2013; Livache et al., 2017) and transient photocurrent measurements (Gao et al., 2016; Livache et al., 2018; Martinez et al., 2018). There are nevertheless not enough data to depict the full range of dynamics in this material from Auger recombination at short time scale to long-lived traps at long time scale.

Thanks to the understanding of the electronic spectrum, the objective will be the design of new photodiodes, accounting for specificity of IR and colloidal material. While in the SWIR, exploiting the concept developed for solar cell was still a reasonable assumption (Jagtap et al., 2018a), this is no longer the case for longer wavelengths. Alternatives to current electron (mostly ZnO and TiO_2) and hole transport layers (MoO_3) will have to be developed. This is even more true to implement the concept of unipolar barrier, which role is to let selectively one carrier flow, while preventing the other carrier to circulate. This concept has been widely used for III-V and II-VI semiconductor IR sensors (White, 1987; Savich et al., 2011, 2013), but remains poorly used in the case or CQD based devices. This might nevertheless be a time-consuming process because the fragility of the IR CQDs will likely require the development of specific carrier transport layer which doping and band alignment will have to be finely tuned and experimentally determined.

Device Performances

Since the main purpose of this road map is the design of effective IR-sensing devices, it is certainly worth determining which level of performances seems to be a reasonable goal to

achieve for colloidal-based IR detectors in each specified range of wavelengths.

SWIR

For wavelengths up to 1.7 μm, the key competitor is the InGaAs technology which performance is again very unlikely to be beaten. Thus, CQDs appear promising for (i) cost disruption and (ii) extending the range of wavelengths toward the so-called extended SWIR (2.5 μm cut-off wavelength) (Jia et al., 2018). InGaAs succeeded to achieve extremely low dark current (<20 fA at 20°C for a 15 μm pixel). Because CQD based devices reported so far are not reaching such low dark current densities, operational scenarii with high photon flux seem more appropriate. This typically relates to active imaging (Geyer et al., 2013), flame detection (Iacovo et al., 2017) and biological tissues imaging for which reasonably fast detection is necessary (sub-ms is mandatory and μs is probably a more appropriate target) and already reported (Lhuillier et al., 2013). Also note that in the SWIR, room temperature operation or at least above water freezing point has to be achieved to preserve the low-cost character of the device. Because this range of wavelengths is fairly easy to reach using PbS CQDs and because of the relatively easy device characterization at such wavelengths, very high performance devices (up to kA.W^{-1} for responsivity and detectivity reaching 10^{13} Jones at 1.4 μm) have been achieved (Yakunin et al., 2014). Device demonstration also includes imaging systems (Calvez et al., 2011; Klem et al., 2015).

MWIR

In this range, targeted applications are thermal imaging (Tang et al., 2018) and gas sensing (Chen et al., 2017). Current bulk-based imaging devices (typically based on InSb and HgCdTe) have presently no road map for operating temperature above 180°C. This clearly sets a first objective. In the scope of preserving low-cost, it likely suggests that only Peltier cooling should actually be used, bringing the targeted operating temperature around 250 K. Recently reported reduced Auger effect (Melnychuk and Guyot-Sionnest, 2018) in HgTe CQDs compared to their bulk HgCdTe equivalent raises great hope to achieve this goal. In terms of performances, detectivity in the few 10^9 Jones at room temperature and reaching 10^{10} Jones at 250 K is a clear objective which will bring CQD based technologies above what can be achieved using thermal sensors. Huge progresses in this direction have been reported this year. This includes responsivity above 1 A.W^{-1} (Tang et al., 2018), detectivity above 10^9 Jones at room temperature (Cryer and Halpert, 2018) and NETD (noise equivalent temperature difference) down to 14 mK (Tang et al., 2018). In the MWIR, the device complexity lags far behind what has been achieved in the SWIR with just a few photodiodes (Guyot-Sionnest and Roberts, 2015; Ackerman et al., 2018) and only one report for focal plane array integration (Buurma et al., 2016).

LWIR

When long wavelengths (8 μm and more) start being involved, the number of reported devices quickly drops (Keuleyan et al., 2014a). It consequently becomes difficult to set some objectives of performance. One key difficulty in this range of wavelengths comes from the fact that it is unlikely that non-cryogenic operating temperatures can be achieved. Thus, the cost disruption brought by the CQDs is not as important as in the MWIR. Since the operating temperature of conventional IR camera in the 8–12 μm range is around 90 K, it is likely that operating temperature for CQD based device around 150 K will be desirable, with a detectivity remaining above 10^{10} jones. Preserving a fast response is also key aspect to compete with bolometers. Regarding the THz range, there is currently no available data.

Device Geometry and Emerging Strategies

Among current difficulties relative to colloidal materials, one key limitation remains connected to the short carrier diffusion length (50 to 100 nm typically) which is shorter than typical absorption length (close to 10 μm Lhuillier et al., 2012 for a band edge in the MWIR), due to the low carrier mobility. In other words, photogenerated carriers are only collected in the vicinity of the electrodes, while the bulk of the film leads to photogenerated charges that end up being trapped. In this sense, strategies to enhance the light-matter coupling are necessary. The objective of this strategy is to concentrate the incident electromagnetic field on the thin optically absorbing layer of CQDs. Some early results have been reported with the introduction of colloidal gold nanorods (Chen et al., 2014) or of resonators (Yifat et al., 2017; Tang et al., 2018). The development of such plasmonic resonance has also been used to obtain polarized emission and imaging system (Le-Van et al., 2016; Yifat et al., 2017).

Another interesting development that has been reported relates to the design of multicolor detectors. This includes visible and MWIR (Lhuillier et al., 2014b), MWIR/LWIR (Tang et al., 2016) and MWIR/MWIR (Cryer and Halpert, 2018) sensors. However it remains unclear if bicolor technology can be compatible with low fabrication cost.

Finally, it is worth mentioning a strategy which has been explored over the last 5 years to boost the device photoresponse is the coupling of the nanocrystals with a 2D material. Graphene is the first to have been explored. Gigantic responsivities (10^7 A.W^{-1}) have been reported (Konstantatos et al., 2012; Sun et al., 2012) but the concept was unsuccessful because the dark current was even larger than in a conventional film of CQDs. The concept was then revisited by replacing graphene by MoS_2 to introduce a gap and reduce the dark current. Simultaneously, the absorption was pushed from telecom range to longer wavelengths by replacing the PbS CQDs by HgTe nanocrystals (Huo et al., 2017). This strategy keeps suffering from two main limitations, which are the fast saturation of the optical response (responsivity is only large under zero photon flux) and large memory effects (i.e., long time response).

Focal Plane Array

Pixel Downsizing and Coupling to Read Out Circuit

When it comes to building a focal plane array, the pixel size matters. Most of current devices reported in the literature are based on a chip with several individual devices, each of them being typically around 1 mm^2 area. When such size is far too

small in the case of solar cells where m^2 are required, it is also far too big for use in cameras, where the pixel should be ideally just above the targeted wavelength to improve image quality. Current IR technologies present pixel sizes in the 10 to 50 μm range. These values are actually limited by technology and more specifically by the indium bump hybridization to the read-out circuit, which becomes very complex for size below 10 μm. There is, in this sense, a true opportunity for quantum dots here (Malinowski et al., 2017). Because the active layer can be directly deposited on a CMOS read-out circuit, demonstration of pixel sizes below 10 μm will bring a significant advantage to CQDs. This nevertheless has still to be demonstrated and also raises new questions such as the ability to design large scale homogeneous films while preventing pixel cross-overs. In the hypothesis where optical coupling between pixels will prevent the use of a continuous film of CQD, the film will have to be etched to effectively split the pixels (Lhuillier et al., 2016). In this case, the material will have to sustain a lithography step (i. e., high temperature exposure and exposition to solvent).

Stability and Encapsulation

Long term stability of CQD based device is a problem which has been mostly swept under the rug. It is conveniently admitted that stability of CQDs is higher than the one of organic materials, however there is a clear lack of data regarding this question. Probably absorption is a much more robust property than photoluminescence, nonetheless lead chalcogenides get oxidized and quickly get a PbO shell, when mercury chalcogenides are also air sensitive (Lhuillier et al., 2013; Jagtap et al., 2018a) even if the exact mechanism remains unclear. Two paths can be followed to address this question: either tuning the surface chemistry to make the CQDs stable in air, or processing the material in air-free conditions followed by the encapsulation of the CQD-based device below a protective layer. Handling of CQDs in glove box has become more or less the regular procedure in the field. Far less work has been devoted to the question of encapsulation. Certainly, concepts from the field of organic electronics and CQD based solar cells (Tan et al., 2017) can be reused. This include deposition of encapsulation polymers such as CYTOP, ALD (atomic layer deposition) deposition of thick alumina layer (Ihly et al., 2011) or nanoparticle shelling (Durmusoglu et al., 2017). Nevertheless, it is critical to consider that current PbX and HgX materials are synthetized at low temperature (<150 and $<100°C$, respectively) and that processing them at temperatures higher than their growth temperature will undoubtedly lead to a significant sintering and its associated dark current rise. As a result, specific low temperature methods need to be developed. Recently (Jagtap et al., 2018a) have reported the low temperature deposition of a combination of water-proof (PMMA and PVDF) and oxygen-proof (PVA) layers, leading to stability over at least 3 months. This is comparable to the stability obtained for solar cell based on PbS CQDs (Chuang et al., 2014). Longer stability investigation (at least up to 1 year) under realistic operational environment will have to be done to confirm the potential of the technology.

CONCLUSION

Thanks to 10 years of intensive research, IR CQDs have undoubtedly reached a maturity level where they can be considered as a possible alternative to historical semiconductors for IR sensing. Main achievements include full tunability of the absorption over the IR range, BLIP photodiode, demonstration of CQD based focal plane array in both SWIR and MWIR range. We have tentatively listed the main technological challenges that still need to be addressed to fully transfer this technology to industry.

AUTHOR CONTRIBUTIONS

All authors listed have made a substantial, direct and intellectual contribution to the work, and approved it for publication.

ACKNOWLEDGMENTS

EL thanks the support ERC starting grant blackQD (grant n°756225). We acknowledge the use of clean-room facilities from the Centrale de Proximité Paris-Centre. This work has been supported by the Region Ile-de-France in the framework of DIM Nano-K (grant dopQD). This work was supported by French state funds managed by the ANR within the Investissements d'Avenir programme under reference ANR-11-IDEX-0004-02, and more specifically within the framework of the Cluster of Excellence MATISSE and also by the grant IPER-nano2. NG and JR thank Nexdot for post doc funding. We thank N. Pere-Laperne, A. Nedelcu and J.-L. Reverchon for their valuable feedback on the manuscript.

REFERENCES

Ackerman, M. M., Tang, X., and Guyot-Sionnest, P. (2018). Fast and sensitive colloidal quantum dot mid-wave infrared photodetectors. *ACS Nano* 12, 7264–7271. doi: 10.1021/acsnano.8b03425

Agrawal, A., Johns, R. W., and Milliron, D. J. (2017). Control of localized surface plasmon resonances in metal oxide nanocrystals. *Annu. Rev. Mater. Res.* 47, 1–31. doi: 10.1146/annurev-matsci-070616-124259

Askari, S., Mariotti, D., Stehr, J. E., Benedikt, J., Keraudy, J., and Helmersson, U. (2018). Low-loss and tunable localized mid-infrared plasmons in nanocrystals of highly degenerate InN. *Nano Lett.*18, 5681–5687. doi: 10.1021/acs.nanolett.8b02260

Buonsanti, R., Llordes, A., Aloni, S., Helms, B. A., and Milliron, D. J. (2011). Tunable infrared absorption and visible transparency of colloidal aluminum-doped zinc oxide nanocrystals. *Nano Lett.* 11, 4706–4710. doi: 10.1021/nl203030f

Buurma, C., Pimpinella, R. E., Ciani, A. J., Feldman, J. S., Grein, C. H., and Guyot-Sionnest, P. (2016). "MWIR imaging with low cost colloidal quantum dot films," in *Optical Sensing, Imaging, and Photon Counting: Nanostructured Devices and Applications 2016* (San Diego, CA: International Society for Optics and Photonics), 993303. doi: 10.1117/12.2239986

Cademartiri, L., Montanari, E., Calestani, G., Migliori, A., Guagliardi, A., and Ozin, G. A. (2006). Size-dependent extinction coefficients of PbS quantum dots. *J. Am. Chem. Soc.* 128, 10337–10346. doi: 10.1021/ja063166u

Calvez, S. L., Bourvon, H., Kanaan, H., Gatta, S. M.-D., Philippot, C., and Reiss, P. (2011). "Enabling NIR imaging at room temperature using quantum dots," in *Infrared Sensors, Devices, and Applications; and Single Photon Imaging II*, (San Diego, CA: International Society for Optics and Photonics) 815506. doi: 10.1117/12.893094

Chang, A. Y., Liu, W., Talapin, D. V., and Schaller, R. D. (2014). Carrier dynamics in highly quantum-confined, colloidal indium antimonide nanocrystals. *ACS Nano* 8, 8513–8519. doi: 10.1021/nn5031274

Chen, M., and Guyot-Sionnest, P. (2017). Reversible electrochemistry of mercury chalcogenide colloidal quantum dot films. *ACS Nano* 11, 4165–4173. doi: 10.1021/acsnano.7b01014

Chen, M., Lu, H., Abdelazim, N. M., Zhu, Y., Wang, Z., Ren, W., et al. (2017). Mercury telluride quantum dot based phototransistor enabling high-sensitivity room-temperature photodetection at 2000 nm. *ACS Nano* 11, 5614–5622. doi: 10.1021/acsnano.7b00972

Chen, M., Shao, L., Kershaw, S. V., Yu, H., Wang, J., Rogach, A. L., et al. (2014). Photocurrent enhancement of HgTe quantum dot photodiodes by plasmonic gold nanorod structures. *ACS Nano* 8, 8208–8216. doi: 10.1021/nn502510u

Chen, M., Yu, H., Kershaw, S. V., Xu, H., Gupta, S., Hetsch, F., et al. (2013). Fast, air-stable infrared photodetectors based on spray-deposited aqueous HgTe quantum dots. *Adv. Funct. Mater.* 24, 53–59. doi: 10.1002/adfm.201301006

Chernomordik, B. D., Marshall, A. R., Pach, G. F., Luther, J. M., and Beard, M. C. (2017). Quantum dot solar cell fabrication protocols. *Chem. Mater.* 29, 189–198. doi: 10.1021/acs.chemmater.6b02939

Chuang, C. H., Brown, P. R., Bulović, V., and Bawendi, M. G. (2014). Improved performance and stability in quantum dot solar cells through band alignment engineering. *Nat. Mater.* 13:796. doi: 10.1038/nmat3984

Chung, D. S., Lee, J.-S., Huang, J., Nag, A., Ithurria, S., and Talapin, D. V. (2012). Low voltage, hysteresis free, and high mobility transistors from all-inorganic colloidal nanocrystals. *Nano Lett.* 12, 1813–1820. doi: 10.1021/nl203949n

Coughlan, C., Ibáñez, M., Dobrozhan, O., Singh, A., Cabot, A., and Ryan, K. M. (2017). Compound copper chalcogenide nanocrystals. *Chem. Rev.* 117, 5865–6109. doi: 10.1021/acs.chemrev.6b00376

Cryer, M. E., and Halpert, J. E. (2018). 300 nm spectral resolution in the mid-infrared with robust, high responsivity flexible colloidal quantum dot devices at room temperature. *ACS Photon.* 5, 3009–3015. doi: 10.1021/acsphotonics.8b00738

De Iacovo, A., Venettacci, C., Colace, L., Scopa, L., and Foglia, S. (2017). Noise performance of PbS colloidal quantum dot photodetectors. *Appl. Phys. Lett.* 111:211104. doi: 10.1063/1.5005805

Della Gaspera, E., Bersani, M., Cittadini, M., Guglielmi, M., Pagani, D., Noriega, R., et al. (2013). Low-temperature processed Ga-doped ZnO coatings from colloidal inks. *J. Am. Chem. Soc.* 135, 3439–3448. doi: 10.1021/ja307960z

Deng, Z., Jeong, K. S., and Guyot-Sionnest, P. (2014). Colloidal quantum dots intraband photodetectors. *ACS Nano* 8, 11707–11714. doi: 10.1021/nn505092a

Dorfs, D., Härtling, T., Miszta, K., Bigall, N. C., Kim, M. R., Genovese, A., et al. (2011). Reversible tunability of the near-infrared valence band plasmon resonance in cu2–xse nanocrystals. *J. Am. Chem. Soc.* 133, 11175–11180. doi: 10.1021/ja2016284

Durmusoglu, E. G., Yildizhan, M. M., Gulgun, M. A., and Yagci Acar, H. (2017). Production of small, stable PbS/CdS quantum dots via room temperature cation exchange followed by a low temperature annealing processes. *J. Phys. Chem. C* 121, 25520–25530. doi: 10.1021/acs.jpcc.7b06153

Franke, D., Harris, D. K., Chen, O., Bruns, O. T., Carr, J. A., Wilson, M. W., et al. (2016). Continuous injection synthesis of indium arsenide quantum dots emissive in the short-wavelength infrared. *Nat. Commun.* 7:12749. doi: 10.1038/ncomms12749

Gao, J., Nguyen, S. C., Bronstein, N. D., and Alivisatos, A. P. (2016). Solution-processed, high-speed, and high-quantum-efficiency quantum dot infrared photodetectors. *ACS Photon.* 3, 1217–1222. doi: 10.1021/acsphotonics.6b00211

Gao, J., Perkins, C. L., Luther, J. M., Hanna, M. C., Chen, H.-Y., Semonin, O. E., et al. (2011). n-type transition metal oxide as a hole extraction layer in PbS quantum dot solar cells. *Nano Lett.* 11, 3263–3266. doi: 10.1021/nl2015729

Geyer, S. M., Scherer, J. M., Jaworski, F. B., and Bawendi, M. G. (2013). Multispectral imaging via luminescent down-shifting with colloidal quantum dots. *Opt. Mater. Express* 3, 1167–1175. doi: 10.1364/OME.3.001167

Ghosh, S., Saha, M., and De, S. K. (2014). Tunable surface plasmon resonance and enhanced electrical conductivity of In doped ZnO colloidal nanocrystals. *Nanoscale* 6, 7039–7051. doi: 10.1039/C3NR05608B

Goubet, N., Jagtap, A., Livache, C., Martinez, B., Portalès, H., Xu, X. Z., et al. (2018a). Terahertz HgTe nanocrystals: beyond confinement. *J. Am. Chem. Soc.* 140, 5033–5036. doi: 10.1021/jacs.8b02039

Goubet, N., Livache, C., Martinez, B., Xu, X. Z., Ithurria, S., Royer, S., et al. (2018b). Wave-function engineering in HgSe/HgTe colloidal heterostructures to enhance mid-infrared photoconductive properties. *Nano Lett.* 18, 4590–4597. doi: 10.1021/acs.nanolett.8b01861

Green, M., and Mirzai, H. (2018). Synthetic routes to mercury chalcogenide quantum dots. *J. Mater. Chem. C.* 6, 5097–5112. doi: 10.1039/C8TC00910D

Gresback, R., Kramer, N. J., Ding, Y., Chen, T., Kortshagen, U. R., and Nozaki, T. (2014). Controlled doping of silicon nanocrystals investigated by solution-processed field effect transistors. *ACS Nano* 8, 5650–5656. doi: 10.1021/nn500182b

Grigel, V., Dupont, D., De Nolf, K., Hens, Z., and Tessier, M. D. (2016). InAs colloidal quantum dots synthesis via aminopnictogen precursor chemistry. *J. Am. Chem. Soc.* 138, 13485–13488. doi: 10.1021/jacs.6b07533

Guyot-Sionnest, P., and Roberts, J. A. (2015). Background limited mid-infrared photodetection with photovoltaic HgTe colloidal quantum dots. *Appl. Phys. Lett.* 107:253104. doi: 10.1063/1.4938135

Hens, Z., and Moreels, I. (2012). Light absorption by colloidal semiconductor quantum dots. *J. Mater. Chem.* 22, 10406–10415. doi: 10.1039/C2JM30760J

Huo, N., Gupta, S., and Konstantatos, G. (2017). MoS2–HgTe quantum dot hybrid photodetectors beyond 2 μm. *Adv. Mater.* 29:1606576. doi: 10.1002/adma.201606576

Iacovo, A. D., Venettacci, C., Colace, L., Scopa, L., and Foglia, S. (2017). PbS colloidal quantum dot visible-blind photodetector for early indoor fire detection. *IEEE Sens. J.* 17, 4454–4459. doi: 10.1109/JSEN.2017.2710301

Ihly, R., Tolentino, J., Liu, Y., Gibbs, M., and Law, M. (2011). The Photothermal Stability of PbS Quantum Dot Solids. *ACS Nano* 5, 8175–8186. doi: 10.1021/nn2033117

Jagtap, A., Goubet, N., Livache, C., Chu, A., Martinez, B., Gréboval, C., et al. (2018a). Short wave infrared devices based on HgTe nanocrystals with air stable performances. *J. Phys. Chem. C* 122, 14979–14985. doi: 10.1021/acs.jpcc.8b03276

Jagtap, A., Livache, C., Martinez, B., Qu, J., Chu, A., Gréboval, C., et al. (2018b). Emergence of intraband transitions in colloidal nanocrystals. *Opt. Mater. Express* 8, 1174–1183. doi: 10.1364/OME.8.001174

Jean, J., Xiao, J., Nick, R., Moody, N., Nasilowski, M., Bawendi, M., et al. (2018). Synthesis cost dictates the commercial viability of lead sulfide and perovskite quantum dot photovoltaics. *Energy Environ. Sci.* 11, 2295–2305. doi: 10.1039/C8EE01348A

Jia, B. W., Tan, K. H., Loke, W. K., Wicaksono, S., Lee, K. H., and Yoon, S. F. (2018). Monolithic integration of insb photodetector on silicon for mid-infrared silicon photonics. *ACS Photon.* 5, 1512–1520. doi: 10.1021/acsphotonics.7b01546

Kanehara, M., Koike, H., Yoshinaga, T., and Teranishi, T. (2009). Indium tin oxide nanoparticles with compositionally tunable surface plasmon resonance frequencies in the near-IR region. *J. Am. Chem. Soc.* 131, 17736–17737. doi: 10.1021/ja9064415

Kershaw, S. V., Susha, A. S., and Rogach, A. L. (2013). Narrow bandgap colloidal metal chalcogenide quantum dots: synthetic methods, heterostructures, assemblies, electronic and infrared optical properties. *Chem. Soc. Rev.* 42, 3033–3087. doi: 10.1039/C2CS35331H

Keuleyan, S., Kohler, J., and Guyot-Sionnest, P. (2014b). Photoluminescence of Mid-infrared HgTe colloidal quantum dots. *J. Phys. Chem. C* 118, 2749–2753. doi: 10.1021/jp409061g

Keuleyan, S., Lhuillier, E., Brajuskovic, V., and Guyot-Sionnest, P. (2011). Mid-infrared HgTe colloidal quantum dot photodetectors. *Nat. Photonics* 5, 489–493. doi: 10.1038/nphoton.2011.142

Keuleyan, S. E., Guyot-Sionnest, P., Delerue, C., and Allan, G. (2014a). Mercury telluride colloidal quantum dots: electronic structure, size-dependent spectra, and photocurrent detection up to 12 μm. *ACS Nano* 8, 8676–8682. doi: 10.1021/nn503805h

Kim, J., Choi, D., and Jeong, K. S. (2018). Self-doped colloidal semiconductor nanocrystals with intraband transitions in steady state. *Chem. Commun.* 54, 8435–8445. doi: 10.1039/C8CC02488J

Klem, E. J. D., Gregory, C. W., Temple, D. S., and Lewis, J. S. (2015). "Colloidal quantum dot Vis-SWIR imaging: demonstration of a focal plane array and camera prototype (Presentation Recording)," in *Optical Sensing, Imaging, and Photon Counting: Nanostructured Devices and Applications* (San Diego, CA: International Society for Optics and Photonics), 955505. doi: 10.1117/12.2190372

Konstantatos, G., Badioli, M., Gaudreau, L., Osmond, J., Bernechea, M., Garcia de Arquer, F. P., et al. (2012). Hybrid graphene-quantum dot phototransistors with ultrahigh gain. *Nat. Nanotechnol.* 7, 363–368. doi: 10.1038/nnano.2012.60

Kovalenko, M. V., Kaufmann, E., Pachinger, D., Roither, J., Huber, M., Stangl, J., et al. (2006). Colloidal HgTe nanocrystals with widely tunable narrow band gap energies: from telecommunications to molecular vibrations. *J. Am. Chem. Soc.* 128, 3516–3517. doi: 10.1021/ja058440j

Kramer, I. J., Levina, L., Debnath, R., Zhitomirsky, D., and Sargent, E. H. (2011). Solar cells using quantum funnels. *Nano Lett.* 11, 3701–3706. doi: 10.1021/nl201682h

Kriegel, I., Jiang, C., Rodríguez-Fernández, J., Schaller, R. D., Talapin, D. V., da Como, E., et al. (2012). Tuning the excitonic and plasmonic properties of copper chalcogenide nanocrystals. *J. Am. Chem. Soc.* 134, 1583–1590. doi: 10.1021/ja207798q

Lai, Y., Li, H., Kim, D. K., Diroll, B. T., Murray, C. B., and Kagan, C. R. (2014). Low-frequency (1/f) noise in nanocrystal field-effect transistors. *ACS Nano* 8, 9664–9672. doi: 10.1021/nn504303b

Le-Van, Q., Le Roux, X. L., Aassime, A., and Degiron, A. (2016). Electrically driven optical metamaterials. *Nat. Commun.* 7:12017. doi: 10.1038/ncomms12017

Lhuillier, E., and Guyot-Sionnest, P. (2017). Recent progresses in mid infrared nanocrystal optoelectronics. *IEEE J. Sel. Top. Quantum Electron.* 23:6000208. doi: 10.1109/JSTQE.2017.2690838

Lhuillier, E., Keuleyan, S., and Guyot-Sionnest, P. (2012). Optical properties of HgTe colloidal quantum dots. *Nanotechnology* 23:175705. doi: 10.1088/0957-4484/23/17/175705

Lhuillier, E., Keuleyan, S., Zolotavin, P., and Guyot-Sionnest, P. (2013). Mid-infrared HgTe/As2S3 field effect transistors and photodetectors. *Adv. Mater.* 25, 137–141. doi: 10.1002/adma.201203012

Lhuillier, E., Pedetti, S., Ithurria, S., Heuclin, H., Nadal, B., Robin, A., et al. (2014a). Electrolyte-gated field effect transistor to probe the surface defects and morphology in films of thick CdSe colloidal nanoplatelets. *ACS Nano* 8, 3813–3820. doi: 10.1021/nn500538n

Lhuillier, E., Robin, A., Ithurria, S., Aubin, H., and Dubertret, B. (2014b). Electrolyte-gated colloidal nanoplatelets-based phototransistor and its use for bicolor detection. *Nano Lett.* 14, 2715–2719. doi: 10.1021/nl5006383

Lhuillier, E., Scarafagio, M., Hease, P., Nadal, B., Aubin, H., Xu, X. Z., et al. (2016). Infrared photodetection based on colloidal quantum-dot films with high mobility and optical absorption up to THz. *Nano Lett.* 16, 1282–1286. doi: 10.1021/acs.nanolett.5b04616

Liu, H., Lhuillier, E., and Guyot-Sionnest, P. (2014). 1/f noise in semiconductor and metal nanocrystal solids. *J. Appl. Phys.* 115:154309. doi: 10.1063/1.4871682

Liu, Z., Janes, L. M., Saniepay, M., and Beaulac, R. (2018). Charge storage and quantum confinement resilience in colloidal indium nitride nanocrystals. *Chem. Mater.* 30, 5435–5443. doi: 10.1021/acs.chemmater.8b02340

Livache, C., Goubet, N., Martinez, B., Jagtap, A., Qu, J., Ithurria, S., et al. (2018). Band edge dynamics and multiexciton generation in narrow band gap HgTe nanocrystals. *ACS Appl. Mater. Interfaces* 10, 11880–11887. doi: 10.1021/acsami.8b00153

Livache, C., Izquierdo, E., Martinez, B., Dufour, M., Pierucci, D., Keuleyan, S., et al. (2017). Charge dynamics and optolectronic properties in HgTe colloidal quantum wells. *Nano Lett.* 17, 4067–4074. doi: 10.1021/acs.nanolett.7b00683

Luther, J. M., Jain, P. K., Ewers, T., and Alivisatos, A. P. (2011). Localized surface plasmon resonances arising from free carriers in doped quantum dots. *Nat. Mater.* 10, 361–366. doi: 10.1038/nmat3004

Malinowski, P. E., Georgitzikis, E., Maes, J., Vamvaka, I., Frazzica, F., Van Olmen, J., et al. (2017). Thin-film quantum dot photodiode for monolithic infrared image sensors. *Sensors* 17:2867. doi: 10.3390/s17122867

Martinez, B., Livache, C., Goubet, N., Jagtap, A., Cruguel, H., Ouerghi, A., et al. (2018). Probing charge carrier dynamics to unveil the role of surface ligands in HgTe narrow band gap nanocrystals. *J. Phys. Chem. C* 122, 859–865. doi: 10.1021/acs.jpcc.7b09972

Martinez, B., Livache, C., Notemgnou Mouafo, L. D., Goubet, N., Keuleyan, S., Cruguel, H., et al. (2017). HgSe self-doped nanocrystals as a platform to investigate the effects of vanishing confinement. *ACS Appl. Mater. Interfaces* 9, 36173–36180. doi: 10.1021/acsami.7b10665

Maurice, A., Haro, M. L., Hyot, B., and Reiss, P. (2013). Quantum dots: synthesis of colloidal indium antimonide nanocrystals using stibine (Part. Part. Syst. Charact. 10/2013). *Part. Part. Syst. Charact.* 30, 821–821. doi: 10.1002/ppsc.201370038

Melnychuk, C., and Guyot-Sionnest, P. (2018). Slow Auger Relaxation in HgTe Colloidal Quantum Dots. *J. Phys. Chem. Lett.* 9, 2208–2211. doi: 10.1021/acs.jpclett.8b00750

Park, M., Choi, D., Choi, Y., Shin, H., and Jeong, K. S. (2018). Mid-infrared intraband transition of metal excess colloidal Ag2Se nanocrystals. *ACS Photon.* 5, 1907–1911. doi: 10.1021/acsphotonics.8b00291

Protière, M., Nerambourg, N., Renard, O., and Reiss, P. (2011). Rational design of the gram-scale synthesis of nearly monodisperse semiconductor nanocrystals. *Nanoscale Res. Lett.* 6:472. doi: 10.1186/1556-276X-6-472

Qu, J., Goubet, N., Livache, C., Martinez, B., Amelot, D., Gréboval, C., et al. (2018). Intraband mid-infrared transitions in Ag2Se nanocrystals: potential and limitations for Hg-free low-cost photodetection. *J. Phys. Chem. C* 122, 18161–18167. doi: 10.1021/acs.jpcc.8b05699

Robin, A., Livache, C., Ithurria, S., Lacaze, E., Dubertret, B., and Lhuillier, E. (2016). Surface control of doping in self-doped nanocrystals. *ACS Appl. Mater. Interfaces* 8, 27122–27128. doi: 10.1021/acsami.6b09530

Rosencher, E. (2002). *Optoelectronics*. Cambridge; New York, NY: Cambridge University Press.

Runnerstrom, E. L., Bergerud, A., Agrawal, A., Johns, R. W., Dahlman, C. J., Singh, A., et al. (2016). Defect engineering in plasmonic metal oxide nanocrystals. *Nano Lett.* 16, 3390–3398. doi: 10.1021/acs.nanolett.6b01171

Sagar, L. K., Walravens, W., Maes, J., Geiregat, P., and Hens, Z. (2017). HgSe/CdE (E = S, Se) core/shell nanocrystals by colloidal atomic layer deposition. *J. Phys. Chem. C* 121, 13816–13822. doi: 10.1021/acs.jpcc.7b02803

Sahu, A., Khare, A., Deng, D. D., Norris, D. J. (2012). Quantum confinement in silver selenide semiconductor nanocrystals. *Chem. Commun.* 48, 5458–5460. doi: 10.1039/C2CC30539A

Sargent, E. H. (2008). Solar cells, photodetectors, and optical sources from infrared colloidal quantum dots. *Adv. Mater.* 20, 3958–3964. doi: 10.1002/adma.200801153

Sargent, E. H. (2012). Colloidal quantum dot solar cells. *Nat. Photon.* 6, 133–135. doi: 10.1038/nphoton.2012.33

Savich, G. R., Pedrazzani, J. R., Sidor, D. E., Maimon, S., and Wicks, G. W. (2011). Dark current filtering in unipolar barrier infrared detectors. *Appl. Phys. Lett.* 99:121112. doi: 10.1063/1.3643515

Savich, G. R., Pedrazzani, J. R., Sidor, D. E., and Wicks, G. W. (2013). Benefits and limitations of unipolar barriers in infrared photodetectors. *Infrared Phys. Technol.* 59, 152–155. doi: 10.1016/j.infrared.2012.12.031

Schimpf, A. M., Lounis, S. D., Runnerstrom, E. L., Milliron, D. J., and Gamelin, D. R. (2015). Redox chemistries and plasmon energies of photodoped In2O3 and Sn-doped In2O3 (ITO) nanocrystals. *J. Am. Chem. Soc.* 137, 518–524. doi: 10.1021/ja5116953

Shen, G., and Guyot-Sionnest, P. (2016). HgS and HgS/CdS colloidal quantum dots with infrared intraband transitions and emergence of a surface plasmon. *J. Phys. Chem. C* 120, 11744–11753. doi: 10.1021/acs.jpcc.6b04014

Spencer, B. F., Graham, D. M., Hardman, S. J. O., Seddon, E. A., Cliffe, M. J., Syres, K. L., et al. (2013). Time-resolved surface photovoltage measurements at n-type photovoltaic surfaces: Si(111) and ZnO(10\{1}0). *Phys. Rev. B* 88:195301. doi: 10.1103/PhysRevB.88.195301

Srivastava, V., Dunietz, E., Kamysbayev, V., Anderson, J. S., and Talapin, D. V. (2018). Monodisperse InAs quantum dots from aminoarsine precursors: understanding the role of reducing agent. *Chem. Mater.* 30, 3623–3627. doi: 10.1021/acs.chemmater.8b01137

Sun, Z., Liu, Z., Li, J., Tai, G. A., Lau, S.-P., and Yan, F. (2012). Infrared photodetectors based on CVD-grown graphene and PbS quantum dots with ultrahigh responsivity. *Adv. Mater.* 24, 5878–5883. doi: 10.1002/adma.201202220

Talapin, D. V., and Murray, C. B. (2005). PbSe nanocrystal solids for n- and p-channel thin film field-effect transistors. *Science* 310, 86–89. doi: 10.1126/science.1116703

Tan, L., Li, P., Sun, B., Chaker, M., and Ma, D. (2017). Stabilities related to near-infrared quantum dot-based solar cells: the role of surface engineering. *ACS Energy Lett.* 2, 1573–1585. doi: 10.1021/acsenergylett.7b00194

Tandon, B., Yadav, A., Khurana, D., Reddy, P., Santra, P. K., and Nag, A. (2017). Size-induced enhancement of carrier density, LSPR quality factor, and carrier mobility in Cr–Sn doped In2O3 Nanocrystals. *Chem. Mater.* 29, 9360–9368. doi: 10.1021/acs.chemmater.7b03351

Tang, X., Ackerman, M. M., and Guyot-Sionnest, P. (2018). Thermal imaging with plasmon resonance enhanced HgTe colloidal quantum dot photovoltaic devices. *ACS Nano* 12, 7362–7370. doi: 10.1021/acsnano.8b03871

Tang, X., Tang, X., and Lai, K. W. C. (2016). Scalable fabrication of infrared detectors with multispectral photoresponse based on patterned colloidal quantum dot films. *ACS Photonics* 3, 2396–2404. doi: 10.1021/acsphotonics.6b00620

Wang, H., Lhuillier, E., Yu, Q., Mottaghizadeh, A., Ulysse, C., Zimmers, A., et al. (2015). Effects of electron-phonon interactions on the electron tunneling spectrum of PbS quantum dots. *Phys. Rev. B* 92:041403. doi: 10.1103/PhysRevB.92.041403

White, A. M. (1987). *Infra Red Detectors*. Available online at: https://patents.google.com/patent/US4679063A/en (Accessed September 13, 2018)

Yakunin, S., Dirin, D. N., Protesescu, L., Sytnyk, M., Tollabimazraehno, S., Humer, M., et al. (2014). High infrared photoconductivity in films of arsenic-sulfide-encapsulated lead-sulfide nanocrystals. *ACS Nano* 8, 12883–12894. doi: 10.1021/nn5067478

Yifat, Y., Ackerman, M., and Guyot-Sionnest, P. (2017). Mid-IR colloidal quantum dot detectors enhanced by optical nano-antennas. *Appl. Phys. Lett.* 110:041106. doi: 10.1063/1.4975058

Zhang, H., Zhang, R., Schramke, K. S., Bedford, N. M., Hunter, K., Kortshagen, U. R., et al. (2017). Doped silicon nanocrystal plasmonics. *ACS Photonics* 4, 963–970. doi: 10.1021/acsphotonics.7b00026

Conflict of Interest Statement: The authors declare that the research was conducted in the absence of any commercial or financial relationships that could be construed as a potential conflict of interest.

Advantages of publishing in Frontiers

OPEN ACCESS
Articles are free to read for greatest visibility and readership

FAST PUBLICATION
Around 90 days from submission to decision

HIGH QUALITY PEER-REVIEW
Rigorous, collaborative, and constructive peer-review

TRANSPARENT PEER-REVIEW
Editors and reviewers acknowledged by name on published articles

Frontiers
Avenue du Tribunal-Fédéral 34
1005 Lausanne | Switzerland

Visit us: www.frontiersin.org
Contact us: info@frontiersin.org | +41 21 510 17 00

REPRODUCIBILITY OF RESEARCH
Support open data and methods to enhance research reproducibility

DIGITAL PUBLISHING
Articles designed for optimal readership across devices

FOLLOW US
@frontiersin

IMPACT METRICS
Advanced article metrics track visibility across digital media

EXTENSIVE PROMOTION
Marketing and promotion of impactful research

LOOP RESEARCH NETWORK
Our network increases your article's readership